GROWTH OF ZnO NANORODS USING HYDROTHERMAL AND MODIFIED CHEMICAL BATH DEPOSITION FOR DEVICE APPLICATIONS

by

SABAH M. MOHAMMAD

Thesis submitted in fulfillment of the requirements

for the degree of

Doctor of Philosophy

March 2017

ACKNOWLEDGEMENT

In the name of Allah, Most Gracious, Most Merciful

First and foremost, I thank the Almighty Allah for granting me health,

patience, and inspiration to complete this research.

I am deeply thankful to my main supervisor, Prof. Dr. Zainuriah Hassan for

her excellent scholar guidance, intellectual support, and continuous support for my

Ph.D study and related research. Thanks again for having your door open every time

I needed help.

I would also like to thank my co-supervisor Dr. Naser Mahmoud Ahmed for

his insight comments and encouragement, and support throughout this study.

I am also very grateful to Universiti Sains Malaysia for providing financial

support for my research and for giving me the chance to be a graduate assistant. I

also express appreciation to the staff of the Nano-Optoelectronics Research and

Technology Laboratory (NOR Lab) for their technical assistance during my

laboratory work.

Finally, I would like to thank all my friends and colleagues for their support.

Sabah M. Mohammad

Penang, Malaysia. 2017

ii

TABLE OF CONTENTS

ACK	NOWLEDGEMENTii
TABL	E OF CONTENTSiii
LIST	OF TABLESviii
LIST	OF FIGURESix
LIST	OF ABBREVIATIONSxiii
LIST	OF SYMBOLSxv
ABST	RAKxvi
ABST	RACTxviii
СНАН	PTER 1: INTRODUCTION1
1.1	Problem Statement
1.2	Thesis Objectives5
1.3	Thesis Originality5
1.4	Thesis Overview6
СНАІ	PTER 2: LITERATURE REVIEW AND THEORETICAL BACKROUND8
2.1	Introduction8
2.2	General Properties of ZnO
	2.2.1 Crystal Structure Properties of ZnO9
	2.2.2 Optical Properties of ZnO10
2.3	Growth Methods of ZnO NRs12
	2.3.1 Growth Mechanism of ZnO NRs by CBD Method13

	2.3.2 Hydrothermal Growth of ZnO NRs on Highly Flexible Nylon
	2.3.3 Direct Heat Substrate-Modified Chemical Bath Deposition (DHS-MCBD) Technique for Growth of Ultralong ZnO NRs15
2.4	Metal-Semiconductor-Metal (MSM) Photodetector
2.5	Operational Parameters of Photodetectors20
	2.5.1 Current Gain
	2.5.2 Responsivity
	2.5.3 The Photoconduction Mechanism in ZnO NRs21
2.6	Overview of ZnO Nanostructures for Gas Sensing23
	2.6.1 H ₂ Gas Sensing Mechanism of ZnO NRs23
2.7	Literature Review of Flexible Electronic Devices25
	2.7.1 Flexible UV Detectors Based on ZnO NRs25
	2.7.2 Flexible Gas Sensor Based on ZnO NRs26
2.8	Light Emitting Diodes (LEDs)
	2.8.1 Forward and Reverse Bias29
	2.8.2 Junction Breakdown32
	2.8.3 Electron and Hole Recombination in Semiconductors
	2.8.4 Radiative Recombination Mechanisms32
	2.8.5 Literature Review of ZnO-Based LED35
	2.8.6 Homojunction and Heterojunction Structure of LED
CHA:	PRER 3: METHODOLOGY AND INSTRUMENTS40
3.1	Introduction40
3.2	Substrate Cleaning40
3.3	Radio Frequency/Direct Current (RF/DC) Sputtering System
3 4	Thermal Treatment Processes

3.5	Thermal Analysis of Thermo-Nylon Substrate44
3.6	Hydrothermal Synthesis of ZnO NRs45
	3.6.1 Hydrothermal Synthesis of ZnO NRs and Fabrication of MSM UV-PDs45
	3.6.2 Hydrothermal Synthesis of ZnO NRs and Fabrication of a MSM H ₂ Gas Sensing Device
3.7	Synthesis of Ultra-Length ZnO NRs by DHS-MCBD Technique49
	3.7.1 Growth of Ultralong ZnO NRs on ZnO Seeded Silicon by DHS-MCBD Technique
	3.7.2 Growth of Ultralong ZnO NRs Directly on Seedless p-GaN/sapphire by DHS-MCBD Technique
	3.7.3 Fabrication of Nano-Size Junction LED56
3.8	Structural, Morphological and Optical Characterizations
	3.8.1 X-Ray Diffraction (XRD)58
	3.8.2 Field Emission Scanning Electron Microscopy (FESEM) and Energy Dispersive X-ray (EDX) Spectroscopy
	3.8.3 Transmission Electron Microscopy (TEM)60
	3.8.4 Atomic Force Microscopy (AFM)61
	3.8.5 Photoluminescence (PL) Measurements62
	3.8.6 Raman Spectroscopy63
	3.8.7 Optical Absorption63
3.9	Shadow Grid Mask65
3.10	Device Characterization Techniques
	3.10.1 Measurements of Ultraviolet (UV) Photodetector66
	3.10.2 Gas Testing System67
	3.10.3 Electroluminescence (EL) Measurements of LED68
CHAI	PTER 4: RESULTS AND DISCUSSION: HIGHLY FLEXIBLE MSM UV PHOTODETECTOR DEVICES70

4.1	Introduction70
4.2	Thermal Properties of Substrate70
4.3	Effect of Different Seed-Heat-Treatment Duration
4.4	Effects of Seed Heat Treatment Duration on Growth of ZnO NRs75
4.5	TEM Images of ZnO NRs77
4.6	Structural Characterization by X-ray Diffraction79
4.7	Optical Properties of the Grown ZnO NRs Array81
4.8	UV Detection Properties82
4.9	Summary85
СНАІ	PTER 5: RESULTS AND DISCUSSION: HIGHLY FLEXIBLE HYDROGEN GAS SENSOR DEVICE86
5.1	Introduction86
5.2	Structural Characterization by X-ray Diffraction
5.3	Optical Properties of the Grown ZnO NRs
5.4	Current-Voltage (I-V) Characteristics of the Device (Pt/ZnO NRs/Pt)90
5.5	Hydrogen Gas Sensing Property91
5.6	Characterization of the Grown ZnO NRs96
5.7	Summary101
CHA	PTER 6: RESULTS AND DISCUSSION: DHS-MCBD SYSTEM FOR THE GROWTH OF ULTRALONG ZnO NRs ON SEEDED SILICON AND SEEDLEES p-GaN SUBSTRATES AND FABRICATION OF A LED102
6.1	Introduction102
6.2	DHS-MCBD System for The Growth of Ultralong ZnO NRs on Seeded Silicon
	6.2.1 Characterization of the Ultralong ZnO NRs
	6.2.2 Energy-Dispersive X-ray Spectroscopy105

	6.2.3 Structural Characterization by X-ray Diffraction	105
	6.2.4 Raman Spectroscopy	107
	6.2.5 Photoluminescence (PL) Measurement	108
6.3	DHS-MCBD System for the Growth of Ultralong ZnO NRs on Seedless GaN and Fabrication of a Nano-Size Junction LED	
	6.3.1 Characterization of the Ultralong ZnO NRs	111
	6.3.2 Structural Characterization by X-ray Diffraction	112
	6.3.3 Raman Spectroscopy	113
	6.3.4 Photoluminescence (PL) Measurements	114
	6.3.5 Current-Voltage (I-V) Characteristics	116
	6.3.6 Electroluminescence Characteristics	117
6.4	Summary	123
CHAI	PTER 7: CONCLUSION AND FUTURE STUDIES	124
7.1	Conclusions	124
7.2	Future Studies	126
REFE	ERENCES	127
APPE	ENDICES	146
LIST	OF PUPLICATIONS	

LIST OF TABLES

		Page
Table 2.1:	The diameter, length and aspect ratio of ZnO NRs grown using different fabrication methods and reported by several groups	
Table 2.2:	Summary of flexible UV detector devices based on ZnO NRs with their different structure used, type flexible substrates, wavelength of light detection, response, decay times, responsivity, and current gain.	
Table 2.3:	EL spectra of LED fabricated using different fabrication methods	39
Table 4.1:	Structural parameters determined from (002) reflection, (FWHM full width at half maximum) and the determined optical band gap values for samples	
Table 4.2:	Dark current, photocurrent, responsivity and average aspect ratio with different time of heat treatment of ZnO seeded layer/nylon substrate	
Table 5.1:	Effect of temperature on the sensitivity, rise time, and recovery time of the fabricated device.	
Table 5.2:	Sensing properties of ZnO gas sensor obtained from previous and present work.	95

LIST OF FIGURES

		Page
Figure 2.1:	Crystal structure model of hexagonal wurtzite ZnO (a) hexagonal wurtzite crystal structure of ZnO [31], (b) polar faces, perpendicular to the 0001 direction, and non-polar faces, parallel to the 0001 direction [32].	9
Figure 2.2:	Schematic energy level diagram of various defect level emissions in ZnO [41, 42].	12
Figure 2.3:	A structure of a conventional MSM-PD: (a) the top of the surface and (b) cross-sectional views	19
Figure 2.4:	A schematic of UV-detection mechanism of ZnO NR with surrounding air: (a) the rod of ZnO in the dark condition and (b) the photogenerated electron-hole pairs during UV illumination. (c) energy band diagram during UV illumination [76].	22
Figure 2.5:	Schematic representations of energy band diagrams of a p-n junction under various biasing conditions. (a) Thermal equilibrium condition, (b) Forward bias condition, and (c) Reverse bias condition [108]	30
Figure 2.6:	Three types of semiconductor heterojunctions [116]	31
Figure 2.7:	The intrinsic radiative recombination in a semiconductor (direct band to band)	34
Figure 2.8:	The extrinsic radiative recombination: (a) Donor state-valence band, (b) Conductive band-acceptor state, (c) Donor-acceptor recombination, and (d) Bound exciton annihilation.	35
Figure 3.1:	Flowchart of the preparation processes for ZnO NRs, and fabrication of MSM PDs, H ₂ gas sensor and nano-size junction LED devices	41
Figure 3.2:	Schematic of the fabrication procedure of MSM UV-PDs	47
Figure 3.3:	Schematic of the fabrication procedure of the hydrogen gas sensor	49
Figure 3.4:	Real optical photo of the direct heat substrate - modified chemical bath deposition (DHS-MCBD) apparatus in accordance with the present work.	53
Figure 3.5:	Schematic figure of the direct heat substrate - modified chemical bath deposition (DHS-MCBD) apparatus in accordance with the present work.	54

Figure 3.6:	A schematic diagram of n-ZnO NRs /p-GaN heterostructure LED in accordance with the procedure described in section 3.7.3
Figure 3.7:	Bragg diffraction in a crystal. The angles at which diffraction occurs are a function of the distance between planes and the X-ray wavelength [146]
Figure 3.8:	The real top-view microscopic image of ZnO NRs MSM photodetector device65
Figure 3.9:	Schematic of experimental setup for photodetection measurements of the spectral response of the devices
Figure 3.10:	Gas sensor test system configuration
Figure 4.1:	DSC spectrum of the flexible nylon substrate71
Figure 4.2:	TGA spectra of the flexible nylon substrate72
Figure 4.3:	Surface morphology of ZnO seeds, (a) at room temperature and heat treated at 180 °C for (b) 0.5 h; (c) 3 h; (d) 6 h
Figure 4.4:	3D-topography obtained by AFM of ZnO films over (3x3) µm² scan area (a) at room temperature and heat treated at 180 °C for (b) 0.5 h; (c) 3 h; (d) 6 h
Figure 4.5:	FESEM images of ZnO NRs grown onto ZnO seeds/nylon-substrate, (a) at room temperature and heat treated at 180 °C for (b) 0.5 h; (c) 3 h; (d) 6 h
Figure 4.6:	TEM images of ZnO NRs grown onto ZnO seeds/nylon substrates, (a) at room temperature and heat treated at 180 °C for (b) 0.5 h; (c) 3 h; (d) 6 h
Figure 4.7:	X-ray diffraction patterns of ZnO NRs formed onto ZnO seeds/nylon-substrate (a) at room temperature and heat treated at 180 °C for (b) 0.5 h; (c) 3 h; (d) 6 h. The insets show the peak (002) reflection
Figure 4.8:	Optical absorption spectra of the ZnO NRs on ZnO seeds /nylon substrate, (a) at room temperature and heat treated at 180 °C for (b) 0.5 h; (c) 3 h; (d) 6 h. The inset shows plot of $\alpha hv2$ versus hv
Figure 4.9:	I-V characteristics of the fabricated MSM UV-photodectectors under UV illumination (lph) (λ =365 nm) and in dark (ld). The inset shows the current gain-voltage curves
Figure 5.1:	X-ray diffraction pattern of ZnO NRs formed onto ZnO seed/nylon substrate

Figure 5.2:	Room-temperature PL spectrum of ZnO NRs formed onto ZnO seed/nylon substrate. The inset shows the zoom in on the PL in the range of wavelength =500 to 800 nm (DLE region)
Figure 5.3:	I-V curves of the device (Pt/ZnO NRs/Pt) as prepared and annealed at 180 °C for 4 h91
Figure 5.4:	Sensitivity and repeatability of ZnO NRs formed onto ZnO seed/nylon gas sensor at different sensor temperatures: (a) RT, (b) 75 °C, (c) 120 °C, and (d) 180 °C
Figure 5.5:	Real-time sensitivity of the ZnO nanorod array sensor upon exposure to H ₂ with various concentrations (750, 1000, 1500, and 2000 ppm) at operating temperature of 75 °C
Figure 5.6:	FESEM images of ZnO NRs grown on ZnO seeds/nylon substrate at 90 °C for 3 h (high magnification and low magnification). The inset is the EDX spectrum
Figure 5.7:	Illustration of presumed paths for electrons through ZnO NRs and between two Pt electrodes
Figure 5.8:	TEM image of ZnO NRs grown onto ZnO seeds/nylon substrate99
Figure 5.9:	The sensitivity versus time of the prepared device at an operating temperature of 100 °C, and under exposure to 500 ppm of H ₂ for 45 min
Figure 6.1:	FESEM cross section images (different magnification) with 30° tilted views of ultralong ZnO NRs grown onto ZnO seeds/silicon-substrate104
Figure 6.2:	EDX spectrum of ZnO NRs formed on ZnO seeds/silicon-substrate for the sample
Figure 6.3:	High-resolution X-ray diffraction pattern of ZnO NRs formed on ZnO seeds/silicon substrate. The inset shows the zoom in on the XRD pattern in the range of $2\theta = 31$ to 38 degree
Figure 6.4:	Raman spectrum of ZnO NRs formed on ZnO seeds/silicon substrate 109
Figure 6.5:	Room-temperature photoluminescence spectrum of ZnO NRs formed on ZnO seeds/silicon substrate
Figure 6.6:	FESEM top-view and cross-sectional images (different magnification) with 30° tilted views of ZnO NRs grown on p-GaN/sapphire substrate, where the left inset shows EDX spectra of ZnO NRs grown on p-GaN/sapphire substrate
Figure 6.7:	X-ray diffraction pattern of ZnO NRs formed on p-GaN/sapphire substrate

Figure 6.8:	Room-temperature Raman spectra of p-GaN/sapphire substrate and n-ZnO NRs formed on p-GaN/sapphire substrate114
Figure 6.9:	PL spectra of p-GaN/sapphire substrate and n-ZnO NRs formed on p-GaN/sapphire substrate
Figure 6.10:	I-V characteristics of n-ZnO NRs /p-GaN LED, where the bottom right inset shows the ohmic characteristic of Pd/ITO contact on p-GaN layer.
Figure 6.11:	Room-temperature EL measurement spectra emission from back side of the n-ZnO NRs/p-GaN LED with different current injections at the reverse breakdown bias, where bottom right inset shows the zoom in on the EL spectra in the range of 450 to 550nm. Top right inset shows real optical photos of the LED in the ambient lighting at the current injection of 22 mA.
Figure 6.12:	Room-temperature EL measurement spectra emission from front side of the n-ZnO NRs /p-GaN LED with different current injections at the reverse breakdown bias, where bottom right inset shows the zoom in on the EL spectra in the range of 450 to 650 nm. Top right inset shows real optical photos of the LED in the ambient lighting at the current injection of 22 mA
Figure 6.13:	Energy band diagram of n-ZnO NRs /p-GaN heterojunction at (a) zero and (b) reverse bias

LIST OF ABBREVIATIONS

a. u. Arbitrary unit

AFM Atomic force microscope

E_g Band gap energy

CBD Chemical bath deposition

CVD Chemical vapor deposition

CB Conduction band

CFI Continuous flow injection

I_{air} Current in the presence of air atmosphere

I_H Currents in the presence of hydrogen gas

I-V Current-voltage

I_d Dark current

DLE Deep level emission

W Depletion layer width

DSC Differential scanning calorimetry

EL Electroluminescence

EDX Energy dispersive X-ray

E_F Fermi level of semiconductor

FESEM Field emission scanning electron microscopy

FWHM Full width at half maximum

IR Infrared radiation

LED Light emitting diode

MOCVD Metal-organic chemical vapor deposition

MSM Metal-semiconductor-metal

MBE Molecular beam epitaxy

NRs Nanorods

1D One-dimensional

I_{ph} Photocurrent

PL Photoluminescence

PVD Physical vapor deposition

PC Polycarbonate

PDMS Polydimethylsiloxane

PES Polyethersulfone

PEN Polyethylene naphthalate

PET Polyethylene terephthalate

PI Polyimide

PLD Pulsed laser deposition

RCA Radio Corporation of America

RF Radio frequency

R Responsivity

RT Room temperature

S Sensitivity

TGA Thermal gravimetric analysis

TEM Transmission electron microscopy

UV Ultraviolet

VB Valence band

XRD X-ray diffraction

LIST OF SYMBOLS

K_B Boltzmann constant

*C Celsius temperature

 θ Diffraction angle

 χ Electron affinity

q Electron charge

eV Electron volt

e-h Electron-hole

v Frequency

d_{hkl} Interplant spacing of the crystal

n Lattice constant

a, c Lattice constants

hkl Miller indices

h Planck's constant

s Second

 ε_{zz} Strain

t Time

λ Wavelength

PERTUMBUHAN NANOROD ZnO MENGGUNAKAN HIDROTERMA DAN PEMENDAPAN RENDAMAN KIMIA YANG DIUBAHSUAI UNTUK APLIKASI PERANTI

ABSTRAK

Zink oksida (ZnO) adalah semikonduktor jurang jalur lebar yang berpotensi dalam aplikasi peranti elektronik dan peranti optoelektronik berkecekapan tinggi. Kajian ini mengandungi dua objektif. Pertama, adalah untuk mensintesis nanorod (NRs) ZnO yang sejajar, menegak dan condong di atas substrat nilon melalui kaedah hidroterma, dan seterusnya memfabrikasikan pengesan foto ultra ungu (UV-PDs) yang berkos rendah dan sangat fleksibel dan peranti pengesan gas hidrogen (H₂). Prarawatan haba untuk benih/substrat ZnO pada suhu 180°C dengan pelbagai tempoh (0.5-6 jam) menunjukkan perubahan penting. Pemerhatian morfologi mendedahkan pembentukan sejajar nanorod berbentuk seperti heksagon apabila diameter, panjang (nisbah aspek), luas permukaan dan kepadatan meningkat dengan peningkatan masa rawatan haba. Analisis pembelauan sinar-X mengesahkan pembentukan fasa wurtzit ZnO bersama dengan orientasi pilihan (002) dan peningkatan penghabluran. fotoluminesen mempamerkan puncak pemancaran pinggir jalur Spektrum berhampiran ultraungu (UV) yang kuat dan tajam dan lebih tinggi berbanding daripada puncak lebar. Berdasarkan keputusan di atas, didapati bahawa suhu rawatan haba yang optimum dan jangka masa untuk menghasilkan benih ZnO seragam adalah 180°C selama 3 jam. Untuk pengesan UV logam-semikonduktor logam (MSM). filem yang optimum (3 jam) menunjukkan sambutan tertinggi dan nisbah arus 0.4774 A/W dan 9.15 masing-masing untuk cahaya UV pada 365 nm di bawah pincangan 5 V, ini disebabkan oleh nisbah permukaan-isipadu yang tinggi dan kualiti hablur yang

tinggi dengan kecacatan struktur yang kurang dalam NRs ZnO. Untuk sensor gas H₂, kepekaan dan masa tindak balas pengesan gas berasaskan ZnO untuk gas hidrogen pada suhu operasi yang berbeza dan dalam pelbagai kepekatan hidrogen telah disiasat. Di bawah pendedahan 500 ppm H₂ pada suhu yang berbeza daripada suhu bilik kepada 180 °C, kepekaan meningkat daripada 109% kepada 264%. Apabila gas H₂ yang didedahkan meningkat daripada 750 ppm hingga 2000 ppm pada suhu tetap 75 °C, kepekaan juga meningkat secara mendadak dari 246% hingga 578%. Selain itu, kedua-dua tindak balas dan masa pemulihan untuk peranti bagi kedua-dua ujian telah dipertingkatkan. Tujuan kedua kajian ini adalah untuk mensintesis NRs ZnO ultra panjang pada substrat berbiji dan tidak berbiji melalui teknik novel iaitu kaedah pemendapan rendaman kimia dengan haba langsung yang diubahsuai ke atas substrat (DHS-MCBD) dan seterusnya mengfabrikasikan peranti diod pemancar cahaya (LED) simpang saiz nano. Khususnya, sistem DHS-MCBD menyediakan satu kaedah yang mudah dan kos rendah untuk membentuk bahan filem berstruktur nano berskala tinggi pada substrat. Ia telah berjaya digunakan untuk mensintesis NRs ZnO menegak, ultra panjang, sejajar, dan berbentuk heksagon pada substrat silikon berbiji dan substrat p-GaN tidak berbiji. Ciri-ciri LED arus-voltan (I-V) mencadangkan bahawa kesan pecahan peranti ini disebabkan oleh kesan terowong di antara muka simpang hetero itu. Sifat luminesen peranti LED yang difabrikasikan telah disiasat dari kedua-dua bahagian LED pada suhu bilik dengan kaedah elektroluminesen (EL). Pemancaran spektrum EL dari bahagian belakang peranti itu terdiri daripada satu pancaran ultra ungu dan jalur lebar pancaran hijau, manakala pemancaran dari sebelah hadapan terdiri daripada pancaran ungu berhampiran dengan jalur lebar pancaran hijau. Pemancaran EL juga adalah cukup terang untuk dilihat dengan mata kasar di bawah pencahayaan bilik biasa.

GROWTH OF ZnO NANORODS USING HYDROTHERMAL AND MODIFIED CHEMICAL BATH DEPOSITION FOR DEVICE APPLICATIONS

ABSTRACT

Zinc oxide (ZnO) is a promising wide band gap semiconductor with applications in high efficiency electronic and optoelectronic devices. The present study follows two objectives. First, synthesis of vertical and inclined well-aligned ZnO nanorods (NRs) on a nylon substrate via the hydrothermal method, and subsequently fabricate the highly flexible low-cost ultraviolet photodiodes (UV-PDs) and hydrogen (H₂) gas sensor devices. Pre-heat treatment of ZnO seeds/substrate at 180°C with varying duration (0.5-6 h) shows important changes. Morphological observations revealed the formation of aligned hexagonal-like shaped nanorods when the diameter, length (aspect ratio), surface area and density increase with increasing heat treatment time. The X-ray diffraction analysis confirms the formation of wurtzite ZnO phase with a preferred orientation along (002) direction and enhanced crystallinity. Photoluminescence spectra exhibited a strong and sharp ultraviolet (UV) near band edge emission peak that was higher than that of the broad peak. According to the above results, it was found that the optimum heat-treatment temperature and duration to produce uniform ZnO seeds was 180°C for 3 h. For metal-semiconductor-metal (MSM) UV detectors, the optimized film (3 h) showed the highest responsivity and current gain of 0.4774 A/W and 9.15, respectively for UV light at 365 nm under a 5 V bias due to the high surface-to-volume ratio and high crystalline quality with less structural defects within ZnO NRs. For H2 gas sensor,

the sensitivity and response time behaviors of the ZnO-based gas sensor to hydrogen gas at different operation temperatures and in various hydrogen concentrations were investigated. Under 500 ppm of H₂ exposure at different temperatures from room temperature to 180 °C, the sensitivity increased from 109% to 264%. When the exposed H₂ gas increased from 750 ppm to 2000 ppm at a fixed temperature of 75 °C, the sensitivity also sharply increased from 246% to 578%. Moreover, both the response and recovery time of the device during both tests were enhanced. The second aim of the study is to synthesize ultralong ZnO NRs on the seeded and seedless substrates via a novel technique, a direct heat substrate-modified chemical bath deposition (DHS-MCBD), and subsequently fabricate a nano-size junction light emitting diode (LED) device. In particular, DHS-MCBD system provides a simple and low-cost method for forming a high-scale nanostructured material film on a substrate. It has been successfully used to synthesize vertically, ultra-long, wellaligned, and hexagonal-shaped ZnO NRs on seeded silicon and seedless p-GaN substrates. Current-voltage (I-V) characteristics of the LED suggested that the breakdown effect of the device is caused by tunnelling effect at the interface of the heterojunction. The luminescence properties of the fabricated LED device were investigated from both sides of LED at room temperature by electroluminescence (EL). EL spectrum emission from back side of the device was composed of an ultraviolet emission and a broad band around green emission, while the emission from front side was composed of a near violet emission with a broad band green emission. EL emission was also bright enough to be seen with the naked eye under normal room illumination.

CHAPTER 1: INTRODUCTION

Zinc oxide (ZnO) semiconductor is of great interest because of its significant and unique properties, such as a wide direct energy gap (3.37 eV), thereby a high transparency in the visible light with a large exciton binding energy (≈60 meV), hence making it luminous efficiency at room temperature comparable with other competitive materials. In addition, it is considered as low cost material, nontoxic and suitable for operating in the ultraviolet (UV) wavelength regions [1, 2]. Among various oxide compounds, ZnO nanostructures present a large interest because of their important and unique properties for a huge range of nanotechnology applications such as UV detectors, chemical sensors, biosensors, pH sensors and UV light emitting devices (LEDs) [3].

Various synthesis methods have been recently developed for 1D ZnO nanomaterial growth, including hydrothermal or wet chemical methods [4], molecular beam epitaxy (MBE) [5], metal-organic chemical vapor deposition (MOCVD) [6, 7], pulsed laser deposition (PLD) [8], top-down approaches by etching [9], electrospinning [10, 11], and physical vapor deposition (PVD) [12, 13], and sputtering Although each synthesis technique [14]. offers unique advantages/disadvantages, the chemical bath deposition (CBD) or hydrothermal deposition is generally an inexpensive and facile method for the deposition of ZnO nanorods (ZnO NRs)-arrays over large areas. In 2001, Vayssieres et al. proposed an inexpensive process for fabricating highly oriented ZnO nanorods-arrays directly onto various type of substrates [15].

Shortly after Nakamura solved the p-type doping problem [16], the researchers have focused on the GaN material, leading to the wide commercialization

of GaN-based visible/blue/ultraviolet LEDs, lasers, and photodetectors. Currently, almost all commercial LEDs for solid-state lighting are manufactured by GaN material. Despite the potential of commercialization of the ZnO-based LEDs has been hampered by issues of simultaneously reducing intrinsic n-type doping semiconductor material as well as the fabrication of the stability and reliability of p-type ZnO still present a great challenge [17], ZnO is considered to be a potentially superior material for use in LEDs and laser diodes. Because of its much larger exciton binding energy (60 meV) compared to 21 meV for GaN (thermal energy at room temperature is about 25 meV), this means that one can expect out brighter and more robust excitonic-based ZnO emitters [18]. On the other hand, noble metals, such as GaN, SiC, etc, are always costly. Therefore, ZnO is a promising candidate for commercialization in a wide variety of applications [19]. Indeed, ZnO NRs-based UV-blue LEDs have been widely reported in the literature and a material that holds much promise for the future of solid-state lighting [20].

1.1 Problem Statement

Several essential problems addressed in this thesis, are summarized as follows:

Nowadays, flexible substrates have been widely used for fabrication of electronic portable devices because of their interesting properties such as thinness, flexibility, transparency, transportability, resistance to degradation or impact damage, light weight, rollable, and low cost. The flexible electrical devices such as photodetectors, gas sensors, and others offer a number of advantages compared with the rigid electrical devices. As a result, such devices are more potential to be applied in the future, especially with increasing demand for portable applications. However,

flexible electronic devices are rapidly developing due to the need of the modern technology for the electrical applications that are light weight, mechanically flexible, and reduced in size. Obviously, a substrate plays a key role and hardly to be a single factor in determining the extent of flexibility or rigidity for any processes of fabrication of electronic device. It is worth mentioning that the thickness of the base plays an important role in setting its flexibility, in which the flexibility increases when its thickness is reduced [21]. Therefore, it is crucial and beneficial to add a new flexible substrate with advanced specifications such as ultra-thin and high flexibility, to the field of fabrication of the flexible electrical devices. In spite of its importance, there has not been an extensive research on this issue.

Most synthesis methods for ultralong ZnO nanorods (NRs) arrays require high temperature, therefore such methods consume more energy and as a result, are expensive. Meanwhile, these methods are complex instruments. However, it is still difficult and challenging to fabricate ultralong ZnO nanorods arrays in order to obtain a high aspect ratio by the chemical bath deposition (CBD). This problematic issue might be due to two main reasons. First, it is because of decreasing in the concentration of a solution (source of ions) in the bath during growth with increase in duration of reaction. Second, it is because of supplying thermal energy indirectly usually in CBD method on a substrate in which the solution is heated. Another disadvantage of this method is that it is difficult to increase the temperature of a substrate because any increase in temperature of bath more than 100 °C leads to boiling of the solution that may cause inhomogeneous growth and undesirable contamination on the substrate.

To reduce a negative property in heterojunction case and increase the carrier injection efficiency, manufacturing of a nano-sized junction has been suggested by fabricating an n-ZnO NRs on p-GaN substrate instead of n-ZnO layer. In order to synthesise ZnO NRs on a substrate by CBD technique (or other low temperature methods), many researchers have proposed the deposition of seeds/layer between ZnO and a substrate or the use of some catalysts because the seed layer plays a significant role in fabricating the rods of ZnO on a substrate.

Although the mismatch between both materials such as ZnO and GaN is small, the fabricating of ZnO on GaN without seed layer has still been a major challenge due to low growth temperature. Meanwhile, there are many disadvantages in using the ZnO seed layer between n-type and p-type materials such as increasing the density of interfacial defects [22, 23]. Hence, the absence of interface layer (such as ZnO seed layer) between ZnO and GaN whereby the rods of ZnO start to grow directly from the surface of GaN layer which leads to the fabrication of a nano-sized junction between ZnO and GaN. It shows that the properties of ZnO NRs are related to the nature of GaN substrate.

In addition, the nano-size junction between ZnO and GaN plays an important role in enhancing the luminescence efficiency property of LED device that increases carrier tunneling efficiency through the junction [24-26]. Furthermore, this phenomenon can also be useful for other device applications, such as sensor, photodetector, and transistor, and so on.

1.2 Thesis Objectives

The main objectives of this thesis can be summarized in the following points:

- 1. To study the characteristics of vertically well-aligned ZnO NRs arrays grown by the low-temperature hydrothermal technique on a novel nylon substrate
- 2. To determine the optimum heat treatment duration applied to ZnO seed layer deposited on the flexible nylon substrate.
- 3. To investigate UV detection and gas sensing properties of the highly flexible metal-semiconductor-metal (MSM) UV photodetector and H₂ gas sensor devices, respectively.
- 4. To study the characteristics of vertically well-aligned ultra-long ZnO NRs arrays synthesized via DHS-MCBD technique on the Si seeded and GaN seedless substrates, and to investigate electroluminescence (EL) of the nano-size junction LED device.

1.3 Thesis Originality

The originality of this research work can be based on the following aspects:

- 1. A hydrothermal method for the growth of ZnO NRs on a cheap, ultrathin (15 μ m), and highly flexible nylon substrate is used.
- 2. The effects of the heat treatment duration applied to the ZnO seeded/nylon substrate are investigated.
- 3. Highly flexible MSM UV-PDs and H₂ gas sensor devices are fabricated.
- 4. DHS-MCBD as a novel technique for forming ultra-long ZnO NRs arrays on Si seeded and GaN seedless substrates is used.

- 5. DHS-MCBD technique is used to fabricate a nano-size junction between ZnO NRs and p-GaN layer, and as a result, a high-extraction-intensity light emitting diode (LED) was successfully fabricated.
- 6. The present work provides the ultaralong and ultradensity of ZnO NRs on the seeded and seedless substrates, and fabrication of a nanojunction device such as LED. What differentiates this work from the previous ones is that a substrate is directly heated (DHS) meanwhile the precursor solution is not exposed to the heat by any external heat sources. After an extensive literature review, it was concluded that no study has been reported on synthesis of ultralong ZnO NRs and the fabrication of LED device based on nanosize junction by modifying CBD method.

1.4 Thesis Overview

This thesis consists of eight chapters and organized as follows: Chapter 1 a brief introduction of ZnO material, its synthesis methods, and its applications. The problem statements are presents. Objectives of the project, and thesis originality are presented. Chapter 2 presents a literature review on general properties of ZnO material and ZnO NRs prepared by hydrothermal and DH-MCBD techniques. Flexible MSM UV-PD, flexible H₂ gas sensing, and LED devices are also included. Sensing mechanism of UV photodetector and H₂ gas sensor are discussed. The working principles of LED with radiative recombination mechanisms are also discussed. Chapter 3 describes the methodology and instrumentation used to analyze the prepared material and fabricated MSM UV-PDs, H₂ gas sensor, and LED devices. The results obtained are characterized and discussed in the next chapters. Chapter 4 presents the characterization results and discussion of the fabricated

MSM UV-PDs, which is highly flexible. The effect of heat treatment duration applied to the ZnO seeded/nylon substrate is also studied. Chapter 5 presents the characterization results and discussion of the highly flexible MSM H₂ gas sensor, that was fabricated. In Chapter 6 morphological, structural, and optical properties of the as-grown ultralong ZnO NRs on silicon and p-GaN substrates are investigated, and then the fabrication and characterization of a nano-size junction LED are discussed. Finally, the conclusions of this study with possible future researches are presented in Chapter 7.

CHAPTER 2: LITERATURE REVIEW AND THEORETICAL BACKROUND

2.1 Introduction

In this chapter, general properties of ZnO material, its synthesis methods as nanorods, and some of its applications such as MSM-photodetector, gas sensor, and LED devices are presented. Two methods are discussed; hydrothermal growth ZnO NRs on a novel highly flexible nylon substrate and DHS-MCBD as a novel technique for the growth of ultralong ZnO NRs on seeded and seedless substrates. Finally, a summary, review of articles, and theoretical background concerning the use of ZnO NRs in ultraviolet (UV) detection, H₂ gas sensing, and light-emitting diode (LED) are discussed.

2.2 General Properties of ZnO

ZnO is a II-VI group compound semiconductor material having a hexagonal (wurtzite-type) structure with lattice parameters at room temperature a = b = 0.3245 nm and c = 0.52066 nm [27]. Additionally, other favorable aspects of ZnO material are that it is cheap, non-toxic, relatively abundant source materials, and chemically stable [28]. The as-grown ZnO material, especially in case of the low growth temperature, is unintentionally n-type, and it is typically believed that it possesses many native defects, such as oxygen vacancy (V_o), interstitial zinc (Z_{ni}), zinc vacancy (V_{zn}), interstitial oxygen (O_i), and background impurities such as hydrogen are source of donors in ZnO. These defects are responsible for the deep level emissions (DLEs) [29, 30].

2.2.1 Crystal Structure Properties of ZnO

In fact, ZnO crystallizes stably at normal atmospheric pressure and thermodynamically in the hexagonal wurtzite structure, but it can be also in the zinc-blende structure, which can be stable when ZnO growth started from surface of the cubic substrates structure, such as ZnS. Figure 2.1 shows crystal structure model of hexagonal wurtzite ZnO, the clarification of its wurtzite structure is not complex. The wurtzite ZnO structure consists of alternating zinc (Zn) and oxygen (O) atoms, where each oxygen ion (0^{2-}) is surrounded tetrahedrally by four zinc ions (Zn^{2+}) , and vice versa. The ZnO structure has two polar surfaces the polar Zn (0001) and O (0001) terminated faces, and has other two most commonly of non-polar (1120) and (1010) surfaces possessing an equal number of Zn and O atoms [31, 32].

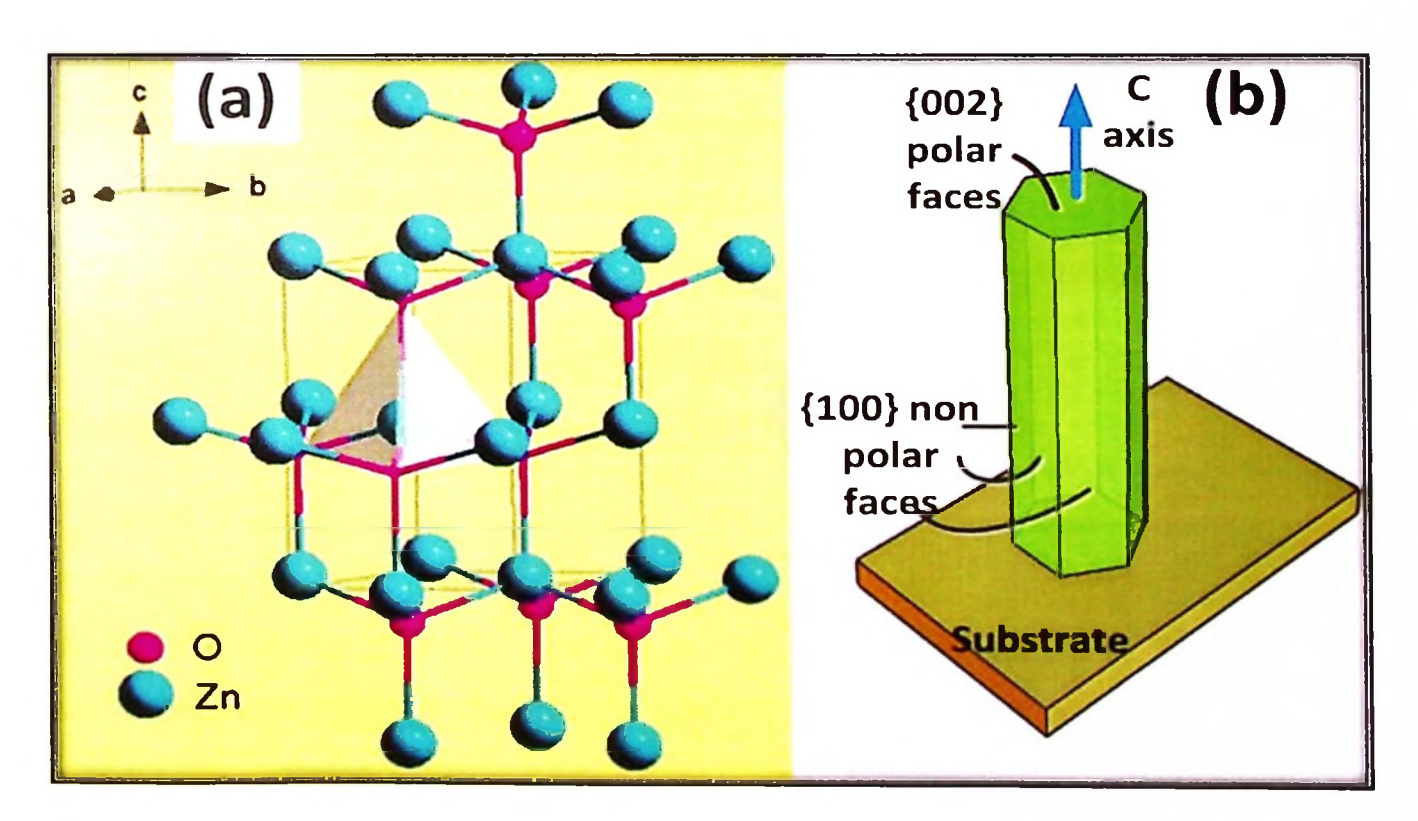


Figure 2.1: Crystal structure model of hexagonal wurtzite ZnO (a) hexagonal wurtzite crystal structure of ZnO [31], (b) polar faces, perpendicular to the [0001] direction, and non-polar faces, parallel to the [0001] direction [32].

The polar surfaces are very important characteristic of ZnO. It has a normal dipole moment along the c-axis due to the oppositely charged ions for Zn⁻ and O⁻, and that lead to the production of positively charged (0001) and negatively charged (000 $\overline{1}$) surfaces, respectively. Also, \pm (0001) surfaces of ZnO are atomically stable, flat and without surface reconstruction, therefore it can be considered that the structure of ZnO is somewhat stable [33].

2.2.2 Optical Properties of ZnO

ZnO semiconductor is of great interest because of its significant and unique properties, such as: large direct band of 3.37 eV, large exciton binding energy of 60 meV at RT, and high light trapping characteristics [27, 34]. Therefore, ZnO semiconductor is among the most promising and beneficial materials for an enormous range of nanotechnology applications, such as ultraviolet (UV) detectors, chemical sensors, biosensors, pH sensors, and UV blue light emitting devices [3]. Generally, direct band gap materials have essentially high luminescence yield compared to indirect band gap materials, and large band gap materials are useful for reducing the leakage current of the devices.

Higher exciton binding energy materials give brighter emissions, because exciton is already a bound system, which radiatively recombine with high efficiency without requiring traps to localize the carriers [35]. Optical properties of crystalline ZnO were mostly studied by the absorption or photoluminescence (PL) spectra. The absorption spectrum of the ZnO shows high transparency in the visible region and at long wavelengths ($\lambda > 380$ nm) as well as strong UV absorption at short wavelengths ($\lambda < 380$ nm), while ultraviolet (UV) emission peak and visible emissions are commonly observed in PL spectrum. Generally, UV emission peak of ZnO, which

represents the near-band-edge emission (NBE) of the wide ZnO band gap, is located at approximately 378 nm (3.28 eV), which resulted from the recombination of the free exciton process.

The PL spectra also reveals broad visible peaks that were related to the deep level emission (DLE) of ZnO, which was attributed to the native defects in ZnO NRs. In fact, the broad visible peaks are observed in the wavelength range starting approximately from 400 nm to 720 nm. However, the origins of deep level emissions of ZnO are still not fully understood, and many researchers suggested different and controversial explanations for these defect emissions (violet, blue, green, orange-red, and red). For example, many researchers have suggested that, within the DLE, the green emission has originated from both oxygen and zinc vacancies [36, 37], while other authors have reported that the green emissions can be attributed to oxygen vacancies (V_o) and zinc interstitial (Zn_i) [38, 39].

In fact, the origins of the ZnO PL emissions, especially for ZnO defect energy levels, are a complicated process and still not completely understood. However, theoretically, the positions of the Z_{ni}, zinc vacancy (V_{Zn}), V_o, and oxygen interstitials (O_i) are located at 0.22 eV, 3.06 eV, 2.47 eV, and 2.28 eV below the conduction band, respectively [40]. Figure 2.2 illustrates the schematic band diagram of the DLE emissions in ZnO, which presents the recombination of electron-hole pairs from different defects back to the valence band and which lead to emission of photon energy [41, 42]. The value of I_{UV}/I_{DLE} ratio (the intensity of the UV emission to the visible deep level) play important role to determine the quality and amount of defects in the ZnO material, in which this high difference in intensity suggests that the grown

ZnO NRs arrays have high quality with small number of detects, and a good hexagonal structure [43, 44].

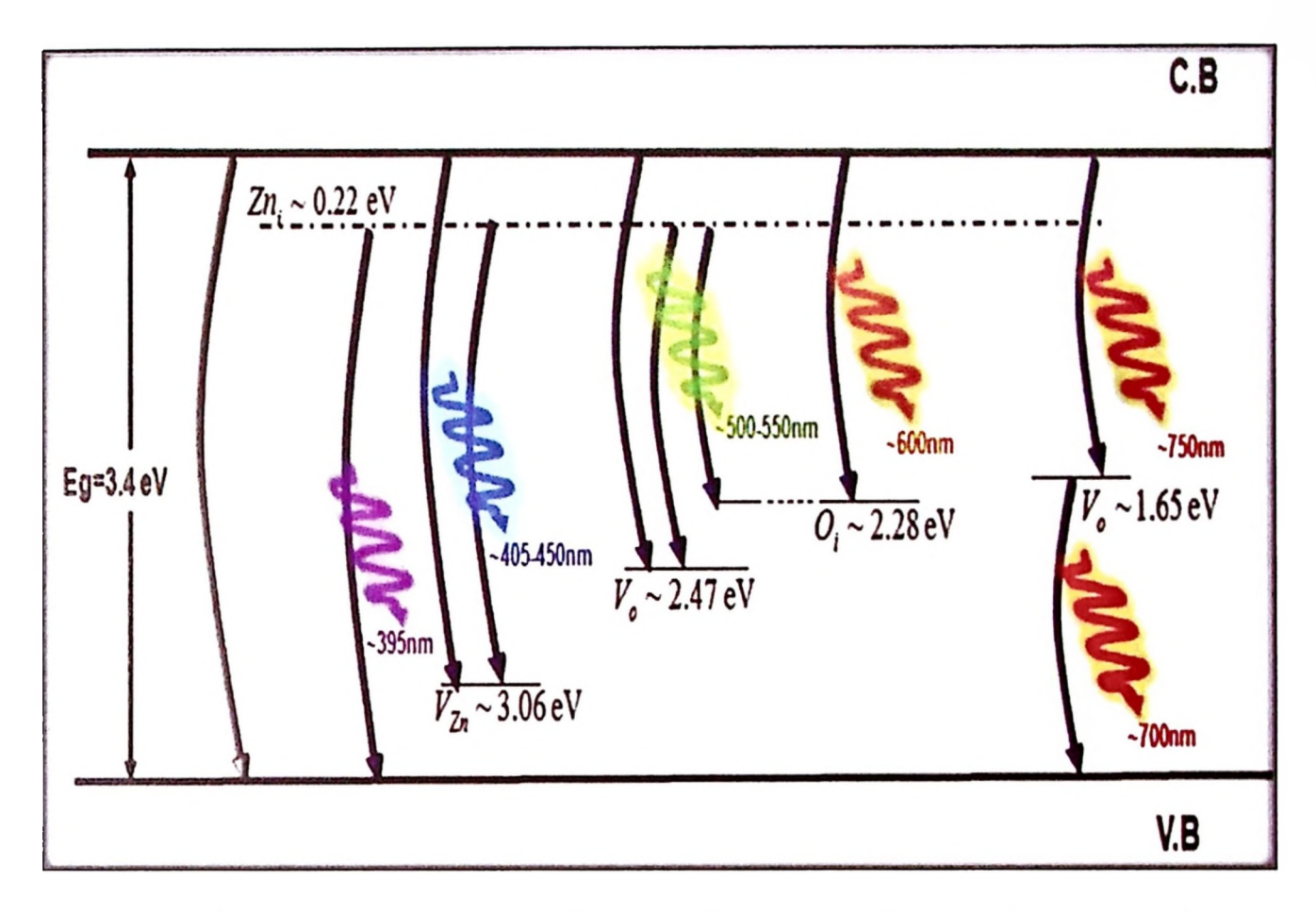


Figure 2.2: Schematic energy level diagram of various defect level emissions in ZnO [41, 42].

2.3 Growth Methods of ZnO NRs

Several synthesis methods have recently been developed for 1D ZnO nanomaterial growth, including metal-organic chemical vapor deposition (MOCVD) [6, 7], hydrothermal or wet chemical methods [4], physical vapor deposition (PVD) [12, 13], molecular beam epitaxy (MBE) [5], pulsed laser deposition (PLD) [8], sputtering [14], top-down approaches by etching [9], eletrospinning [10, 11] and so on. In this context, it is essential to show the difference between three important terms, hydrothermal, solvothermal, and CBD. Hydrothermal process includes the use of supersaturated aqueous (water) as the solvent of the material used inside a closed

vessel under high temperature and pressure in order to prepare and crystallize the nanomaterials.

Solvothermal method includes an organic solvent used instead of water inside a closed vessel under high temperature and pressure. As for CBD method, similar to hydrothermal method, water is used as the solvent of the other materials, but under low temperature (less than 100 °C) and the reactions is inside an opened vessel (under ambient pressure) [45, 46]. However, the system used for the fabrication of nanomaterials in both methods, hydrothermal and CBD, is the same but the vessel that contains the solution in the first method, hydrothermal, should be tightly closed, while in the second method, CBD, is not necessary to be closed.

2.3.1 Growth Mechanism of ZnO NRs by CBD Method

In CBD method (or hydrothermal method), in order to grow the units of ZnO NRs two ions are needed, namely, Zn²⁺ and OH⁻. These ions have a significant function in producing colloidal Zn(OH)₂ clusters. In all experiments in this project were used the most common chemicals, zinc nitrate hexahydrate Zn(NO₃)₂. 6H₂O and hexamethylamine (HMTA) C₆H₁₂N₄. Zinc nitrate salt provides Zn²⁺ ions required for building up the ZnO NRs, while water molecules in the solution provide O²⁻ ions. Even though the exact function of HMTA during the ZnO NRs growth is still under investigation, it is believed to serve as a weak base and slowly hydrolyzing in the water solution to supply OH⁻ ions [47, 48].

The chemical reactions for the growing of ZnO NRs can be summarized into the following four steps: decomposition reaction Eq. (2.1), hydroxyl supply reaction Eq. (2.2), supersaturation reaction (Eq. (2.3) and Eq. (2.4), and ZnO nanowire growth reaction Eq. (2.5) [35, 49, 50]:

$$C_6H_{12}N_4 + 6H_2O \rightarrow 6HCHO + 4NH_3$$
 (2.1)

$$NH_3 + H_2O \rightarrow NH_4^+ + OH^-$$
 (2.2)

$$Zn(NO_3)_2 \to Zn^{2+} + 2NO_3^-$$
 (2.3)

$$Zn^{2+} + 2OH^- \to Zn(OH)_2$$
 (2.4)

$$Zn(OH)_2 \to ZnO + H_2O \tag{2.5}$$

Four main parameters, namely, precursor materials, precursor concentration, duration and temperature have significant influence in controlling structure stability, morphology and optical properties of nanomaterials produced by CBD method. In this context, the polar surface of ZnO has higher energy, therefore it plays an important key role in the column growth. The polar {001} surfaces have approximately 60% higher cleavage energy than the nonpolar {100} and {110} faces [51]. Therefore, due to this difference in the surface energy of different crystal planes, the high-energy surface, {001}, would grow faster than other lower energy surface. Therefore, in the case of the formation of 1D ZnO nanostructures, this process is repeated during ZnO crystallization, thus leading to a growth rate along the [001] direction to be faster than other directions (Figure 2.1 (b)) [45, 52, 53].

It is worth mentioning that the ZnO seed layer play an important role for the growth of well aligned ZnO NRs arrays on the substrate by CBD method. the presence of the ZnO seed layer on the substrate lead to decreasing significantly in the interface energy between ZnO crystal and the substrate, as a consequence, the nucleation process occur quickly and the NRs -arrays can grow more easily [54, 55].

2.3.2 Hydrothermal Growth of ZnO NRs on Highly Flexible Nylon

In general, ZnO materials can be grown experimentally on rigid or flexible substrate. However, flexible substrates offer several advantages and valuable properties compared with rigid substrates, including transparency, transportability, flexibility, small volume, light weight, high resistance to damage, and low cost. Several types of polymer substrates can be used as flexible substrates, such as flexible Kapton, polyimide, polyethylene terephthalae, polyethersulfone, and polyethylene naphthalate [56, 57]. A flexible transparent substrate has an amorphous structure.

Hydrothermal method is usually adopted to synthesize ZnO NRs. The method offers some advantages such as low deposition temperature and does not require any harsh fabrication process of target substrates. This enables the use of unconventional substrates such as a plastic, polymer, fabric, and paper due to flexible polymer substrates also have a low heat resistance at high-temperature processes. However, because of the low temperature, this method faces some disadvantages, such as poor crystallinity and high defects concentration, which weakens the device's performance (especially when compared with other high temperature methods such as chemical vapor deposition (CVD) [58]. In many works reported so far, the authors have used thin flexible substrates such as a flexible Kapton (50 μm) as substrate to grow vertically ZnO NRs [56, 57], for developing UV detector and H₂ gas sensor [59].

2.3.3 Direct Heat Substrate-Modified Chemical Bath Deposition (DHS-MCBD) Technique for Growth of Ultralong ZnO NRs

Both synthesis methods, hydrothermal and CBD have many advantages to synthesis of ZnO NRs and both have attracted great interest by researchers. The

fabrication of ultralong ZnO NRs by these methods is still challenging, all the reasons anticipated for this problematic issue were mentioned and have been explained in section 1.1. To address these problems, researchers have used many strategies in order to increase the length of ZnO NRs arrays for high aspect ratio of ZnO NRs where this could lead to increase in efficiency for the devices fabricated.

However, there were several reports on hydrothermal synthesis of ultralong ZnO NRs by using different precursor materials as ions source, instead of the aqueous zinc nitrate- hexamethylamine HMTA. Hua *et al.* reported the synthesis of ZnO NRs with large aspect ratio by using zinc nitrate hexahydrate and HMTA with aluminum iso-propylate. They prepared ZnO NRs arrays with a length of 10 µm and aspect ratio of 70. Nevertheless, the significant improvement in the aspect ratio requires far more effort by this method, due to that their method was based on the principle of addition of aluminum-iso-propylate and the number of cycles for the enhancement of the aspect ratio [60].

There are also other precursors which have been used by the researchers for ultralong growth of nanorods. Xu et al. reported the growth of ultralong ZnO NRs (length up to 30 µm within 10 h) using zinc hydroxide, ammonium hydroxide, polyethyleneimine (PEI), and seed nanoparticles [61]. Qiu et al. used the PEI-assisted preheating hydrothermal method (PAPHT) to prepare ZnO NRs arrays with a long length of more than 40 µm [62]. Recently the continuous flow injection (CFI) hydrothermal synthesis reaction was used by several researchers to obtain ultralong ZnO NRs arrays. For instance, Chen et al. have shown that a continuous flow of Zn precursors can yield ultralong ZnO nanowires by hydrothermal method. Zinc acetate dihydrate and HMTA were continually injected to the complex reactor for ZnO

growth. The concentration of the reactor was refreshed every 4 h and a 24 h of growth yield a length of 15 μ m [63].

To obtain an ultralong ZnO nanorod on a substrate by the CBD or hydrothermal methods, the growth of ZnO rod should be accelerated. Due to the length of the ZnO NRs increased with increasing the temperature [64], therefore, It is believed that the best way to accelerate the growth of ZnO rods can be by increasing the temperature of a substrate, in other words, by increasing the supply of energy on a substrate. Temperature here can be referred as solution temperature or substrate temperature. The vast majority of the researchers have focused in their research on the effect of a solution temperature and not a substrate temperature on growth of ZnO NRs or other materials via hydrothermal method.

However, there is maybe one report, somewhat similar to this work with some important differences. Tae Lee and his group constructed a system for a modified CBD method by heating a seeded substrate directly on a hot plate which continuously delivers a constant concentration of hot solution (80 °C) to the seeded substrate. [65]. However, this group did not mention about nanosize-junction because of they used only ZnO seeded silicon as the substrate, and they did not fabricate any kind of nanosize electrical device. In this context, the fabrication of nanorods of high aspect ratio with length typically more than 100 µm are still difficult and challenging by a low temperature method. However, a high temperature method provides an easy way to obtain high length of ZnO NRs. It is worth mentioning that the main advantage of the high temperature technique is the growth of high quality single crystalline nanowires which are mandatory for electronic and optoelectronic

applications. Table 2.1 summarizes the results reported by several groups on the growth of ultralong ZnO NRs.

Table 2.1: The diameter, length and aspect ratio of ZnO NRs grown using different fabrication methods and reported by several groups.

Synthesis method	Growth temperature (°C)	Growth time	Diameter (nm)	Length (µm)	Aspect ratio	Ref.
Hydrothermal	75	28 h	~140	~10	~70	[60]
Hydrothermal	88	10 h	150-300	~30	~133	[61]
Hydrothermal	85	24 h	~120	~15	~125	[63]
Anodization	70	4 h	~100	~100	~1000	[66]
Carbothermal	917	15 min	100-300	~100	~500	[67]
Vapour Phase Transport	950	40 min	100-200	~180	~1200	[68]

2.4 Metal-Semiconductor-Metal (MSM) Photodetector

Metal-semiconductor-metal photodetector (MSM-PD) was first proposed and demonstrated by Sugeta *et al.* in 1979 [69]. Since then, many research groups started to improve and develop the fast response, high sensitivity and high speed MSM-PDs [70]. Fundamentally, a conventional MSM-PD is a symmetrical device matching to two Schottky connected back-to-back diodes on a semiconductor layer. When a voltage is applied, one of the contacts (electrodes) of interdigitated fingers is foreward-biased and the other one is reverse-biased, and so on [71]. The conventional MSM-PD structure is shown in Figure 2.3 (a). When the conventional device is illuminated by light from the top on surface, a significant amount of this incident light is reflected, especially from the top surface of the fingers, which was

fabricated from a metal. Therefore, only the area of the exposed surface for the semiconductor layer of the device will interact with the incident light.

In fact, the active area of light absorption is the area of semiconductor between the metal fingers. When the light which has energy greater than the bandgap energy of the semiconductor is incident on the top of the MSM device surface, electron-hole (e-h) pairs are generated, as shown from cross-sectional views of device in Figure 2.3 (b). The carriers are transferred to the metal contact pads without or with applied external bias voltage and current are detected in the external circuit under the application of an external bias voltage. MSM-PDs are extremely important in optical communication systems and other applications because they present a variety of benefits such as simplicity of fabrication, high-current gain, small dark current, high responsivity and high-speed operation.

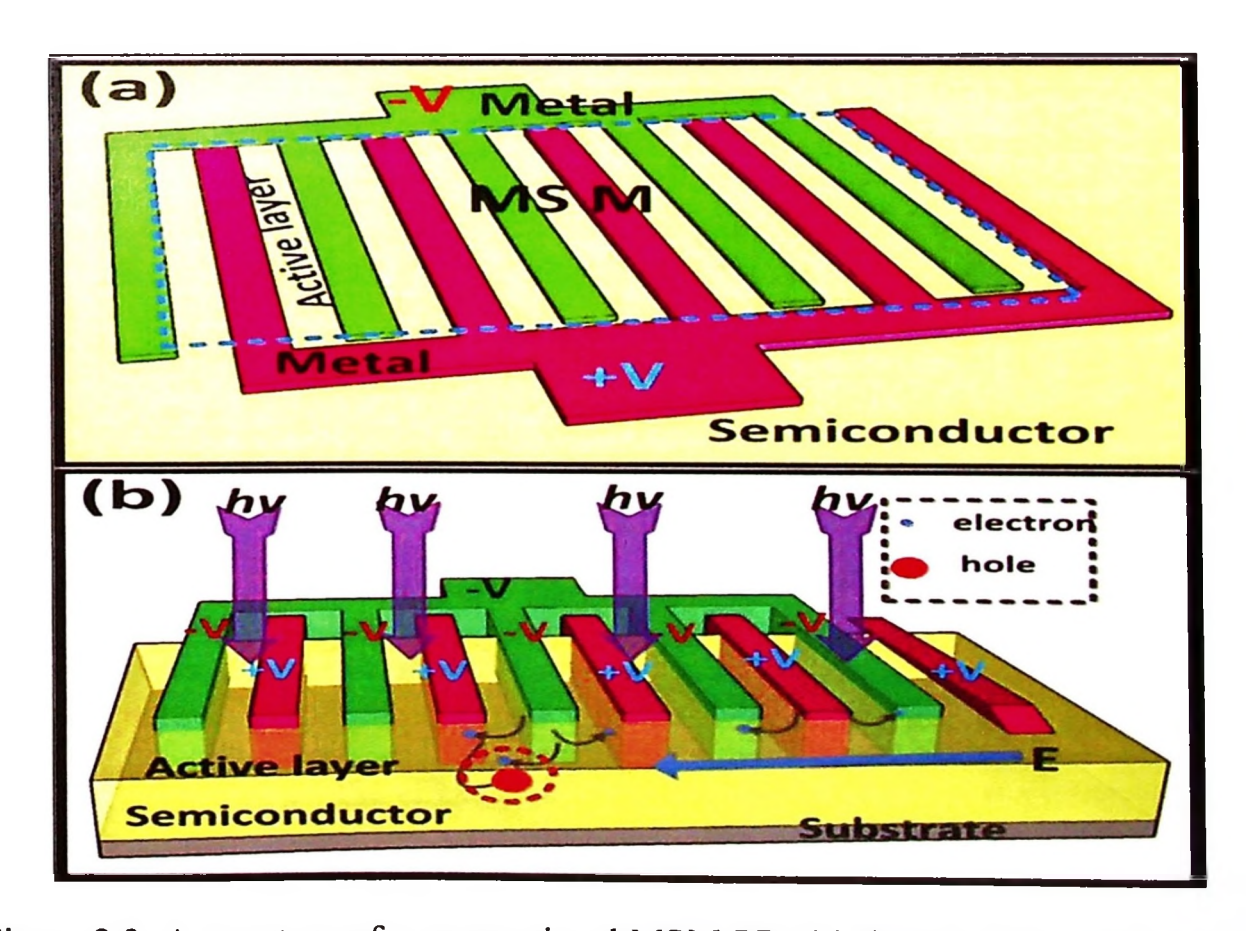


Figure 2.3: A structure of a conventional MSM-PD: (a) the top of the surface and (b) cross-sectional views.

2.5 Operational Parameters of Photodetectors

There are some important parameters of MSM-PD which are of interest such as, current gain and responsivity.

2.5.1 Current Gain

The current gain is an important parameter, which is useful to evaluate photodetection ability. It represents the ratio of photocurrent to dark current, which can be calculated by the following equation:

Current gain =
$$\frac{I_{ph}}{I_d}$$
 (2.6)

where I_{ph} is the photocurrent generated, when the device is under incident light and I_d , is the dark (leakage) current which was generated with no incident light [72]. It is worth to mention that to enhance current gain for MSM-PD, the leakage current should be decreased and the photocurrent increased for the device.

2.5.2 Responsivity

The responsivity (R) of as-fabricated MSM-PD device is defined as the ratio of the electrical output to the optical input for a given wavelength and can be calculated using the following equation [73]:

$$R = \frac{I_{ph} - I_d}{P_{op}} = \frac{I_{ph} - I_d}{E_{op} \cdot A}$$
 (2.7)

where I_{Ph} is the photocurrent which was generated per unit optical power of incident light (P_{op}) on the effective area of the device (A), I_d is the dark current, and E_{op} is the irradiance of light. According to some previous reports, a high surface-to-

volume ratio [74] and highly crystalline [75] of the ZnO NRs, play important roles in the enhancement of the photoresponse mechanism.

2.5.3 The Photoconduction Mechanism in ZnO NRs

Considering that presence of oxygen vacancy states on the surface of n-ZnO NR and according to PL spectra of n-ZnO type semiconductor, oxygen element plays a significant role on the observed photoresponse [76-78]. In fact, ZnO NRs photodetectors have better performance than ZnO film photodetectors due to the aspect ratio of nanorods is higher than the ratio of thin film [79]. The mechanism to produce a photocurrent gain includes a surface reaction between free carriers and air ambient in which oxygen adsorption/desorption processes control the sensing mechanism. When an electrical field is applied, the I-V characteristics of ZnO NRs when exposed to UV light do not resemble the situation under darkness. The first process, when ZnO NRs are placed in darkness, free electrons, which are withdrawn from the conduction band (CB) are absorbed and capture the oxygen molecules from surrounding air (Figure 2.4 (a)), according to the following reaction:

$$O_{2(gas)} + e^- \to O_{2(ad)}^-$$
 (2.8)

where e^- is a free electron, $O_{2(gas)}$ is an oxygen molecule and $O_{2(ad)}^-$ is adsorbed oxygen on the surface of the nanorods. This adsorption leads to the bending of conduction and valence bands, a band bending upwards near the ZnO surface (depletion layer near the surface become larger), as well as trap center-related band (E_T) on upward direction (Figure 2.4 (c)). Formation of large number of ionized oxygen on the NRs surface enhanced the band bending, resulting in a very low conductivity. The dark current-voltage characteristics obviously indicate the presence of surface defects related trap centers on the ZnO NRs. The second process, when

ZnO NRs are illuminated by UV light with an energy greater (or equal to) than the band gap of ZnO, the photogenerated (electron (e^-) – hole (h^+)) pairs are generated (Figure 2.4 (b)), according to the reaction (2.9), where hv is the incident photon energy:

$$hv \to e^- + h^+ \tag{2.9}$$

In this situation, the photogenerated holes will migrate to the surface of ZnO NRs and recombine with adsorbed oxygen molecule ions producing oxygen molecules according to the reaction (2.10):

$$O_{2(ad)}^{-} + h^{+} \to O_{2(gas)}$$
 (2.10)

Thus, this results in increase in the density of electrons in conduction band which leads to decrease of the degree of band bending upwards, thereby increase the conductivity, in other words, this leads to an increase in the total current of the device [80-82].

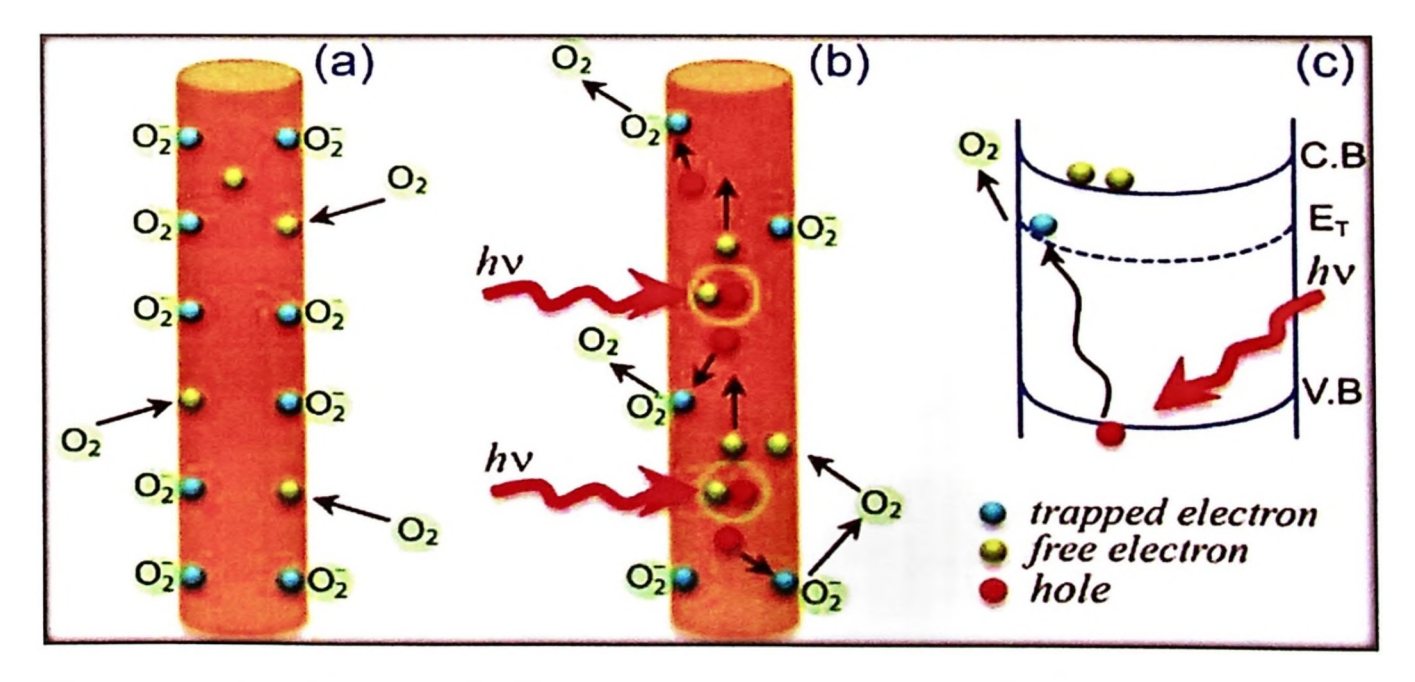


Figure 2.4: A schematic of UV-detection mechanism of ZnO NR with surrounding air: (a) the rod of ZnO in the dark condition and (b) the photogenerated electron-hole pairs during UV illumination. (c) energy band diagram during UV illumination [76].

2.6 Overview of ZnO Nanostructures for Gas Sensing

ZnO nanostructures, such as nanorods, have high chemical sensitivity to many gases because of their large surface area and great electron transport compared with single crystal ZnO. These qualities render them suitable to produce several gas sensors, especially for H₂ sensing devices. Different types of gasses, such as H₂, CO₂, CO, NO₂, O₂, O₃, NH₃, i-butane, CH₄, SO₂, and ethanol, can be detected by ZnO material [83-88]. Hydrogen gas can be used in various ways. It is currently being used in numerous industries and in our daily lives.

The most common uses of hydrogen include chemical processes, reactions, preparation of ammonia, and heating oil. Hydrogen is also suitable for use as a fuel in the internal combustion engines of vehicles and rockets [89, 90]. The uses of this gas are expected to increase in many applications in the future, because H₂ gas is invisible, odorless, highly reactive, and possesses explosive properties [91]. Hence, a sensor that can detect and respond to hydrogen outflow in the environment, especially under low concentrations, must be fabricated.

2.6.1 H₂ Gas Sensing Mechanism of ZnO NRs

In ambient air, the surface of the metal oxides (ZnO NRs) adsorbed oxygen (O₂) molecules from the atmosphere. Such adsorption resulted in the capture of electrons from the conduction band of ZnO and led to the formation of three types of chemisorbed oxygen anions according to ambient temperature. Takata *et al.* [92], found that stable oxygen ions O₂ formed at low temperatures (less than 100 °C), O⁻ ions formed between 100 °C and 300 °C, and O²⁻ ions formed at temperatures greater than 300 °C. In all those cases, the resistivity of the sensing material increased.

In the present work, the oxygen ions were adsorbed on the surface of ZnO NRs in the two forms of O_2^- and O^- because the maximum operating temperature for all the tests were 180 °C. The reactions on the surface of rods with the absence of H_2 can be described by the following equations [93]:

$$O_2(gas) \leftrightarrow O_{2(ads)} \xleftarrow{T \le 100} O_{2(ads)} + e^- \xleftarrow{T \le 100} O_{2(ads)}^-$$
 (2.11)

$$O_2(gas) \leftrightarrow O_{2(ads)} \xleftarrow{100 < T \le 300} O_{2(ads)} + 2e^- \xleftarrow{100 < T \le 300} 2O_{(ads)}^-$$
 (2.12)

When the ZnO nanorod sensor was exposed to hydrogen gas, the hydrogen atoms reacted with the adsorbed oxygen ions on the surface of ZnO NRs and produced water vapor molecules. This reaction decreased the amount of surface O_2^- and O^- ions. Meanwhile, electrons returned to the conduction band of ZnO, which eventually decreased the resistance of ZnO NRs. The reactions under the presence of H₂ at low and high temperatures can be described by the following equations:

$$2H_2 + O_{2(ZnO)}^- \xleftarrow{-at O_2 \text{ sites of } ZnO} + H_2O_{(gas)} + e^-$$
(2.13)

$$2H_2 + O_{2(ads)}^- \longleftrightarrow 2H_2O_{(gas)} + 2e^-$$
 (2.14)

$$H_2 + O_{(ads)}^- \longleftrightarrow H_2 O_{(gas)} + e^-$$
 (2.15)

The aforementioned reactions showed that the adsorption—desorption sensing mechanism was responsible for changes in the resistivity of ZnO NRs. The n-type ZnO material changed its conductivity (or sensitivity) from low to high in the absence or presence of hydrogen gas.

2.7 Literature Review of Flexible Electronic Devices

Flexible electronic development dates back in 1940, when the solar cell arrays were assembling on a plastic substrate to provide flexibility [94]. By 1968, the first flexible thin film transistor (TFT) was fabricated by Peter Brody [95]. Since then, researches on the flexible substrates have been expanded very quickly in a large area of applications. In general, several types of polymer substrates have been used in flexible optoelectronic and electronic devices such as polycarbonate (PC), polyethylene terephthalate (PET), polyethylene naphthalate (PEN), polyethersulfone (PES), polyimide (PI), polydimethylsiloxane (PDMS), and ext. [56, 57].

2.7.1 Flexible UV Detectors Based on ZnO NRs

Metal—Semiconductor—Metal photodetector (MSM-PD) was first proposed and demonstrated by Sugeta et al in 1979 [69]. Since then, many research groups started to improve and develop the fast response, high sensitivity and high speed MSM-PDs [70]. The first report on UV photodetector based on ZnO nanowire was published can be dated back to 2002 by Kind et al. [96]. They found that the conductivity of a single ZnO nanowire greatly depends to the UV illumination. Up to now, research on a flexible UV detector has been carried out in many research groups.

Table 2.2 summarizes the important flexible UV detector devices based on ZnO NRs with their different structure used, type flexible substrates, wavelength of light detection, response, decay times, responsivity, and current gain.

Table 2.2: Summary of flexible UV detector devices based on ZnO NRs with their different structure used, type flexible substrates, wavelength of light detection, response, decay times, responsivity, and current gain.

Device structure	Substrate	Growth method	λ (nm)	Rise time (s)	Decay time (s)	R (A/W)	Gain	Ref.
Ag/ZnO NRs/Ag	PET	CBD	365	100	120	-		[97]
Pt/ ZnO NRs/Pt	Paper	Hydrothermal	360			-	80	[98]
Pt/ ZnO NRs/Pt	Kapton	CBD	395	44	126	-	•	[59]
Pt/ ZnO NRsPt	PEN	CBD	325	1.2	1.8	2.85	12.8	[99]
Ag/ZnO NRs/Ag	PI	CBD	370	30	60	-	1740	[79]
Au/ZnO NRs/Au	PDMS	Hydrothermal	365	80	20	•	150	[100]

2.7.2 Flexible Gas Sensor Based on ZnO NRs

Ong et al. fabricated a flexible device for RT hydrogen sensor based on undoped ZnO NRs using PET substrate. The ZnO NRs gas sensor exhibited the response for hydrogen gas increased from 5% to 26.4% with increased in the concentration of hydrogen gas from 1000 ppm to 5000 ppm [101]. Rashid et al. fabricated a flexible device for RT hydrogen sensor based on vertically well-aligned ZnO NRs, which grown on polyimide (PI) tape substrate using a low temperature hydrothermal method. Thin layers of Pd nanoparticles were sputtered on the ZnO NRs by RF magnetron sputtering. The thickness of the Pd NPs catalyst plays an important role in sensor performance. The flexible H₂ sensor with 15 s-sputtered Pd NPs (8 nm) showed superior sensitivity (91.2%) toward 1000 ppm H₂ [102].

The authors also reported a H₂ gas sensor based on the PI/PET film. They reported that modification of the seed layer leads to the smaller diameter of the ZnO NRs, as a result, an improved surface-to-volume ratio and higher aspect ratio can be

obtained, and this facilitates in more oxygen adsorption and thus better sensor response [103]. Uddin et al. fabricated an acetylene (C₂H₂) gas sensor consisting of Ag-loaded vertical ZnO NRs, supported by a polyimide/polytetrafluoroethylene (PI/PTFE) substrate. The device exhibited a high response magnitude of 27.2 (at 1000 ppm) with short rise and decay times (62 and 39 s, respectively), at a low operating temperature of 200 °C [104]. Hassan et al. reported a flexible Pt/ZnO NRs/Pt hydrogen gas sensor based on flexible Kapton tape substrate. Toward of concentration 2% H₂ in N₂ at operating temperature 200 °C, The device exhibited a maximum sensitivity at 175%, while the response and recovery times were equal to 320 s and 52 s [59].

Iftekhar and Chung fabricated a self-powered active H₂ sensor based on triboelectric effect using a layer of Pd NPs/ZnO NRs/Au/PET and a micropyramid polydimethylsiloxane (PDMS) film. Upon exposure to 1% H₂ gas concentration, the output voltage and maximum sensitivity of their sensor were found to be nearly 1.1 V and 373%, respectively and the response time was measured to be around 100 sec [105]. Shuaishuai et al. suggested that the microstructure and morphology of the products had an important influence on their gas sensing properties. They fabricated gas sensors by synthesis of orderly aligned ZnO nanorods and nanoflowers on various substrates rigid and flexible plastic sheets) via a facile one-step hydrothermal route. They found that the ZnO nanorod arrays exhibited better impressive gas sensing performance towards alcohols, while the ZnO nanoflowers demonstrated enhanced gas sensing performance towards acetic acid [106].

2.8 Light Emitting Diodes (LEDs)

When p-type and n-type semiconductor are brought incontact with each other then the excess carriers on either side will begin to diffuse across the junction. Electrons from the n-side diffuse into the p-side whereas holes from the p-side diffuse into the n-side. In other words, the electrons would flow from regions of higher Fermi energy to regions of lower Fermi energy and holes would flow in the opposite direction. This current component is called diffusion current. As holes continue to leave the p-side, some of the negative acceptor ions (N_A) near the junction are left uncompensated, since the acceptors are fixed in the semiconductor lattice, whereas the holes are mobile. Similarly, some of the positive donor ions (N_D⁺) near the junction are left uncompensated as the electrons leave the n-side.

This net flow of carriers across the junction will continue until the Fermi level for PN junction become a single constant thus they reach the thermal equilibrium at the junction. This process leads to form a positively charged region on the n-side and a negatively charged region, and finally, will form a depletion region. Therefore, a potential (electric field) is created across the junction, which is directed from the positive charge toward the negative charge, and this potential is called "built-in potential" (Vbi). The corresponding potential energy difference from the p-side to the n-side is qVbi. as indicated in the upper illustration of Figure 2.5 (b). The electric field is in the direction opposite to the diffusion current for each type of charge carrier. The lower part of Figure 2.5 (b) shows that the hole diffusion current flows from p-side to n-side, whereas the hole drift current due to the electric field flows from n-side to p-side. The electron diffusion current also flows from n-side to p-side, whereas the electron drift current flows in the opposite direction.

2.8.1 Forward and Reverse Bias

Forward bias occurs by applying a positive voltage (VF) to the p-type material with respect to the n-type material. By contrast, by applying a negative voltage (VR) to the p-type material with respect to the n-type material lead to the p-n junction becomes reverse-biased. Both bias modes are illustrated with Figure 2.5. The applied voltage on the pn-junction device is proportional to the difference between the Fermi energy level in the n-type and p-type region. In the case of the forward bias, as shown in Figure 2.5 (b), the total electrostatic potential across the junction decreases by V_F, therefore, it should be replaced by the built-in potential minus the applied voltage. Thus, forward bias reduces the depletion layer width. By contrast, in the case of the reverse bias, the total electrostatic potential across the junction increases by V_R. So, it should be replaced by (V_{bi}+V_R). Here, we find that the reverse bias increases the depletion layer width, as shown in Figure 2.5 (c).

The expression for depletion layer width W can be simplified as [107]:

$$W = \sqrt{\frac{2\varepsilon_s(V_{bi} - V)}{qN_B}} \tag{2.16}$$

where V is applied voltage, and it is zero for the thermal equilibrium at the junction, positive for forward bias, and negative for reverse bias. N_B is the lightly doped bulk concentration, and ε_s is a dielectric constant.

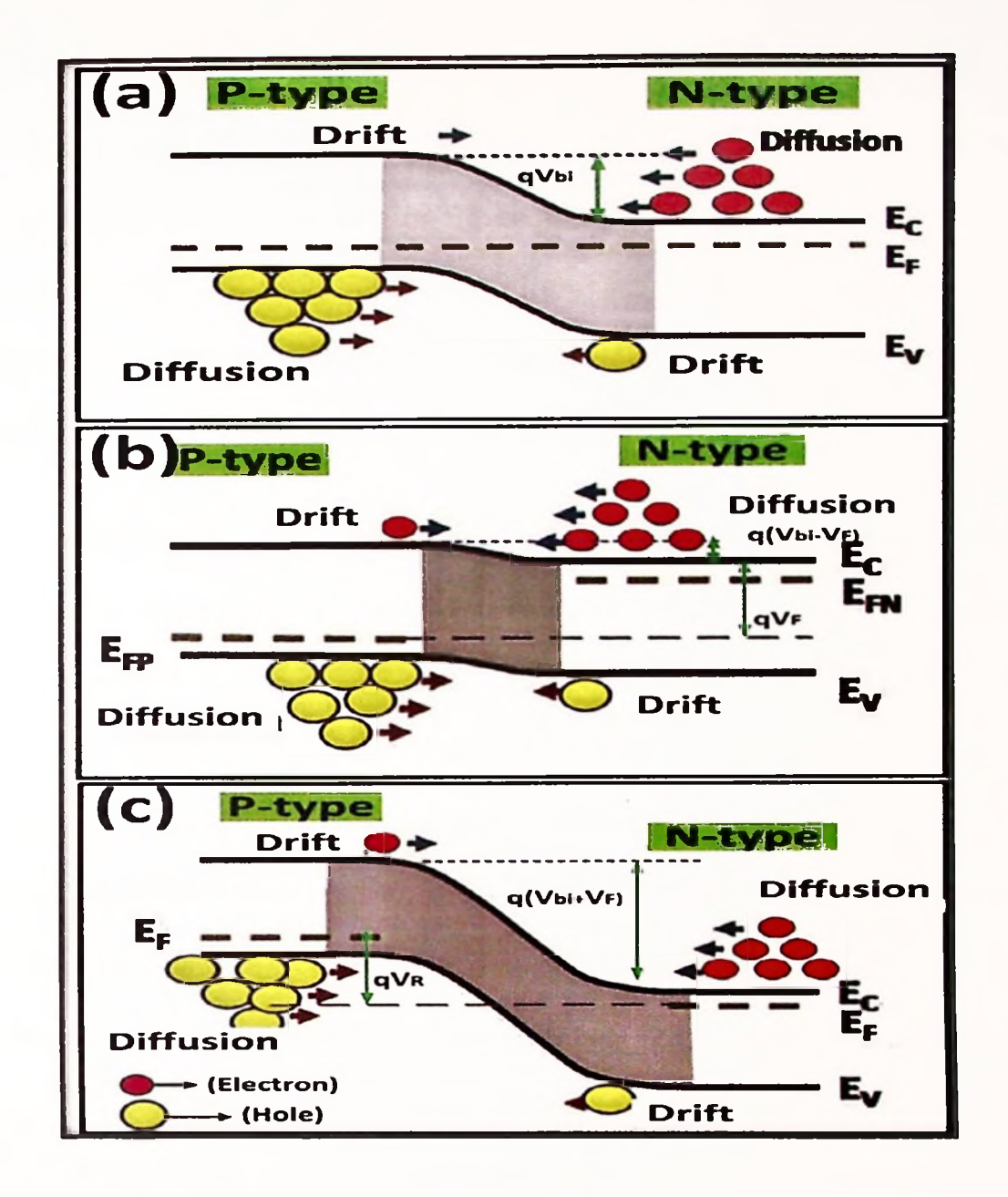


Figure 2.5: Schematic representations of energy band diagrams of a p-n junction under various biasing conditions. (a) Thermal equilibrium condition, (b) Forward bias condition, and (c) Reverse bias condition [108].

Lighting up under both forward and reverse bias has been previously reported in n-ZnO NRs/p-GaN LEDs. However, even for similar p-GaN/n-ZnO heterojunction LED device architectures, very dissimilar device behavior has been reported. For instance, many studies have reported the EL from n-ZnO NRs/p-GaN LEDs operated at reverse bias [109-112], or forward bias [111, 113, 114], while other reports show that using both forward and reverse biases can stimulate EL [111, 115].

Based on the alignment of energy levels, heterostructures can be classified in three kinds; (i) type-I (straddling gap), (ii) type-II (staggered gap), and (iii) type-III (broken gap), they are shown in figure 2.6 [116]. However, the n-ZnO NRs/-GaN heterojunction exhibits a type-II band alignment (staggered heterojunction). Because of the large band offsets in the type-II heterojunction, the carrier transport across the junction at forward bias would be difficult [24].

Additionally, in this type-II n-ZnO/p-GaN heterojunction, band-to-band tunneling is more likely to occur (an electron tunneling from the occupied valence band in p-GaN to the empty conduction band in n-ZnO), which would result in breakdown under reverse bias. Therefore, substantial attention has been paid to the electroluminescence (EL) from n-ZnO NRs/p-GaN heterojunction LEDs under the reverse breakdown bias instead of forward bias. However, with all the explanations and analysis that were reported by researchers before, the origin of the EL and the carrier transport mechanism are still not fully understood [110].

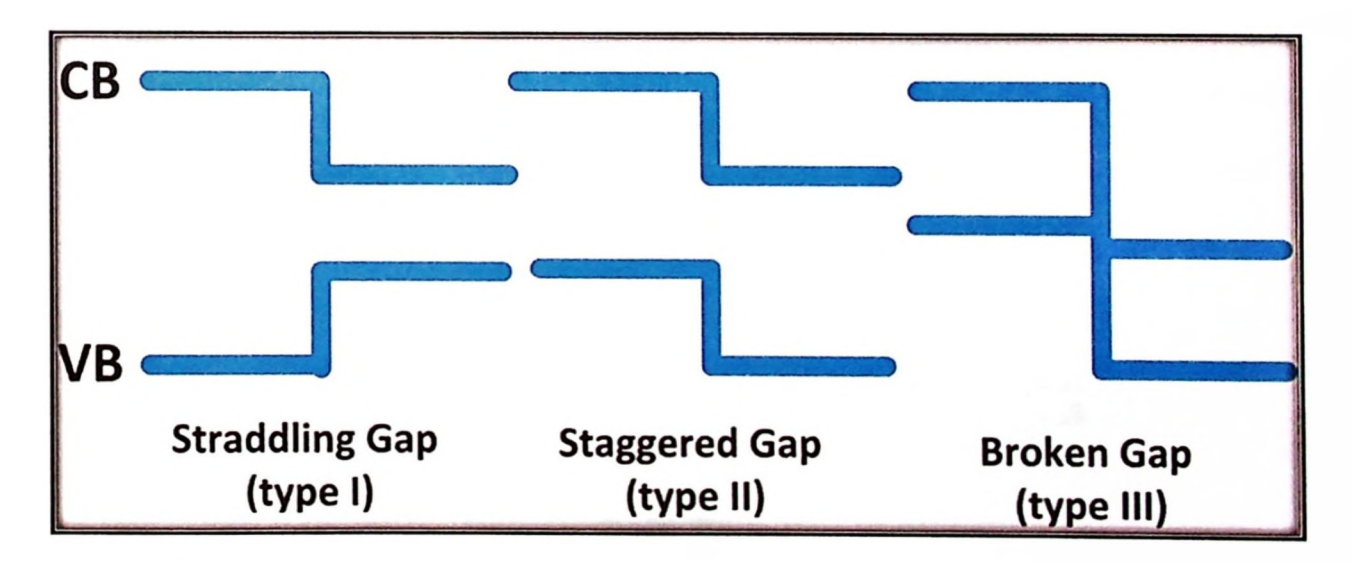


Figure 2.6: Three types of semiconductor heterojunctions [116].

2.8.2 Junction Breakdown

When a p-n junction device is under a sufficiently high reverse voltage, the device often is subjected to breakdown, tunneling effect, avalanche multiplication or a combination of both. The tunneling effect often occurs in highly doped semiconductors; a valence electron can make the transition, crossing very narrow depletion widths, from the valence band to the conduction band, while the avalanche breakdown is caused by impact ionization of electron-hole pairs. If the electric field in the depletion region is sufficient, an electron receives a high kinetic energy, which in turn leads to accelerate electron and thus may collide with the atom and knock electron from its bond, and this new electron also receives a high kinetic energy to create another electron-hole pair, and so on. This is continued the process creating additional electron-hole pairs and is called avalanche breakdown [107]

2.8.3 Electron and Hole Recombination in Semiconductors

Recombination is the inverse of optical generation, and is defined as process by which electrons and holes in a semiconductor are annihilated or destroyed. Generally, there are two principle modes: radiatively and non-radiadtively. Radiative recombination occurs which the emission of the photons, while non-radiative recombination takes place when these are no emission of the photons [117].

2.8.4 Radiative Recombination Mechanisms

Radiative recombination is related to the direct annihilation of an electron hole pair. During radiative recombination, most part of excess energy is released as a photon (see Figure 2.7). In general, there are two types of radiative recombination: intrinsic radiative recombination and extrinsic radiative recombination. Intrinsic radiative recombination is the result of the band-to-band transition while extrinsic

radiative recombination occurs due to the sub-band transition of impurities such as doping atoms, defects and impurity-bound excitons [29]. In fact, in intrinsic radiative recombination, band-to-band recombination is typically radiative in the case of direct bandgap semiconductors, but it is very slow in indirect bandgap semiconductors, and it cannot compete with non-radiative processes. Band-to-band transition take place when an electron moves from the conduction band down to the valence band and emits a photon (light) (Figure 2.7). This photon possessing an energy E, which is equal to the band gap energy (E_g) of the semiconductor plus the energy K_BT , where K_B is Bolzmann constant ($K_B = 8.63 \times 10^{-5} \ eV/K$) and T is the temperature (Kelvin skale) (T = 300K), therefore this energy can be expressed by the following relationship:

Photon energy =
$$E = hv = E_g + K_BT$$
 (2.17)

The most probable energy that both an electron and the hole in conduction and valence band, respectively, can possess depends on temperature. These energies for the electron (E_e) and the hole (E_h) are given by:

$$E_e = E_c + \frac{K_B T}{2} {(2.18)}$$

$$E_h = E_v - \frac{K_B T}{2} {(2.19)}$$

Therefore, the difference of energy between the electron and the hole is;

Photon energy =
$$hv = E_e - E_h = E_g + K_B T$$
 (2.20)

The value of $(K_BT=25.887 \text{ meV})$ is neglected because of this value is very small as compared to the value of energy bandgap of semiconductors, and therefore

the value of the emitting photon energy is approximately equal to the value of the band gap energy of the concerned semiconductor, in relation, photon energy = $hv \approx E_g$ [29].

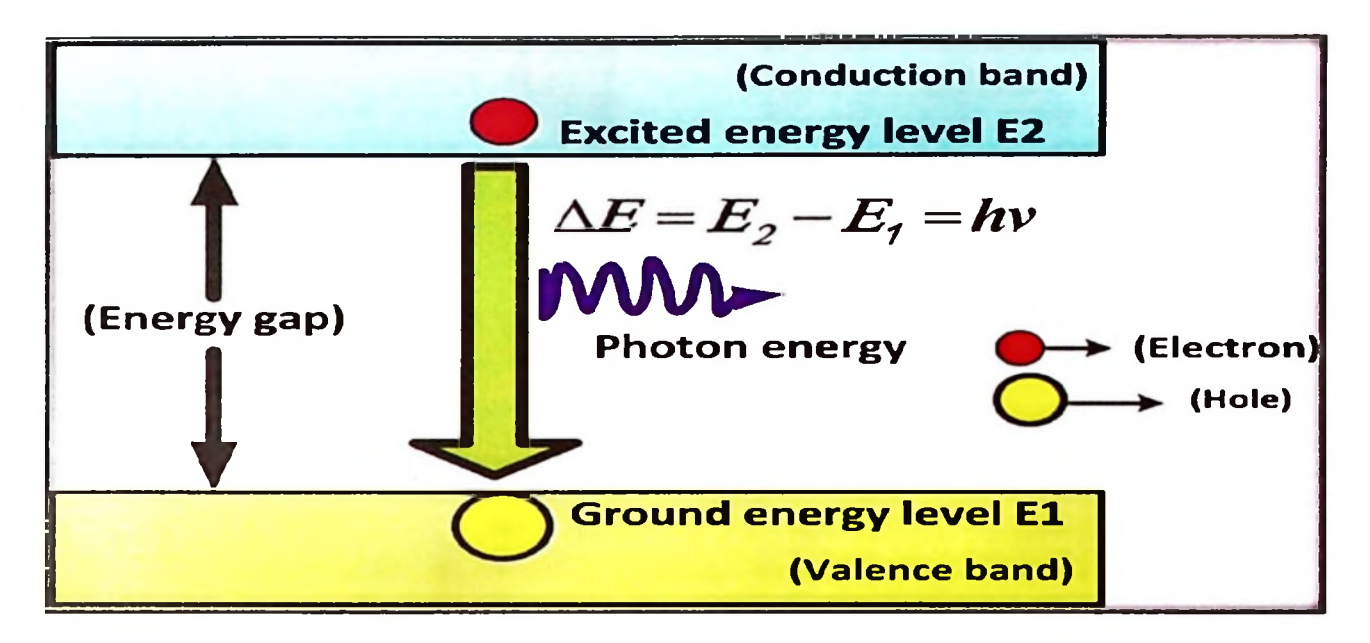


Figure 2.7: The intrinsic radiative recombination in a semiconductor (direct band to band).

In extrinsic radiative recombination, there are four possibilities for the occurrence of recombination of opposite carriers at donor or acceptor states and in bands with free carriers trapped at impurity or defect levels (see Figure 2.8) [29]. (a) The donor state-valence band transition, which occurs when an electron in the donor state slump down to the valence band and recombination with a hole, thus lead to losing energy in the form of photons. (b) Conduction band-acceptor state transition, which occurs when an electron in the conduction band moves to the acceptor state, and recombine with a hole, thus lead to losing energy in the form of photons. (c) Donor-acceptor transition, which occurs when an electron falls from donor state into the acceptor state, and which is associated with the hole. Finally, (d) Impurity-bound exciton radiative annihilation, which occurs when a trapped carrier form an exciton with the opposite carrier.

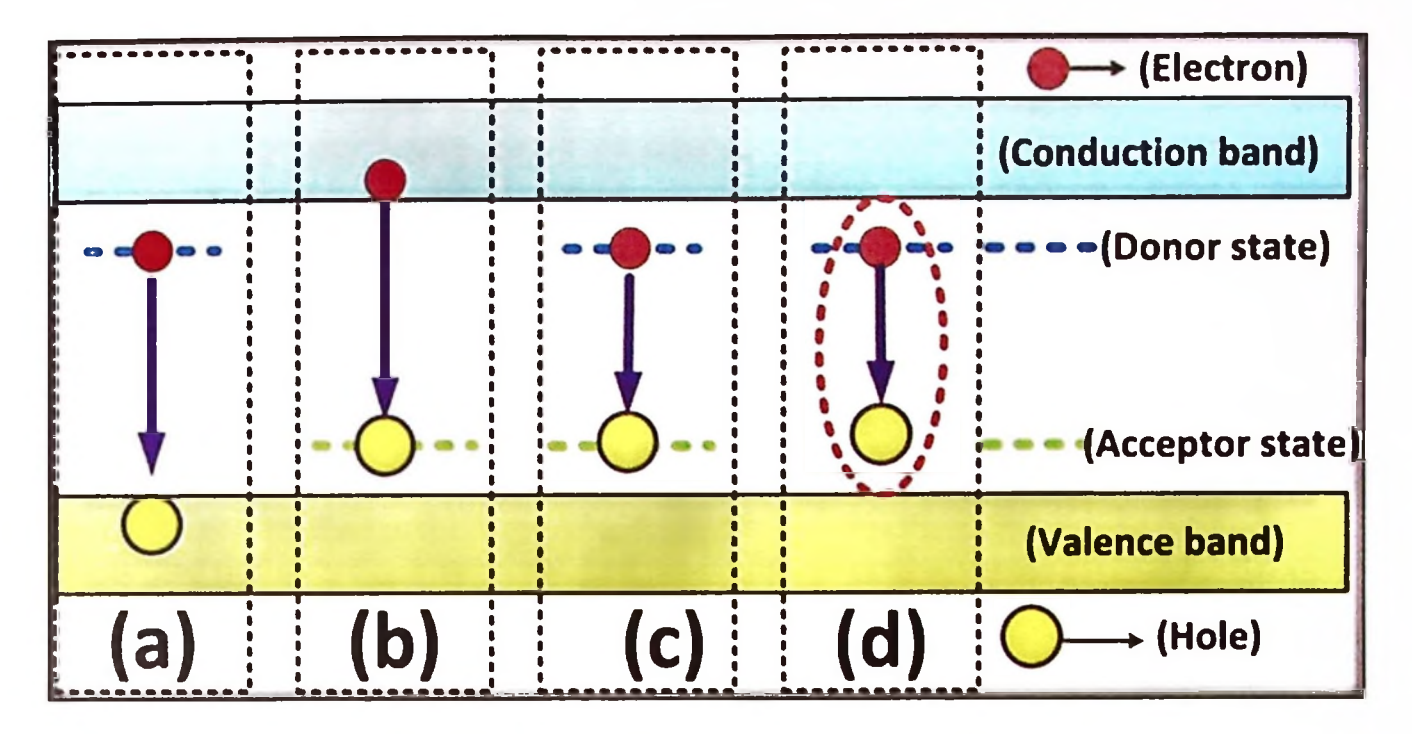


Figure 2.8: The extrinsic radiative recombination: (a) Donor state-valence band, (b) Conductive band-acceptor state, (c) Donor-acceptor recombination, and (d) Bound exciton annihilation.

It is concluded that the energy of emitted photon owing to the transition of an electron during four kinds of transition process, which are mentioned above, is somewhat smaller than the energy of emitted photon due to the band-to-band transition process. It is because the difference in energies between conduction band and valence band is the largest.

2.8.5 Literature Review of ZnO-Based LED

Our lives had lit up when the first electric lamp (carbon-arc lamps) was discovered in the beginning of the 19th Century [118], and then after many decades the high-efficiency compact fluorescent lamp (CFL) was discovered. However, both electric lamps and CFLs have many problems. For instance, in the incandescent bulbs, a big part of the electrical power is converted into heat instead of visible light, which leads to economic loss. In addition, there are some environmental concerns in the use of mercury element in the design of CFLs. Therefore, solid-state lighting or

LEDs are considered as the best solution for saving energy and preserving the ecology.

The electroluminescence phenomenon was discovered in 1907 [119], when the first LED was fabricated by H.J. Round in 1907. Interestingly, it was a metal-semiconductor LED device, not a p-n junction diode and its active material was only silicon carbide (SiC) crystallites. Later, in the mid-1920s, a Russian scientist, Oleg Vladimirovich Losev, found out that the light emission from ZnO and SiC crystal rectifier diodes were used in radio receivers. In fact, he noticed that some diodes emitted the light when they were under reverse bias, while other diodes were biased in the reverse or forward direction. Therefore, he studied this electroluminescence phenomenon in details and reported his finding in a publication in 1927 [120], but unfortunately his research was ignored [29]. In 1955, Rubin Braunstein at the Radio Corporation of America (RCA) reported on infrared radiation (IR) emission from gallium arsenide (GaAs) and other semiconductor alloys [121].

In 1962, two of the qualitative leaps occurred in the world of the development of the LED. The first, the Texas Instruments, Bob Biard and Gary Pittman, announced the first IR-LED commercial product, which utilized a pure GaAs single crystal to emit a infrared radiation (900 nm) of output [122], while the second, Nick Holonyak Jr. (father of LED), at the General Electric Company (GEC), fabricated the first practical visible-spectrum red LED [123]. After four years, Holonyak's former graduate student, George Craford, fabricated the first yellow LED and enhanced the brightness of red and red-orange LEDs [124]. However, the first high-brightness blue LED based on indium gallium nitride (InGaN) was invented by Shuji Nakamura of Nichia Corporation in Japan in 1994 [125]. It is worth

mentioning that the 2006 Millennium Technology Prize was awarded to Nakamura for his invention. Minami *et al.* [126] reported the first ZnO-based LED in 1974. The device used in their experiment was made of single crystal ZnO synthesised by hydrothermal method, and deposited a thin film of SiO₂ on ZnO layer, which acted as an insulating layer. With later developments, the ZnO-based LEDs have been fabricated from several approaches.

2.8.6 Homojunction and Heterojunction Structure of LED

In general, a p-n homojunction device has higher efficiency than p-n heterojunction because the carrier injection efficiency in a heterojunction structure is lower due to the large band offset formed at the junction interface. It leads to the reduction of carrier injection efficiency in the device with a large band offset formed. However, because of the difficulty of fabricating and controllable a high-conductivity p-type ZnO [17, 18], high-quality p-GaN, as an alternative approach to p-ZnO, has been suggested to be used in optoelectronic devices. It is owing to both of materials (ZnO and GaN) have approximately similar physical properties including small lattice mismatches (as 1.9% and 0.4% along the a-axis and c-axis, respectively), similar wide band energy (~3.4 eV), and the same wurtzite structure [127, 128]. Generally, a heterojunction structure should be formed between semiconductors with closely matched lattice constants. Therefore, an n-ZnO/p-GaN heterojunction has been suggested as a strong candidate for device application [24, 129, 130].

The different growth methods have been developed to fabricate ZnO NRs arrays can be classified into two main groups; high and low temperature techniques [131]. The high temperature techniques (vapor phase processes) are favored and

usual used to synthesize high quality functional heterojunctions specially to fabricate a nano-size junction between ZnO NRs and GaN layer but these techniques generally require expensive equipment as well as consume more energy compared with the low temperature methods. In contrast, low temperature techniques (the wet chemical route) have many desirable specifications such as, low-cost, low-processing temperature, environmental friendliness, and ease of morphology.

To get a high enough atomic substrate surface mobility, the substrate surface should be at a high temperature, and this leads to favor diffusion in exogenic heterojunctions. In other words, high temperature plays an important role to provide epitaxial ordering at the hetero-interface [127]. To grow ZnO NRs on various substrates by CBD, a seed layer is usually required to improve the density and vertical alignment of the nanorods because of the low temperature of the substrate. Therefore, although the small lattice mismatch between the ZnO and GaN, the synthesis of well-aligned arrays ZnO NRs on GaN layer via CBD method without a catalyst (fabrication of a nano-size junction) is difficult [132, 133].

The first report on the growth of n-ZnO thin films on p-type GaN heterojunction LEDs was reported in 2003 by Alivov *et al.* [134]. They used CVD method to deposite ZnO thin films on p-type GaN, and fabricate n-ZnO/p-GaN heterojunction LED which was emitting in the blue-violet region under forward bias. They were able to observe an emission of electroluminescence (EL) wavelength at 430 nm from the LED. Park *et al.* synthesized ZnO NRs by metal organic vapour phase epitaxy (MOVPE) directly on p-GaN, and without any catalyst to fabricate LED device with nano-sized junction between ZnO and GaN [24].

This device exhibited different EL spectra at 450 nm and 560 nm at the reverse bias voltage due to the Mg acceptor level in GaN and the deep level in the ZnO, respectively. It is worth mentioning that they did not observe any light emission from the device under forward bias. With the continuous development, several groups reported the heterojunction LEDs using n-ZnO nanorod/p-GaN film heterojunction structures using various techniques for growth. Table 2.3 presents some of these results on heterojunction structure LED.

Table 2.3: EL spectra of LED fabricated using different fabrication methods.

Growth method	Structure	Emission color	Emission wavelength (nm)	Biased voltage (V)	Ref.
CBD	n-ZnO NRs/p-GaN	Near-UV	400-420	10	[111]
Aqueous	n-ZnO NRs/p-GaN	Near-blue	450-540	25	[135]
Chemical Growth	n-ZnO nanotubes/p-GaN	Near-blue	450-540		
(ACG)	n-ZnO nanowalls/p-GaN	Near-visible	420-450-700		
	n-ZnO nanoflowers/p-GaN	Near-visible	400-450-700		
MOCVD	n-ZnO NRs/p-GaN	Near-blue	440-560	10	[136]
Electrodeposition	n-ZnO NRs/p-GaN	UV	397	7.5	[137]
PLD	n-ZnO NRs/p-GaN	UV	380	30	[138]

CHAPRER 3: METHODOLOGY AND INSTRUMENTS

3.1 Introduction

This chapter discusses the synthesis of ZnO NRs grown on nylon substrate using hydrothermal method, as well as the synthesis of ultra-long ZnO NRs grown on various substrates using DHS-MCBD technique. The main instruments used in this study to obtain data to characterize the morphological, structural, and optical properties of the grown ZnO NRs are described. They include field emission scanning electron microscopy (FESEM), X-ray diffraction (XRD), energy dispersive X-ray (EDX), atomic force microscopy (AFM), UV-vis, and photoluminescence (PL), as well as the electroluminescence (EL) measurements of LED. MSM PDs, H₂ gas sensor, and LED devices are fabricated and characterized based on the grown ZnO NRs on various substrates. Figure 3.1 illustrates the experimental steps of the present study.

3.2 Substrate Cleaning

Proper cleaning is extremely crucial for a substrate before epitaxial growth process in order to remove any contamination, that leads to achieve high quality between a metal or a semiconductor and the substrate, and eventually to fabricate a successful device of the produced materials. In this study, three types of substrates have been used: thermo-nylon, silicon, and GaN thin film deposited on a sapphire substrate. Naturally, the suitable procedures for each substrate type should be used to achieve a perfect cleaning for surface of the substrate.

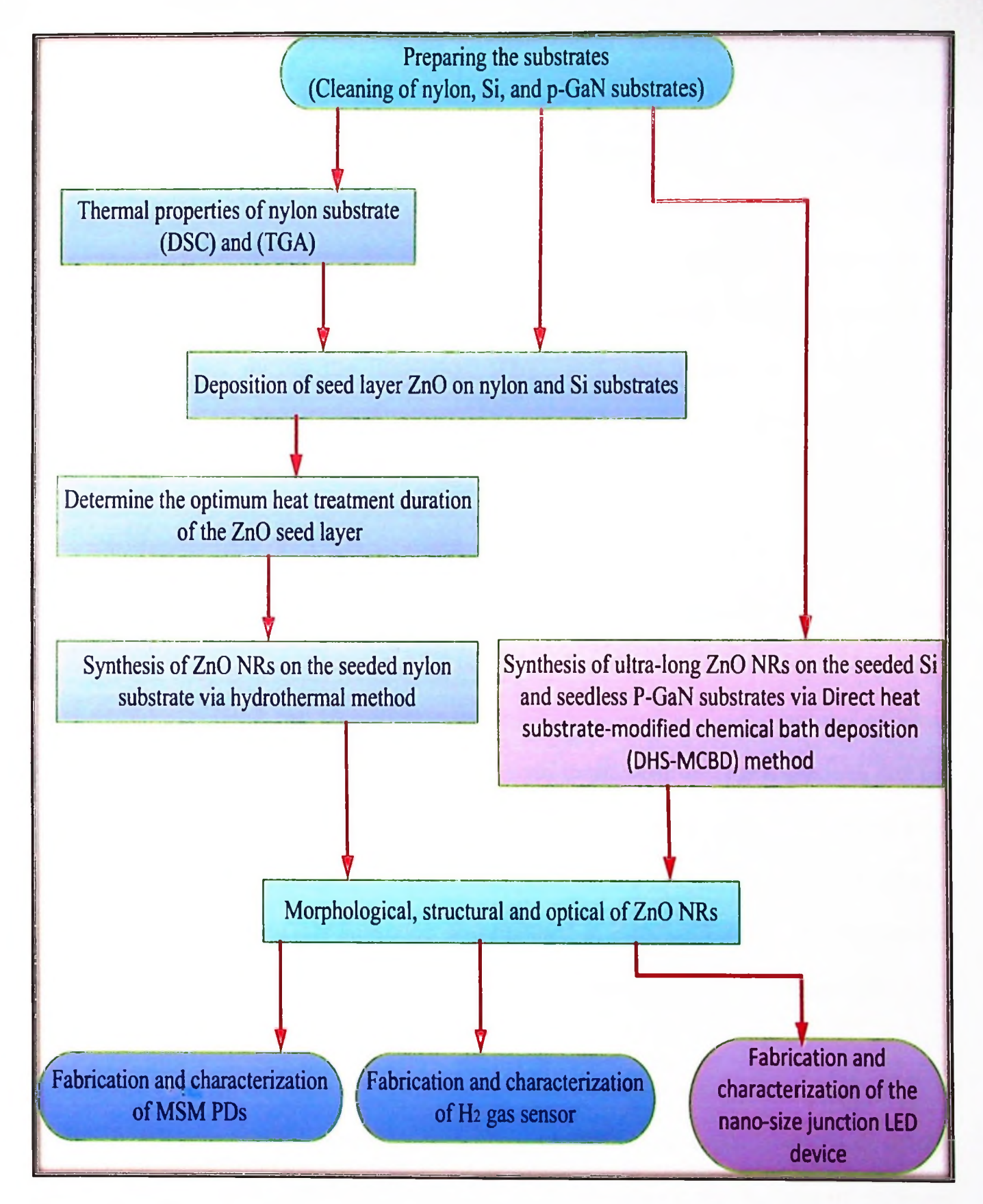


Figure 3.1: Flowchart of the preparation processes for ZnO NRs, and fabrication of MSM PDs, H₂ gas sensor and nano-size junction LED devices.

propanol alcohol and DI water for 10 min in each stage to remove any contamination, and then dried with nitrogen gas. The silicon substrate was cleaned by using 2-propanol and acetone to remove any contamination then it was cleaned by using the Radio Corporation of America (RCA) method which was necessary to remove the oxide layer on the wafer [139]. The RCA cleaning technique consists of three major steps: during the first stage (Organic Clean stage), the Si wafer was immersed in a 5:1:1 H₂O:H₂O₂:NH₄OH solution for 10 min at a temperature from 75 °C to remove insoluble organic contaminants.

The memo-nyion (~15 mm) substrate was unfastinearly cleaned in 2=

In the second stage (Oxide Strip stage), it was immersed in a diluted 30:1 H₂O: HF solution for 20 s in order to remove a thin layer of silicon dioxide. Finally, in the third stage (Ionic Clean stage), the Si wafer was immersed in a solution of 6:1:1 H₂O:H₂O₂: HCl for 10 min at a temperature from 75 °C for removal of ionic and heavy metal atomic contaminants, and then dried with nitrogen gas. As for the Mg-doped p-GaN substrate, p-type GaN thin film (thickness: ~5μm) deposited on a sapphire substrate (thickness: ~400μm), was purchased commercially and served as a substrate. Mg-doped p-GaN substrate was cleaned in ethanol followed by immersion in the diluted hydrofluoric acid solution, and then it was dried with nitrogen gas.

3.3 Radio Frequency/Direct Current (RF/DC) Sputtering System

A RF magnetron sputtering technique is a physical vapor deposition (PVD) process that is used to fabricate a thin film of materials on the surface of different substrates. In this technique, a substrate and the target (source material) are placed in magnetron sputtering chambers. The air is then removed while the sputtering gas is often an inert gas such as argon. Because of the positive ions which may be present

in the plasma region which are rapidly accelerated toward the target, the strong collision between these positive charges and negatively biased target lead to ejection of atomic size particles from the target. Eventually, these particles are deposited as a thin film into the surface of the substrate.

In this thesis, a radio frequency/direct current (RF/DC) sputtering system (Auto HHV 500 SPUTTER COATER Model: Auto 500) with a ZnO target was used to deposit ZnO seeds/layer onto the nylon and silicon substrate. Approximately 150 nm thick ZnO seeds/layer was deposited onto the nylon or Si substrate under argon gas environment, with the sputtering power and process pressure maintained at 150 W and 5.5 mTorr, respectively. In addition, RF/DC sputtering system was used for the deposition of metals contacts on the ZnO NRs and layer of GaN for all devices fabricated in this study, such as platinum (Pt), palladium (Pd), and indium tin oxide (ITO). The targets for all metals and semiconductors were of high-purity (approximately 99.999%).

3.4 Thermal Treatment Processes

It has been reported that the annealing treatment of ZnO sputtered seeds/layer has an important influence on its crystallinity as well as on the growth rate of the corresponding ZnO NRs. Also, thermal annealing plays an important role for enhancement of the ohmic and Schottky contacts especially at the final step of processes for a device fabrication. It is worth to mention that J Garnier and his group [140] reported that the annealing under air atmosphere is more beneficial than the annealing under another gas atmosphere, such as nitrogen. However, the platinum and Palladium are hard to be oxidized at low temperature [141, 142] and also the semiconductor used in this work already is the metal oxide, in other words, choosing

air as ambiance during heat treatment has no negative effects on the fabricated device. To achieve those goals, Tube furnace model: F21100 was used in this study (shown in Appendix A).

3.5 Thermal Analysis of Thermo-Nylon Substrate

The thermal behavior of this novel thermo-nylon substrate was also studied using differential scanning calorimetry (DSC) and thermal gravimetric analysis (TGA) [143, 144]. In this study, thermal properties of nylon substrate were investigated by differential scanning calorimetery (DSC) and thermogravimetric analysis (TGA) using 822eMETTLER TOLEDO and Perkin Elmer TGA7, respectively. The nylon substrate was investigated by DSC under dry nitrogen at a heating rate of 20 °C per minute from -10 to 300 °C, while the scan of TGA was recorded in the range 30-920 °C with a heating rate of 20 °C/min under nitrogen atmosphere.

In this context, DSC measurement is commonly used to determine the following: (i) Glass transition temperature (T_g), temperature at which an amorphous polymer or an amorphous part of a crystalline polymer goes from a hard-brittle state to a soft rubbery state. (ii) Melting point (T_m), temperature at which a crystalline polymer melts. (iii) The amount of energy (ΔH_m) (joules/gram (J/g)) which a sample absorbs while melting. (iv) Crystallization point (T_m), Temperature at which a polymer crystallizes upon heating or cooling. (v) The amount of energy (ΔC_p) (joules/gram) a sample release while crystallizing.

3.6 Hydrothermal Synthesis of ZnO NRs

In this study, hydrothermal method was used to synthesise ZnO NRs on the novel ultra-thin, high flexible, and low cost substrate. This substrate is normally used for cooking food in classic or microwave oven. It can be found in local markets. The flexible nylon has a thickness of 15 μ m (measured by using a high accuracy digimatic micrometer series (293 MDC-MX Lite).

The hydrothermal reaction was performed in a preheated laboratory oven and on a hot plate to fabricate a low-cost and highly flexible UV- photodetector and hydrogen gas sensing devices, respectively. The novelty of this work consists of using this thinnest nylon substrate to fabricate a low-cost and a highly flexible UV-photodetector and hydrogen gas sensing devices. To the best of knowledge of the authors, no reports have been reported so far in the literature on the use of this ultrathin flexible nylon as substrate, as well as use it as a substrate for fabricating highly flexible photodetector and H₂ gas sensor devices.

3.6.1 Hydrothermal Synthesis of ZnO NRs and Fabrication of MSM UV-PDs

All used chemicals were analytical grade and used without further purification. The aqueous zinc nitrate- hexamethylamine HMTA $(Zn(NO_3)_2 \ 6H_2O - C_6H_{12}N_4)$ chemistry is one of the most common CBD chemistries for ZnO NRs synthesis. Thermonylon (15 μ m) was used as a flexible substrate to grow ZnO NRs. The processes included three stages; during the first stage, after the nylon substrate was cleaned using the same procedure described in section 3.2, it was fixed onto a microscope glass slide (76.2×25.4×1.2 mm) substrate, and then RF/DC sputtering system was used to deposit approximately 150 nm-thick ZnO seed/layer onto the

ZnO seeds/nylon was cut into four pieces and denoted as (a, b, c and d).

To obtain ZnO seeds for hydrothermal growth, the samples (b, c and d) were inserted into the quartz tube (lab furnace) for heat treatment in air at a temperature of 180 °C for various periods of time (0.5, 3, and 6 h), the remaining sample (a) was untreated. In the third stage, ZnO seeded substrates were placed in a screw capped bottle (Schott bottle) containing an equimolar (0.10 M) aqueous solution of Zn(NO₃)₂ 6H₂O and HMTA as a precursor solution. The two materials were separately dissolved in deionized (DI) water at 80°C in order to obtain the correct precursor concentrations; the two solutions were then mixed in a bottle. After that, the hydrothermal reaction was performed in a preheated laboratory oven at 85 °C for 4.5 h.

Finally, the samples were initially washed with hot DI water followed by hot ethanol to remove the remaining salt. The samples were then dried with nitrogen gas. The fabrication of the metal-semiconductor-metal (MSM) (Pd/ZnO NRs/Pd) UV devices were performed using RF sputtering of a palladium (Pd) grid with the use of a shadow mask. In order to improve the quality of electrode contact, the devices were inserted in the quartz tube of lab furnace for heat treatment in air at the temperature of 180 °C for 4 h under air (Figure 3.2).

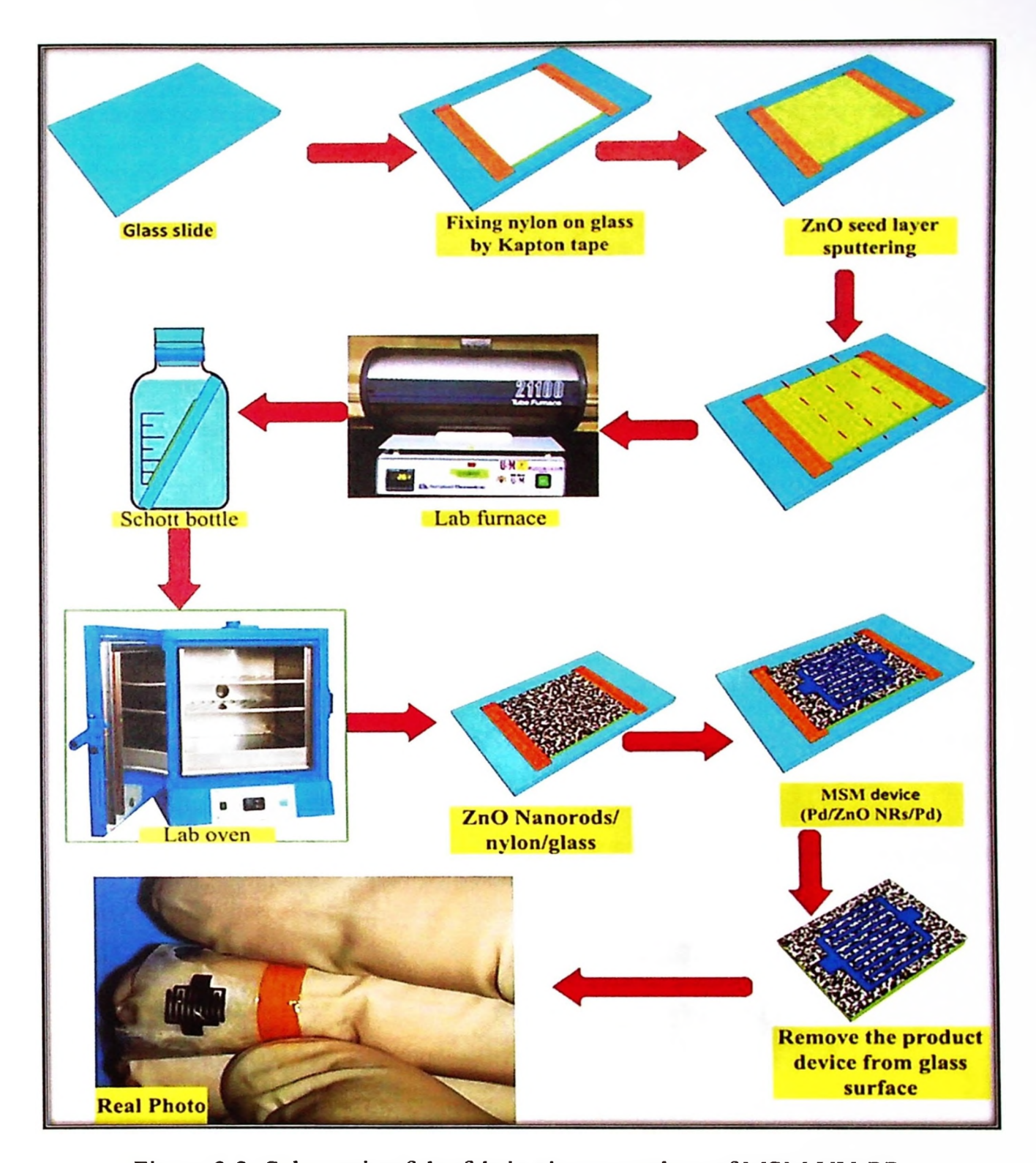


Figure 3.2: Schematic of the fabrication procedure of MSM UV-PDs.

3.6.2 Hydrothermal Synthesis of ZnO NRs and Fabrication of a MSM H₂ Gas Sensing Device

In this section, the same strategy, which was mention in section 3.6.1 used to hydrothermal synthesis of ZnO NRs on same nylon substrate. There are only two main differences with this experiment. First, to grow ZnO NRs, hydrothermal

reaction was performed in a simple and low-cost system that was placed on a hot plate at 90 °C for 3 h. Second, radio frequency (RF) sputtering of a platinum (Pt) metal grid was conducted with the use of a shadow mask instead of palladium (Pd) metal to fabricate the metal-semiconductor-metal (MSM) gas detector device.

The complete fabrication procedures of the hydrogen gas sensor (Pt/ZnO NRs/Pt) are schematically described in Figure 3.3 In brief, at the first stage, a piece of nylon substrate was cleaned using the same procedure described in section 3.2., and then fixed onto a microscope glass slide. In the second stage, an RF sputtering system was used to deposit approximately 150 nm-thick ZnO seed/layer onto the nylon substrate, as described in section 3.3.

The sample was inserted into a quartz tube (lab furnace) for heat treatment in air at 180 °C for 3 h to obtain ZnO seeds for hydrothermal growth. In the third stage, ZnO-seeded substrate was placed in a screw cap bottle (Schott bottle) containing an equimolar (0.10 M) aqueous solution of Zn(NO₃)₂ 6H₂O and hexamethylamine (C₆H₁₂N₄) as a precursor solution. Subsequently, the system was placed on a hot plate at 90 °C for 3 h (Figure 3.3).

Finally, the sample was initially washed with hot DI water followed by hot ethanol to remove the remaining salt. Then, the sample was dried with nitrogen gas. The fabrication of the metal-semiconductor-metal (MSM) gas sensing device was performed using RF sputtering of a Pt metal grid using a shadow mask. In order to improve the quality of electrode contact, the device was inserted in the quartz tube of lab furnace for heat treatment in air at the temperature of 180 °C for 4 h under air.

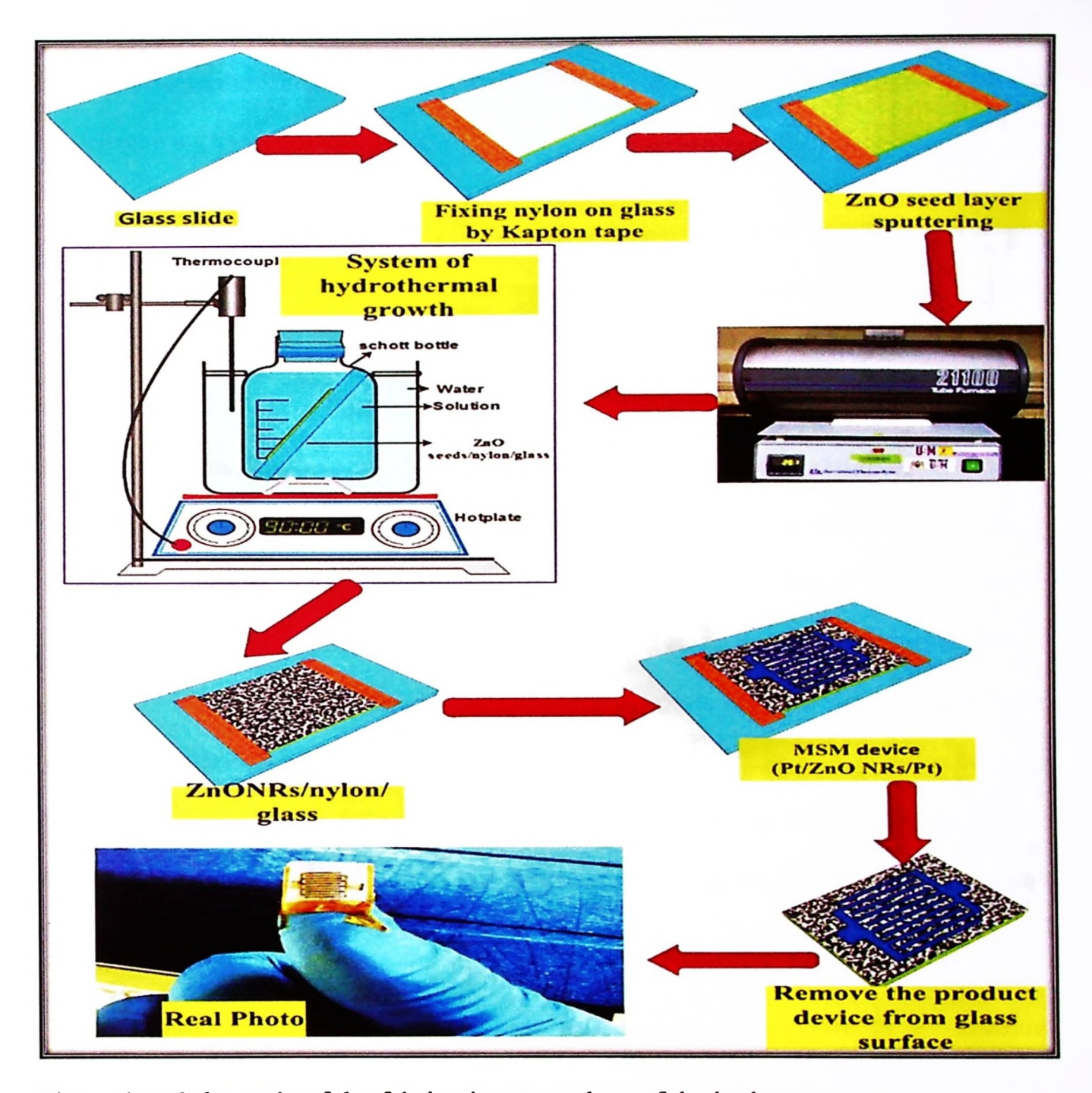


Figure 3.3: Schematic of the fabrication procedure of the hydrogen gas sensor.

3.7 Synthesis of Ultra-Length ZnO NRs by DHS-MCBD Technique

One aspect of the present novel work provides a direct heat substrate-modified chemical bath deposition (DHS-MCBD) system for forming a nanostructured material film on a substrate, such as ultra-length ZnO NRs and fabricating nano-size electrical devices such as LED. In fact, embodiments of a

DHS-MCBD system have been developed for performing CBD. Figures 3.4 and 3.5 show the real optical photo and the schematic diagram, respectively, of the direct heat substrate-modified chemical bath deposition (DHS-MCBD) apparatus in accordance with the present work.

DHS-MCBD system comprises of a cooling basin, a deposition solution chamber, a heat exchanger, a fixing means, a heating means, an alternating current (AC) source, and agitating deposition solution. The cooling basin functions as a container for a cooling liquid; the cooling liquid could be an aqueous solution or organic solution. The exemplary cooling liquid is water. The exemplary materials that can be used to make the cooling basin include plastic and glass. The cooling liquid during the process functions as a cooler for deposition solution as described herein below. The deposition solution chamber functions as a container for a deposition solution. The exemplary deposition solution chamber is a beaker. The deposition solution chamber is disposed within the cooling basin so that the cooling liquid forms a cooling bath for the deposition solution chamber during operation. The deposition solution is an equimolar aqueous solution of Zn(NO₃)₂ 6H₂O and hexamethylamine (HMTA).

The heat exchanger enables heat to be provided directly to a substrate submerged in the deposition solution. The heat exchanger has an inner tube that has one closed head end being able to prevent the deposition solution from entering into the inner tube when the closed head end is disposed within the deposition solution during operation. The heat exchanger further comprises a sleeve, where the inner tube can be inserted tightly into the sleeve. The sleeve is used to prevent heat transfer from the heater to the deposition solution.

The exemplary heat exchanger has a glass tube as the inner tube and a Teflon tube with O-ring as the sleeve. The exemplary fixing is a Teflon nut. The Teflon nut can be made of polytetrafluoroethylene (PTFE). The fixing functions to keep a substrate in contact with the external surface of the closed head end of the inner tube of the heat exchanger, so that the substrate has one surface submerged in the deposition solution (front) and one surface insulated from the deposition solution (back side). The exemplary heating is a solder heater. The heating is disposed within the inner tube of the heat exchanger and heats the closed head end of the inner tube of the heat exchanger. Therefore, the heat from the heating is directly transferred to the substrate when the back side of the substrate is in contact with the external surface of the closed head end of the inner tube of the heat exchanger during operation.

For this configuration, the substrate with its submerged front can be "directly" heated by the heating means. The AC source functions to provide power to the heating means. The standard voltage of AC 220 V was applied to the heater of the system. The exemplary deposition solution agitating means is a magnetic stirrer bar, where it immersed in the deposition solution with slow rotation speed (~100 rpm). The agitating deposition solution functions to move the deposition solution within the deposition solution chamber so as to achieve better heat exchange between the deposition solution and the cooling liquid.

Compared with conventional process heating, our system heating provides the homogeneous distribution of temperature to the whole substrate, then the heat transfers from the substrate to the nearby area. Thus, the solution at the surrounding and this small volume from the aqueous solution inside the beaker become hot, while

the large amount of aqueous solution is colder. Further, away from the front of the substrate, the temperature of the solution decreases and excess heat will be transferred to the water in the outer basin. Thus, a thermal equilibrium occurs between the water and solution and this leads to the temperature of the aqueous solution to be less than approximately 40 °C, while the temperature of the solution at the vicinity of substrate is more than approximately 60 °C.

According to the principle of heat convection for fluid, the heat transfer is by the movement of the solution away from front of substrate and this causes a continuous refresh for solution surrounding the substrate during the process of growth. It was known there are several hydrothermal parameters effects on structural and optical properties for ZnO NRs. In many works reported so far, the authors have studied the effect of these parameters and some of them have suggested the optimum parameters to grow ZnO NRs via hydrothermal method. However, the main objective of this work is to proof and emphasize that this novel method is a successful way for growth of ultralong ZnO NRs with the hexagonal wurtzite phase containing very less structural defects and have good crystal quality and it is also a successful way to fabricate nano-size electrical devices such as LED or other sensors.

Therefore, the determination of the optimum parameters to grow ultra-long ZnO NRs via our method will be carried over to future studies. The following examples are provided for the sole purpose of illustrating the principles of the present novel work. In the first example (section 3.7.1), the DHS-MCBD system was used to grow ultralong ZnO NRs on ZnO seeded silicon substrate, and then the morphological, structural, and optical properties of the ZnO NRs were studied to prove the success of the system and process. In the second example (section 3.7.2),

the DHS-MCBD system was used to grow ZnO NRs directly on seedless p-GaN/sapphire substrate to prove the success of the system and process for growth of vertically ultra-well-aligned, high density and hexagonal-shaped ZnO NRs. Finally, in the third example (section 3.7.3), the nano-size LED device which has high intensity of electroluminescence (EL) was fabricated. The light emissions were from both sides of ZnO NRs /p-GaN heterojunction LED, which was operated at different reverse bias.

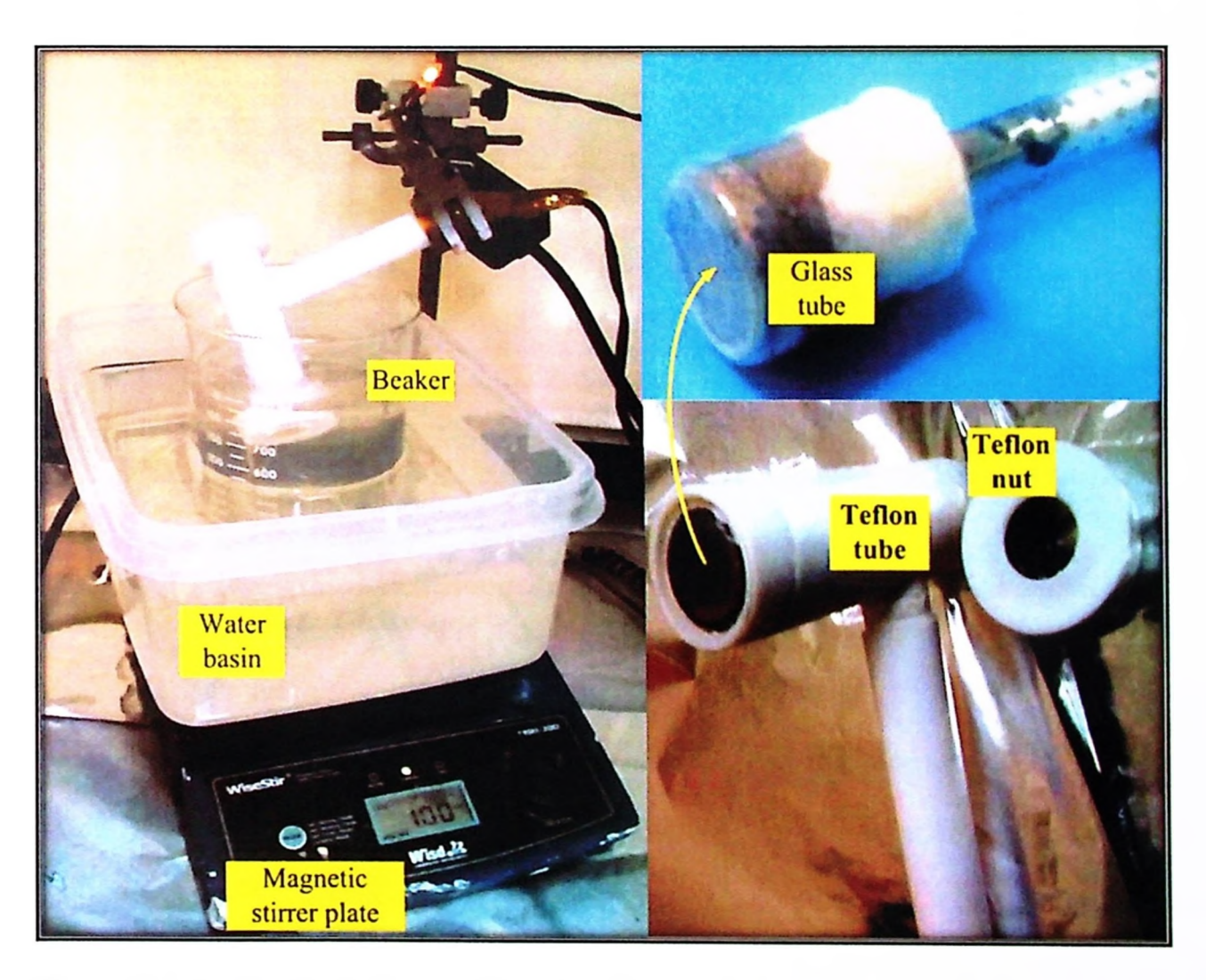


Figure 3.4: Real optical photo of the direct heat substrate - modified chemical bath deposition (DHS-MCBD) apparatus in accordance with the present work.

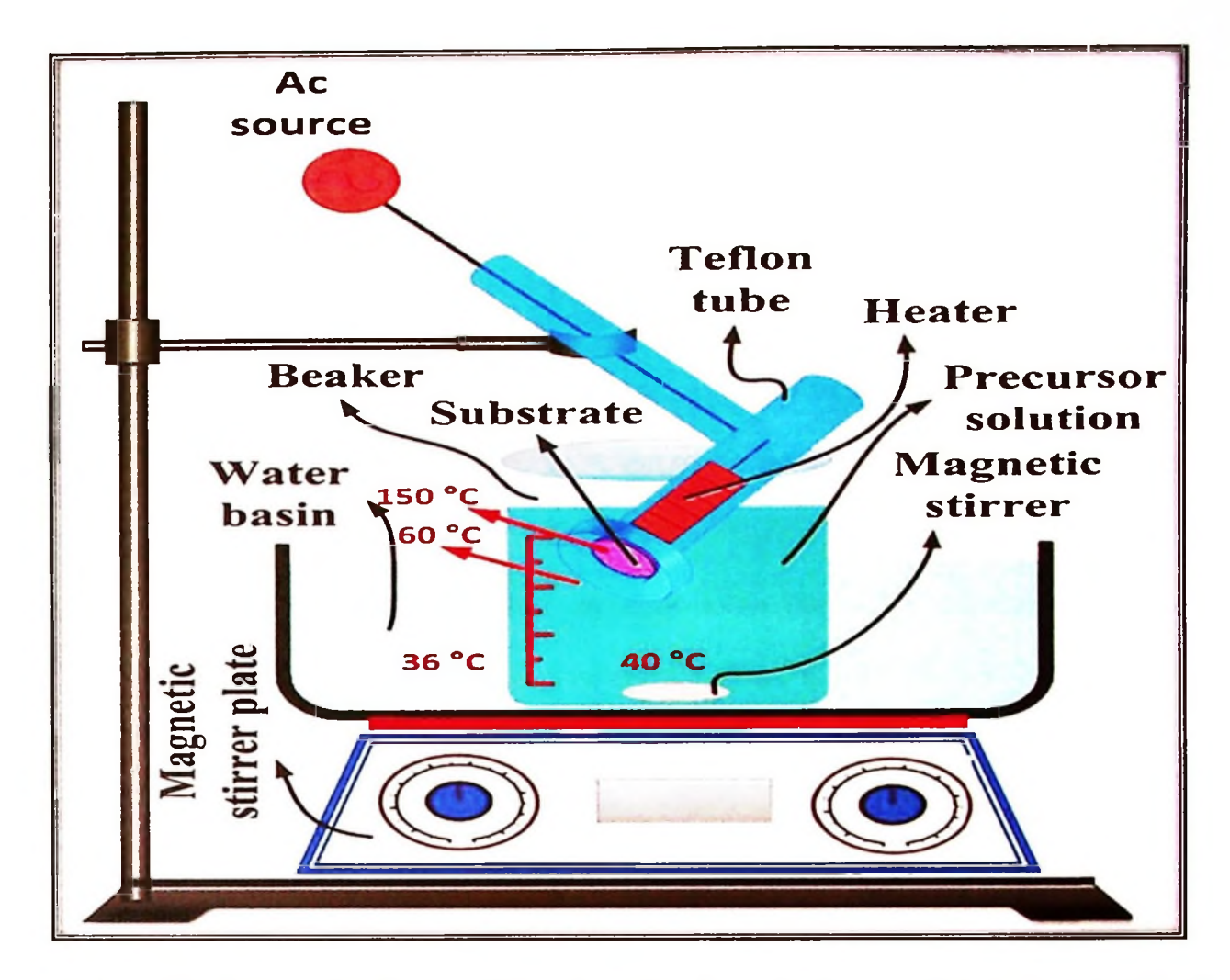


Figure 3.5: Schematic figure of the direct heat substrate - modified chemical bath deposition (DHS-MCBD) apparatus in accordance with the present work.

3.7.1 Growth of Ultralong ZnO NRs on ZnO Seeded Silicon by DHS-MCBD Technique

All chemicals used were analytical grade and used without further purification. Silicon was used as a substrate to grow ultra-length ZnO NRs. The processes included three stages: In the first stage, the silicon substrate was cleaned using the same procedure described in section 3.2, and then RF/DC sputtering system was used to deposit approximately 150 nm-thick ZnO seed/layer onto the Si substrate, as described in section 3.3. In the second stage, to obtain ZnO seeds for hydrothermal growth, the seeded silicon was inserted in the quartz tube of the lab furnace for heat treatment in air at a temperature of 400 °C for 0.5 h. In the third stage, the ZnO-seeded silicon substrate was connected with the surface of the glass

of the Teflon tube by an external Teflon nut; the Teflon tube contains the solder heater (the power of heater was 25 W) that is in contact with the internal surface of the glass of the Teflon tube.

The ZnO-seeded silicon substrate was plugged on the screw of the head end of Teflon tube tightly so as to fix the silicon substrate in place thus the efficiency of the heat transfer from the heater to the substrate remain stable and does not decrease during the synthesis of the ZnO NRs. The substrate was placed diagonally (see Figure 3.4) in a beaker containing an equimolar (0.06 M) aqueous solution of Zn(NO₃)2 6H2O and hexamethylamine (HMTA) as a precursor solution. The two materials were separately dissolved in deionized (DI) water at 80 °C to obtain the correct precursor concentrations.

The two solutions were then mixed in the beaker as a precursor solution with a stir bar, which was immersed in the liquid to spin slowly (~100 rpm). Then the standard voltage of alternating current (AC) used in homes (220 V) was applied to the heater of the system for 6.0 h. Finally, the substrate was washed with hot DI water and then with hot ethanol to remove the remaining salt. The substrate was then dried with nitrogen gas.

3.7.2 Growth of Ultralong ZnO NRs Directly on Seedless p-GaN/sapphire by DHS-MCBD Technique

In this section, unlike section 3.7.1, a p-GaN/sapphire was used as substrate to grow ZnO NRs, while the process of fabrication of zinc oxide NRs was similar to the procedure described in section 3.7.1, except for some of the following details. P-type GaN thin film (thickness: ~5μm) deposited on a sapphire substrate (thickness: ~400 μm), was purchased commercially and served as a substrate. Mg-doped p-GaN

substrate was cleaned using the same procedure described in section 3.2, and unlike in section 3.2, no ZnO seed layer or any catalyst was deposited onto p-GaN substrate, namely seedless p-GaN/sapphire was used as the substrate for ZnO NRs. The same precursor solution (equimolar aqueous solution of Zn(NO₃)₂ 6H₂O and hexamethylamine (HMTA)) was used but the concentration of each material was 0.04 M and growth duration was 5.5 h.

3.7.3 Fabrication of Nano-Size Junction LED

This section serves to illustrate alternative design for the ultra-violet and blue LED device of the present work. After growth of ZnO NRs on the p-GaN/sapphire substrate (in section 3.7.2), an n-ZnO NRs /p-GaN heterostructure LED device was fabricated.

Referring now to Figure 3.6, there is provided a schematic diagram of the n-ZnO NRs /p-GaN heterostructure LED device. The device was fabricated as follows: prior to the growth of ZnO NRs on the p-GaN substrate, an ohmic contact Pd/ITO on p-GaN was made by RF sputtering. After the growth of ZnO nanorod arrays, the device is inserted in the quartz tube of the lab furnace for heat treatment in N₂ atmosphere at a temperature of 500 °C for 5 min in order to reduce ohmic contact resistance. A direct probe on top of the n-ZnO NRs was applied for the current injection into the LED, namely no any metal electrode was deposited on top of the n-ZnO NRs because the metal contact may avoid light emission from the underlying region during the process of measuring the EL from the front side of the device.

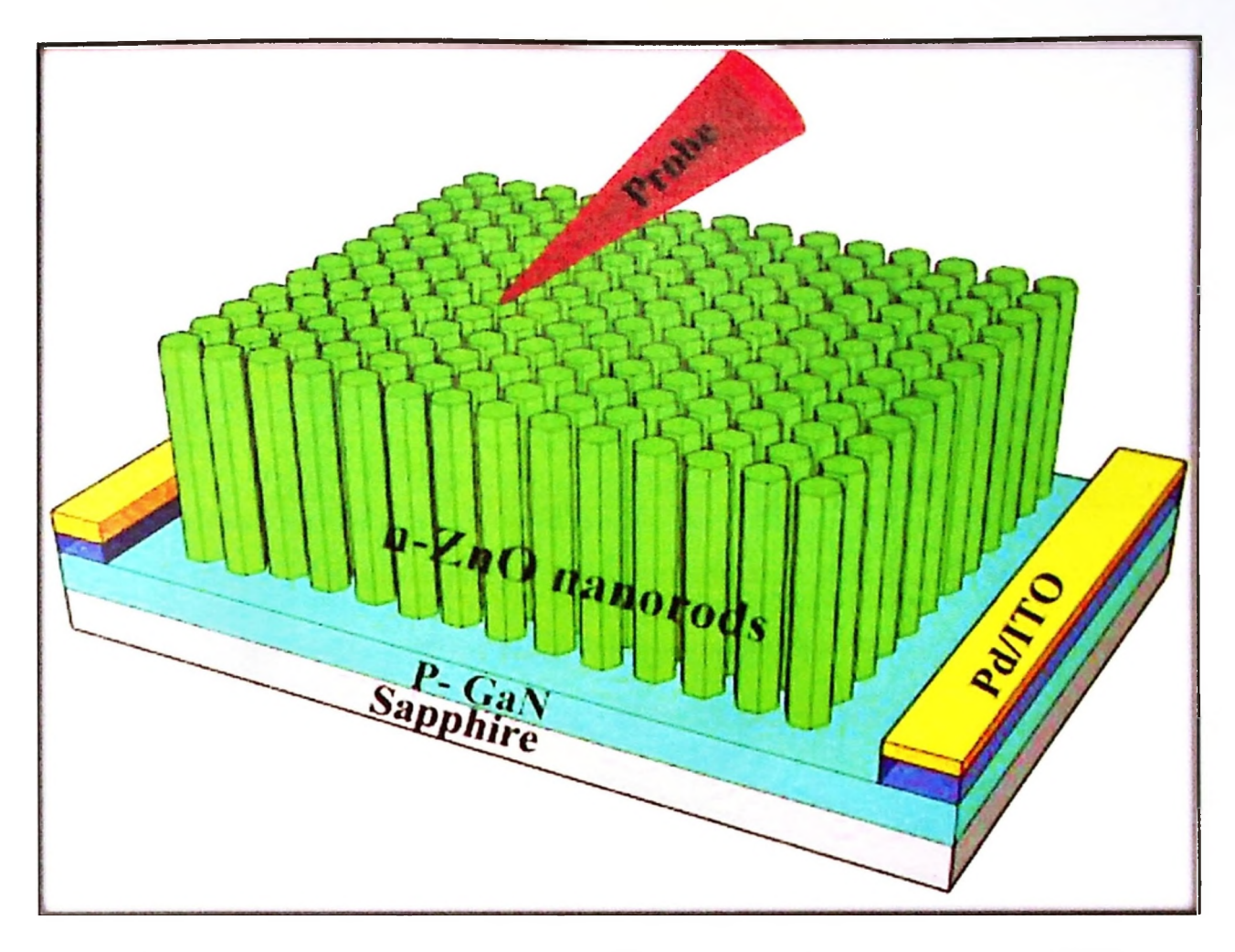


Figure 3.6: A schematic diagram of n-ZnO NRs /p-GaN heterostructure LED in accordance with the procedure described in section 3.7.3.

3.8 Structural, Morphological and Optical Characterizations

In this thesis, structural, morphological, and optical characterization properties of a synthesized material were investigated using various techniques. These include high-resolution X-ray diffraction (HR-XRD), field emission scanning electron microscopy (FESEM) attached with an energy-dispersive X-ray spectroscopy (EDX) spectroscopy, transmission electron microscopy (TEM), atomic force microscopy AFM, photoluminescence (PL), Raman spectroscopy, and UV-Vis spectroscopy. Therefore, it is essential to provide brief description of the general setting parameters and operating conditions for each of the equipment used.

3.8.1 X-Ray Diffraction (XRD)

X-ray diffractometry one of the most powerful tools commonly used to study the structural characteristics of materials. The values of lattice parameters, residual stress, and the crystallite size were widely obtained by this technique. Therefore, it is a useful tool in determining the quality and crystallinity of a crystallite structure. In this study, high-resolution XRD measurements were carried out within the 20° to 80° range using system model (PANalytical X'Pert PRO MRD PW3040, Netherland). When the X-ray radiation is incident on the material crystal planes at a certain angle (Figure 3.7), interaction between the radiation and electrons in atoms lead to a diffraction at the intersecting planes according to conditions of Bragg's Law, which can be expressed in symbols as follows [145]:

$$2d_{hkl}\sin\theta = n\lambda \tag{3.1}$$

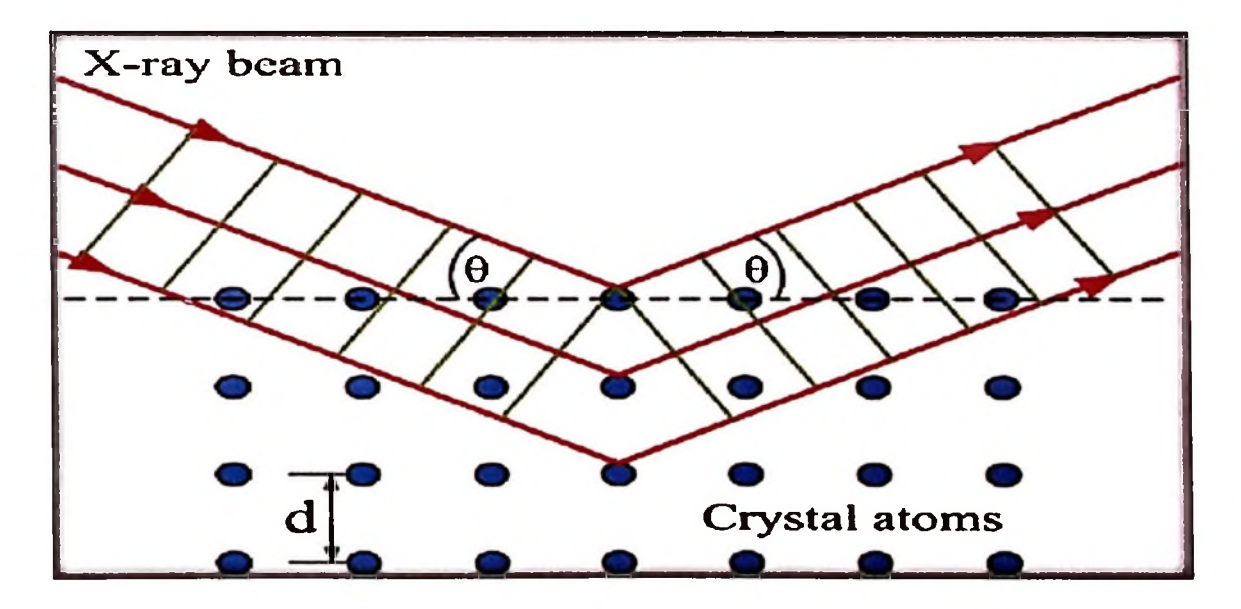


Figure 3.7: Bragg diffraction in a crystal. The angles at which diffraction occurs are a function of the distance between planes and the X-ray wavelength [146].

where d_{hkl} is the distance between adjacent planes with Miller-Bravais indices (hkl), θ is the angle of the diffraction peak, n is the order of diffraction (in an integer form), and where $\lambda = 0.15405$ nm is the wavelength of the X-ray source

(CuKα). The lattice constants a=b≠c of the würtzite hexagonal structure of ZnO NRs can be calculated using the following formula:

$$\frac{1}{d^2} = \frac{4}{3} \frac{h^2 + hk + k^2}{a^2} + \frac{l^2}{c^2} \tag{3.2}$$

Furthermore, the microstrain (\mathcal{E}_{zz}) of ZnO NRs along the c-axis can be calculated using the following equation [147, 148];

$$\varepsilon_{zz}(\%) = \frac{c - c_o}{c_o} \times 100 \tag{3.3}$$

where c_o represents the standard lattice constant for unstrained ZnO NRs. A positive value of the obtained strain is associated with the tensile strain and pointed to an expansion in the lattice constant, whereas a negative value is related to the compressive strain and indicates a lattice contraction. Moreover, the low obtained tensile microstrain confirmed the high quality of the crystalline structure of ZnO NRs.

3.8.2 Field Emission Scanning Electron Microscopy (FESEM) and Energy Dispersive X-ray (EDX) Spectroscopy

To characterize and analyze the product micro-and nanostructured (surface or cross-section) morphology, field emission scanning electron microscope was applied. The schematic diagram of FESEM and various emissions from the sample when electron beams interact with the sample are shown in Appendix B. Electrons generated from a field emission gun scan and enter a surface of a selected part of a sample through the column of the electromagnetic lens and generate many low energy secondary electrons. The secondary electrons are collected by the detector; an image is obtained which it shows a selected part the surface or cross-section

morphology of the sample. Both FESEM and SEM have the same fundamental principles of working, but they differ in the electron gun used to scan specimen. In FESEM a field emission gun is used while in SEM a typical electron gun source is used.

The EDX system detects X-rays emitted from the sample as a result of the interactions between the high-energy electron beam penetrating into the sample and the electron shell of the atoms of the constituent elements of the sample. This interaction generates photons in the X-ray wavelength range. Finally, the detected X-ray is analyzed by EDX. FESEM model FEI Nova NanoSEM 450 was used in this research to study morphology and measured EDX for the synthesized materials.

3.8.3 Transmission Electron Microscopy (TEM)

Transmission electron microscope (TEM) is a powerful equipment for and very useful imaging and characterization of materials in nanosize (1 nm) resolution. A real optical photo and schematic diagram for the cross section of TEM are shown in Appendix C [149]. The task and unique feature in TEM is that the incident beam of electrons pass through the sample. In SEM, an image of the sample surface is formed when a narrow accident beam is scanned on the surface of a sample and then measuring backscattered electrons, while in TEM, a broad beam of the electrons is usually generated by the electron source (gun) situated at the top of the microscope column and on the way to the specimen, the beam of electrons is accelerated and condensed by the rest of electromagnetic lenses and electrostatic plates. The fast electrons then interact with an ultrathin (150 nm) specimen which leads to penetration of the electrons through a specimen producing an image due to diffraction or mass-thickness contrast. Finally, this image of the sample is finally

recorded on a visible fluorescent screen or to be documented digitally by a detector such as a charge-coupled device (CCD) camera. However, a set of electromagnetic lenses is used to achieve a magnification and high-resolution of the image. In this study, TEM model Philips CM12, FEI (The Netherlands) was used to gather TEM images.

3.8.4 Atomic Force Microscopy (AFM)

AFM is an important technique for imaging surfaces. It is commonly used to characterize surface features of material such as surface roughness and grain size. In the AFM, the force produced from the interaction between the probe and a chosen sample surface plays a central role for obtained the imaging surfaces of the sample [150]. In other words, the operation in this technique is not based on the focus electron or photons beams on the surface to collect data. The system of AFM consists of a sharp tip at the end of a cantilever. A laser beam is focused on the back of the cantilever. When the tip came into very close proximity with a sample surface, it will result in deflections of the cantilever because of Vanderwaals force occurring between the AFM tip and the surface of the sample [151]. It is worth to mention that this force depends on the distance between the sample and the probe, the nature of the surface, sample surface contamination, and the geometry of the tip. When the cantilever flexes and approaches the surface, the laser beam from the back side of the cantilever is reflected onto position-sensitive photodetector.

The changes in the bending of the cantilever can be measured by the difference of the signal. Analyzing by computerized software is done in order to obtain the image of the sample surface topography and reflects into a four-quadrant photodetector. Normal forces deflect the cantilever up or down, lateral forces twist

the cantilever left and right [152]. The deflections are simultaneously and independently measured by monitoring the deflection of the reflected laser beam. The AFM images were analyzed using NanoScope III software. The schematic of an AFM system is shown in Appendix D [149]. In the current study, the AFM model Veeco NanoScope version 1.20) was used to obtain 3D surface structure and measure the roughness of the surface of ZnO seed layer on the substrate.

3.8.5 Photoluminescence (PL) Measurements

In this study, optical properties were measured at room temperature by photoluminescence (PL) spectroscopy, The PL spectra were collected using PL model: Jobin Yvon Horiba HR 800 UV, Edison, NJ, USA. In this equipment, the used excitation light source to encourage PL emissions from ZnO and GaN was a He-Cd laser with a wavelength of 325 nm (3.82 eV). PL spectroscopy is one of the most powerful techniques used to probe the optical properties. Therefore, it can be used to estimate the energy bandgap, the density of defects and the quality of a semiconducting material [153].

In this process, because of a photon energy of the laser source, which is incident on a surface of the sample has an energy higher than the material's band gap energy for the sample (Eexc > Eg), an electron raise from the valence band up to the conduction band across the forbidden energy gap, which results in hole formation. An electron-hole pair recombines occurs when these excited electrons falls back down to their ground (equilibrium) states, and naturally the excess energy is released through either radiative process (luminescence) or nonradiative process (phonon emission). Eventually, the CCD detector records this emission. A typical set-up for a PL measurement system is shown in Appendix E [154].

3.8.6 Raman Spectroscopy

Raman spectroscopy is an excellent practical tool for quickly identifying molecules and minerals and others scientific applications. Raman spectroscopy is a vibrational spectroscopic technique based on inelastic scattering (Raman scattering) of the high-energy monochromatic light (usually from a laser source). It was discovered, in 1928, by C. V. Raman and K. S. Krishnan (who was a student of C.V. Raman) [155]. In this research, the Raman spectra were collected using Raman model: Jobin Yvon Horiba HR 800 UV, Edison, NJ, USA.

Generally, photons of the laser light, which are incident on the sample, are absorbed by the material, thus lead to occurring scattering in incident light and the photon transfers some of its energy to the target molecules, which occurs either elastically (Rayleigh scattering) or inelastically (Raman scattering). In the Rayleigh scattering, the wavelength of the incident photon and the reemitted photon is the same, which indicates that the incident photon is transmitted through a target material without any changing in its energy. While unlike to Rayleigh scattering, in the Raman scattering, a small portion of photons is scattered and the energy transfer between the incident photon and molecule. This mean, the wavelength of the incident photon and the reemitted photon is similar, the wavelength of the reemitted photon may be shorter or longer than wavelength of incident photon. In addition, depending on increasing and decreasing in energy of the scattering photon, they can be classified into Raman stokes and Raman anti-stokes, respectively.

3.8.7 Optical Absorption

Although both the optical absorption and the photoluminescence are used broadly in determination of bandgap, they have different ways to analyze a sample.

Since PL is the spontaneous emission of light from a material under optical excitation, it needs absorption, while the optical absorption is not necessarily associated with occurrence of photoluminescence. The principle of the UV-Vis spectroscopy is based on the absorption of UV or visible photons by a material of a sample. As the result, an electron is transmitted from lower to higher energy states. In other words, the excitation of electrons from the filled valence band to the empty conduction bands occurs when the frequency of the incident light matches the difference in energy between these two electronic bands. Therefore, the optical absorption is an easy way to measure the energy bandgap and other optical properties of semiconductor materials.

In general, these two techniques are rather complementary. The schematic of a double beam UV-vis spectrophotometer is shown in Appendix F [156].. In this thesis, UV-vis spectra of ZnO NRs measurements were conducted at room temperature using a Shimadzu UV-vis 1800 spectrophotometer at wavelengths ranging from 300 to 800 nm. The optical band gap of ZnO NRs was determined by the extrapolation of the linear portion of $(\alpha hv)^2$ versus hv plots using Tauc formula [157]:

$$(\alpha h v)^2 = A_o (h v - E_g)^n \tag{3.4}$$

where α is the absorption coefficient, hv is the photon energy, A_0 is a constant associated with the transition probability, E_g is the optical band gap energy, and the parameter n depends on the transmission type (equals to 1 for allowed direct interband transmission, such as in a ZnO). The absorption coefficient is calculated from the absorbance data using the following formula:

$$\alpha = \frac{2.3A}{t} \tag{3.5}$$

where *A* is the absorbance and *t* is the film thickness.

3.9 Shadow Grid Mask

In this research, shadow grid mask was used for the deposition of metal grid contacts on top of ZnO NRs. The fabrication of the metal-semiconductor-metal (MSM) UV and hydrogen gas sensing devices were performed using RF sputtering of palladium (Pd) and platinum (Pt), respectively, as metal grids (100 nm thickness) on top of ZnO NRs using metal shadow grid mask. The active area of the (Pd/ZnONRs/Pd) MSM structured UV-PD and of the (Pt/ZnONRs/Pt) MSM structured H₂-sensor was 0.148 cm². Figure 3.8 shows the real top-view microscopic image of ZnO NRs MSM photodetector device.

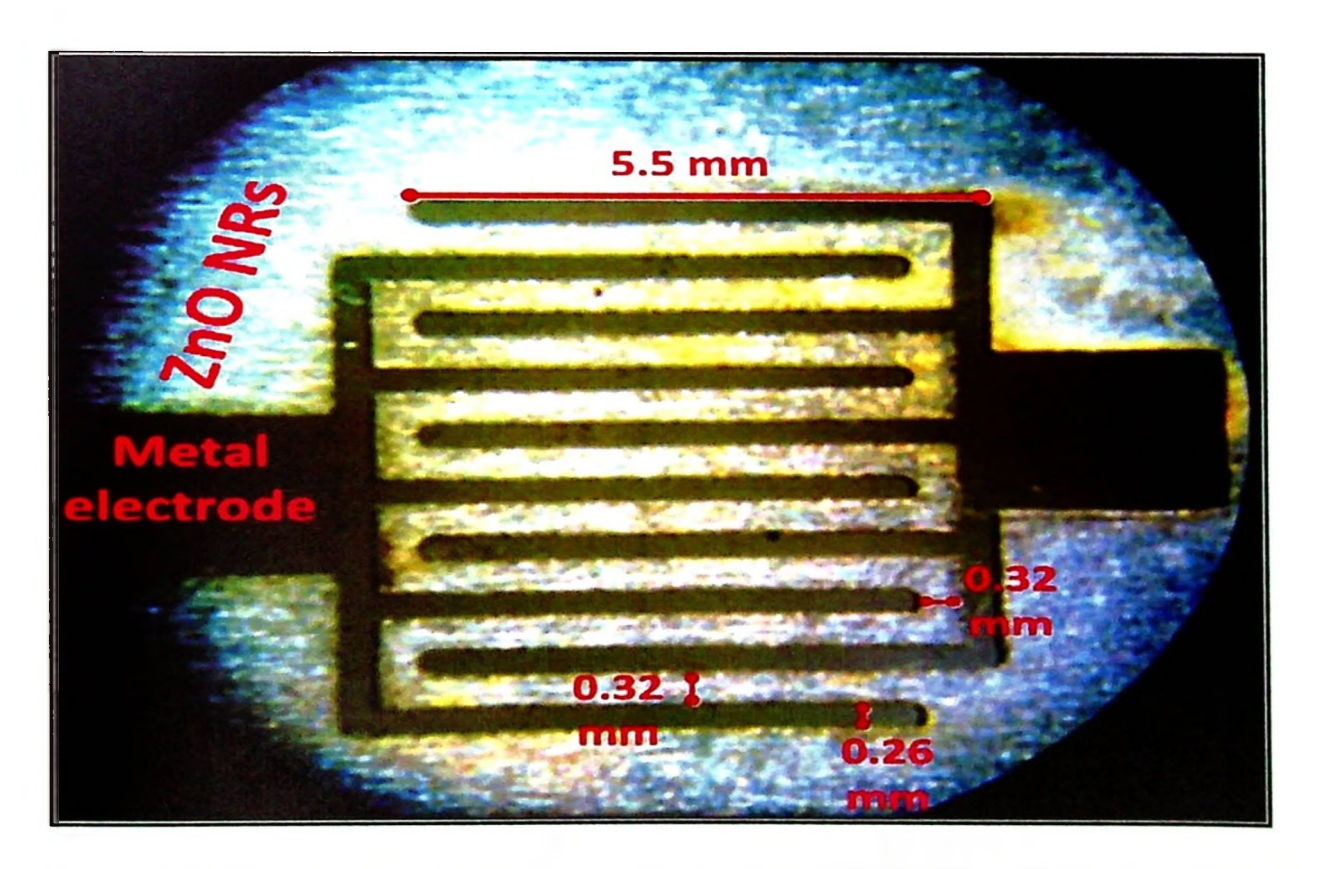


Figure 3.8: The real top-view microscopic image of ZnO NRs MSM photodetector device.

3.10 Device Characterization Techniques

In this study, a current source Keithley 2400 SourceMeter connected to a PC was used to measure current-voltage (I-V) characteristics of all the as-fabricated devices, MSM UV photodetectors, H₂ gas sensor and n-ZnO/p-GaN heterojunction LED. It was also used to measure current-time (I-t) characteristic of H₂ gas sensor. All measurements were performed at room temperature.

3.10.1 Measurements of Ultraviolet (UV) Photodetector

An UV lamp was used as illumination source with a wavelength λ =365 nm and the incident light power density was (approximately 1.5 mW when the UV source was placed 4 cm above the samples). All experiments were conducted at atmospheric pressure under UV illumination and in dark conditions. Figure 3.9 shows a schematic illustration of the experimental setup for the determination of the spectral response of the devices.

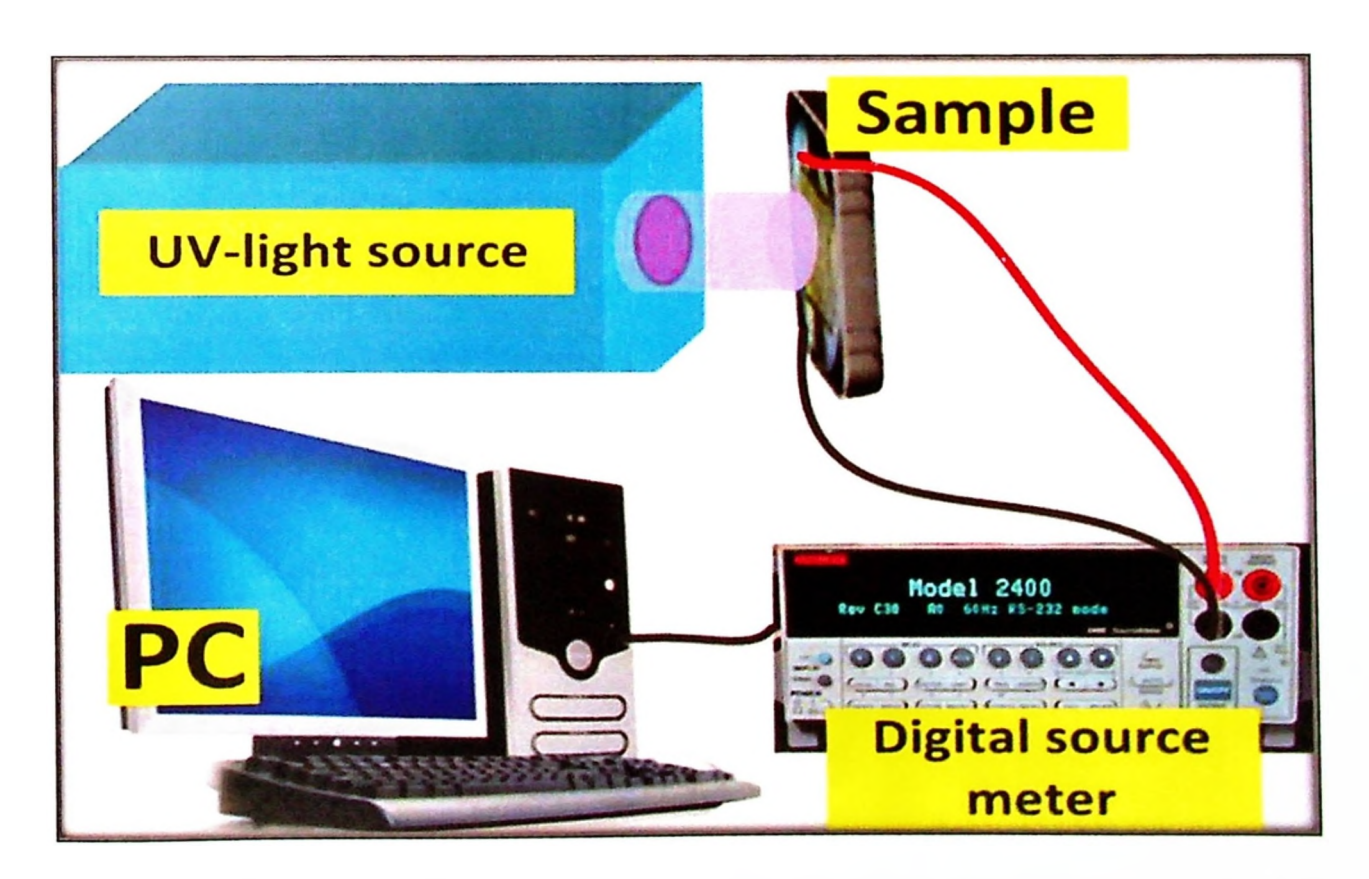


Figure 3.9: Schematic of experimental setup for photodetection measurements of the spectral response of the devices.

3.10.2 Gas Testing System

Gas sensor was placed in a homemade dark cylindrical stainless steel chamber, which was linked to a computerized system with a Keithley 2400 source meter to record the real-time data (Figure 3.10). The chamber volume was 1100 cm³. The final hydrogen gas concentration was controlled by adjusting the mixing ratio of the two gases (2000 ppm H₂, balanced in N₂) and dry N₂ through two gas flow controllers. The sample was placed onto an alumina plate inside the chamber with contact to the heater which allows adjustment of testing temperature. The gas responses to various H₂ concentrations ranging from 500 ppm up to 2000 ppm H₂ were analyzed. Hydrogen gas sensing measurements were carried out at temperatures ranging from room temperature (RT; ~25 °C) to 180 °C. All experiments were conducted at atmospheric pressure and RT.

The produced concentration of H₂ gas (C₂; in ppm) was calculated using the following equation [158]:

$$C_2 = \frac{C_1 \times F_H}{F_H + F_N} \tag{3.6}$$

Where C_1 is the concentration of hydrogen gas in the bottle (0.2% =2000 ppm), F_H is the flow of 0.2% H_2 / balance N_2 , and F_N is the flow of diluted N_2 gas. The sensitivity, response, and recovery behaviors were measured by exposing ZnO NRs to the air and hydrogen gas. The sensitivity of the H_2 sensor was determined according to the following equation [159]:

$$S(\%) = \frac{I_{H} - I_{air}}{I_{air}} \times 100$$
 (3.7)

where I_H and I_{air} are the currents of the gas sensor in the presence of hydrogen gas and air atmosphere (in the absence of H₂ gas), respectively. Additionally, the rising and falling times were the significant parameters in the fabrication of gas sensors. Rising time is defined as the time required to reach 90% of the response peak, whereas falling time is defined as the time needed to decline to 10% of the response [160, 161].

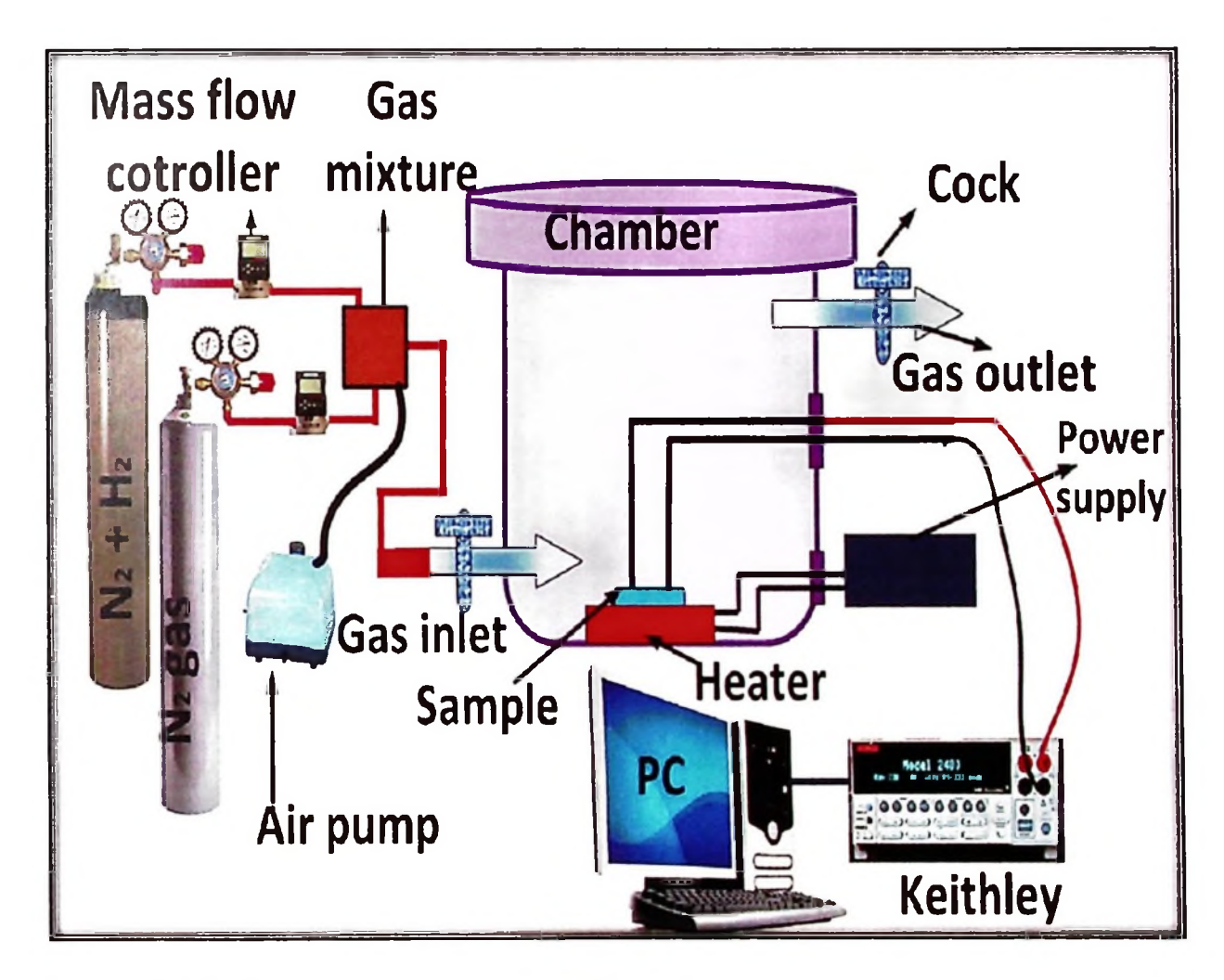


Figure 3.10: Gas sensor test system configuration.

3.10.3 Electroluminescence (EL) Measurements of LED

Electroluminescence (EL) is a light emission from a solid-state material. EL measurement is complementary and similar to PL measurement. But the main difference being that in EL the excitation is attained by an electrical current injection, instead of photons as in PL. When an electric current is applied to an optical

material, photons are emitted when radiative recombination of electron and holes occur. Then the light emission is collected by an optical fiber and that transports the light to the spectrometer in order to be analyzed and recorded. In this study, EL measurements were done using the USBB 2000 and Jaz Module (Ocean Optics) Spectrometer, which are linked to a computerized system with a Keithley 2400 SourceMeter as the current supply.

CHAPTER 4: RESULTS AND DISCUSSION: HIGHLY FLEXIBLE MSM UV PHOTODETECTOR DEVICES

4.1 Introduction

In this chapter, hydrothermal method is used to synthesise ZnO NRs. The novelty of this work consists of using a new ultra-thin (15 µm) and low cost flexible substrate to grow ZnO NRs, subsequently used for the fabrication of a highly flexible low-cost MSM UV-PDs. The experimental features of this method were explained in section 3.6.1. First, the thermal behavior of this nylon substrate was studied using differential scanning calorimetry (DSC) and thermal gravimetric analysis (TGA). To determine the optimum heat treatment duration applied to this ultra-thin flexible substrate after the deposition of a thin ZnO seeds/layer, the effects of hydrothermal heat-treatment temperature duration on ZnO NRs formation were systematically studied. The morphology of ZnO seeds/layer and the subsequently deposited ZnO NRs were investigated by FESEM and TEM. The surface morphology of ZnO seeds/layer was also investigated by AFM. The structural, optical and electronic properties of the samples are investigated using XRD, Raman, and UV-vis spectroscopy. Finally, UV detection properties for the whole samples are also investigated.

4.2 Thermal Properties of Substrate

It is well know that thermal analysis (DSC and TG) is used for the identification of neat basic polymers as well as to determine their purity and stability [144, 162]. In this study, the nylon substrate was investigated by DSC analysis under dry nitrogen at a heating rate of 20 °C per minute from -10 to 300 °C. From Figure 4.1, it can be found that the nylon substrate has a relatively high melting point

temperature of 251 °C. This value corresponds with the type 6, 6 nylon (PA66) which has a melting temperature in the range of 255-265 °C [163]. This higher melting point indicates that the thermonylon has thermal stability making it more resistant to heat, hence an appropriate substrate for the growth of ZnO nanostructures by hydrothermal method for optoelectronics applications. Moreover, it can be observed from Figure 4.1 that the values of quantities Tg, Tc, ΔC_p and ΔH_m were 78.98 °C, 137.22 °C, 0.227 J/g and 42.49 J/g, respectively.

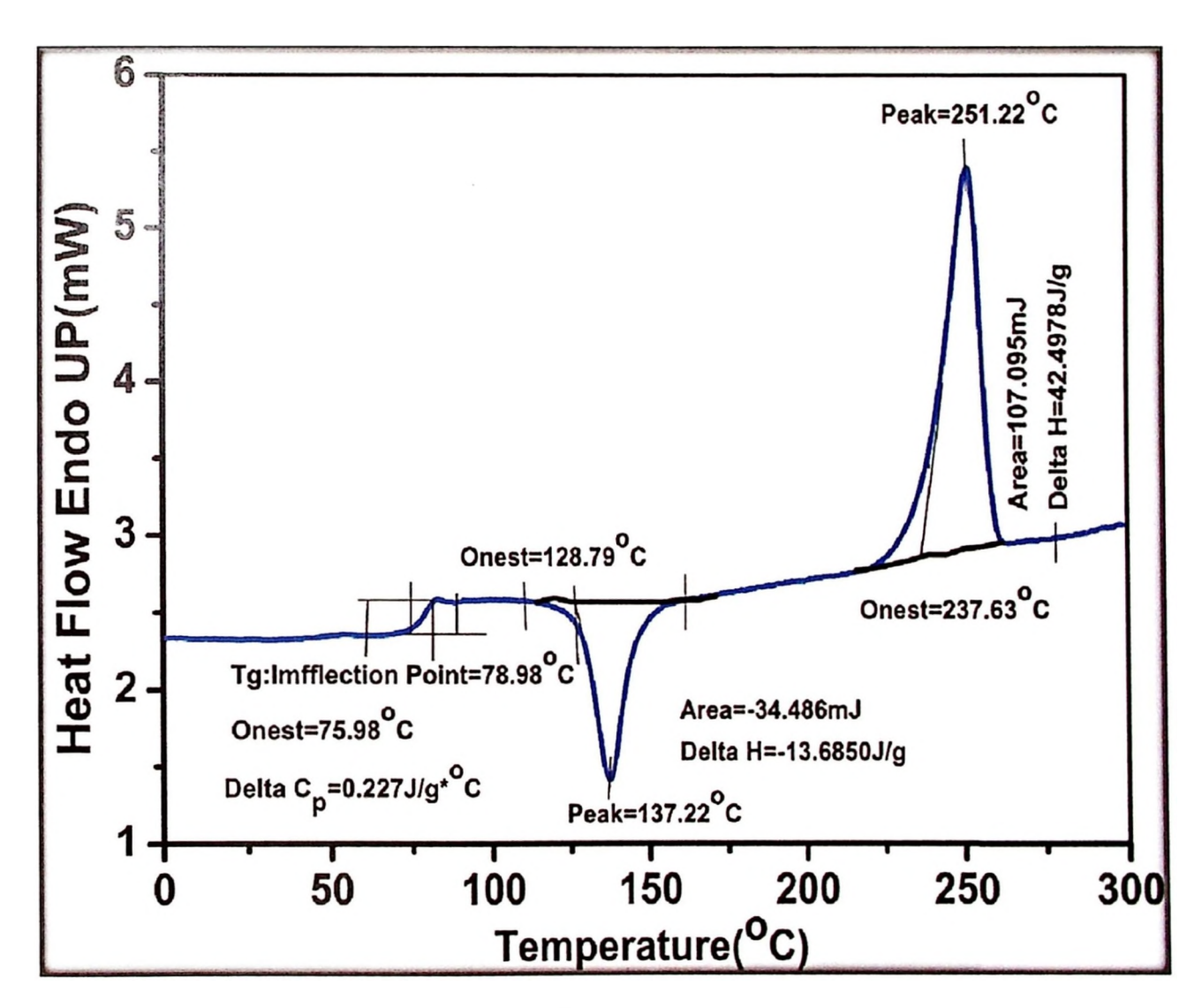


Figure 4.1: DSC spectrum of the flexible nylon substrate.

The thermal stability of nylon substrate was also investigated by thermogravimetric analysis under dry nitrogen atmosphere. DGT (rate of weight

loss) and TG (weight loss of substance in relation to the temperature of thermal degradation) curves are shown in Figure 4.2. It is obvious that nylon began to degrade at approximately 375 °C and completely decomposed at approximately 850 °C. The maximum rate of weight loss (DGT_{max}) for nylon substrate occurred at 447 °C (37.85%) and appeared in the range of 400–500°C. Above 447 °C, the nylon exhibited a gradual weight loss up to 900 °C. However, the temperature of nylon substrate compound is stable up to at least 375 °C under the above mentioned conditions.

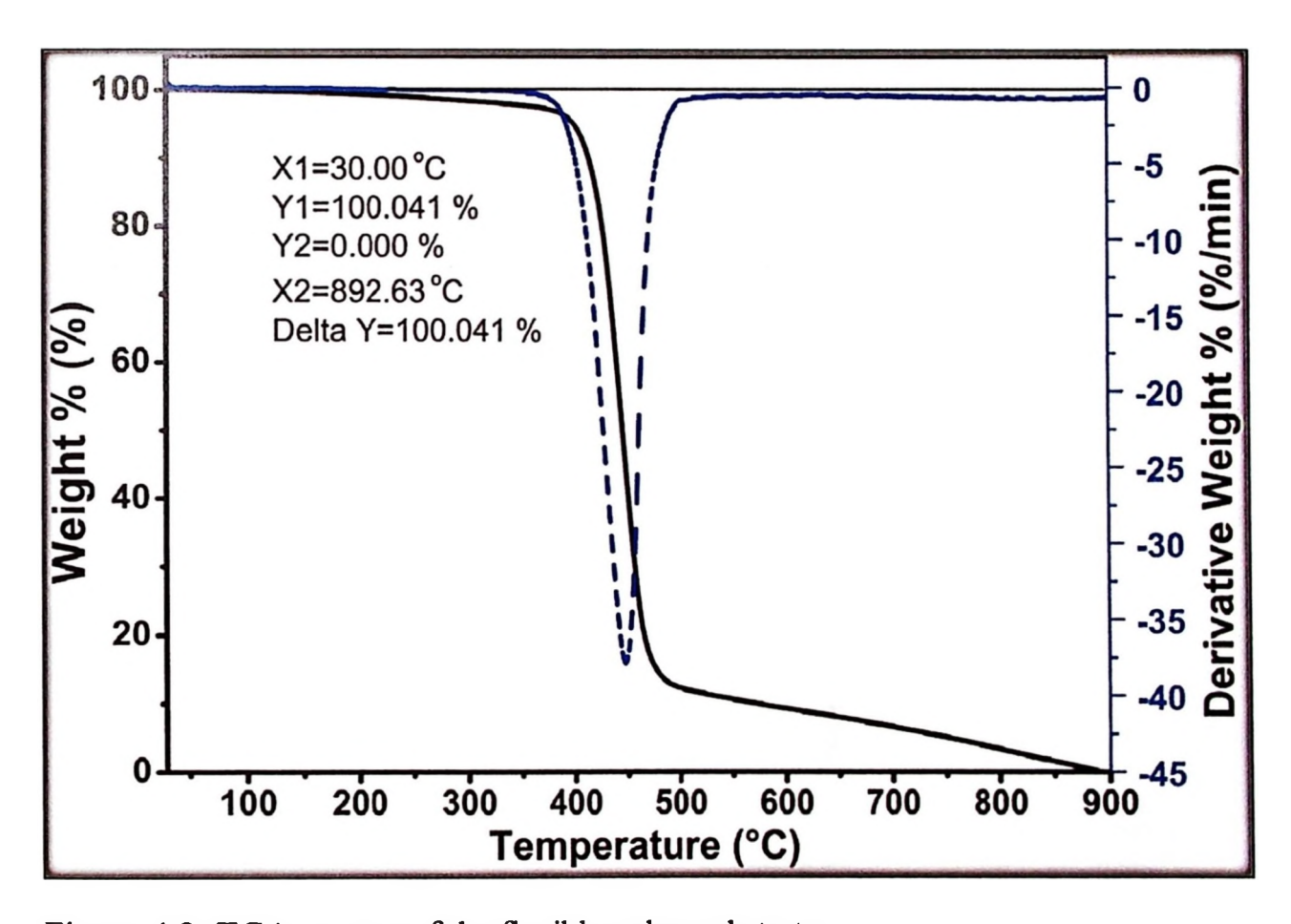


Figure 4.2: TGA spectra of the flexible nylon substrate.

4.3 Effect of Different Seed-Heat-Treatment Duration

The evolution of surface morphology of ZnO films deposited onto nylon substrate after heat treatment in air at fixed temperature of 180 °C for various periods of time (0.5-6 h) and as-deposited, is shown in Figure 4.3. In order to grow the best

ZnO NRs array by hydrothermal method, ZnO seeds (ZnO thin layer) is needed. Usually, ZnO seeds after deposition onto a substrate without any prior treatments do not show uniform size and the distribution is too compact, as can be seen in FESEM image of sample (a). After the heat treatment, ZnO seeds are more uniform in size, more homogeneous distribution and well separated. Also, Figure 4.3 reveals that ZnO seeds became smaller with increasing annealing time [74]. In this study, a constant temperature of 180 °C was chosen for ZnO seeds/flexible substrate heat treatment but the duration of the heat treatment was varied.

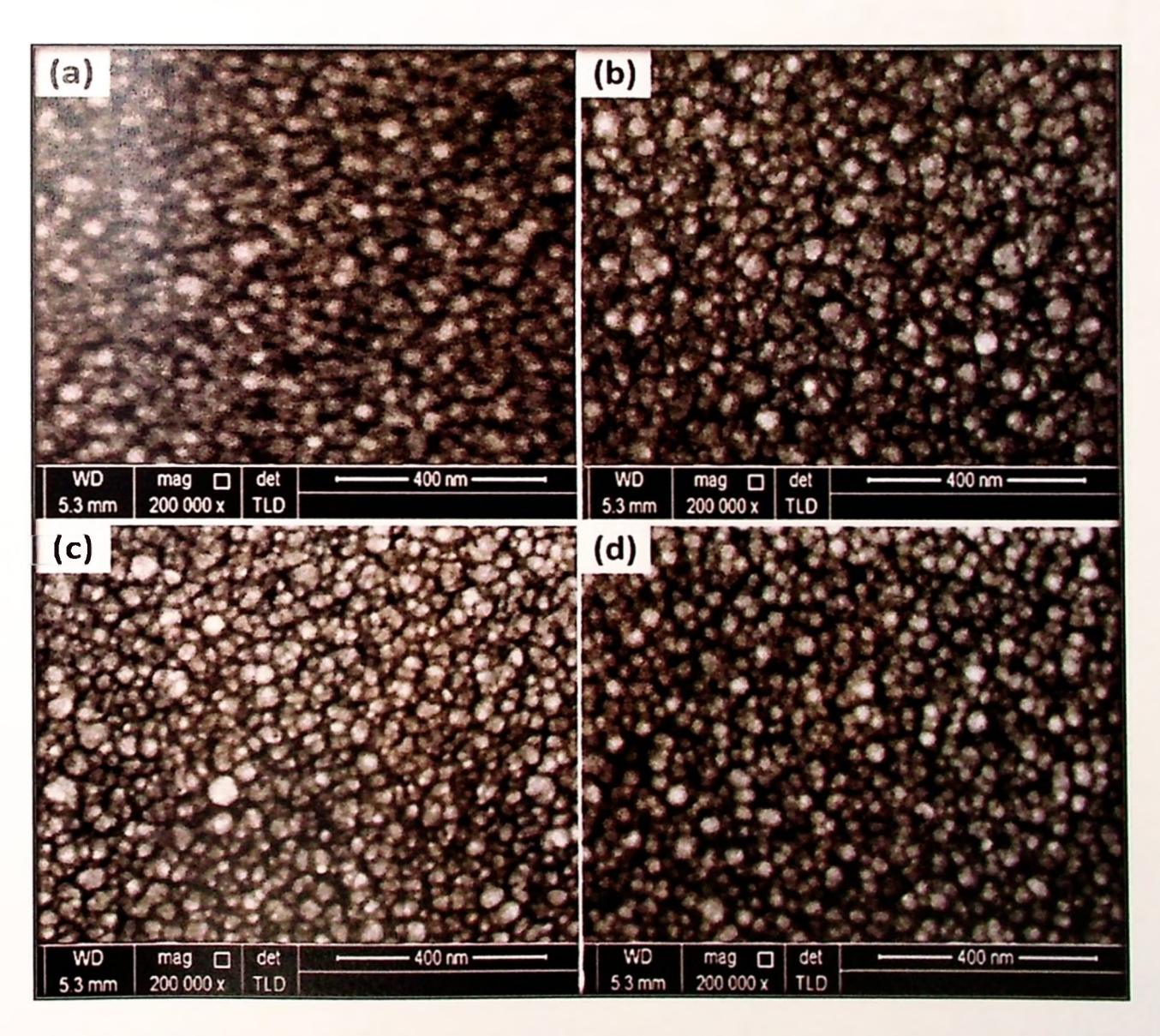


Figure 4.3: Surface morphology of ZnO seeds, (a) at room temperature and heat treated at 180 °C for (b) 0.5 h; (c) 3 h; (d) 6 h.

AFM images (Figure 4.4) reveal the surface morphology of ZnO films deposited onto nylon substrates. It shows that ZnO grains grow along Z-direction (perpendicular to the nylon substrate) and that the grains mean-size decreases with increasing heat treatment duration. Due to the low temperature used for annealing ZnO seeds/nylon substrate, the island coalescence was not observed.

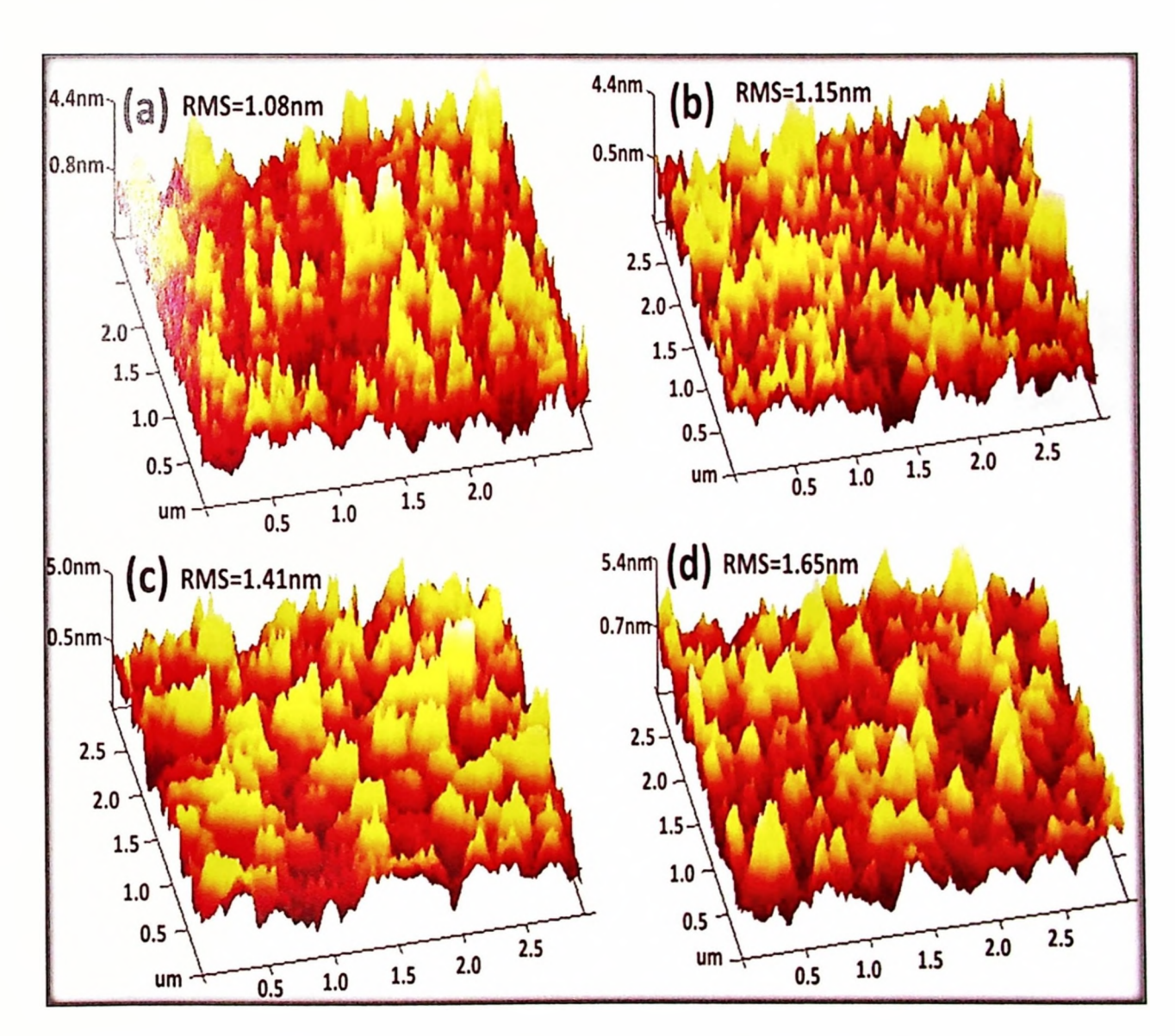


Figure 4.4: 3D-topography obtained by AFM of ZnO films over (3x3) μ m² scan area (a) at room temperature and heat treated at 180 °C for (b) 0.5 h; (c) 3 h; (d) 6 h.

Additionally, it can be noticed that the surface roughness increases with increasing heat treatment duration, the value of root-mean-square (RMS) changed

from 1.08 nm up to 1.65 nm over (3x3) µm² scan area. This can be attributed to the increase in the distance from the island base to the top, because the diameter of grains became smaller [164]. Based on top-view FESEM and AFM images (Figures 4.3 and 4.4), it can be noticed that the sample for which ZnO seeds have been heat treated for a duration of 3 h shows the best ZnO thin layer used as seed for the successful growth ZnO NRs by hydrothermal method [74, 164, 165].

4.4 Effects of Seed Heat Treatment Duration on Growth of ZnO NRs

In order to investigate the effect of ZnO seeds/nylon after annealing at 180 °C for different periods of time on ZnO NRs formation, the seeded substrates were subjected to hydrothermal growth at 85 °C for 4.5 h. Figure 4.5 presents FESEM of ZnO NRs grown onto ZnO seeds/nylon-substrate after being heat treated in air at 180 °C for various duration (0.5-6 h) and as-deposited (used as reference for comparison). It can be observed that the obtained ZnO NRs for all samples were vertically oriented with respect to the nylon/substrate direction, while at the top end of the rods for samples (a, b and c) looks like a bit tilted.

This gives a good advantage for increasing the efficiency of light absorption or raising the percentage of penetration of gas atoms into the material. Additionally, ZnO NRs show regular hexagonal-like shape because the precursor concentration used in this study was 0.1M, whereas the hexagonal structure becomes irregular when the precursor concentration is higher than 0.1 M [166-168]. It is worth mentioning that for sample (a), a small percentage of the rods were not exactly hexagonal but more close to a rectangular shape.

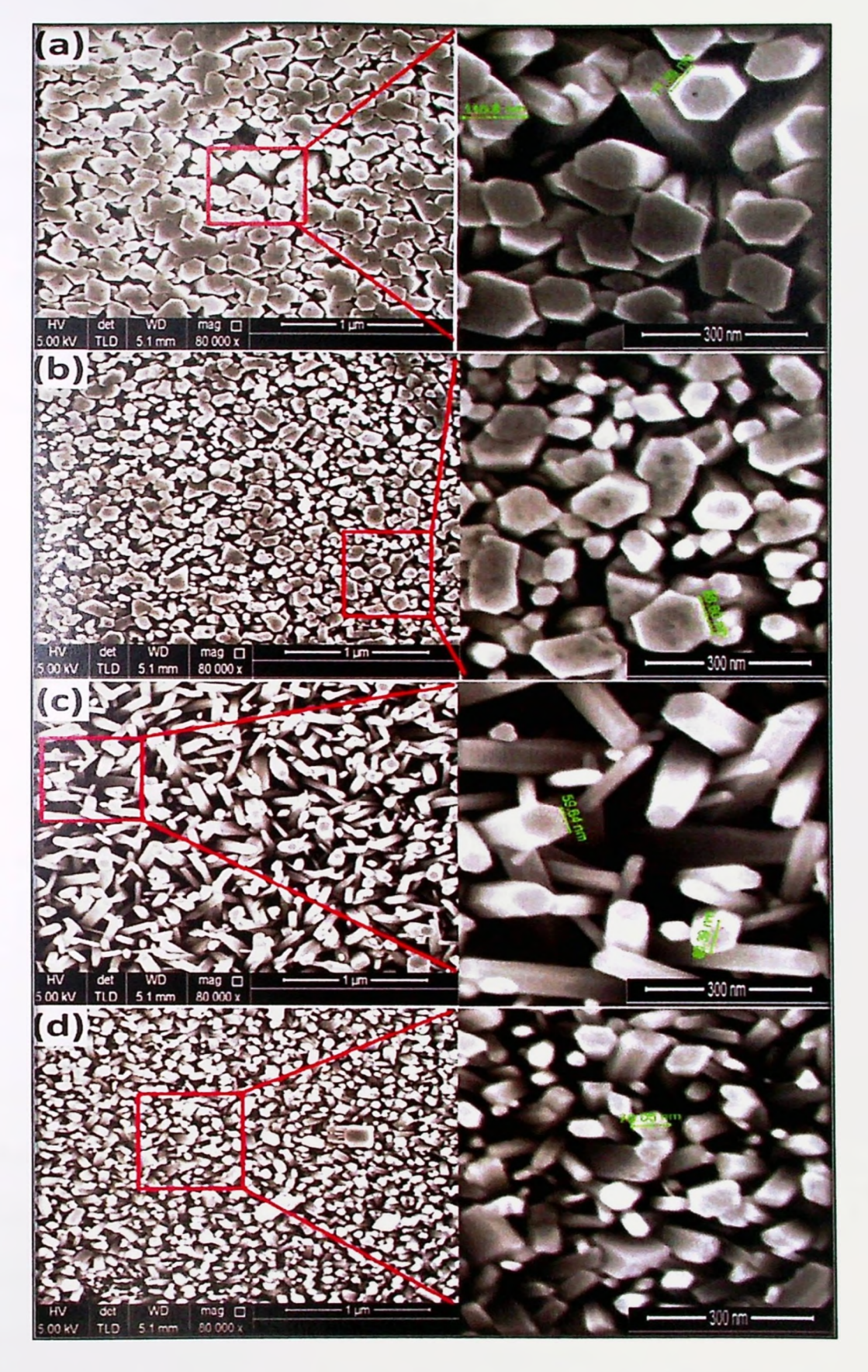


Figure 4.5: FESEM images of ZnO NRs grown onto ZnO seeds/nylon-substrate, (a) at room temperature and heat treated at 180 °C for (b) 0.5 h; (c) 3 h; (d) 6 h.

However, for sample (c), all nanorods were found to have perfect hexagonal shape without any quasi-hexagonal shape. In addition, in this study, it is clear from Figure 4.5 that the density of ZnO NRs formed onto ZnO seeds/nylon increased when the time of seeds annealing increased [166]. This may be due to the fact that the diameter of ZnO seeds became smaller, leading to an increase of the number of ZnO grains within the same area of the substrate. Each grain of ZnO seeds represents the base for one grown nanorod.

Moreover, one can notice from the top-view of FESEM images (Figure 4.5), that the nanorods for samples (a and b) are very close to each other while the distance between the nanorods for sample (c) becomes larger. This indicates that the absorption of light or the penetration of gas atoms into the sample (c) will be much easier and more efficient in comparison to other samples. This result demonstrates that the growth rate of ZnO NRs has a strong dependence on the formation and characteristics of seeds layer.

4.5 TEM Images of ZnO NRs

Figure 4.6 illustrates TEM images of ZnO NRs grown onto ZnO seeds/nylon-substrate. It can be seen that the obtained ZnO NRs for all samples have smooth surface, hexagonal-like shape, and a uniform diameter along their whole lengths. It is found also that the average diameter of ZnO NRs decreases, while the length increases with increasing pre-heat treatment duration of ZnO seeds/nylon substrate for samples (a), (b) and (c). However, the average diameter and length of ZnO NRs for sample (d) increases and decreases respectively: 110 nm and 490 nm for sample (a), 170 nm and 1314 nm for sample (b), 96 nm and 1460 nm for sample (c) and 110 nm and 1200 nm for sample (d), respectively.

Therefore, the average aspect ratio (average length / average diameter), to which the surface area (important factor for detector devices) is usually associated, increases for all samples, see Table 4.2.

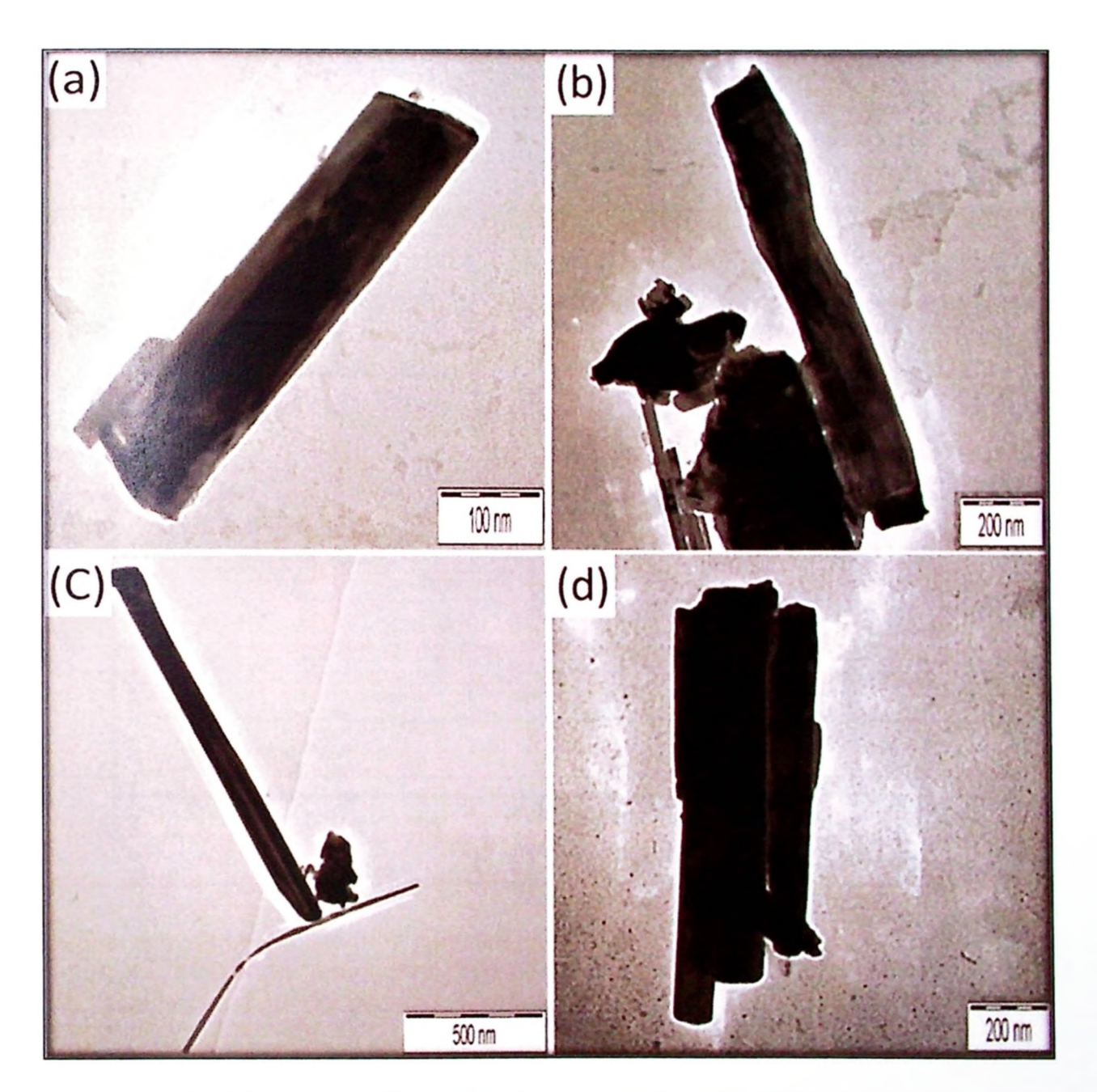


Figure 4.6: TEM images of ZnO NRs grown onto ZnO seeds/nylon substrates, (a) at room temperature and heat treated at 180 °C for (b) 0.5 h; (c) 3 h; (d) 6 h.

4.6 Structural Characterization by X-ray Diffraction

Figure 4.7 presents graphs showing the evolution of XRD patterns for hydrothermally ZnO NRs grown onto ZnO seeded layer/thermonylon-substrate heat treated at 180 °C for various periods of the time. All observed diffraction peaks match well with the wurtzite hexagonal phase of ZnO (JCPDS Card No. 01-079-0207) except for the peak located at 2θ =25.975°, which was assigned to the flexible thermonylon substrate [169].

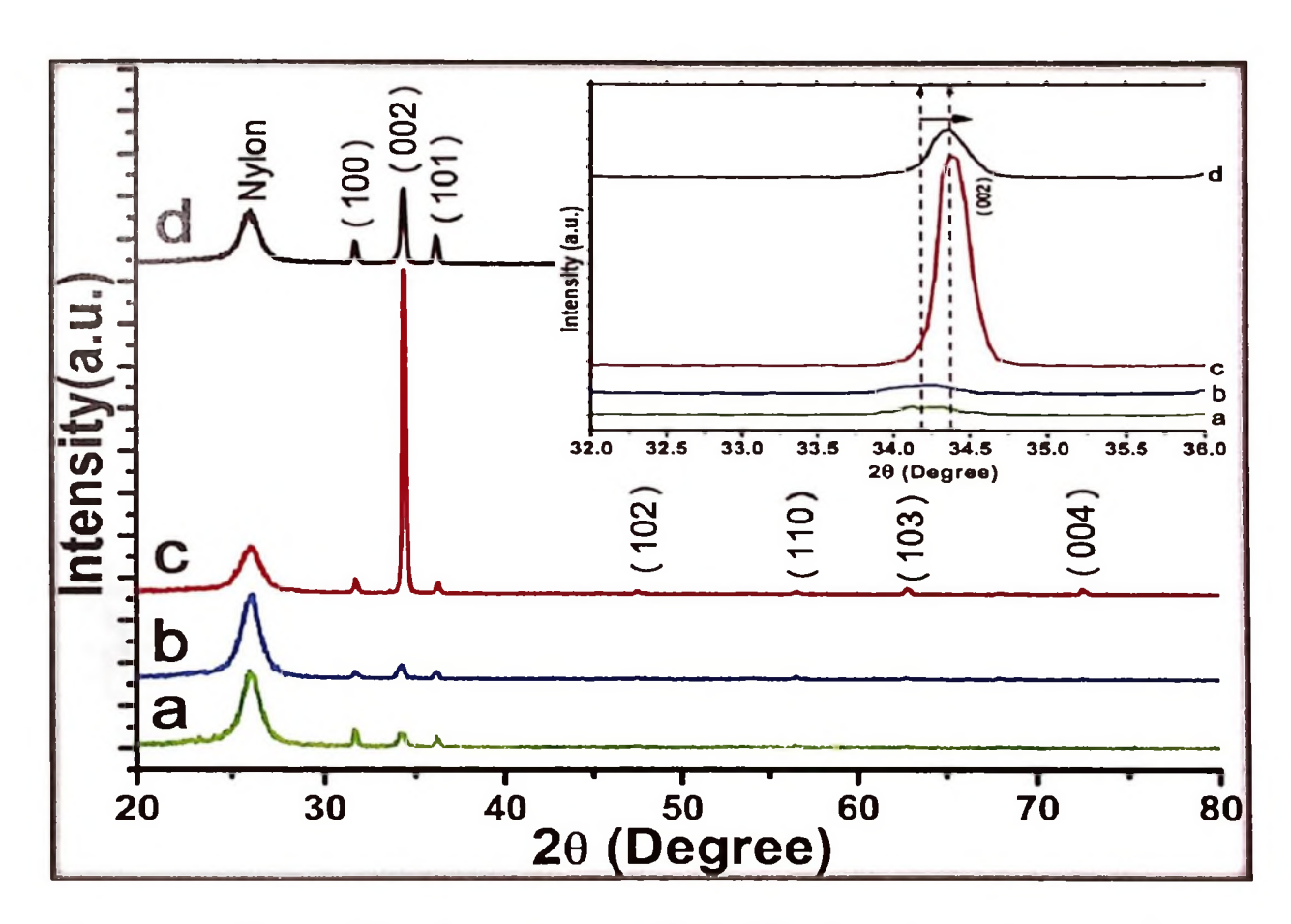


Figure 4.7: X-ray diffraction patterns of ZnO NRs formed onto ZnO seeds/nylon-substrate (a) at room temperature and heat treated at 180 °C for (b) 0.5 h; (c) 3 h; (d) 6 h. The insets show the peak (002) reflection.

The inset in Figure 4.7 showing the evolution of (002) reflection reveals a shift towards higher 20 angles, from 34.125° for sample (a) to 34.375° for sample (d). This indicates that for longer heat treatment duration of ZnO seeds, the intrinsic strain volatilization (usually induced the presence of residual strain resulting from

imperfections within the crystalline lattice, including vacancies, stacking faults, and interstitials) takes place, thereby leading to that Zn and O atoms to be perfectly stacked at order [164]. The lattice constant c_o and the strain (ε_{zz}) along the c-axis of the würtzite structure of ZnO NRs were calculated by using the XRD data according to Eqs. 3.2, and 3.3, respectively (in section 3.8.1). The parameters are summarized and listed in Table 4.1.

Table 4.1: Structural parameters determined from (002) reflection, (FWHM full width at half maximum) and the determined optical band gap values for samples.

Sample	Heat treatment duration (h)	FHWM (°)	Intensity (a.u.)	Peak position (°)	C (nm)	E ₁₂ (%)	Eg (eV)
а	0	0.464	173	34.125	0.52502	0.6739	3.266
b	0.5	0.476	174	34.225	0.52353	0.3886	3.274
С	3.0	0.266	3833	34.375	0.52132	-0.0363	3.285
d	6.0	0.267	896	34.375	0.52132	-0.0363	3.288

From Figure 4.7 and Table 4.1, the positive values of strain for samples a and b were associated with the tensile strain while the negative values for the samples c and d revealed the compressive strain for ZnO nanorods. In general, these very low values of tensile and compressive strains suggest that the synthesized ZnO nanorods have high quality crystal geometry.

It can be observed that sample (c) has the highest intensity for (002) reflection while (100) and (101) reflections show lower intensity. This indicates a strong preferred orientation of the grown ZnO NRs along (002) direction (z direction perpendicular to the substrate) with high crystallinity. On the other hand, it was also

observed that the intensity of both (100) and (101) reflections of sample (d) increases while that of (002) reduces. This shows the importance of ZnO seeds pre-treatment on the grains growth direction of ZnO NRs. A longer heat treatment time of ZnO seeds, leads to the growth of ZnO NRs along (100), (101) and (002) planes simultaneously. FESEM images of sample (d) show that some of the NRs are not exactly hexagonal but close to the rectangular or semi-hexagonal shape.

4.7 Optical Properties of the Grown ZnO NRs Array

Figure 4.8 presents graphs showing UV-vis absorbance spectra of samples (a-d). The exciton absorption is observed in the range 367-379 nm. The sample (c) shows the highest absorption at highest peak of wavelength while the sample (a) has the lowest absorption at the lowest peak of wavelength.

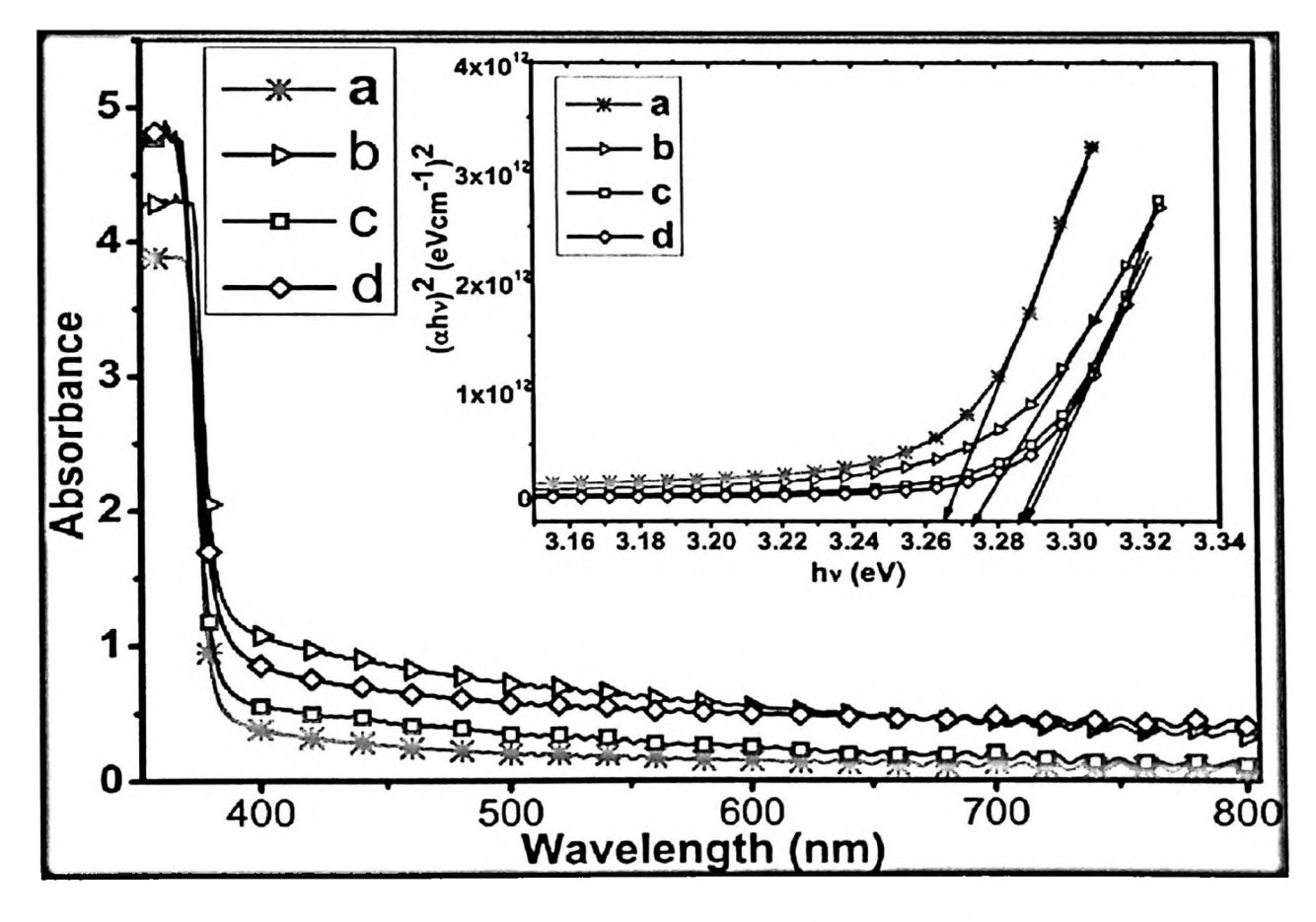


Figure 4.8: Optical absorption spectra of the ZnO NRs on ZnO seeds /nylon substrate, (a) at room temperature and heat treated at 180 °C for (b) 0.5 h; (c) 3 h; (d) 6 h. The inset shows plot of $(\alpha hv)^2$ versus hv.

The optical band gap energy of ZnO NRs was determined by the extrapolation of the linear portion of $(\alpha h v)^2$ versus hv plots using Tauc Eq (3.4) (Section 3.8.7). The inset in Figure 4.8 shows the evaluation $(\alpha h v)^2$ versus hv plots. The determined optical band gap values are 3.266, 3.274, 3.285 and 3.288 eV for samples (a, b, c and d), respectively. Obviously, all the above values are very close to the band gap of intrinsic ZnO powder and are in good agreement with the literature reports [170, 171]. However, compared with the band gap energy of ZnO single crystal (3.3 eV), the calculated optical band gap energies of the ZnO NRs for all samples were somewhat smaller. The small variation of the band gap energy might be originated from the defects in ZnO NRs [172]. Moreover, the variation in Eg for all samples with heat treatment duration of ZnO seeds layer is minor. It can be seen that the optical band gap energy is slightly increased from 3.266 to 3.288 eV as heat treatment time of ZnO seeds is increased.

4.8 UV Detection Properties

The room temperature current-voltage (I-V) characteristics of MSM UV photodetectors based on ZnO NRs are measured under UV illumination (λ =365 nm) and in dark. I-V characteristics results (photocurrent (I_{ph}), dark current (I_d) and the current gain (ratio of light current to dark current (I_{ph}/I_d) are shown in Figure 4.9 and from the insert, respectively. The responsivity (R) of as-fabricated UV detector devices based on ZnO NRs was calculated using Eq. 2.7 (section 2.5.2). In order to give a better comparison between the samples with different heat treatment duration of ZnO seeds layer/nylon substrate, the values of the dark current, photocurrent, current gain, responsivity (all values were measured at volage equal to 5 V) and the average aspect ratio are summarized in Table 4.2.

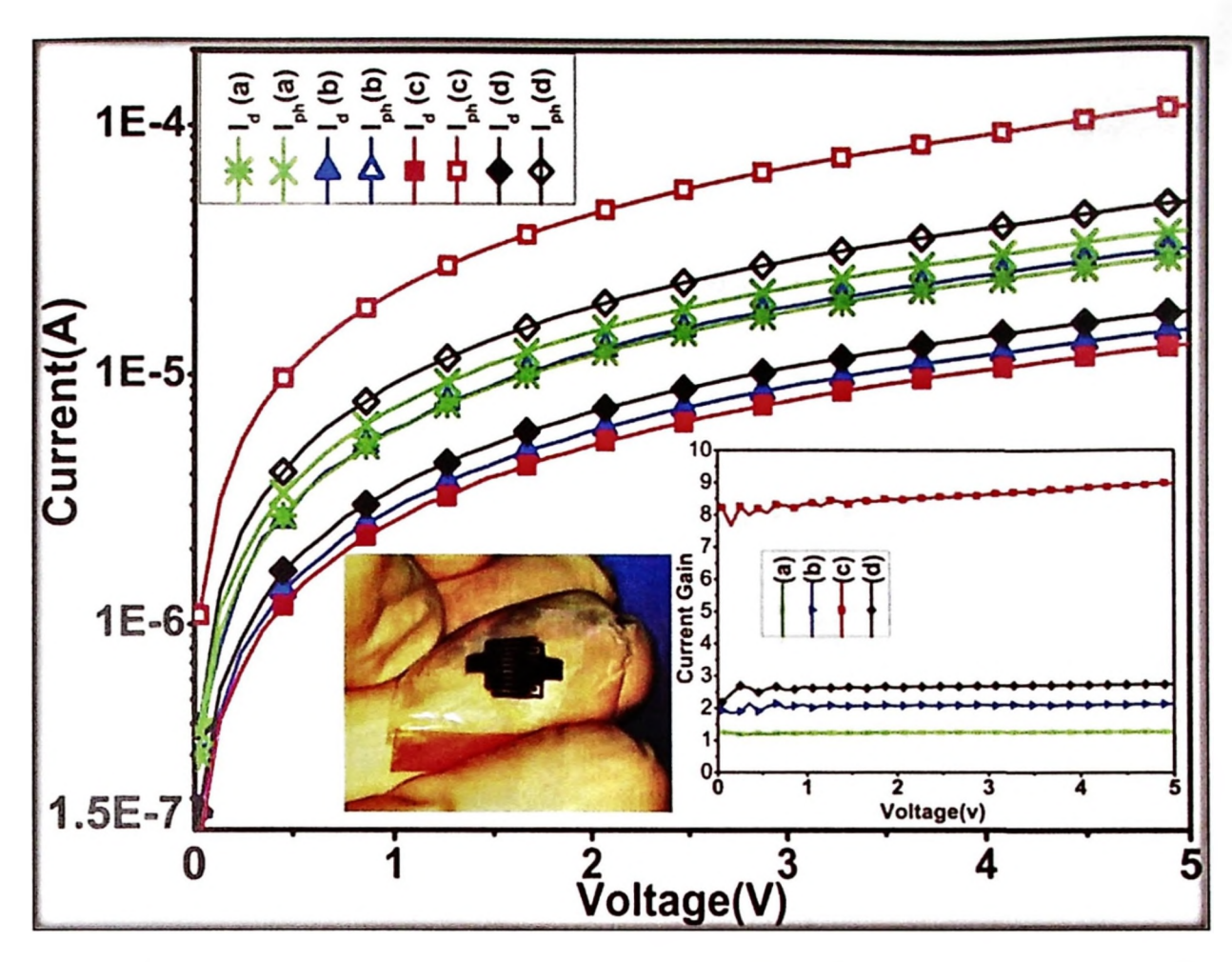


Figure 4.9: I-V characteristics of the fabricated MSM UV-photodectectors under UV illumination (I_{ph}) (λ =365 nm) and in dark (I_d) . The inset shows the current gain-voltage curves.

Table 4.2: Dark current, photocurrent, responsivity and average aspect ratio with different time of heat treatment of ZnO seeded layer/nylon substrate.

Sample	I _d (mA) at 5 V	I ph (mA) at 5 V	Current gain at 5 V	R (A/W) at 5 V	Average aspect ratio
а	0.030	0.038	1.26	0.0360	4.45
b	0.015	0.032	2.13	0.0766	7.73
c	0.013	0.119	9.15	0.4774	15.21
d	0.018	0.049	2.72	0.1396	10.90

From Figure 4.9 and Table 4.2, it can be noticed that sample (c) has the highest photocurrent and responsivity, due to two main reasons: (i) its larger aspect ratio which refers to the higher surface area, as well as the presence of deep level surface trap states within the NRs which greatly prolongs the photocarrier lifetime [81], and (ii) X-ray diffraction indicate that the formed hexagonal-shaped ZnO NRs are highly crystalline with wurtzite hexagonal phase having significantly less structural defects. Moreover, one can point out from Figure 4.8 and Table 4.2, that sample (c) has the lower dark current, because its NRs have the highest surface area which enhanced its resistivity and thus decreased the dark current value. Thereby, this results in sample (c) having higher gain among the other samples as can be seen in the insert of Figure 4.8.

The value obtained of the photocurrent in this chapter $(0.119\times10^{-3} \text{ A})$ at operating voltage of 5V is higher than many published works [97, 98, 173, 174]; where they obtained the photocurrent values by applied voltage biases in the range (5-10 V). Ji, L. W. et al. [173]; and Manekkathodi et al. [98]; measured the photocurrent values of $(0.18\times10^{-6} \text{ A})$ and $(70\times10^{-6} \text{ A})$, respectively, at applied voltage bias 10 V. Ghosh et al. [174]; and Yao et al. [97]; measured a low photocurrent values of $(4.67\times10^{-6} \text{ A})$ and $(70\times10^{-6} \text{ A})$, respectively, at applied voltage bias 5 V. However, the lower values of responsivity for different values of aspect ratio in this study might be due to different approach of controlling the aspect ratio of the prepared ZnO NRs compared with the previous works.

4.9 Summary

Novel "ultra-thin - high flexible - low cost" nylon was successfully used as a substrate to grow vertically well-aligned and hexagonal-shaped ZnO NRs by hydrothermal method at 85 °C for 4.5 h. The thermal behavior and properties for this nylon substrate were studied. The effects of pre-annealing duration of ZnO seeds layer on structural, morphological and optical properties were investigated. A pre-heat treatment at 180 °C for 3 h was found to be the most appropriate procedure to produce uniform nanosized ZnO seeds. Highly flexible low-cost Pd/ZnO NRs/Pd MSM UV detector using this flexible thermo-nylon substrate was successfully fabricated and investigated. It can be easily inserted on a device with moving parts. High surface-to-volume ratio and high crystalline quality with less structural defects within ZnO NRs are necessary to produce a large current gain (9.15) and an excellent responsivity (0.4774 A/W) for a UV detector at a voltage bias equal to 5 V and upon exposure to 365 nm UV light.

CHAPTER 5: RESULTS AND DISCUSSION: HIGHLY FLEXIBLE HYDROGEN GAS SENSOR DEVICE

5.1 Introduction

In this chapter, the same novel flexible nylon was used as a substrate for the growth of ZnO NRs, as in chapter 4. In addition, the hydrothermal technique was used to synthesize ZnO NRs on this selected substrate. The novelty of this work consists of using the thinnest substrate that fabricates a highly flexible low-cost hydrogen gas sensing device instead of a photodetector. The experimental features of this method have been explained in Section 3.6.2. The morphology, structural, and optical properties of ZnO NRs are investigated by FESEM, EDX, XRD, and PL. Finally, the gas responses to various H₂ concentrations at various temperatures are also investigated.

5.2 Structural Characterization by X-ray Diffraction

The crystal structure properties of the ZnO NRs grown on ZnO seeded layer/nylon substrate are shown in Figure 5.1. The XRD pattern for the hydrothermally grown ZnO NRs showed that the observed diffraction peaks matched well with the würtzite hexagonal phase of ZnO (JCPDS Card No. 01-080-0074), but the peak located at $2\theta = 25.869^{\circ}$ was assigned to the flexible thermonylon substrate [169]. The main peak of the (002) reflection located at $2\theta = 34.32^{\circ}$ demonstrated very high intensity, indicating that ZnO NRs grew preferentially along the c-axis (perpendicular to the substrate). The strong intensity and low value of the full width at half maximum (FWHM) (0.17°) of the (002) peak indicated that ZnO NRs exhibited good crystalline quality. The very weak peak (004) at 72.52° represented

the second order of the main peak (002). The standard lattice constant c_o for unstrained ZnO NRs was equal to 0.52151 nm [175].

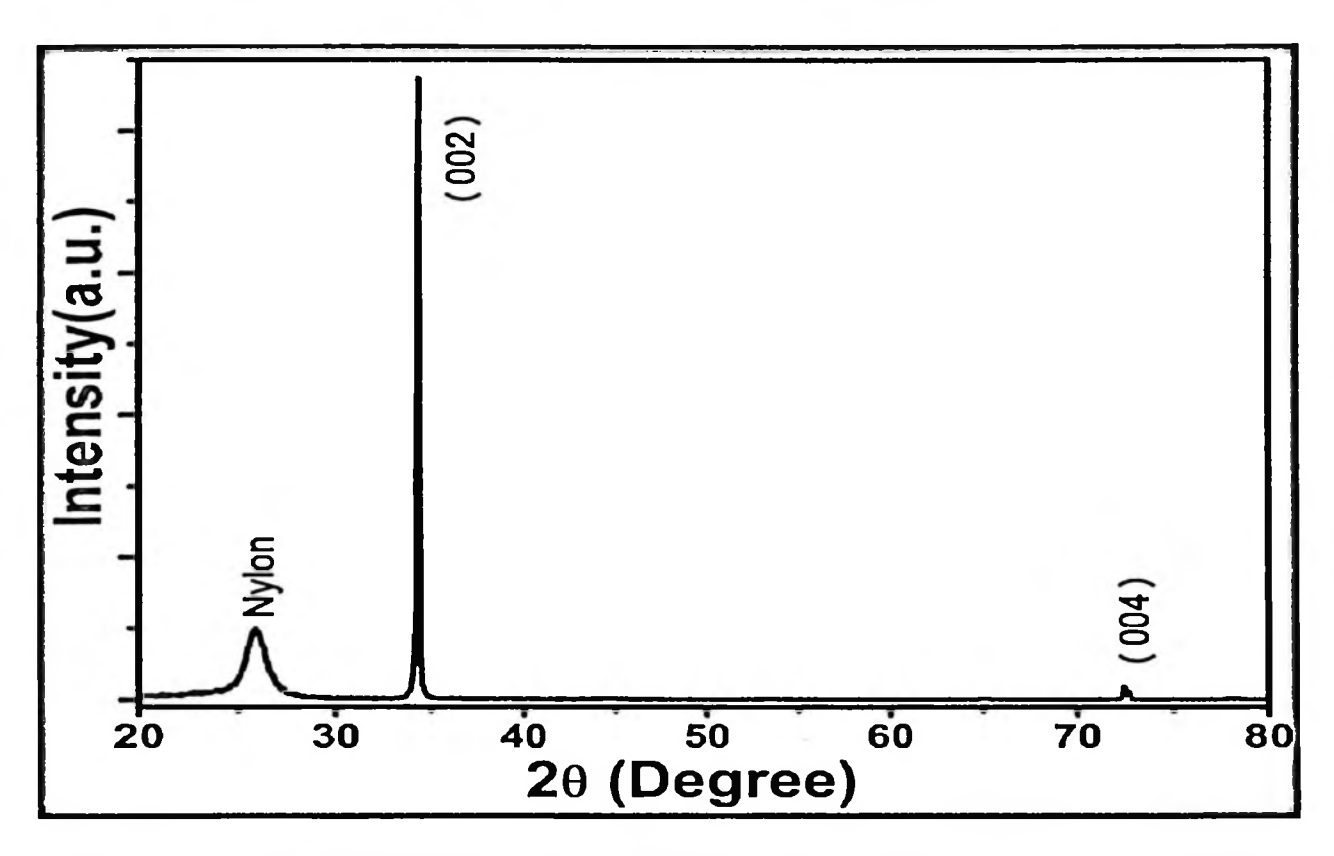


Figure 5.1: X-ray diffraction pattern of ZnO NRs formed onto ZnO seed/nylon substrate.

The lattice constant c_o and the strain (ε_{zz}) along the c-axis of the würtzite structure of ZnO NRs were calculated by using the XRD data according to Eqs. 3.2 and 3.3, respectively (in the section 3.8.1). The calculated lattice constant and microstrain were 0.52213 nm and 0.119%, respectively. The obtained lattice constant was close to the values reported in the literature [175]. The positive value of microstrain indicated the presence of a tensile strain for the as-grown ZnO NRs, as well as an expansion in the lattice constant, which usually occurs when a mismatch (difference in lattice parameters) exists between the material and the substrate. A positive value of the obtained strain was associated with the tensile strain and pointed

to an expansion in the lattice constant, whereas the low obtained tensile microstrain confirmed the high quality of the crystalline structure of ZnO NRs.

Furthermore, a comparison of the XRD patterns of samples (Figure 5.2 and Figure 4.2) revealed the appearance of two peaks corresponding to the (100) and (101) planes of hexagonal wurtzite crystal structure of ZnO NRs for all samples in Chapter 4 and not present in the sample in Chapter 5. This mean that the wurtzite crystal structure of ZnO NRs in this chapter is more to the formation of a single phase compound and highly oriented along c-axis than the samples in Chapter 4. The difference of the mentioned results might be due to the difference in approach and the concentrations of the zinc nitrate solution used for the prepared ZnO NRs.

5.3 Optical Properties of the Grown ZnO NRs

Figure 5.2 illustrates the room-temperature PL spectrum of the ZnO NRs grown on ZnO seed/nylon substrate. The high UV emission peaks for the sample located at approximately 378 nm (3.28 eV), with a FWHM as narrow as 12 nm, were due to the near-band-edge emission (NBE) of the wide ZnO band gap, which resulted from the recombination of the free exciton process. In addition, the broad visible peaks were related to the deep level emission (DLE) of ZnO, which was attributed to the native defects in ZnO NRs. The green emission centered at 540 nm (2.30 eV) is common in the ZnO structures which is often attributed to the recombination of electrons and holes in singly ionized oxygen vacancies [176, 177]. The origin for the emission at approximately 561 nm (2.21 eV) and 588 nm (2.10 eV) are attributed to the transition of electrons from oxygen vacancy (Vo) to the valence band [178, 179]. while the peak at approximately 618 nm (2.01 eV) is possibly caused in the following ways: transition from the conduction band to the monovalent vacancies

(Vo⁺); and transition from the interstitial zinc (Zn_i) or oxygen vacancy (Vo) to the monovalent vacancies (Vo⁺) [180]. Moreover, the emission bands are localized in the emission spectral range of 650-680 nm (1.90-1.82 eV), for red bands. The red emission is attributed to defect levels associated with oxygen vacancies or Zn interstitials [181-183].

These defects and vacancies were expected because of the ZnO NRs already synthesized on the nylon substrate via the hydrothermal method and it is believed that Hydrothermally grown ZnO NRs have inherent crystalline defects primarily due to oxygen vacancies [58, 184]. The intensity of this UV peak was much higher than that of the broad peak. The high I_{UV}/I_{DLE} ratio (the intensity of the UV emission to the visible deep level) associated with luminescence intensity suggested that the grown ZnO nanorod arrays showed a small number of defects [185].

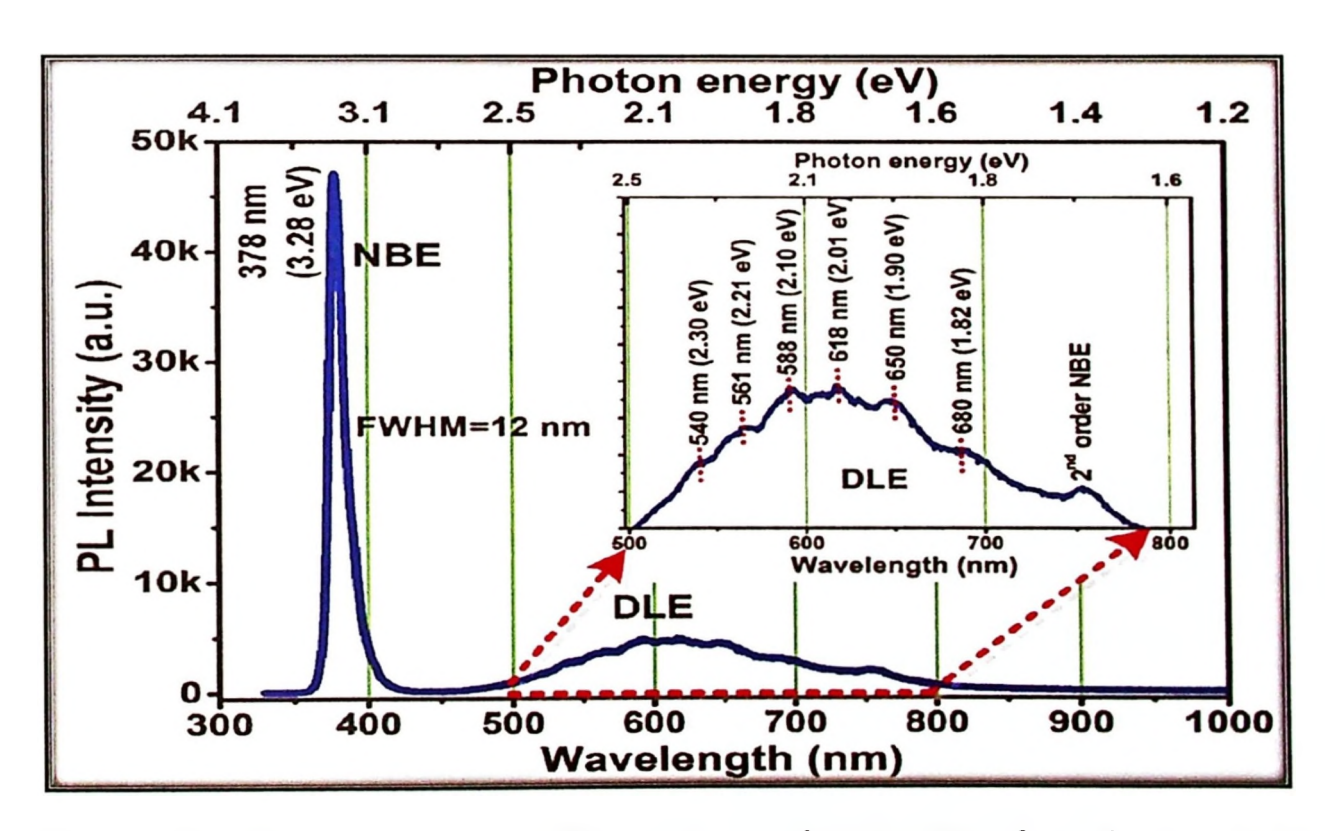


Figure 5.2: Room-temperature PL spectrum of ZnO NRs formed onto ZnO seed/nylon substrate. The inset shows the zoom in on the PL in the range of wavelength =500 to 800 nm (DLE region).

5.4 Current-Voltage (I-V) Characteristics of the Device (Pt/ZnO NRs/Pt)

Figure 5.3 presents graphs showing I–V curves of the MSM device (Pt/ZnO NRs/Pt) as prepared and annealed at 180 °C for 4 h in ambient air. Although theoretically, the Pt/n-type ZnO contact should show a Schottky behaviour (due to that the work function of Pt metal is greater than work function of n-type ZnO), in this work, from both curves, it can be seen that the MSM device shows back-to-back semi-Schottky contact (or semi-ohmic contact). Because of the work function of a semiconductor varies with the concentration of impurities and defects. In other words the work function difference (between a metal and a semiconductor) also is related to the electrode materials and the semiconductor impurities and defects concentration [186].

Therefore, due to the low temperature of hydrothermal method, high defects concentration formed in the fabricated ZnO NRs, which lead to difficulty to form perfect Schottky contacts, even the contacts between as-prepared ZnO NRs and an electrode with large work function metals [187]. However, the annealing for the MSM device (Pt/ZnO NRs/Pt) at 180 °C for 4 h did not change significantly the contact behavior, but as can be seen clearly in Figure 5.3 the decrease in the resistivity occurred and the contact resistance became somewhat lower after annealing. It is believed that the population of the defects in ZnO increases when ZnO to be on both the process conditions during a heat treatment, which leads to increase in the leakage current, hence a decrease in the resistivity of the contact regions [188].

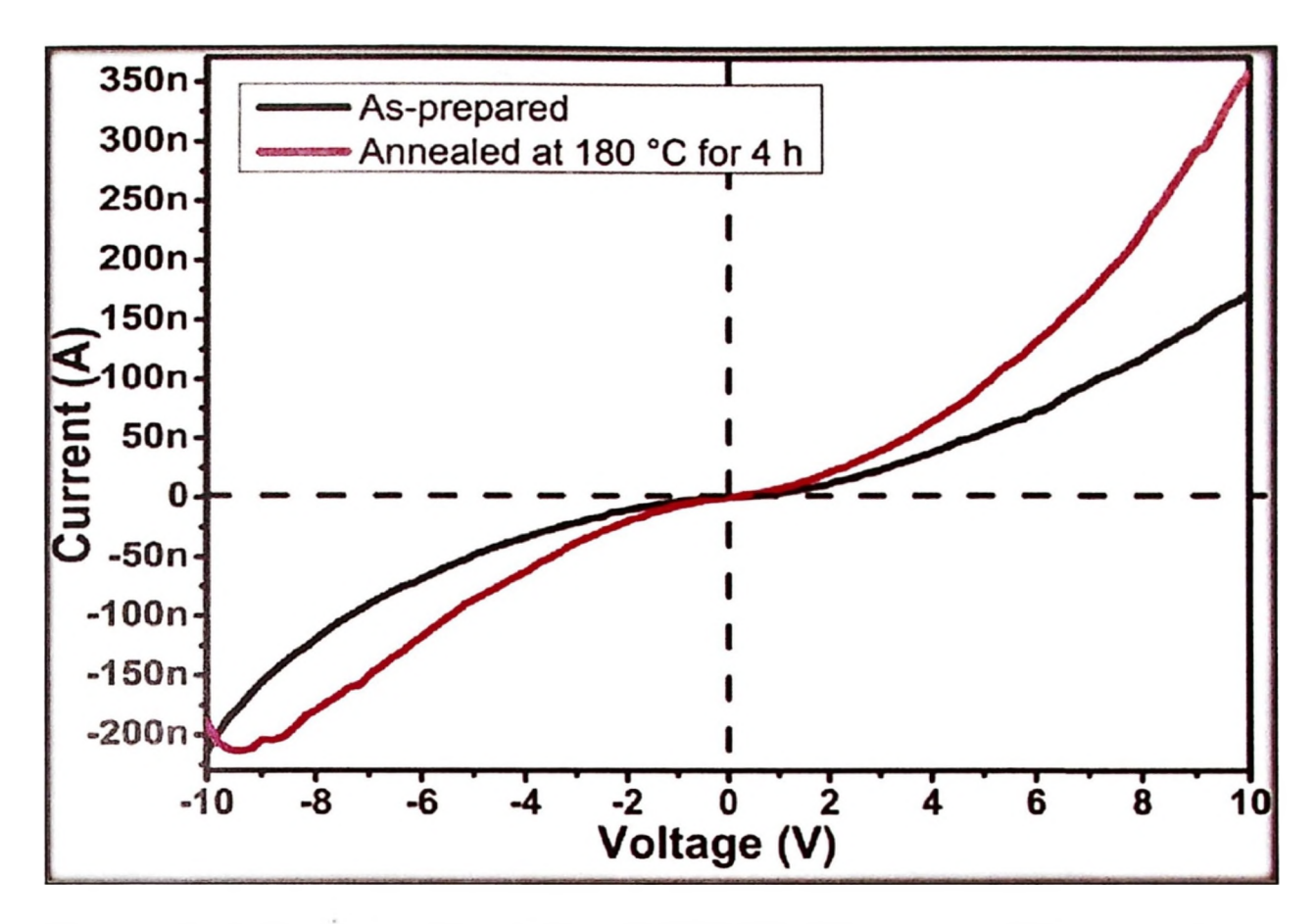


Figure 5.3: I-V curves of the device (Pt/ZnO NRs/Pt) as prepared and annealed at 180 °C for 4 h.

5.5 Hydrogen Gas Sensing Property

The fabricated device was tested at different operating temperatures (RT, 75 °C, 120 °C, and 180 °C) and under exposure to different H₂ concentrations (750, 1000, 1500, and 2000 ppm) for ZnO nanorod sensor at an operating temperature of 75 °C. In all the testing of operating temperatures and different concentrations of H₂ gas, the device showed reasonably measured currents. The sensitivity, response, and recovery behaviors were measured by exposing ZnO NRs to the air and hydrogen gas. The sensitivity of the H₂ sensor was determined according to Eq. 3.7 (section 3.10.2). Figure 5.4 reveals the sensitivity versus time of the prepared device at different operation temperatures under exposure to 500 ppm of H₂ for 4 min. The sensitivity, response times, and recovery times for ZnO NRs sensor operating in the range of various temperatures are tabulated in Table 5.1.

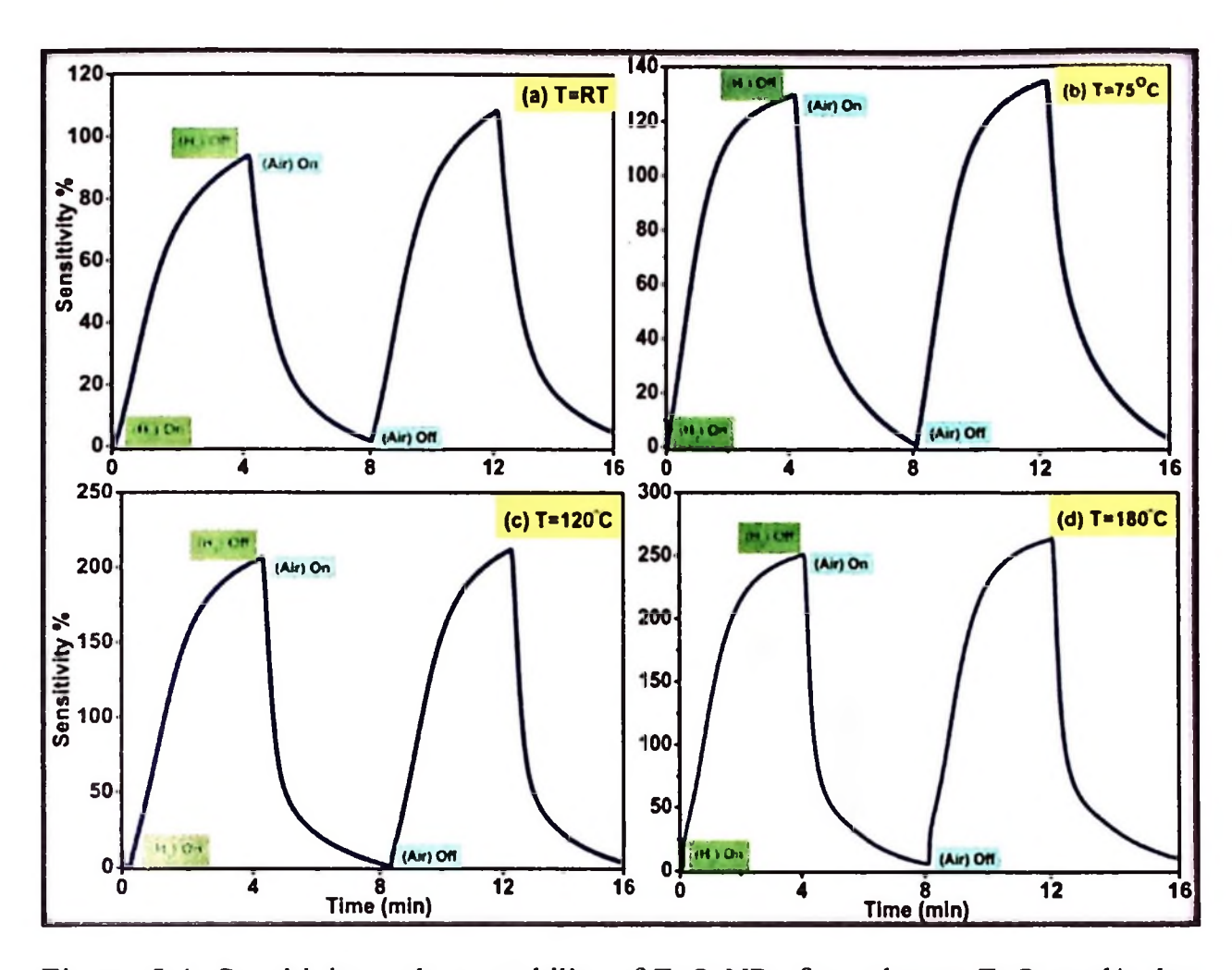


Figure 5.4: Sensitivity and repeatability of ZnO NRs formed onto ZnO seed/nylon gas sensor at different sensor temperatures: (a) RT, (b) 75 °C, (c) 120 °C, and (d) 180 °C.

Table 5.1: Effect of temperature on the sensitivity, rise time, and recovery time of the fabricated device.

Temperature (°C)	Sensitivity (%)	Rise time (s)	Recovery time (s)	
RT	109	149	122	
75	135	130	134	
120	212	129	100	
180	264	127	103	

As shown in Figure 5.4 and Table 5.1, the sensitivity improved with the operating temperature. Moreover, the response time slightly increased with the operating temperature, whereas the recovery time was obviously enhanced when the operating temperature was more than 100 °C. The surface activity of ZnO increased as the operating temperatures increased, which lead to the enhancement in the adsorption/desorption rate of the gases at higher operating temperature and increasing the conductivity and sensitivity of the devices. The increasing of the temperature of the sensor may be lead to enhanced oxygen adsorption from the atmosphere on the surface of ZnO NRs, in other words, the concentration of adsorbed oxygen become higher with increasing temperature which leads to the amount of the free electrons from the bulk of ZnO which captured by adsorbed oxygen become larger. Therefore, when the ZnO NRs sensor was exposed to hydrogen gas, a large amount of adsorbed oxygen molecules are desorbed from the ZnO surface, thereby emancipating the trapped electrons and increasing the conductivity and sensitivity [189]. Additionally, the plots in Figure 5.4 demonstrate the good repeatability of the sensor.

Figure 5.5 shows the sensor response for different H₂ concentrations (750, 1000, 1500, and 2000 ppm) of ZnO NRs sensor at an operating temperature of 75 °C. The results showed that the sensor device presented the best sensitivity at an H₂ gas concentration of 2000 ppm. However, the sensitivity decreased as the gas concentration decreased. As shown in the inset of Figure 5.5, the sensitivity also sharply increased from 246% to 578% when the exposed H₂ gas increased from 750 ppm to 2000 ppm at a fixed temperature of 75 °C.

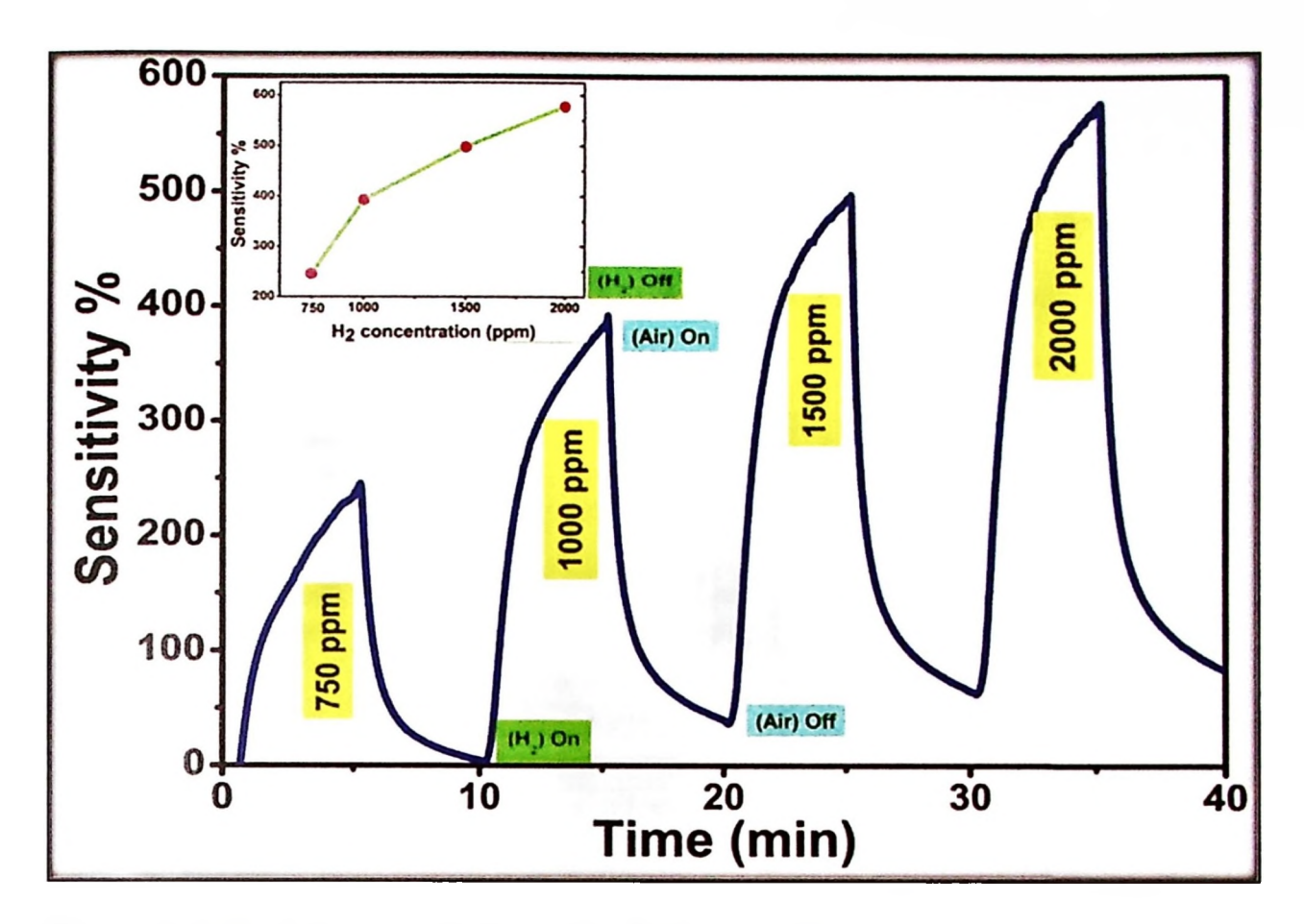


Figure 5.5: Real-time sensitivity of the ZnO nanorod array sensor upon exposure to H₂ with various concentrations (750, 1000, 1500, and 2000 ppm) at operating temperature of 75 °C.

In this work, humidity is a serious problem for the sensor, in which the sensitivity of the sensor decreases with increasing relative humidity [190]. In general, physisorbed water requires low temperatures, 150 °C, to be removed, but the chemisorption process of water (OH groups) onto oxides is quite strong, and high temperature is required to remove it [191, 192]. In this work, it can be observed that the sensitivity of device keep increasing with the temperature and the sample sensitivity did not drop at certain temperature, implying that the water has no effect at this temperature due to no decrease of sensitivity sensor. Therefore, it can be concluded from these results that the hydroxyl and water have no effect on the sensor sensitivity. This is probably due to the lower diffusion efficiency of the water molecules into the longer ZnO NRs [193], in other words, the high aspect ratio and a

high density of ZnO NRs play an important role to reduce the negative effects for molecules of H₂O which may be formed on the ZnO NRs surface. Table 5.2 presented a comparison of hydrogen gas concentration, the sensitivity, operating temperature, rise time, and recovery time obtained in the previous studies and in the present work.

Table 5.2: Sensing properties of ZnO gas sensor obtained from previous and present work.

Material	Substrate	Growth method	Concentration (ppm)	T _{opt} (°C)	S (%)	Rice time (s)	Recovery time (s)	Ref.
ZnO NRs	PET	Hydrothermal	1000	RT	373	100		[194]
ZnO thin	PET	RF	1000	250	99.5	1		[195]
ZnO NRs	PI/PET	Hydrothermal	1000	100	69.8	5	76	[196]
ZnO NRs	Kapton	M-CBD	2000	150	140	339	63	[59]
ZnO NRs	PI	CBD	1000	RT	91	18.8	=	[103]
ZnO thin	Metallic Zn film	Thermal oxidation	1200	400	23	110		[197]
ZnO NRs	Glass	Hydrothermal	3000	300	99.2	74	40	[198]
ZnO NRs	Silicon	Hydrothermal	10000	100	58	5	-	[199]
ZnO NRs	Nylon	Hydrothermal	500	180	264	127	103	This work
			2000	75	578	156	117	

5.6 Characterization of the Grown ZnO NRs

Figure 5.6 shows ZnO NRs (high magnification and low magnification) grown at 90 °C for 3 h on ZnO seed/nylon substrate after heat treatment in air at 180 °C for 3 h. The obtained ZnO NRs were inclined at different angles (from 45° to 90°) with respect to normal nylon substrate, so one can notice from the top-view of field emission scanning electron microscopy images that the top end of the rods appeared slightly slanted. Although the tops of NRs were not very close to each other, most of the nanorods were in contact and soldered together at many of the points during the growth of ZnO NRs. Notably, a positive side for these contact points was found between rods.

As shown in Figure 5.6 (inside the small yellow circles), some of these contact points between rods formed at the top of rods, at the middle of rods (approximately 500 nm from the top), and between the top and middle of rods. In other words, the greatest rate of these contact points was located between the middle and top of rods, and the ZnO NRs were already connected to each other at their base through the ZnO seed layer.

The huge number of contact points formed a net for electrical contacts between ZnO NRs, and this configuration was expected to increase because of the paths of the electric carriers. Consequently, the passage of electric current through the nanorods was improved. In this context, the thickness of the metal electrode on the ZnO NRs for the Pt/ZnO NRs/Pt device was 100 nm and the complex configuration from electrical contacts was at the upper layer of ZnO NRs [143]. Meanwhile, the seed layer of ZnO also played an important role for these movements of charges because it was already in contact with all the ZnO NRs. Therefore, one

can suppose, there are also many numbers of travel paths of the electric carriers from the seed layer to reach the Pt electrodes.

The electrons may encounter many hurdles before reaching to the Pt electrodes. The paths of electrons in the upper layer of nanorods and near the metal contacts contributed to the electric current between metal contacts when a bias voltage was applied to an MSM device and under hydrogen gas exposure (or light exposure in the case of a photodetector device). So, it is believed that the movement of electrons between negative and positive electrodes occurred through the top, mid and bottom (seed) layers of ZnO NRs.

Figure 5.7 shows the three presumed paths of electrons through ZnO NRs and between two Pt electrodes. Due to increasing in a number of interactions between the hydrogen atoms with the adsorbed oxygen ions on the surface of ZnO NRs when the device was exposed to a certain gas, therefore, the intensity of electrons increased with increasing hydrogen concentration. Due to this large number of electrons between two electrodes, may be and as theoretically expected, the number of electrons paths increases relatively. The obtained ZnO NRs showed surfaces clean from defects and impurities.

Moreover, the nanorods exhibited high intensity, with a hexagonal structure and diameters ranging from 40 nm to 100 nm. These features were advantageous for raising the percentage of the penetration of gas atoms into the material. Additionally, the inset of Figure 5.6 shows the energy-dispersive X-ray spectrum of the asdeposited ZnO NRs, which revealed the existence of only Zn and O elements, thereby confirming its high purity, which was consistent with the XRD results.

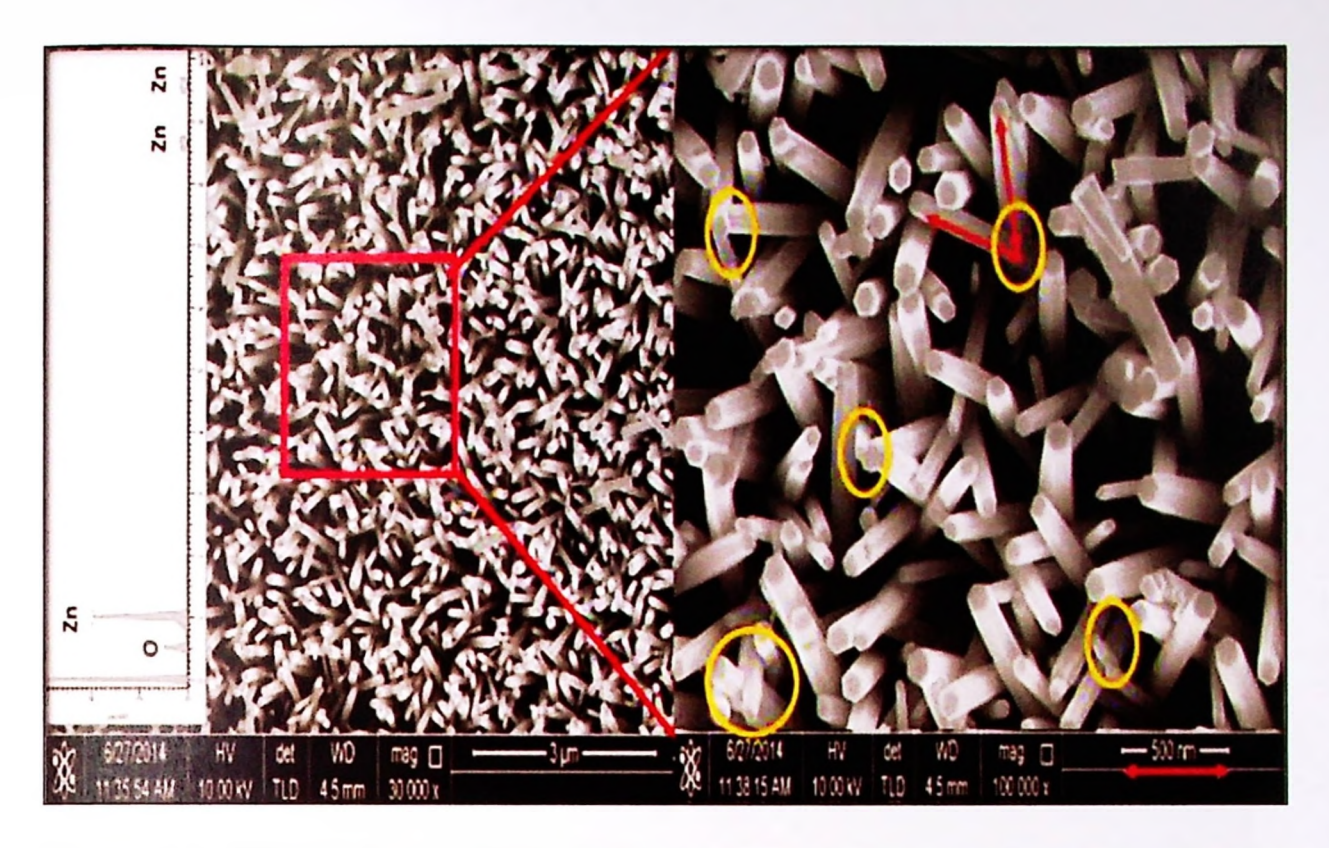


Figure 5.6: FESEM images of ZnO NRs grown on ZnO seeds/nylon substrate at 90 °C for 3 h (high magnification and low magnification). The inset is the EDX spectrum.

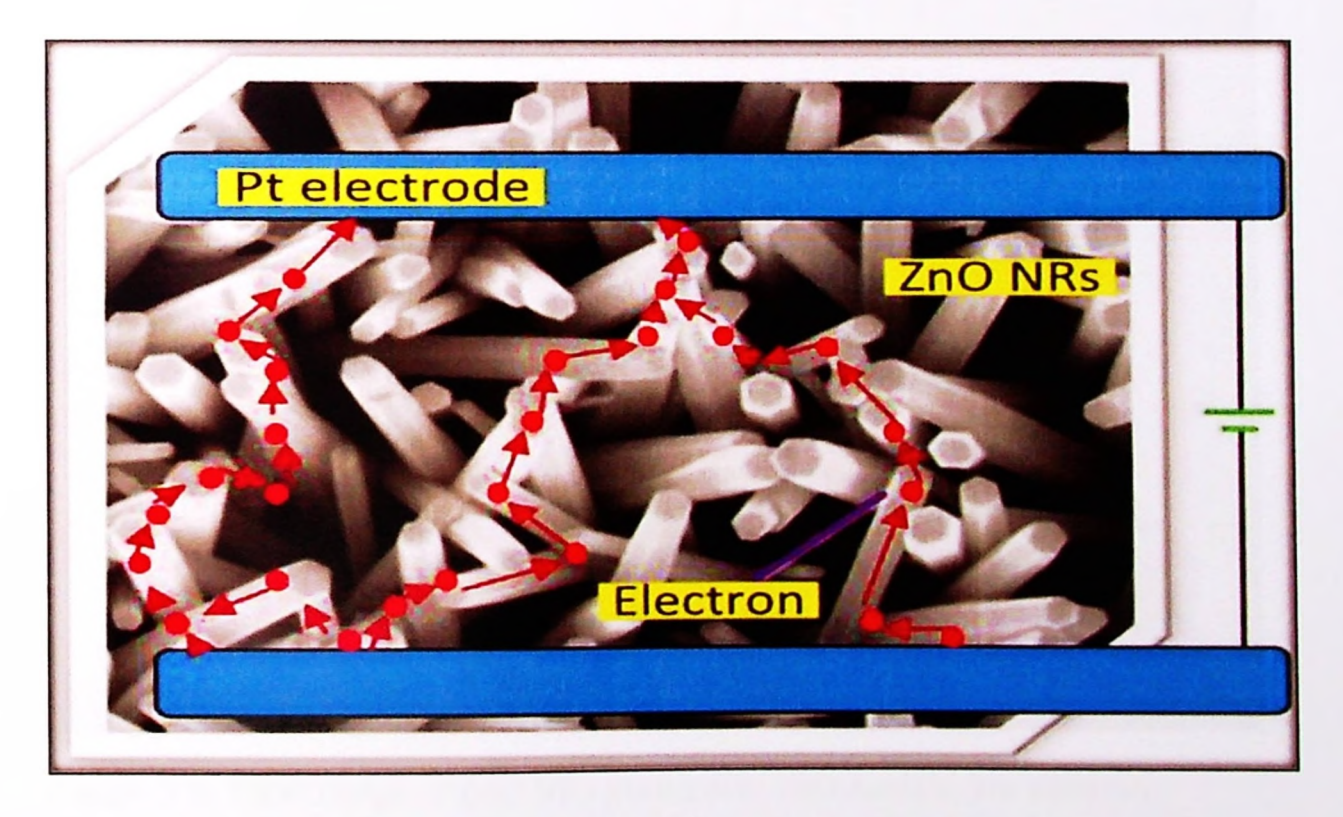


Figure 5.7: Illustration of presumed paths for electrons through ZnO NRs and between two Pt electrodes.

Figure 5.8 illustrates the transmission electron microscopy (TEM) image for one rod among millions of rods for ZnO grown onto ZnO seed/nylon substrate. A small part from the rod had broken and was lost from its length during sample preparation for TEM analysis. The length and diameter of the rod were approximately 950 and 90 nm, respectively. The ZnO NRs possessed a smooth surface and a regular diameter along its entire length. The aspect ratio refers to a proportion of the surface area of a material grown on a substrate.

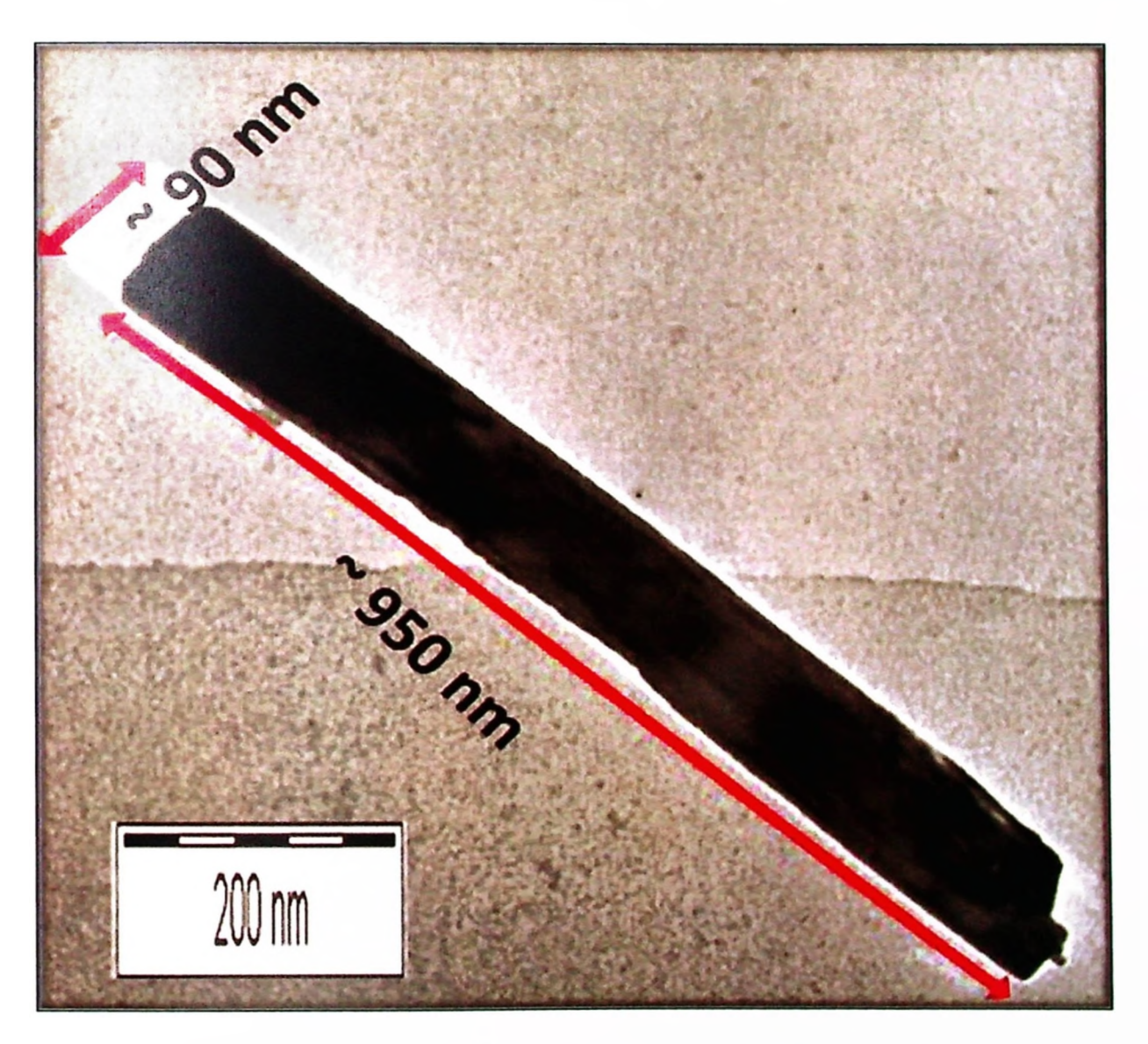


Figure 5.8: TEM image of ZnO NRs grown onto ZnO seeds/nylon substrate.

Therefore, researchers regard aspect ratio as an important factor for detector devices, and its value must be measured to determine and evaluate how well these

devices work. The average aspect ratio is defined average length/average diameter. The length of the rod from TEM is 950 nm and the average diameter from FESEM is 70 nm, as the result, the average aspect ratio is around 13.6.

This high aspect ratio and the high intensity of ZnO NRs provide a high surface-to volume ratio. According to several previous studies, the high surface area [74, 200], and high crystalline quality [201, 202], of ZnO NRs play an important role to enhance the gas detection mechanism. Although the large surface-to-volume of ZnO NRs provides gas sensors with several positive advantages, reaching a saturation point or steady state is difficult for the ZnO nanorod sensor upon exposure to H₂ during a short time period [203, 204].

This phenomenon is clear from the shape of the plot of sensitivity with time (see Figures 5.4 and 5.5), as for 4 or 5 min of exposure time to H₂, it can be observed from both figures that the sensitivity profile seems to level-off when nearing 4 min or 5 min. In this context, even selecting the longer exposure time (35 min) to the test H₂ gas (see Figure 5.9) the plot of sensitivity was not significant or significantly changing. The sensitivity was insufficient for the ZnO nanorod sensor to reach saturation because the molecules of H₂ gas needed a longer time to be distributed on ZnO NRs. Thus, the processes of adsorption-desorption became slow.

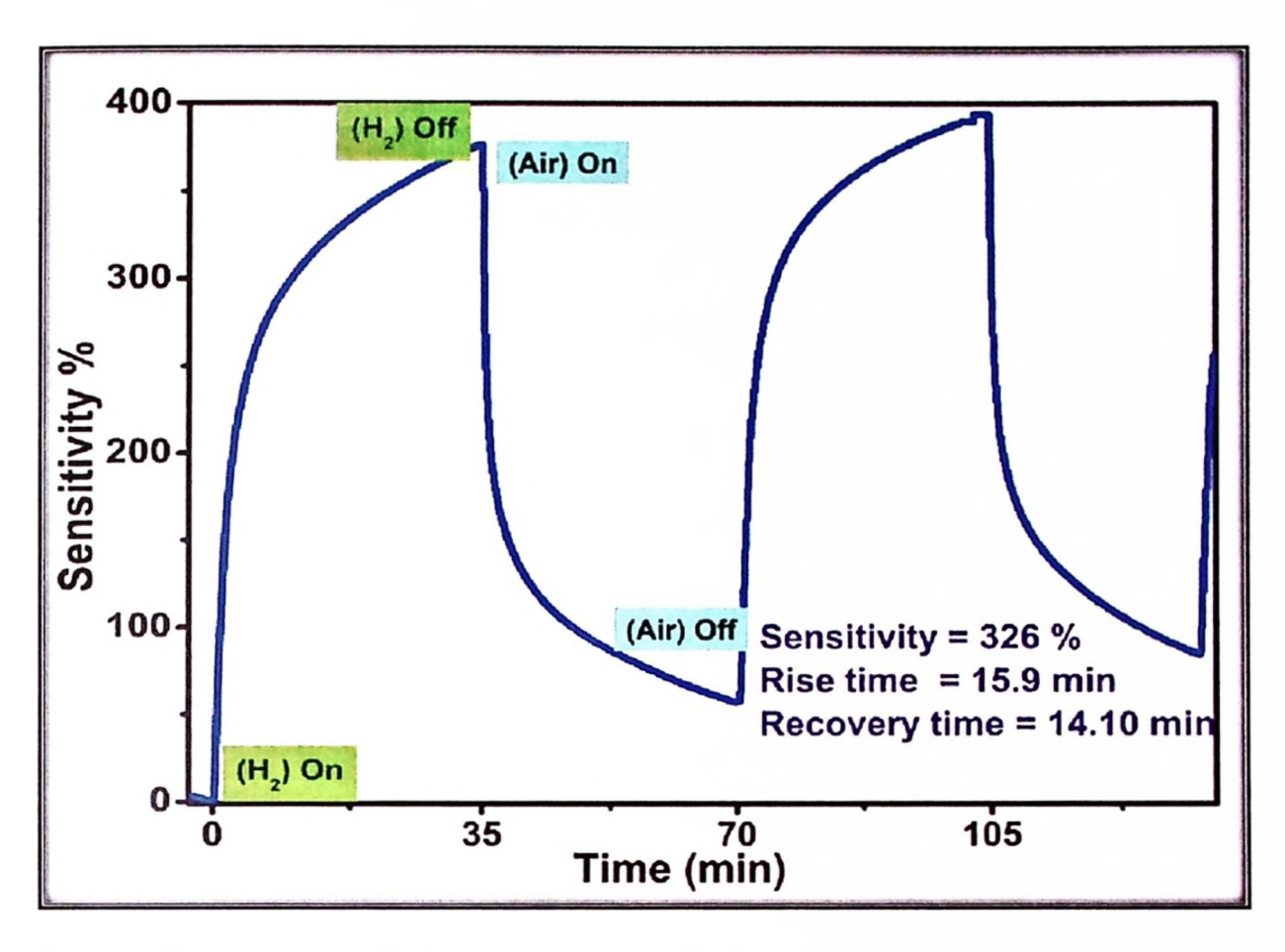


Figure 5.9: The sensitivity versus time of the prepared device at an operating temperature of 100 °C, and under exposure to 500 ppm of H₂ for 45 min.

5.7 Summary

Well-aligned and hexagonal-shaped ZnO NRs were successfully synthesized under hydrothermal conditions onto the ZnO seed layer/ cheap, thin, and highly flexible substrate at a low temperature, highly flexible low-cost H₂ gas sensor device has been fabricated. The sensitivity and response time behaviors of the ZnO-based gas sensor to hydrogen gas were investigated. The effects at different operation temperatures (RT-180 °C) and in various hydrogen concentrations (500–2000 ppm) at a fixed temperature of 75 °C on MSM gas sensing behavior were examined. The sensitivity of the fabricated device increased sharply with temperature and the concentration of hydrogen gas under enhanced response and recovery time. The sensing mechanism for gas at low and high operation temperatures was explained.

CHAPTER 6: RESULTS AND DISCUSSION: DHS-MCBD SYSTEM FOR THE GROWTH OF ULTRALONG ZnO NRs ON SEEDED SILICON AND SEEDLEES p-Gan SUBSTRATES AND FABRICATION OF A LED

6.1 Introduction

In this chapter, direct heat substrate-modified chemical bath deposition (DHS-MCBD) system is used as a novel technique for the growth of ultralong ZnO NRs on seeded Silicon and seedlees p-GaN substrates. The morphology, structural, optical, and electrical properties of ultralong ZnO NRs are investigated by FESEM, EDX, XRD, Raman, PL. In addition, current-voltage (I-V) and the electroluminescence (EL) of the applications of the nano-size junction n-ZnO NRs/p-GaN LED device, which was fabricated by the DHS-MCBD technique, were also studded. Finally, the conclusions obtained from these investigations are summarized at the end of this chapter.

6.2 DHS-MCBD System for The Growth of Ultralong ZnO NRs on Seeded Silicon

This section focuses on the structural and optical properties of the fabricated ultralong ZnO NRs on seeded Silicon substrate using DHS-MCBD system. The experimental features of this method have been explained in Section 3.7.1. The morphology, structural, and optical properties of ultralong ZnO NRs are investigated by using FESEM, EDX, XRD, Raman, and PL.

6.2.1 Characterization of the Ultralong ZnO NRs

Figure 6.1 presents pictures showing FESEM cross section images (different magnification) with 30° tilted views of ZnO NRs grown on ZnO seeds/silicon-substrate. It can be observed that the obtained ZnO NRs for the samples was

crystallized with a vertical orientation with respect to the silicon-substrate direction. Moreover, all rods were found to have perfect regular hexagonal—like shape without any semi-hexagonal shape, because the maximum precursor concentration used in this study was less than 0.1M, whereas the hexagonal structure becomes irregular when the precursor concentration is higher than 0.1 M [166-168]. In addition, it can be observed from Figure 6.1 that the sample has high-growth distribution density of ZnO NRs formed onto ZnO seeds/silicon. This may be due to the fact that the direct heating with high temperature for back side of substrate stimulates more number of ZnO grains of the seed layer to be the source for the growth of the rods within the same area of the substrate. It is known that each grain of ZnO seeds represents the base or origin for one grown nanorod. Generally, the rods have ultra-length, wherein the average lengths and diameter of ZnO NRs are around 17 µm and 100-200 nm, respectively. As the result, the average aspect ratio is around 127.5.

It is important to mention that the process of activating for the solution take place in this technique and thus caused the growth of high distribution density and well-aligned with ultra-length of ZnO NRs. Subjecting the substrate to the direct heating at high temperature (approximately 150°C) and without the subjecting the solution to any heat caused only the small amount of solution, in front of the substrate, to be active (both Zn and O ions were combined to create the ZnO NRs), where the temperature of the solution to be approximately 60 °C. Meanwhile, the rest of the solution remained fresh (the solution remains constant in the ions content) and the temperature of the solution was equal to approximately 37 °C. With a slowly closed cycle, the fresh solution turns to be active and so on. In other words, since the solution which is close to the front of the substrate has high temperature, this means

high energy, thus the ions have large enough mobility and diffusion length to reach the sites of the grown nanorods [47].

It is believed that this method presents a new development on growth of nanostructured material by direct heat to a substrate and to maintain the solution in order for it remain fresh as long as possible. Generally, for the DHS-MCBD system of the present work, the heat is transferred from the heater to the substrate to the deposition solution to the cooling liquid during the process. The thermal equilibrium among the substrate, deposition solution and cooling liquid is controlled depending upon the size of the substrate, the volume of the deposition solution and cooling liquid.

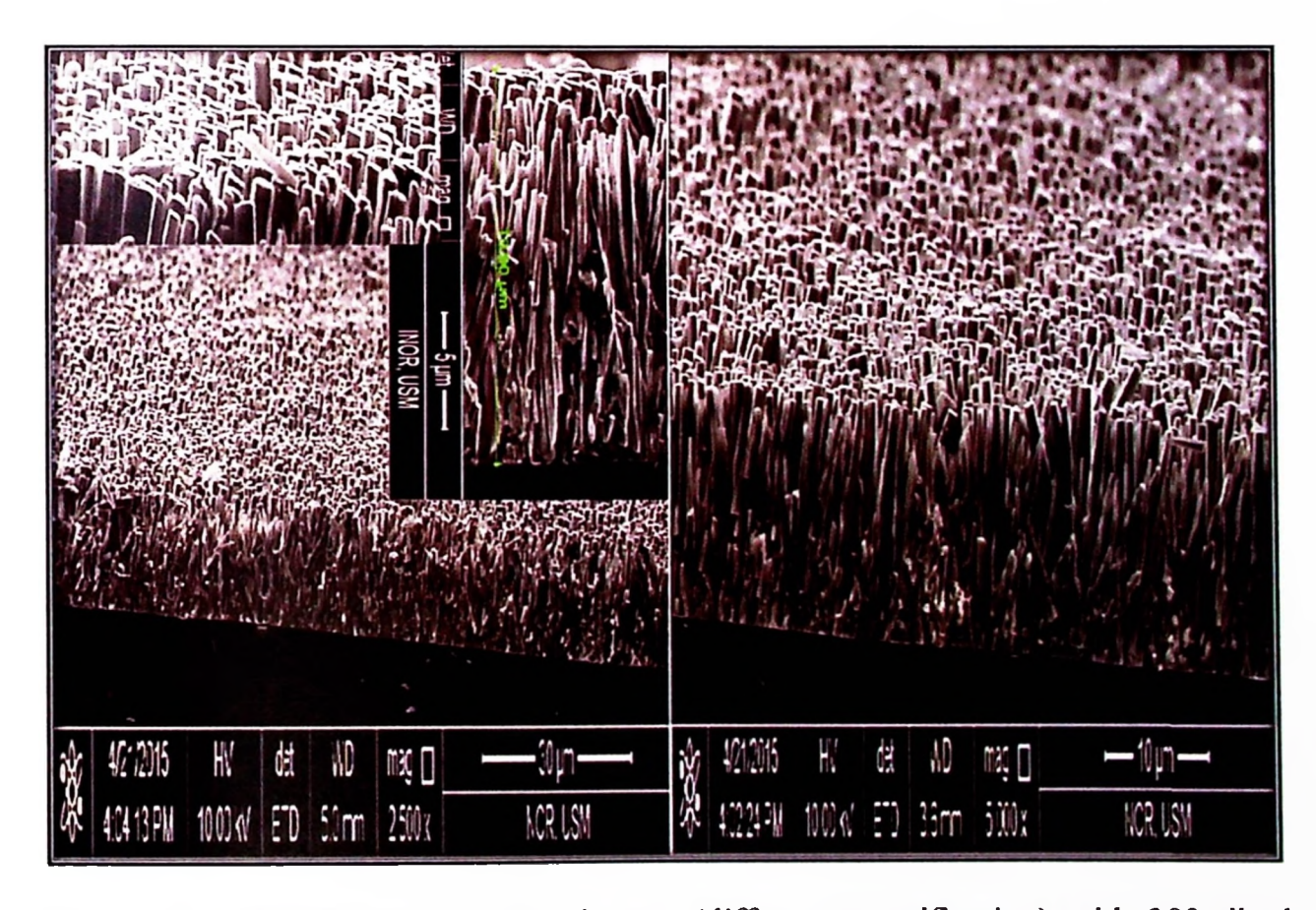


Figure 6.1: FESEM cross section images (different magnification) with 30° tilted views of ultralong ZnO NRs grown onto ZnO seeds/silicon-substrate.

6.2.2 Energy-Dispersive X-ray Spectroscopy

Figure 6.2 presents graphs illustrating energy-dispersive X-ray spectroscopy spectrum of the as-deposited ultralong ZnO NRs formed on ZnO seeds/silicon substrate for the sample, which revealed the existence of only Zn, O elements, which corresponds to the characteristic composition of ZnO, without any other impurity contamination or substrate signal. This result confirms the high purity of ZnO NRs. In addition, the values in the table for the sample (inset Figure 6.2) indicate that the atomic percentage of two elements for the sample is almost similar. It is worth mentioning that no Si signals were detected in x-ray spectra, this confirmed the high length of the ZnO NRs growth onto silicon where it was seen in images of FESEM.

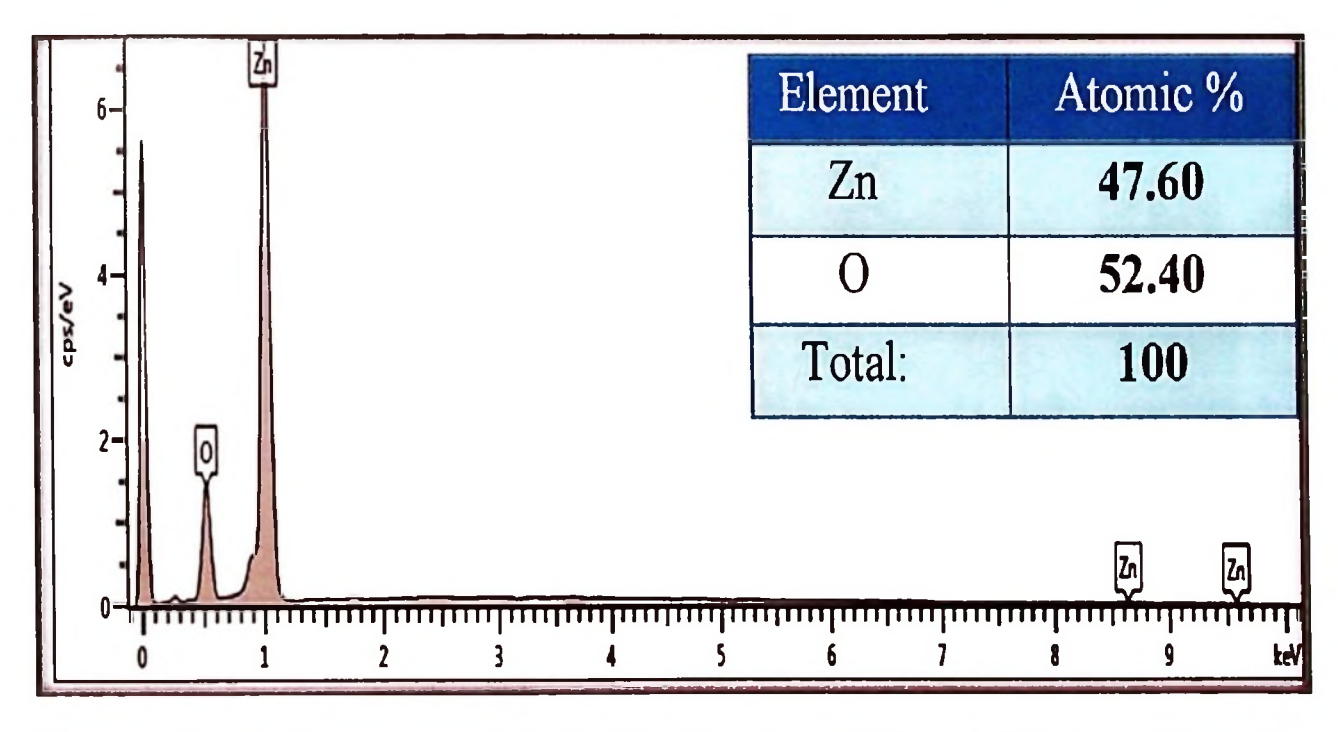


Figure 6.2: EDX spectrum of ZnO NRs formed on ZnO seeds/silicon-substrate for the sample.

6.2.3 Structural Characterization by X-ray Diffraction

Figure 6.3 presents graph illustrating the crystal structure and the orientation of ZnO NRs film for the sample by X-ray diffraction. The XRD pattern exhibits typical diffraction peaks at $2\theta = 31.70^{\circ}$, 34.40° , 36.20° , and 72.20° , and these

diffraction peaks correspond to the reflection of the (100), (002), (101), and (004) planes, respectively. These observed diffraction peaks match well with the wurtzite hexagonal phase of ZnO (ICSD Card No. 01-080-0074). It can be noticed that (002) reflection for the sample has a very high intensity, while other peaks are very weak. Meanwhile, the measurement value of the full width at half maximum (FWHM) of (002) peak for the sample is 0.137°.

The strong intensity and the low value of the full width at half maximum (FWHM) indicates that ZnO NRs grow onto the substrate preferentially along c-axis (perpendicular to the substrate) and have good crystalline quality. In addition, two other peaks were also observed for the sample, namely, (111) and (222); these peaks were indexed within the wurtzite cubic phase of silicon (ICSD Card No. 01-077-2111).

The lattice constant c_o and the strain (ε_{zz}) along the c-axis of the würtzite structure of ZnO NRs were calculated by using the XRD data according to Eqs. 3.2 and 3.3, respectively (in the section 3.8.1). The calculated lattice constant and microstrain were 0.52058 nm and - 0.177 %, respectively. The obtained value lattice constant was close to the values reported in the literature (standard value), thus the value of the strain became low, which mean that the ultralong ZnO NRs have high quality crystal structure. Moreover, the as-grown ZnO NRs has a compressive strain due to the calculated strain value, which was negative.

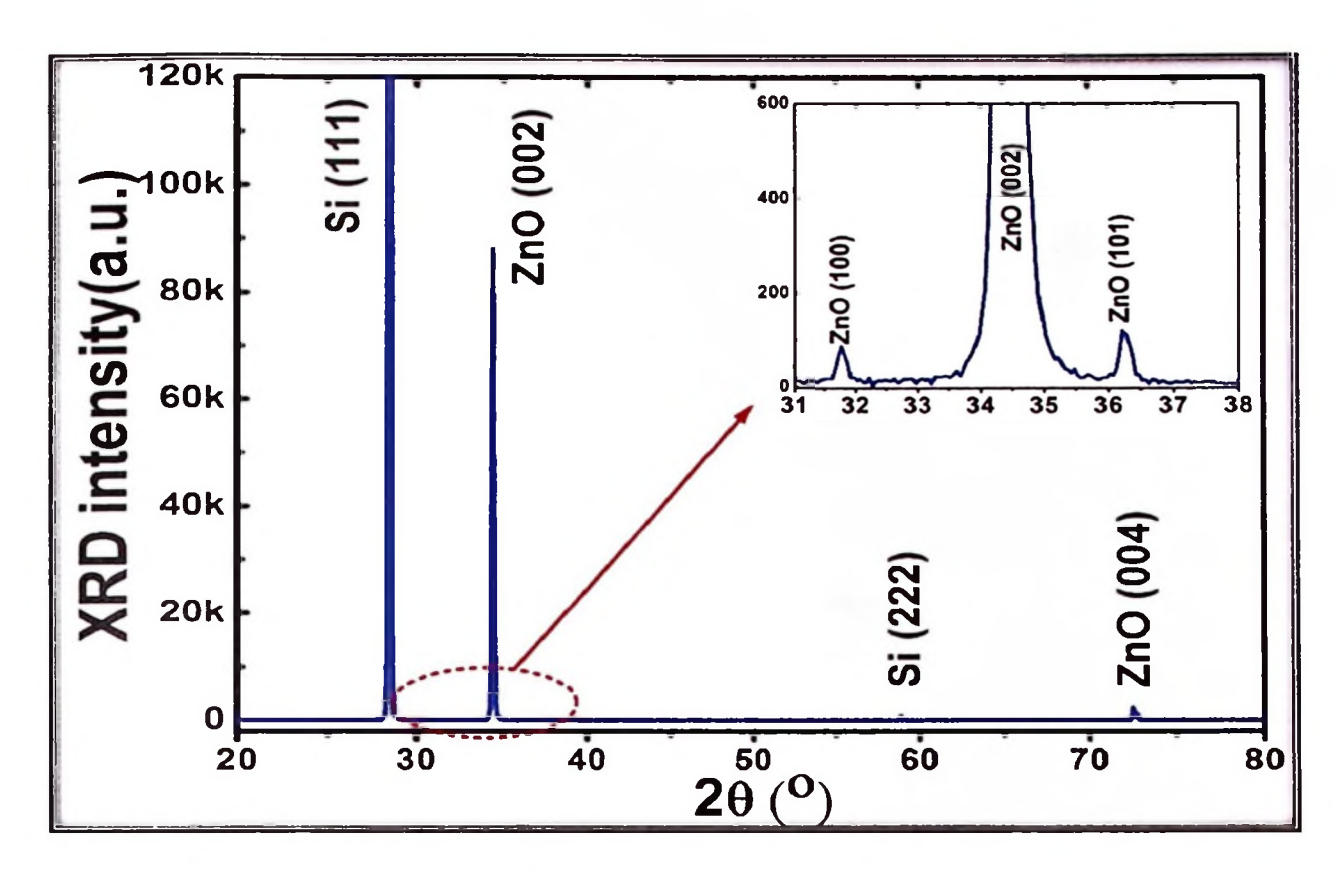


Figure 6.3: High-resolution X-ray diffraction pattern of ZnO NRs formed on ZnO seeds/silicon substrate. The inset shows the zoom in on the XRD pattern in the range of $2\theta = 31$ to 38 degree.

6.2.4 Raman Spectroscopy

Figure 6.4 presents graph showing a typical Raman spectrum of ZnO NRs formed on ZnO seeds/silicon substrate, and recorded in the range of 50–800 cm⁻¹. Micro-Raman spectroscopy was used to further analyze the quality of the ZnO NRs. Wurtzite form of ZnO belongs to the space group $C_{6\nu}^4$ [205], which predicts the following optical modes at the Γ point of the Brillouin zone: $\Gamma = 1A_1 + 2B_1 + 1E_1 + 2E_2$. Among these modes, A_1 , E_1 , and $2E_2$ modes are Raman active, $2B_1$ modes are silent, and A_1 and E_1 modes are infrared active. Both A_1 and E_1 modes usually split into transverse optical (TO) and longitudinal optical (LO) phonons [206].

The sample exhibits the two strong and dominant peaks at 100 cm^{-1} and 438 cm^{-1} which are the Raman active optical-phonon E_2 mode of ZnO crystal. They

represented the low-E₂ and high-E₂ modes of non-polar optical phonons respectively [207, 208]. Sharp and dominated E₂ mode indicates that the as-grown ZnO NRs, have good crystalline quality with less structural defects and impurities. Additionally, the small peak at 334 cm⁻¹ was also observed for the sample; this peak is assigned to the second-order Raman spectrum arising from zone-boundary phonons of hexagonal ZnO [209].

In addition, the two peaks located at 302 cm⁻¹ and 521 cm⁻¹ for ZnO NRs /silicon are for silicon substrate [210]. Finally, it is obvious from Figure 6.4, that the blue shift of the value of $E_{2(high)}$ (438 cm⁻¹) with respect to the bulk value (437 cm⁻¹) for the sample can be associated with the presence of compressive strain [211], therefore, the Raman scattering results for the sample are very consistent with the XRD results in this study.

6.2.5 Photoluminescence (PL) Measurement

Figure 6.5 presents graph showing room-temperature PL spectrum emission spectra of ZnO NRs formed on ZnO seeds/silicon-substrate. The high ultraviolet (UV) emission peak for the sample, which is located at approximately 377 nm (3.29 eV), with a narrow FWHM equal to 15 nm. was attributed to the near-band-edge emissions (NBE) of the wide ZnO band gap, which resulted from the recombinations of the free-exciton process.

Morever, it can be seen from Figure 6.5, the broad visible peaks were observed in the wavelength range approximately between 450 nm to 720 nm for the sample. This broad visible peak is related to the deep energy levels' emission (DLE) of ZnO, which is due to the intrinsic defects in ZnO NRs, such as oxygen vacancies, zinc interstitials, zinc vacancies, and oxygen interstitials. The origin of these emissions

was already mentioned before in the section 5.3. However, it is reasonable to expect the presence of these defects and vacancies in the synthesized ultralong ZnO NRs by DHS-MCBD technique because of this technique can be considered as modified technique for CBD method [184].

In addition, the intensity of the UV intensity peak is much higher than that of the broad peak in the sample. This high difference (I_{UV}/I _{DLE}) in intensity suggests that the grown ZnO nanorod arrays have high quality with small number of defects, and a good hexagonal structure.

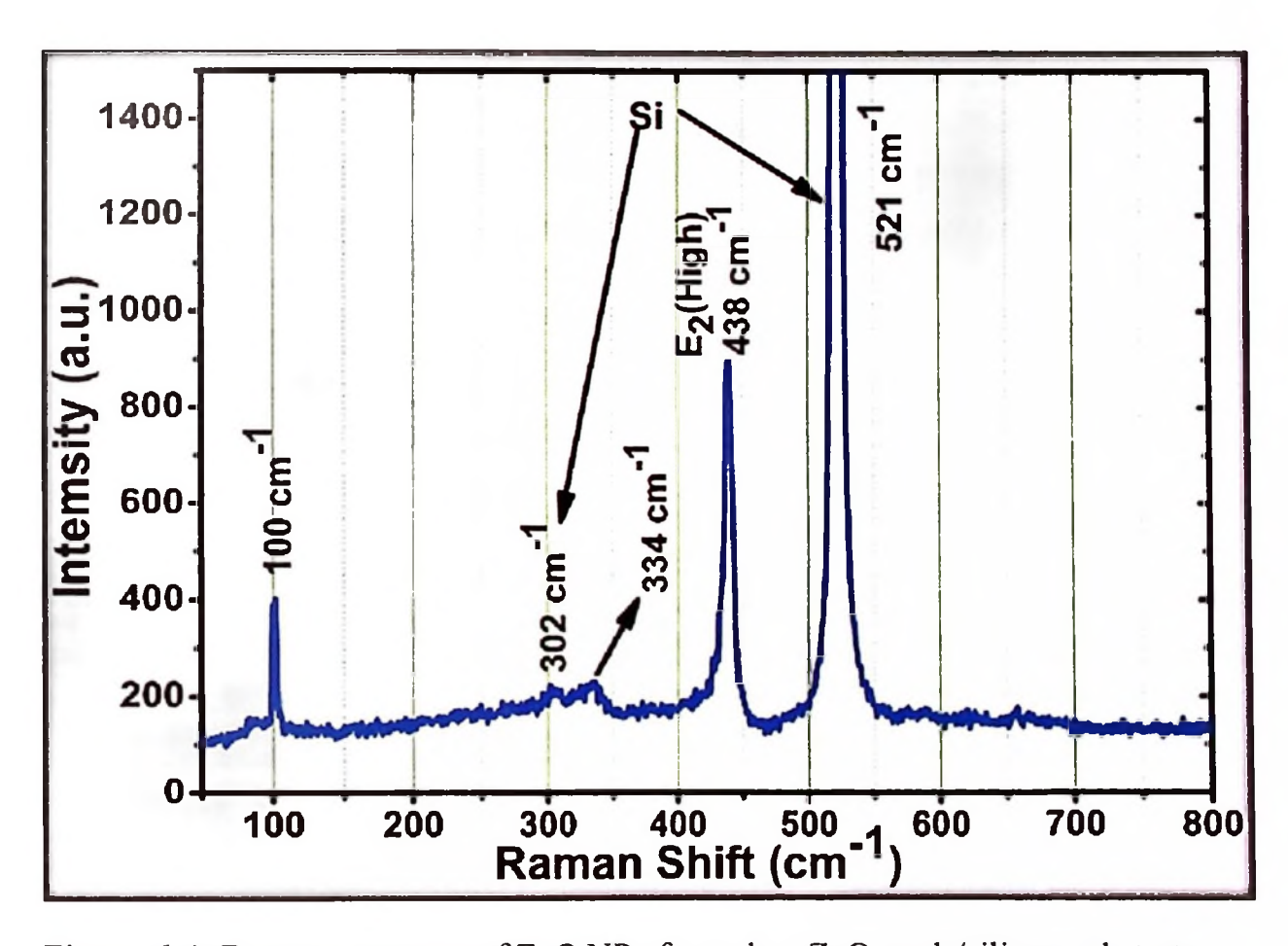


Figure 6.4: Raman spectrum of ZnO NRs formed on ZnO seeds/silicon substrate.

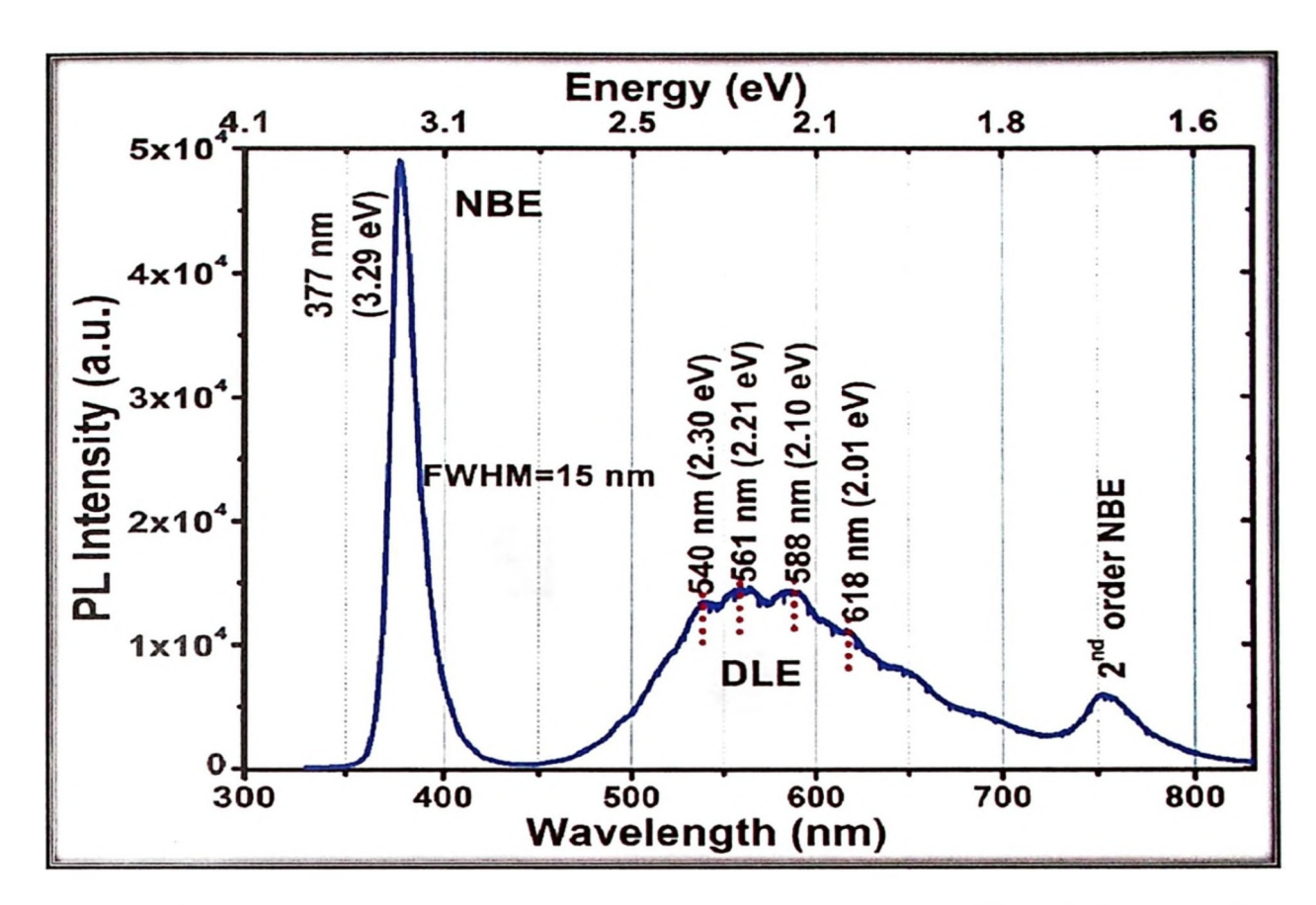


Figure 6.5: Room-temperature photoluminescence spectrum of ZnO NRs formed on ZnO seeds/silicon substrate.

6.3 DHS-MCBD System for the Growth of Ultralong ZnO NRs on Seedless P-GaN and Fabrication of a Nano-Size Junction LED

This section focuses on the structural and optical properties of the fabricated ultralong ZnO NRs on seedlees p-GaN substrate. The experimental features of this method have been explained in sections 3.7.2, and 3.7.3. The morphology, structural, optical, and electrical properties of ultralong ZnO NRs are investigated by FESEM, EDX, XRD, Raman, PL, as well as current-voltage (I-V) and electroluminescence (EL) properties of ultralong n-ZnO NRs/p-GaN LED device are studied. Finally, the mechanism of charge carriers transportation and recombination of EL for the n-ZnO/p-GaN heterojunction LED under the reverse breakdown bias were clarified

6.3.1 Characterization of the Ultralong ZnO NRs

Figure 6.6 presents images showing FESEM top-view and cross-sectional images (different magnification) with 30° tilted views of ultralong ZnO NRs grown on p-GaN/sapphire substrate. It can be observed, the obtained ZnO NRs are oriented perpendicularly to the p-GaN substrate by a simple DHS-MCBD technique. It can be seen ZnO NRs are well crystallized with a hexagonal-like shape with diameters ranging from 50 nm to 200 nm from the top-view image and length of 16000 nm from the cross-sectional FESEM image. Therefore, the corresponding average aspect ratio (length/diameter) of rods is around 128.

One can notice from the FESEM cross-sectional image (scale bar 1 µm, and the inset of Figure 6.6) how ZnO NRs were grown directly from GaN surface and there was no material layer (like ZnO seed layer) between the top of GaN layer and the bottom of rods. It is believed that this technique is a promising candidate to offer the easy way to form the nano-junctions between ZnO NRs and GaN film. In addition, the ZnO NRs have high-growth distribution density on GaN substrates.

The left inset of Figure 6.6 shows the energy-dispersive X-ray spectroscopy spectrum of the as-deposited ZnO NRs on p-GaN/sapphire-substrate, which revealed the existence of only Zn, O, Ga, N and Al elements. This result confirms the high purity of ZnO NRs, which is consistent with XRD results.

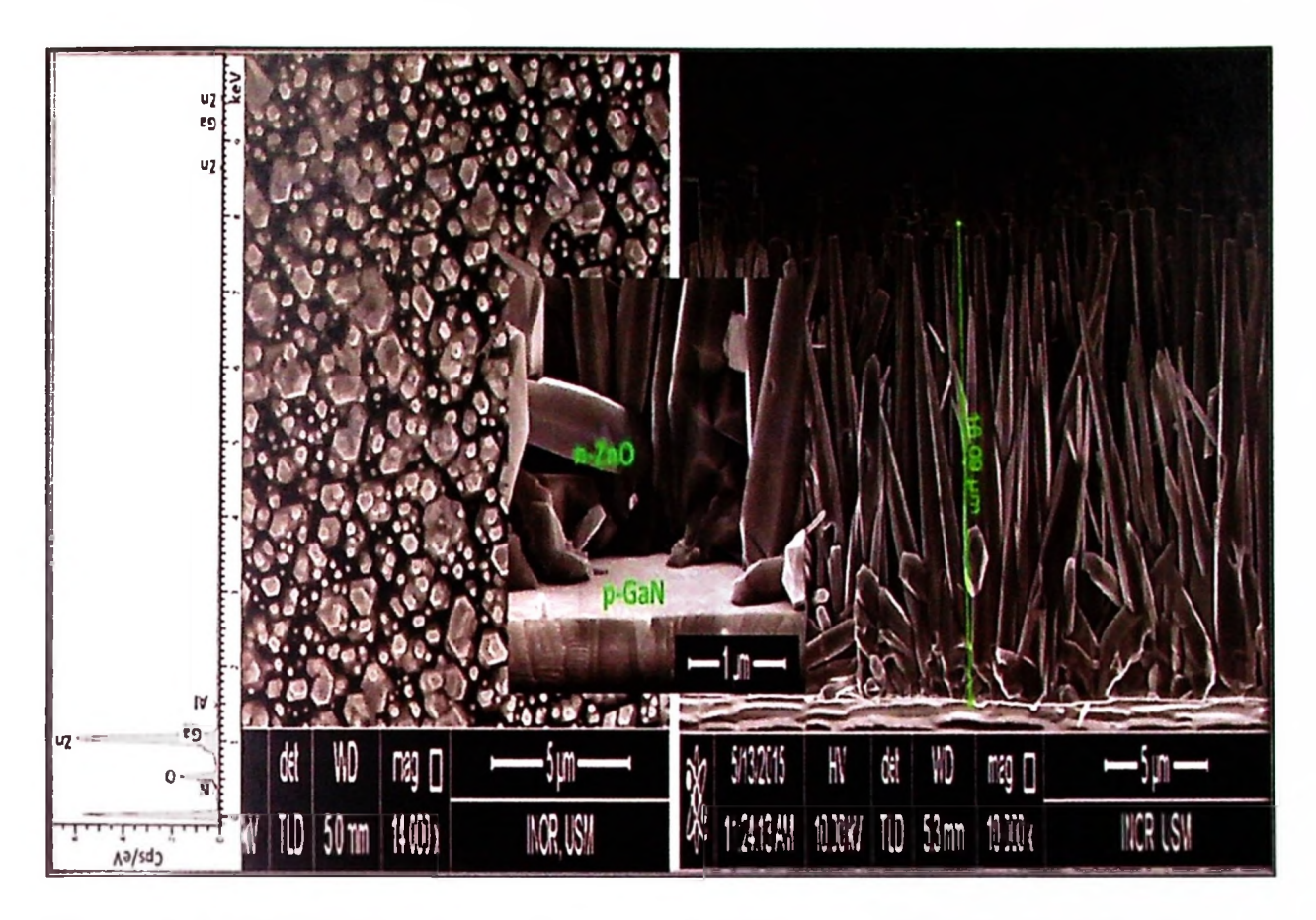


Figure 6.6: FESEM top-view and cross-sectional images (different magnification) with 30° tilted views of ZnO NRs grown on p-GaN/sapphire substrate, where the left inset shows EDX spectra of ZnO NRs grown on p-GaN/sapphire substrate.

6.3.2 Structural Characterization by X-ray Diffraction

The crystal structure and the orientation of the ultra-long ZnO NRs /GaN film on sapphire were investigated by X-ray diffraction (XRD) (see Figure 6.7). All observed diffraction peaks match well with the wurtzite hexagonal phase of ZnO and GaN (ICSD Card No. 01-075-1526 and No. 00-050-0792, respectively) except for the peak (006) which is located at 2θ =41.70°, which was assigned to the sapphire (Al₂O₃) substrate (ICSD Card No. 01-073-1512).

It is believed that the n-ZnO NRs and p-GaN have the same crystalline phase and a close lattice constant (small lattice mismatch), and having the same (002) orientation. Therefore, it is expected the growth of ZnO NRs will follow the orientation along the [002] direction of the GaN substrate, Hence, the

crystallographic orientation of the p-GaN layer could extend to the ZnO NRs [212-214]. However, the strongest (002) peak in Figure may be due to the high crystalline quality of GaN substrate which was purchased commercially and Meanwhile, the ZnO (002) peak was masked by GaN (002) peak. In other words, the (0002) X-ray diffraction does not allow clear separation of the ZnO and GaN related peaks, due to their close nearness [127].

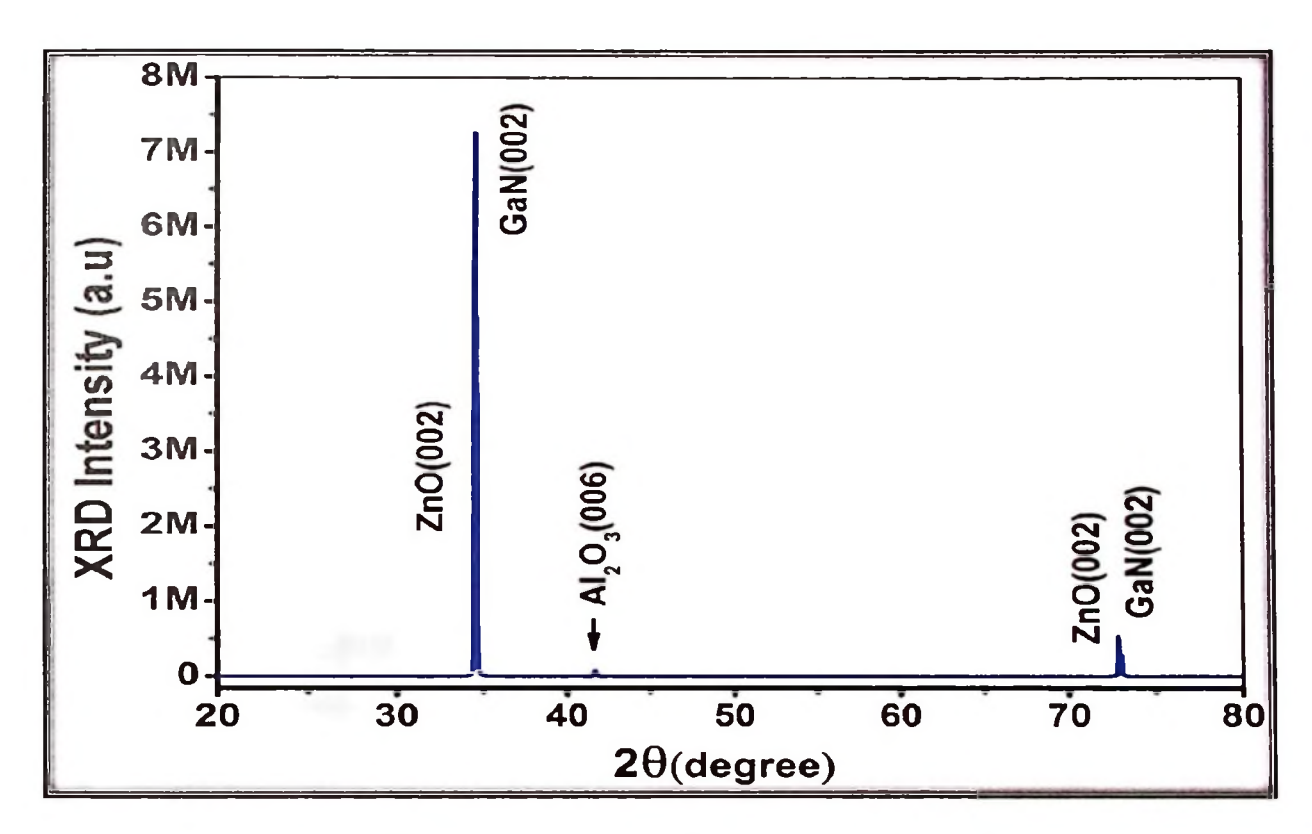


Figure 6.7: X-ray diffraction pattern of ZnO NRs formed on p-GaN/sapphire substrate.

6.3.3 Raman Spectroscopy

Figure 6.8 presents graphs illustrates room-temperature Raman spectra of p-GaN/sapphire substrate and n-ZnO NRs formed on p-GaN/sapphire substrate recorded in the range of 200–800 cm⁻¹. The curve of ZnO/ GaN/sapphire exhibits a sharp and dominant peak at 438 cm⁻¹ which is attributed to the Raman-active E_2 mode and characteristic of the hexagonal wurtzite phase of ZnO [215]. Additionally, two small peaks at 332 and 379 cm⁻¹ were also observed, which are assigned to

multiple-phonon processes and transverse optical components $A_1(TO)$, respectively [208, 215, 216]. The sharp and high intensity E_2 mode indicates that the as-grown ZnO NRs, have good crystalline quality with less structural defects and impurities. The Raman scattering results are very consistent with the XRD results.

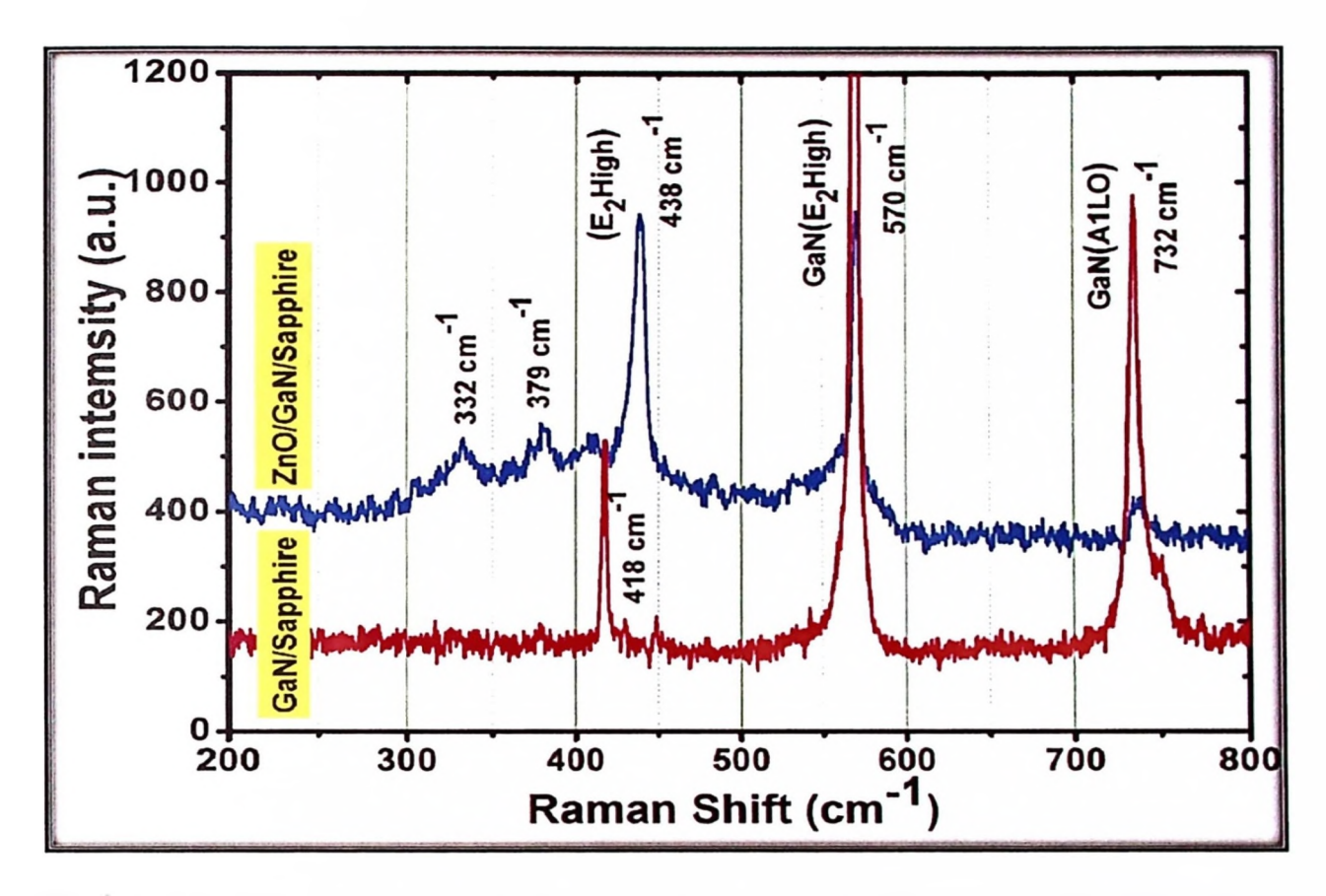


Figure 6.8: Room-temperature Raman spectra of p-GaN/sapphire substrate and n-ZnO NRs formed on p-GaN/sapphire substrate.

6.3.4 Photoluminescence (PL) Measurements

Figure 6.9 presents graphs showing PL spectra on p-GaN film and then on ZnO NRs grown at room-temperature was performed. The high ultraviolet (UV) emission located at approximately 382 nm (3.25 eV), were attributed to the near-band-edge emission (NBE) of the wide ZnO band gap, which resulted from the recombination of the free-exciton process. In addition, it can be seen from Figure 6.9 the broad visible peaks in the wavelength range of 480 nm to 826 nm and centered around 616 nm. These broad visible peaks are related to the deep energy level

emissions (DLE) of ZnO, which is due to the intrinsic defects in ZnO NRs. Due to the defect emission related to oxygen vacancies or zinc interstitials [184], the presence of these defects and vacancies have also been reported for ZnO NRs synthesized by hydrothermal method [184].

In addition, one can notice that the intensity of this UV peak is much higher than that of the broad peak. The ratio of the UV intensity peak to the visible intensity peak (I_{UV}:I_{Vis}) is approximately 8:1. This high ratio of the intensity suggests that the grown ZnO nanorod arrays have small number of defects and a good hexagonal structure [43, 44].

On the other hand, it can be seen from the PL spectrum for p-GaN layer, a dominant peak at 362 nm (3.43 eV) which corresponds to its NBE transition. In addition, a secondary blue band between 370 nm (3.35 eV) to 440 nm (2,82 eV) and centered around 379.5 nm (3.267 eV) were observed. This blue band can be ascribed to donor - acceptor pairs (DAP) recombination process involving the transitions from the conduction band or unidentified shallow donors to the Mg acceptor levels in GaN. It is worth mentioning that a number of researchers reported that Mg-doped GaN exhibits two main PL peaks: UV-PL peak, at 3.27 eV, and a blue PL peak near 2.8 eV [217-220]. Moreover, the two weak peaks appearing at 764 nm and 724 nm were related to the second order diffraction of the UV emission (NBE) for ZnO and GaN, respectively.

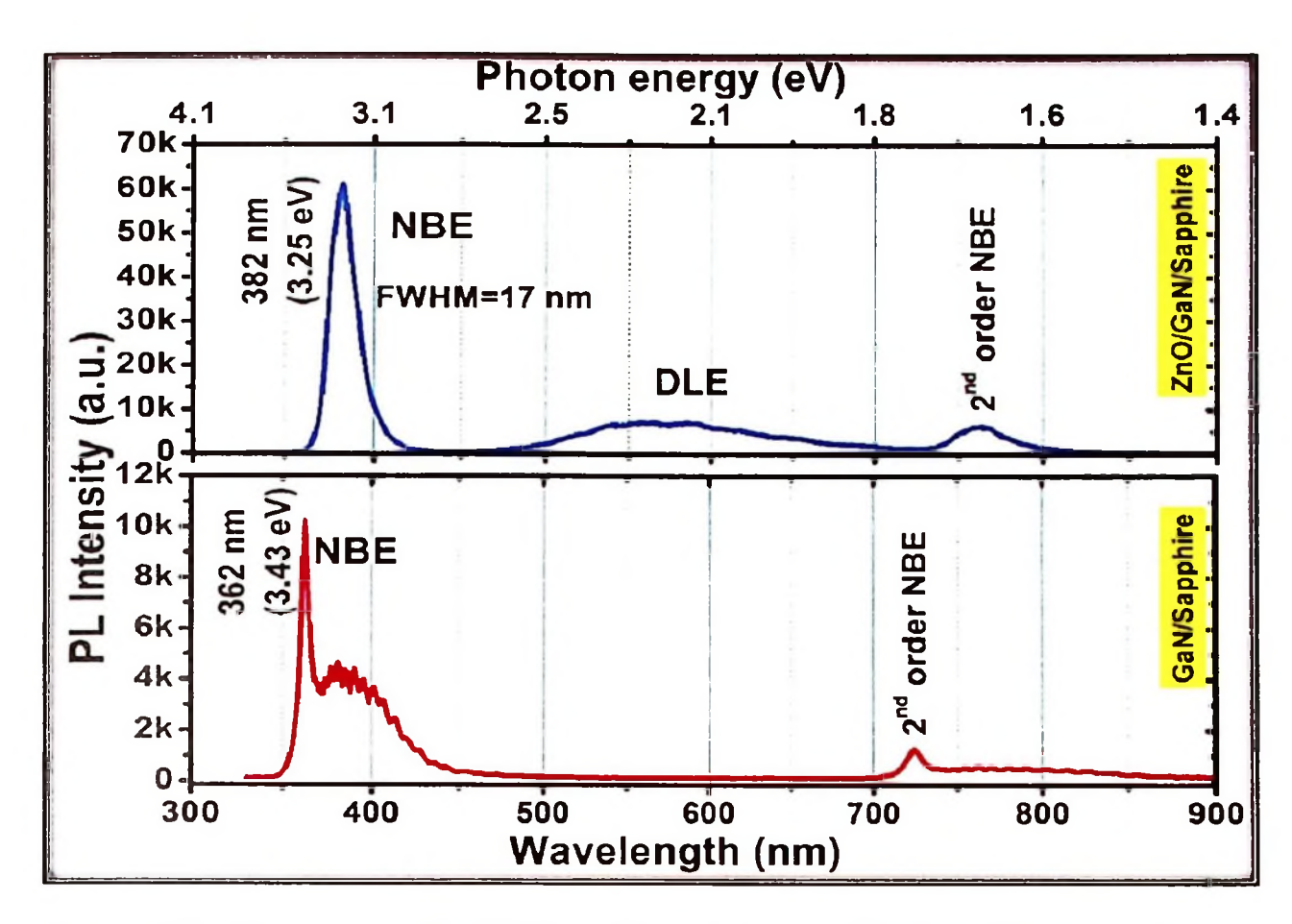


Figure 6.9: PL spectra of p-GaN/sapphire substrate and n-ZnO NRs formed on p-GaN/sapphire substrate.

6.3.5 Current-Voltage (I-V) Characteristics

The current–voltage (I-V) characteristics curve of n-ZnO NRs/p-GaN heterojunction LED measured at RT are illustrated in Figure 6.10. I-V relationship between the contact of the probe on top of the n-ZnO NRs and the contact on the GaN clearly shows a rectifying behavior for the ZnO NRs /p-GaN heterojunction. It was clearly observed that the reverse breakdown is at around -5.1 V, therefore the mechanism of breakdown for the device is caused by tunneling effect and not the avalanche multiplication process because the breakdown voltage is less than $4E_g/q$ ($E_g\sim3.4~eV$ is the band-gap energy of ZnO or GaN) [221]. It can be seen that the current rapidly increased with the reverse bias when the applied negative voltage was greater than the breakdown voltage.

The inset of Figure 7.5 shows the I-V characteristics of ohmic contacts to p-GaN ((Pd/ITO)-(Pd/ITO)) that reveal linearity indicative of good ohmic properties.

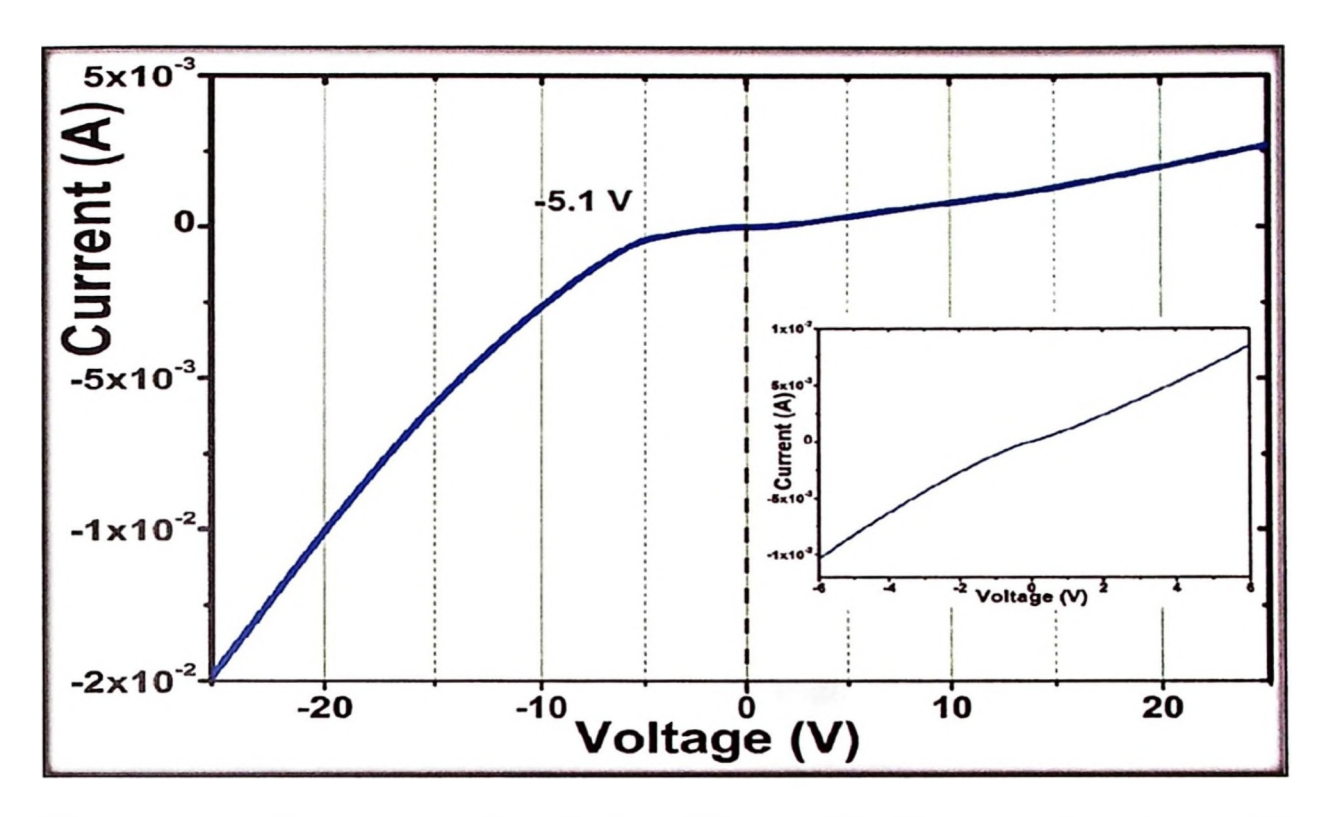


Figure 6.10: I-V characteristics of n-ZnO NRs /p-GaN LED, where the bottom right inset shows the ohmic characteristic of Pd/ITO contact on p-GaN layer.

6.3.6 Electroluminescence Characteristics

The EL intensities were measured from both sides of n-ZnO/p-GaN/sapphire substrate LED, the front side (top side through the ZnO layer) and the back side (through the transparent sapphire side). Because our device was operated at the reverse breakdown, no trusty light emission was observed under forward biases. In other words, the forward biased n-p junction acts as a resistor while the reverse biased n-p junction becomes the LED.

Figure 7.6 presents graphs showing room-temperature the EL spectra of the heterojunction LED under reverse bias (under various currents (voltages) ranging from 3 mA (-4.2 V) to 28 mA (-28.5 V)) that were measured from the back side of n-

ZnO/p-GaN /sapphire substrate LED. It is shown that the spectrum was composed of the ultraviolet emission centered at ~368 nm (3.37 eV), the near blue light at ~395 nm and a broad band around ~450 to ~550nm (see the images inset Figure 6.11).

It can be seen, as the injection current is increased from 3 mA to 28 mA (by increasing the applied reverse bias voltages), EL intensity is dramatically increased and a small red shift of the emission peak can be seen. This phenomena may be due to thermal effects [222]. Top right inset of Figure 6.11 shows the EL real optical photos of the LED in ambient lighting, which is emitting from the back side of LED at the current injection of 22 mA. Figure 6.12 presents graphs showing room-temperature EL spectra of the heterojunction LED under reverse bias (under various currents (voltages) ranging from 3 mA (-4.2 V) to 28 mA (-28.5 V)) that were measured from the front side of n-ZnO/p-GaN /sapphire substrate LED. It can be seen that the spectrum was composed of the near blue light emission at ~395 nm, and a broad band around ~450 to ~600 nm (see the inset image of Figure 6.12).

Comparing the EL with the PL spectra, It is believed that the ultra violet emission peaks which are located at 366 nm are attributed to the NBE radiative recombination in p-GaN while the emission peaks located at~395 nm are the sum of two results; the Mg acceptor levels in p-GaN [26], and the NBE radiative recombination n-ZnO. The emission peaks from front side are attributed to the NBE radiative recombination in n-ZnO. It is worth to mention that the green emission originates from the oxygen vacancies and is emitted from both sides which overlap with the violet light and the blue light.

It should be noted that the difference between the EL and PL is normal because both of them have different operating mechanisms. The recombination

occurs within the penetration depth from the top of the NRs in PL measurement, while the recombination of EL measurement is produced at the interface between the ZnO and p-GaN. Therefore, the interface between the ZnO and p-GaN is responsible for EL measurement [223]. Therefore, the EL depends on the interface between the ZnO and p-GaN intensively [110]. Top right inset of Figure 6.12 shows the EL real optical photos of the LED in ambient lighting, which is emitting from the front side of LED at the current injection of 22 mA.

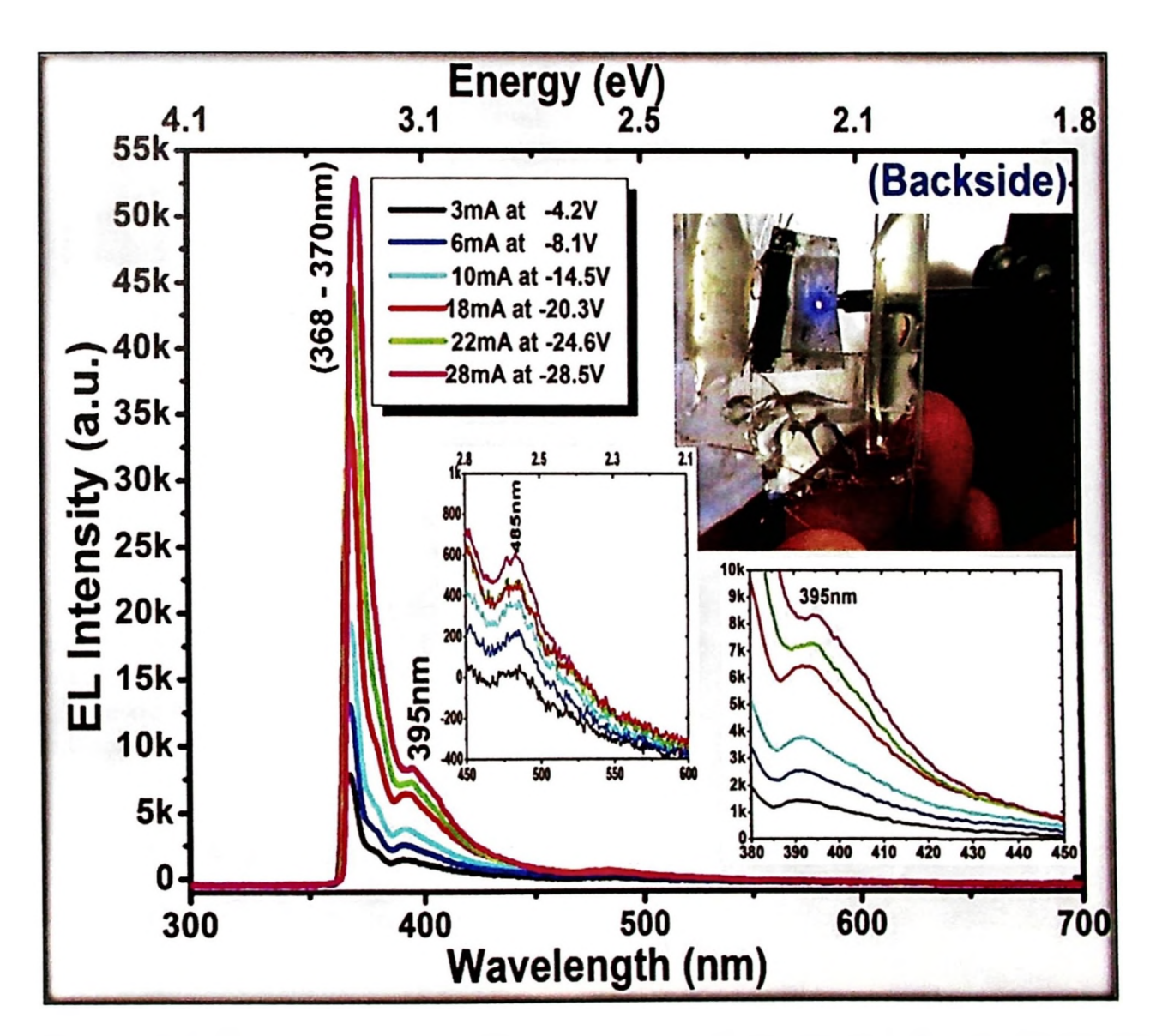


Figure 6.11: Room-temperature EL measurement spectra emission from back side of the n-ZnO NRs/p-GaN LED with different current injections at the reverse breakdown bias, where bottom right inset shows the zoom in on the EL spectra in the range of 450 to 550nm. Top right inset shows real optical photos of the LED in the ambient lighting at the current injection of 22 mA.

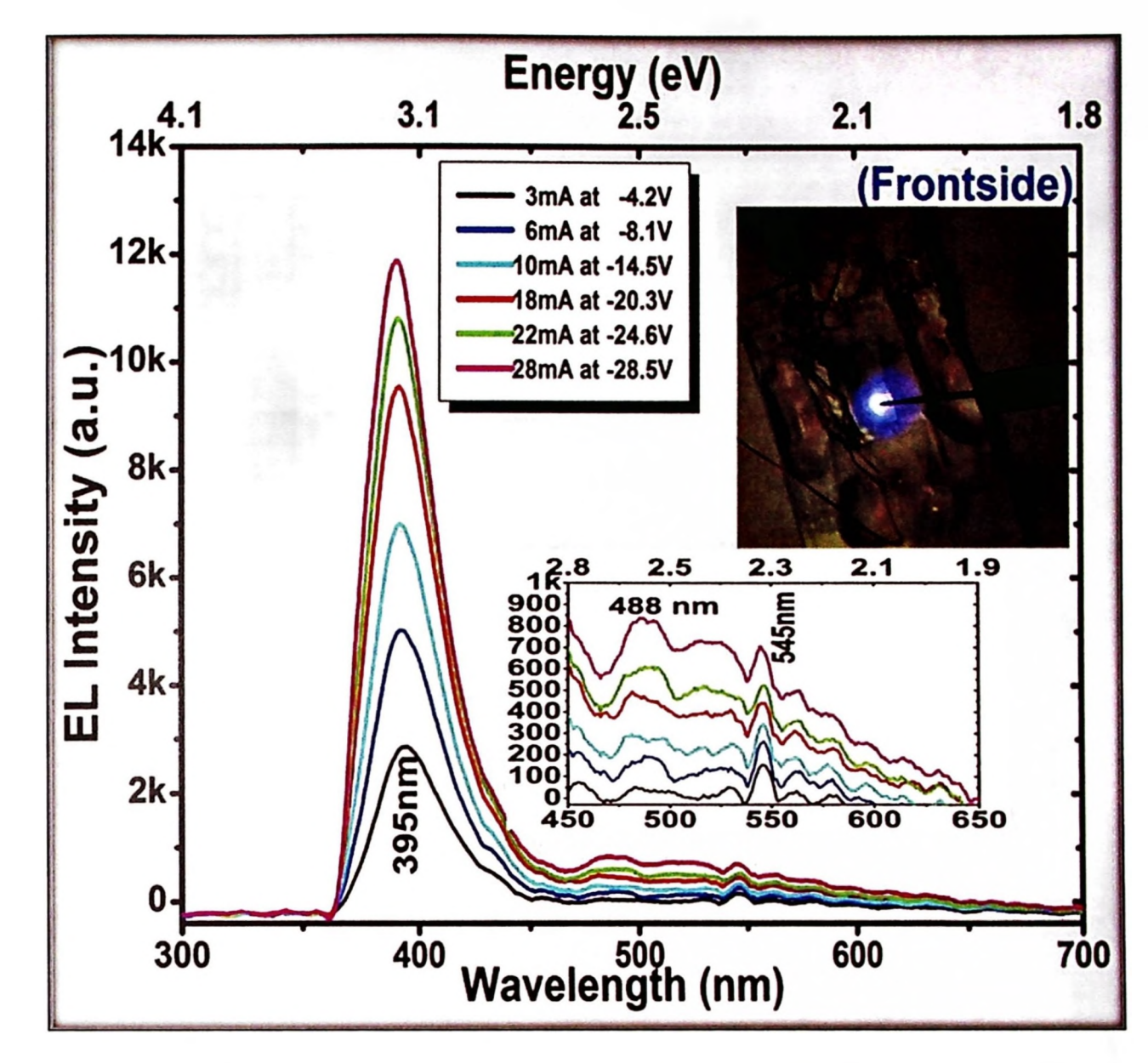


Figure 6.12: Room-temperature EL measurement spectra emission from front side of the n-ZnO NRs /p-GaN LED with different current injections at the reverse breakdown bias, where bottom right inset shows the zoom in on the EL spectra in the range of 450 to 650 nm. Top right inset shows real optical photos of the LED in the ambient lighting at the current injection of 22 mA.

Furthermore, in order to gain a deeper insight into the mechanism of carrier transportation and recombination of EL of the n-ZnO/p-GaN heterojunction under the reverse breakdown bias, an ideal schematic energy band diagram of the relevant n-ZnO/p-GaN determined by the Anderson model type II band alignment is proposed. Figure 6.13 (a) presents graph showing the band diagram of the n-ZnO/p-

GaN heterojunction at zero reverse bias, while Figure 6.13 (b) displays the energy band diagram of LED heterojunction under the reverse bias.

Because of the difference between the electron affinity energies (χ) and the band gap (E_g) of ZnO and GaN, the band is shifted at the heterojunction between the valence band of p-GaN (occupied maximum) and conduction band of n-ZnO (unoccupied minimum) under reverse bias voltage [224]. Therefore, the VB of p-GaN is higher than the CB of n-ZnO and this facilitates the tunneling of the electrons from p-GaN to n-ZnO under even the small reverse bias voltage. It should be noted that any increase in the value of negative supply voltage leads to increase in the value of this offset at the heterojunction.

Under the influence of electric field, the electrons drift across the p-GaN layer and some of them recombine with holes in the Mg acceptor levels in p-GaN to produce the EL at 395 nm and that emission is enhanced with the emission which resulted from the near-band-edge emission of ZnO. The other electrons which possessed higher energy move towards the valence band in p-GaN to recombine with holes to produce the EL in the range of 368 to 370nm. The rest which has more higher energy drifts to the heterojunction interface.

Furthermore, it is believed that irradiative recombinations occurred in both sides of the heterojunction under reverse bias due to the transfer of the electrons from the VB for p-GaN into the CB for n-ZnO and at the same time the holes from the CB for n-ZnO are injected into the VB for p-GaN. In addition, it is worth to mention that some of the electrons, which tunnel across the heterojunction interface are captured by the oxygen vacancies near the interface yielding the green emission.

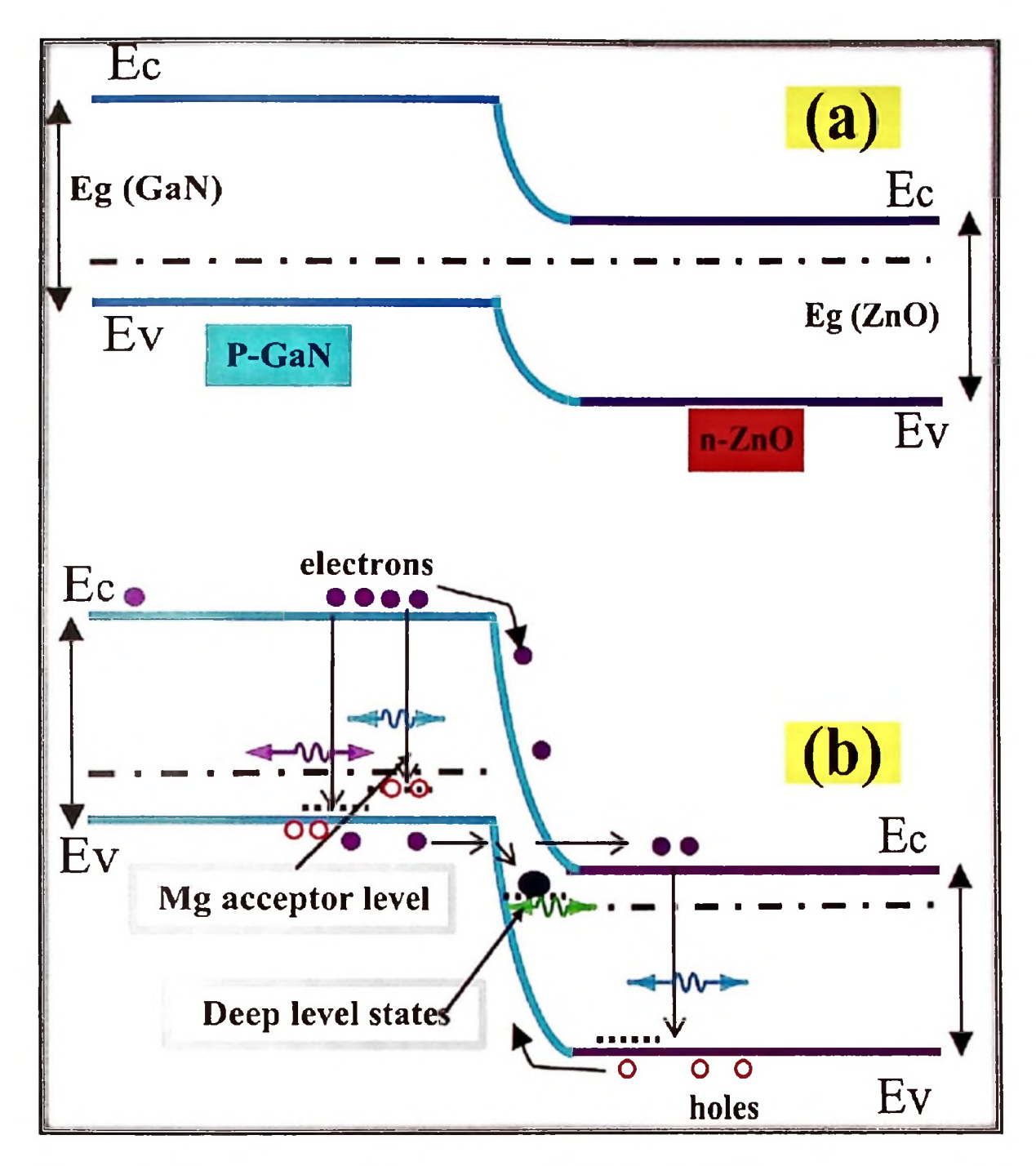


Figure 6.13: Energy band diagram of n-ZnO NRs /p-GaN heterojunction at (a) zero and (b) reverse bias.

6.4 Summary

DHS-MCBD process has been successfully used to grow vertically ultralong, well-aligned and hexagonal-shaped n-ZnO NRs with fewer defects on the ZnO seeded/Si and the seedless p-GaN substrates, and to be applied for fabrication of the nano-size junction n-ZnO NRs /p-GaN LED device. The results were confirmed by FESEM, EDX, XRD, Raman, PL, I-V, and EL measurements. FESEM shows how ZnO NRs were grown directly from the ZnO seeded/Si and the GaN surface, where there was no material layer between the top of GaN layer and the bottom of rods. The structural investigation by XRD shows that ZnO NRs exhibit c-axis orientation. It is worth noting that Raman results are very consistent with the XRD results. PL measurement showed a high difference (I_{UV}/I_{DLE}) in intensity indicating that the ultra-long ZnO NRs prepared using DHS-MCBD technique, have high quality with small number of defects.

The I-V characteristic of the heterojunction LED device indicates that the breakdown voltage is less than 4Eg/q. Therefore, it suggested that the breakdown effect for the device is caused by tunnelling effect at the interface of the hetrojunction. The electroluminescence EL intensities were measured from both sides of n-ZnO/p-GaN/heterojunction LED under different reverse bias. EL spectrum emission from back side of the device was composed of the ultraviolet emission and a broad band green emission, while the emission from front side was composed of the near ultraviolet emission with a broad band green emission. Meanwhile, the different excitation (PL) and recombination mechanisms (EL) were explained.

CHAPTER 7: CONCLUSION AND FUTURE STUDIES

7.1 Conclusions

This thesis evaluated the growth of ZnO NRs and ultralong ZnO NRs on various substrates using hydrothermal and DHS-MCBD techniques, respectively, and then experimentally fabricated different kinds of electrical devices. By the first method, hexagonal ZnO NRs structures were successfully grown on a cheap, very thin, and highly flexible substrate in order to fabricate the metal-semiconductormetal (MSM) of UV-PDs and the H₂ gas sensor devices, making them attractive for the highly flexible and low-cost sensing applications. As far as the literature on this issue shows, there has not been any reports on the use of this type of ultra-thin (15 µm) flexible nylon as a substrate, and subsequently on the fabrication of the highly flexible sensing devices.

At first, the thermal behavior and properties for this nylon substrate were studied. Then, the effects of pre-annealing duration of ZnO seeds layer on structural, morphological and optical properties were studied. It was found that the optimum heat-treatment temperature and duration to produce uniform nanosized ZnO seeds was 180°C for 3 h. Morphological, crystallinity, and optical properties of the prepared ZnO NRs were studied by FESEM, TEM, EDX, XRD, UV-Vis, and PL measurements. Results obtained revealed the formation of aligned hexagonal-like nanorods with high aspect ratio and density. For the highly flexible MSM (Pd/ZnO NRs/Pd) UV-PDs devices, the optimized device (with film heat treated at 180 °C for 3 h) showed the highest responsivity and current gain of 0.4774 A/W and 9.15, respectively upon exposure to UV light at 365 nm and under 5 V bias voltage.

For the highly flexible MSM (Pt/ZnO NRs/Pt) H₂ gas sensor device, the sensitivity and response time behaviors of the ZnO NRs-based gas sensor to hydrogen gas were investigated at different operation temperatures and in various hydrogen concentrations. One of the most important findings of this study is that the obtained ZnO NRs were inclined at different angles (from 45° to 90°) with respect to the nylon substrate and generated the huge number of contact points between rods. As a result, the passage of electric current through the nanorods improved when a bias voltage was applied to the MSM device under hydrogen gas exposure.

DHS-MCBD system provides the homogeneous distribution of high temperature to the whole substrate in a low temperature solution, that lead to fabrication of ultralong ZnO NRs on various kinds of substrates, with and without seed layer or catalyst. The results of FESEM measurement confirmed that ZnO NRs were grown directly from GaN surface and without material layer (like ZnO seed layer or any catalysts) between the top of GaN layer and the bottom of rods. In addition, a new promising nano-size n-ZnO NRs /p-GaN LED device with high intensity of EL was successfully fabricated.

The EL intensities were measured from both sides of n-ZnO/p-GaN/sapphire substrate LED under the reverse bias. EL spectra of the heterojunction LED under reverse bias measured from the back side of LED was composed of the ultraviolet emission, near blue light, and green light, while EL spectra measured from the front side of the device was composed of the near ultraviolet emission, near blue light, and with a broad band around 450 to 600 nm. In this context, the light intensity from both sides of the fabricated LED device was strong enough to be easily seen with the naked eye, even in the ambient lighting and it has been documented in real optical

photos. In addition, cancellation of the interfacial layer between ZnO NRs and GaN substrate and fabrication of the nano-size junction between ZnO and GaN plays an important role to enhance the luminescence efficiency property of LED because of the increase in the carrier tunneling efficiency through the junction. Finally, the configuration of DHS-MCBD system is simpler compared to the previous reported of system and it is believed that HDS-MCBD as the novel technique will occupy a unique place in modern science and technology.

7.2 Future Studies

The recommendations for future studies based on the findings of the present study are as follows:

- 1. Instead of ZnO, other materials nanostructures can be synthesised at low temperature on this ultra-thin nylon substrate.
- 2. Instead of UV-PD and the H₂ gas sensor devices, fabrication of other kinds of highly flexible electrical devices are possible using this ultra-thin nylon as a substrate.
- DHS-MCBD process can be used to fabricate other material nanostructures
 especially those that can be synthesised by CBD method or hydrothermal
 method and on different substrates.
- 4. Finally, it is expected that DHS-MCBD technique to be well-received by future researchers, especially developers because it will open up new horizons for them to fabricate the various kinds of electrical devices.

REFERENCES

- [1] Klingshirn, C.F., A. Waag, A. Hoffmann, and J. Geurts, Zinc Oxide: From Fundamental Properties Towards Novel Applications. Vol. 120. (2010): Springer Science & Business Media.
- [2] Janotti, A. and C.G. Van de Walle, Fundamentals of Zinc Oxide as a Semiconductor. Reports on progress in physics, (2009). 72(12): p. 126501.
- [3] Wei, A., L. Pan, and W. Huang, Recent Progress in the ZnO Nanostructure-Based Sensors. Materials Science and Engineering B, (2011). 176(18): p. 1409-1421.
- [4] Laudise, R. and A. Ballman, Hydrothermal Synthesis of Zinc Oxide and Zinc Sulfide1. The Journal of Physical Chemistry, (1960). 64(5): p. 688-691.
- [5] Heo, Y., V. Varadarajan, M. Kaufman, K. Kim, D. Norton, F. Ren, and P. Fleming, Site-Specific Growth of ZnO Nanorods Using Catalysis-Driven Molecular-Beam Epitaxy. Applied physics letters, (2002). 81(16): p. 3046-3048.
- [6] Park, W.I., D. Kim, S.-W. Jung, and G.-C. Yi, Metalorganic Vapor-Phase Epitaxial Growth of Vertically Well-Aligned ZnO Nanorods. Applied Physics Letters, (2002). 80(22): p. 4232-4234.
- Yuan, H. and Y. Zhang, Preparation of Well-Aligned ZnO Whiskers on Glass Substrate by Atmospheric Mocvd. Journal of crystal growth, (2004). 263(1): p. 119-124.
- [8] Sun, Y., G.M. Fuge, and M.N. Ashfold, Growth of Aligned Zno Nanorod Arrays by Catalyst-Free Pulsed Laser Deposition Methods. Chemical Physics Letters, (2004). 396(1): p. 21-26.
- [9] Wu, J.J., H.I. Wen, C.H. Tseng, and S.C. Liu, Well-Aligned ZnO Nanorods Via Hydrogen Treatment of ZnO Films. Advanced Functional Materials, (2004). 14(8): p. 806-810.
- [10] Sui, X., C. Shao, and Y. Liu, White-Light Emission of Polyvinyl Alcohol Zno Hybrid Nanofibers Prepared by Electrospinning. Applied Physics Letters, (2005). 87(11): p. 113115.
- [11] Lin, D., H. Wu, and W. Pan, Photoswitches and Memories Assembled by Electrospinning Aluminum-Doped Zinc Oxide Single Nanowires. Advanced Materials, (2007). 19(22): p. 3968-3972.
- [12] Huang, M.H., Y. Wu, H. Feick, N. Tran, E. Weber, and P. Yang, Catalytic Growth of Zinc Oxide Nanowires by Vapor Transport. Advanced Materials, (2001). 13(2): p. 113-116.

- [13] Yao, B., Y. Chan, and N. Wang, Formation of ZnO Nanostructures by a Simple Way of Thermal Evaporation. Applied Physics Letters, (2002). 81(4): p. 757-759.
- [14] Chiou, W.-T., W.-Y. Wu, and J.-M. Ting, Growth of Single Crystal Zno Nanowires Using Sputter Deposition. Diamond and Related Materials, (2003). 12(10): p. 1841-1844.
- [15] Vayssieres, L., K. Keis, S.-E. Lindquist, and A. Hagfeldt, Purpose-Built Anisotropic Metal Oxide Material: 3D Highly Oriented Microrod Array of Zno. The Journal of Physical Chemistry B, (2001). 105(17): p. 3350-3352.
- [16] Nakamura, S., N. Iwasa, M. Senoh, and T. Mukai, Hole Compensation Mechanism of P-Type GaN Films. Japanese Journal of Applied Physics, (1992). 31(5R): p. 1258.
- [17] Krames, M.R., O.B. Shchekin, R. Mueller-Mach, G.O. Mueller, L. Zhou, G. Harbers, and M.G. Craford, Status and Future of High-Power Light-Emitting Diodes for Solid-State Lighting. Journal of display technology, (2007). 3(2): p. 160-175.
- [18] Rogers, D.J., P. Bove, E.V. Sandana, F.H. Teherani, R. McClintock, and M. Razeghi, Solid-State Deep Uv Emitters/Detectors: Zinc Oxide Moves Further into the Ultraviolet. Laser Focus World, (2013). 49(10): p. 10.
- [19] Xiu, F., J. Xu, P.C. Joshi, C.A. Bridges, and M.P. Paranthaman, ZnO Doping and Defect Engineering—a Review, in *Semiconductor Materials for Solar Photovoltaic Cells*. (2016), Springer. p. 105-140.
- [20] Choi, Y.-S., J.-W. Kang, D.-K. Hwang, and S.-J. Park, Recent Advances in ZnO-Based Light-Emitting Diodes. IEEE Transactions on Electron Devices, (2010). 57(1): p. 26-41.
- [21] Guo, W., L. Woobong, J. Guo, H. Zhang, and R. Qingrong, Substrate Tray and Manufacturing Method of a Flexible Electronic Device. (2012), Google Patents.
- [22] Dong, J., X. Zhang, Z. Yin, J. Wang, S. Zhang, F. Si, H. Gao, and X. Liu, Ultraviolet Electroluminescence from Ordered ZnO Nanorod Array/P-GaN Light Emitting Diodes. Applied Physics Letters, (2012). 100(17): p. 171109.
- [23] Dong, J.-J., C.-Y. Zhen, H.-Y. Hao, J. Xing, Z.-J. Fan, and Z.-L. Zhang, Highly Ordered ZnO Nanostructure Arrays: Preparation and Light-Emitting Diode Application. Japanese Journal of Applied Physics, (2014). 53(5): p. 055201.
- [24] Park, W.I. and G.C. Yi, Electroluminescence in N-ZnO Nanorod Arrays Vertically Grown on P-GaN. Advanced Materials, (2004). 16(1): p. 87-90.

- [25] Yi, G.-C. and W.-I. Park, Pn Heterojunction Structure of Zinc Oxide-Based Nanorod and Semiconductor Thin Film, Preparation Thereof, and Nano-Device Comprising Same. (2009), Google Patents.
- [26] Liu, S.-Y., J.-H. Wu, S.-T. Li, T. Chen, S.-R. Deng, Y.-L. Jiang, G.-P. Ru, and X.-P. Qu. The El Properties of Well-Aligned n-ZnO Nanorods/p-GaN Structure. in Solid-State and Integrated Circuit Technology (ICSICT), 2010 10th IEEE International Conference on. (Year) of Conference.: IEEE.
- [27] Klingshirn, C., Zno: From Basics Towards Applications. physica status solidi (b), (2007). 244(9): p. 3027-3073.
- [28] Jagadish, C. and S.J. Pearton, Zinc Oxide Bulk, Thin Films and Nanostructures: Processing, Properties, and Applications. (2011): Elsevier.
- [29] Khanna, V.K., Fundamentals of Solid-State Lighting: Leds, Oleds, and Their Applications in Illumination and Displays. (2014): CRC press. p. 71.
- [30] Seghier, D. and H. Gislason, Shallow and Deep Donors in n-Type ZnO Characterized by Admittance Spectroscopy. Journal of Materials Science: Materials in Electronics, (2008). 19(8-9): p. 687-691.
- [31] Ren, G.-K., J.-L. Lan, K.J. Ventura, X. Tan, Y.-H. Lin, and C.-W. Nan, Contribution of Point Defects and Nano-Grains to Thermal Transport Behaviours of Oxide-Based Thermoelectrics. npj Computational Materials, (2016). 2: p. 16023.
- [32] Kamble, A.S., B.B. Sinha, K. Chung, M.G. Gil, V. Burungale, C.-J. Park, J.H. Kim, and P.S. Patil, Effect of Hydroxide Anion Generating Agents on Growth and Properties of ZnO Nanorod Arrays. Electrochimica Acta, (2014). 149: p. 386-393.
- [33] Wang, Z.L., Zinc Oxide Nanostructures: Growth, Properties and Applications. Journal of Physics: Condensed Matter, (2004). 16(25): p. R829.
- [34] Ma, S., H. Liang, X. Wang, J. Zhou, L. Li, and C.Q. Sun, Controlling the Band Gap of ZnO by Programmable Annealing. The Journal of Physical Chemistry C, (2011). 115(42): p. 20487-20490.
- [35] Xu, S. and Z.L. Wang, One-Dimensional ZnO Nanostructures: Solution Growth and Functional Properties. Nano Research, (2011). 4(11): p. 1013-1098.
- [36] Zhao, Q., P. Klason, M. Willander, H. Zhong, W. Lu, and J. Yang, Deep-Level Emissions Influenced by O and Zn Implantations in ZnO. Applied Physics Letters, (2005). 87(21): p. 211912-211912-3.
- [37] Yamauchi, S., Y. Goto, and T. Hariu, Photoluminescence Studies of Undoped and Nitrogen-Doped Zno Layers Grown by Plasma-Assisted Epitaxy. Journal of Crystal Growth, (2004). 260(1): p. 1-6.

- [38] Djurišić, A., et al., Defect Emissions in ZnO Nanostructures. Nanotechnology, (2007). 18(9): p. 095702.
- [39] Tam, K., et al., Defects in ZnO Nanorods Prepared by a Hydrothermal Method. The Journal of Physical Chemistry B, (2006). 110(42): p. 20865-20871.
- [40] Alvi, N., M. Riaz, G. Tzamalis, O. Nur, and M. Willander, Fabrication and Characterization of High-Brightness Light Emitting Diodes Based on N-Zno Nanorods Grown by a Low-Temperature Chemical Method on p-4h-Sic and p-GaN. Semiconductor Science and Technology, (2010). 25(6): p. 065004.
- [41] Lim, K., M.A. Abdul Hamid, R. Shamsudin, N. Al-Hardan, I. Mansor, and W. Chiu, Temperature-Driven Structural and Morphological Evolution of Zinc Oxide Nano-Coalesced Microstructures and Its Defect-Related Photoluminescence Properties. Materials, (2016). 9(4): p. 300.
- [42] Alvi, N., K. Ul Hasan, O. Nur, and M. Willander, The Origin of the Red Emission in n-ZnO Nanotubes/p-GaN White Light Emitting Diodes. Nanoscale research letters, (2011). 6(1): p. 1-7.
- [43] Tonon, C., C. Duvignacq, G. Teyssedre, and M. Dinguirard, Degradation of the Optical Properties of Zno-Based Thermal Control Coatings in Simulated Space Environment. Journal of Physics D: Applied Physics, (2001). 34(1): p. 124.
- [44] Petersen, J., et al., Structural and Photoluminescence Properties of ZnO Thin Films Prepared by Sol-Gel Process. Journal of Applied Physics, (2008). 104(11): p. 113539.
- [45] Tjong, S.-C., Nanocrystalline Materials: Their Synthesis-Structure-Property Relationships and Applications. (2013): Newnes.
- [46] Srivastava, A.K., Oxide Nanostructures: Growth, Microstructures, and Properties. (2014): CRC Press.
- [47] Xu, S., C. Lao, B. Weintraub, and Z.L. Wang, Density-Controlled Growth of Aligned ZnO Nanowire Arrays by Seedless Chemical Approach on Smooth Surfaces. Journal of Materials Research, (2008). 23(08): p. 2072-2077.
- [48] Sun, Y. and J.A. Rogers, Semiconductor Nanomaterials for Flexible Technologies: From Photovoltaics and Electronics to Sensors and Energy Storage. (2010): William Andrew.
- [49] Zhang, Y., M.K. Ram, E.K. Stefanakos, and D.Y. Goswami, Synthesis, Characterization, and Applications of ZnO Nanowires. Journal of Nanomaterials, (2012). 2012: p. 20.

- [50] Li, Q., V. Kumar, Y. Li, H. Zhang, T.J. Marks, and R.P. Chang, Fabrication of ZnO Nanorods and Nanotubes in Aqueous Solutions. Chemistry of Materials, (2005). 17(5): p. 1001-1006.
- [51] Solís-Pomar, F., E. Martínez, M.F. Meléndrez, and E. Pérez-Tijerina, Growth of Vertically Aligned ZnO Nanorods Using Textured ZnO Films. Nanoscale research letters, (2011). 6(1): p. 1.
- [52] Arbiol, J. and Q. Xiong, Semiconductor Nanowires: Materials, Synthesis, Characterization and Applications. (2015): Elsevier.
- [53] Chen, R., P. Zhu, L. Deng, T. Zhao, R. Sun, and C. Wong, Effect of Aluminum Doping on the Growth and Optical and Electrical Properties of Zno Nanorods. ChemPlusChem, (2014). 79(5): p. 743-750.
- [54] Tong, Y., Y. Liu, L. Dong, D. Zhao, J. Zhang, Y. Lu, D. Shen, and X. Fan, Growth of ZnO Nanostructures with Different Morphologies by Using Hydrothermal Technique. The Journal of Physical Chemistry B, (2006). 110(41): p. 20263-20267.
- [55] Yuan, K., X. Yin, J. Li, J. Wu, Y. Wang, and F. Huang, Preparation and Dsc Application of the Size-Tuned ZnO Nanoarrays. Journal of Alloys and Compounds, (2010). 489(2): p. 694-699.
- [56] Qin, Y., R. Yang, and Z.L. Wang, Growth of Horizonatal ZnO Nanowire Arrays on Any Substrate. The Journal of Physical Chemistry C, (2008). 112(48): p. 18734-18736.
- [57] Weintraub, B., Y. Deng, and Z.L. Wang, Position-Controlled Seedless Growth of ZnO Nanorod Arrays on a Polymer Substrate Via Wet Chemical Synthesis. The Journal of Physical Chemistry C, (2007). 111(28): p. 10162-10165.
- [58] Riaz, M., J. Song, O. Nur, Z.L. Wang, and M. Willander, Study of the Piezoelectric Power Generation of ZnO Nanowire Arrays Grown by Different Methods. Advanced functional materials, (2011). 21(4): p. 628-633.
- [59] Hassan, J., M. Mahdi, S. Kasim, N.M. Ahmed, H.A. Hassan, and Z. Hassan, Fast Uv Detection and Hydrogen Sensing by ZnO Nanorod Arrays Grown on a Flexible Kapton Tape. Materials Science-Poland, (2013). 31(2): p. 180-185.
- [60] Hua, G., Y. Tian, L. Yin, and L. Zhang, Reproducible Growth of Ultralong Zno Nanowire Arrays in the Metastable Supersaturated Solution. Crystal Growth & Design, (2009). 9(11): p. 4653-4659.
- [61] Xu, C., P. Shin, L. Cao, and D. Gao, Preferential Growth of Long ZnO Nanowire Array and Its Application in Dye-Sensitized Solar Cells. The Journal of Physical Chemistry C, (2009). 114(1): p. 125-129.

- [62] Qiu, J., X. Li, F. Zhuge, X. Gan, X. Gao, W. He, S.-J. Park, H.-K. Kim, and Y.-H. Hwang, Solution-Derived 40 µm Vertically Aligned ZnO Nanowire Arrays as Photoelectrodes in Dye-Sensitized Solar Cells. Nanotechnology, (2010). 21(19): p. 195602.
- [63] Chen, L.-Y. and Y.-T. Yin, Facile Continuous Flow Injection Process for High Quality Long ZnO Nanowire Arrays Synthesis. Crystal Growth & Design, (2012). 12(3): p. 1055-1059.
- [64] Amin, G., M. Asif, A. Zainelabdin, S. Zaman, O. Nur, and M. Willander, Influence of Ph, Precursor Concentration, Growth Time, and Temperature on the Morphology of ZnO Nanostructures Grown by the Hydrothermal Method. Journal of Nanomaterials, (2011). 2011: p. 5.
- [65] Lee, T.-h., H. Ryu, and W.-J. Lee, Fast Vertical Growth of ZnO Nanorods Using a Modified Chemical Bath Deposition. Journal of Alloys and Compounds, (2014). 597: p. 85-90.
- [66] Hu, Z., Q. Chen, Z. Li, Y. Yu, and L.-M. Peng, Large-Scale and Rapid Synthesis of Ultralong ZnO Nanowire Films Via Anodization. The Journal of Physical Chemistry C, (2009). 114(2): p. 881-889.
- [67] Zhao, X., T. Shaymurat, T. Pei, L. Bai, B. Cai, Y. Tong, Q. Tang, and Y. Liu, Low-Temperature, Catalyst-Free Vapor-Solid Growth of Ultralong ZnO Nanowires. Materials Chemistry and Physics, (2012). 136(2): p. 455-459.
- [68] Wen, L., K.M. Wong, Y. Fang, M. Wu, and Y. Lei, Fabrication and Characterization of Well-Aligned, High Density ZnO Nanowire Arrays and Their Realizations in Schottky Device Applications Using a Two-Step Approach. Journal of Materials Chemistry, (2011). 21(20): p. 7090-7097.
- [69] Sugeta, T., T. Urisu, S. Sakata, and Y. Mizushima, Metal-Semiconductor-Metal Photodetector for High-Speed Optoelectronic Circuits. Japanese Journal of Applied Physics, (1980). 19(S1): p. 459.
- [70] Slayman, C. and L. Figueroa, Frequency and Pulse Response of a Novel High-Speed Interdigital Surface Photoconductor (Idpc). Electron Device Letters, IEEE, (1981). 2(5): p. 112-114.
- [71] Rahimi, R., Electrical Properties of Strained 3c-Silicon Carbide/Silicon Heterostructures. (2008): ProQuest.
- [72] Zanger, H. and C. Zanger, Fiber Optics: Communication and Other Applications. (1991): Merrill Pub Co.
- Yingying, L., C. Chuanwei, D. Xiang, G. Junshan, and Z. Haiqian, Facile Fabrication of Uv Photodetectors Based on ZnO Nanorod Networks across Trenched Electrodes. Journal of Semiconductors, (2009). 30(6): p. 063004.

- [74] Ridhuan, N.S., K.A. Razak, Z. Lockman, and A.A. Aziz, Structural and Morphology of ZnO Nanorods Synthesized Using ZnO Seeded Growth Hydrothermal Method and Its Properties as Uv Sensing. PloS one, (2012). 7(11): p. e50405.
- [75] Mamat, M.H., et al., Controllable Growth of Vertically Aligned Aluminum-Doped Zinc Oxide Nanorod Arrays by Sonicated Sol-Gel Immersion Method Depending on Precursor Solution Volumes. Japanese Journal of Applied Physics, (2011). 50(6).
- [76] Dhara, S. and P. Giri, Enhanced Uv Photosensitivity from Rapid Thermal Annealed Vertically Aligned ZnO Nanowires. Nanoscale research letters, (2011). 6(1): p. 1-8.
- [77] Ahn, S.E., J.S. Lee, H. Kim, S. Kim, B.H. Kang, K.H. Kim, and G.T. Kim, Photoresponse of Sol-Gel-Synthesized Zno Nanorods. Applied physics letters, (2004). 84(24): p. 5022-5024.
- [78] Bera, A. and D. Basak, Role of Defects in the Anomalous Photoconductivity in Zno Nanowires. Applied Physics Letters, (2009). 94(16): p. 163119.
- [79] Chen, T., S. Young, S. Chang, C. Hsiao, and C. Huang, Field-Emission and Photoelectrical Characteristics of ZnO Nanorods Photodetectors Prepared on Flexible Substrate. Journal of The Electrochemical Society, (2012). 159(5): p. J153-J157.
- [80] Yang, P.-Y., J.-L. Wang, W.-C. Tsai, S.-J. Wang, J.-C. Lin, I.-C. Lee, C.-T. Chang, and H.-C. Cheng, Photoresponse of Hydrothermally Grown Lateral Zno Nanowires. Thin Solid Films, (2010). 518(24): p. 7328-7332.
- [81] Soci, C., A. Zhang, B. Xiang, S.A. Dayeh, D. Aplin, J. Park, X. Bao, Y.-H. Lo, and D. Wang, Zno Nanowire Uv Photodetectors with High Internal Gain. Nano letters, (2007). 7(4): p. 1003-1009.
- [82] Wei, A., L. Pan, and W. Huang, Recent Progress in the ZnO Nanostructure-Based Sensors. Materials Science and Engineering: B, (2011). 176(18): p. 1409-1421.
- [83] Hui-Qing, C., H. Ming, Z. Jing, and W. Wei-Dan, The Light-Enhanced No2 Sensing Properties of Porous Silicon Gas Sensors at Room Temperature. Chinese Physics B, (2012). 21(5): p. 058201.
- [84] Karaduman, I., M. Demir, D.E. Yıldız, and S. Acar, CO₂ Gas Detection Properties of a Tio2/Al2o3 Heterostructure under Uv Light Irradiation. Physica Scripta, (2015). 90(5): p. 055802.
- [85] Kang, B., Y. Heo, L. Tien, D. Norton, F. Ren, B. Gila, and S. Pearton, Hydrogen and Ozone Gas Sensing Using Multiple ZnO Nanorods. Applied Physics A: Materials Science & Processing, (2005). 80(5): p. 1029-1032.

- [86] Zhang, P., G. Pan, B. Zhang, J. Zhen, and Y. Sun, High Sensitivity Ethanol Gas Sensor Based on Sn-Doped ZnO under Visible Light Irradiation at Low Temperature. Materials Research, (2014). 17(4): p. 817-822.
- [87] Lupan, O., L. Chow, and G. Chai, A Single ZnO Tetrapod-Based Sensor. Sensors and Actuators B: Chemical, (2009). 141(2): p. 511-517.
- [88] Al-Hardan, N., M. Abdullah, A.A. Aziz, H. Ahmad, and L. Low, ZnO Thin Films for Voc Sensing Applications. Vacuum, (2010). 85(1): p. 101-106.
- [89] Ramachandran, R. and R.K. Menon, An Overview of Industrial Uses of Hydrogen. International Journal of Hydrogen Energy, (1998). 23(7): p. 593-598.
- [90] Holladay, J.D., J. Hu, D.L. King, and Y. Wang, An Overview of Hydrogen Production Technologies. Catalysis Today, (2009). 139(4): p. 244-260.
- [91] Al-Hardan, N., M. Abdullah, and A.A. Aziz, Sensing Mechanism of Hydrogen Gas Sensor Based on Rf-Sputtered Zno Thin Films. International journal of hydrogen energy, (2010). 35(9): p. 4428-4434.
- [92] TAKATA, M., D. TSUBONE, and H. YANAGIDA, Dependence of Electrical Conductivity of ZnO on Degree of Sintering. Journal of the American Ceramic Society, (1976). 59(1-2): p. 4-8.
- [93] Lupan, O., G. Chai, and L. Chow, Novel Hydrogen Gas Sensor Based on Single Zno Nanorod. Microelectronic Engineering, (2008). 85(11): p. 2220-2225.
- [94] Meneses, A. and M. Isela, Development of Ozone and Ammonia Gas Sensors on Flexible Substrate. (2014), Aix-Marseille.
- [95] Brody, T., F.C. Luo, Z.P. Szepesi, and D.H. Davies, A 6× 6-in 20-Lpi Electroluminescent Display Panel. IEEE transactions on electron devices, (1975). 22(9): p. 739-748.
- [96] Kind, H., H. Yan, B. Messer, M. Law, and P. Yang, Nanowire Ultraviolet Photodetectors and Optical Switches. Advanced materials, (2002). 14(2): p. 158.
- [97] Yao, I.-C., T.-Y. Tseng, and P. Lin, ZnO Nanorods Grown on Polymer Substrates as Uv Photodetectors. Sensors and Actuators A: Physical, (2012). 178: p. 26-31.
- [98] Manekkathodi, A., M.Y. Lu, C.W. Wang, and L.J. Chen, Direct Growth of Aligned Zinc Oxide Nanorods on Paper Substrates for Low-Cost Flexible Electronics. Advanced materials, (2010). 22(36): p. 4059-4063.
- [99] Shabannia, R. and H.A. Hassan, Characteristics of Photoconductive Uv Photodetector Based on ZnO Nanorods Grown on Polyethylene Naphthalate

- Substrate by Chemical Bath Deposition Method. Electronic Materials Letters, (2014). 10(4): p. 837-843.
- [100] Albiss, B.A., M.-A. AL-Akhras, and I. Obaidat, Ultraviolet Photodetector Based on ZnO Nanorods Grown on a Flexible Pdms Substrate. International Journal of Environmental Analytical Chemistry, (2015). 95(4): p. 339-348.
- [101] Ong, W.L., C. Zhang, and G.W. Ho, Ammonia Plasma Modification Towards a Rapid and Low Temperature Approach for Tuning Electrical Conductivity of ZnO Nanowires on Flexible Substrates. Nanoscale, (2011). 3(10): p. 4206-4214.
- [102] Rashid, T.-R., D.-T. Phan, and G.-S. Chung, A Flexible Hydrogen Sensor Based on Pd Nanoparticles Decorated Zno Nanorods Grown on Polyimide Tape. Sensors and Actuators B: Chemical, (2013), 185: p. 777-784.
- [103] Rashid, T.-R., D.-T. Phan, and G.-S. Chung, Effect of Ga-Modified Layer on Flexible Hydrogen Sensor Using ZnO Nanorods Decorated by Pd Catalysts. Sensors and Actuators B: Chemical, (2014). 193: p. 869-876.
- [104] Uddin, A.I., U. Yaqoob, D.-T. Phan, and G.-S. Chung, A Novel Flexible Acetylene Gas Sensor Based on Pi/Ptfe-Supported Ag-Loaded Vertical ZnO Nanorods Array. Sensors and Actuators B: Chemical, (2016). 222: p. 536-543.
- [105] Iftekhar, A. and G.-S. Chung, Fabrication and Characterization of Self-Powered Active Hydrogen Sensor Based on Triboelectric Nanogenerator. Procedia Engineering, (2016). 168: p. 239-242.
- [106] Ma, S., R. Li, C. Lv, W. Xu, and X. Gou, Facile Synthesis of ZnO Nanorod Arrays and Hierarchical Nanostructures for Photocatalysis and Gas Sensor Applications. Journal of hazardous materials, (2011). 192(2): p. 730-740.
- [107] Sze, S.M., Semiconductor Devices: Physics and Technology. (2008): John Wiley & Sons. p. 79.
- [108] Lai, E.M., Zinc Oxide and Nitride Nanowire Based Light Emitting Diodes. (2009).
- [109] Zhang, L., Q. Li, C. Qu, Z. Zhang, R. Huang, and F. Zhao, White Electroluminescence from ZnO Nanorods/P-Gan Heterojunction Light-Emitting Diodes under Reverse Bias. Journal of Optics, (2012). 15(2): p. 025003.
- [110] Fu, Q.-M., W. Cao, G.-W. Li, Z.-D. Lin, Z. Chen, C.-B. Xu, Y.-F. Tu, and Z.-B. Ma, Blue/Green Electroluminescence from a ZnO Nanorods/P-Gan Heterojunction Light Emitting Diode under Different Reverse Bias. Applied Surface Science, (2014). 293: p. 225-228.

- [111] Xu, S., et al., Ordered Nanowire Array Blue/near-Uv Light Emitting Diodes. Advanced Materials, (2010). 22(42): p. 4749-4753.
- [112] Chen, H., M. Chen, Y. Huang, W. Sun, W. Li, J. Yang, H. Kuan, and M. Shiojiri, White-Light Electroluminescence from n-ZnO/p-GaN Heterojunction Light-Emitting Diodes at Reverse Breakdown Bias. IEEE Transactions on Electron Devices, (2011). 58(11): p. 3970-3975.
- [113] Dalui, S., C.-C. Lin, H.-Y. Lee, S.-F. Yen, Y.-J. Lee, and C.-T. Lee, Electroluminescence from Solution Grown n-ZnO Nanorod/p-GaN-Heterostructured Light Emitting Diodes. Journal of The Electrochemical Society, (2010). 157(5): p. H516-H518.
- [114] Mo, X., et al., Near-Ultraviolet Light-Emitting Diodes Realized from n-ZnO Nanorod/p-GaN Direct-Bonding Heterostructures. Journal of Luminescence, (2013). 137: p. 116-120.
- [115] Ng, A., et al., GaN/ZnO Nanorod Light Emitting Diodes with Different Emission Spectra. Nanotechnology, (2009). 20(44): p. 445201.
- [116] Roul, B., M. Kumar, M.K. Rajpalke, T.N. Bhat, and S. Krupanidhi, Binary Group Iii-Nitride Based Heterostructures: Band Offsets and Transport Properties. Journal of Physics D: Applied Physics, (2015). 48(42): p. 423001.
- [117] Madelung, O., Festkörper Probleme Xi: Advances in Solid State Physics. (2016): Elsevier. p. 227.
- [118] Sparavigna, A.C., Carbon-Arc Light as the Electric Light of 1870. International Journal of Sciences, (2014). 3(10): p. 1-7.
- [119] Round, H.J., A Note on Carborundum. Electrical world, (1907). 49(6): p. 309.
- [120] Zheludev, N., The Life and Times of the Led—a 100-Year History. Nature Photonics, (2007). 1(4): p. 189-192.
- [121] Braunstein, R., Radiative Transitions in Semiconductors. Physical Review, (1955). 99(6): p. 1892.
- [122] Sparavigna, A.C., Light-Emitting Diodes in the Solid-State Lighting Systems. arXiv preprint arXiv:1411.6620, (2014).
- [123] Holonyak Jr, N. and S. Bevacqua, Coherent (Visible) Light Emission from Ga (As1-Xpx) Junctions. Applied Physics Letters, (1962). 1(4): p. 82-83.
- [124] Perry, T.S., M. George Craford [Biography]. Spectrum, IEEE, (1995). 32(2): p. 52-55.

- [125] Nakamura, S., T. Mukai, and M. Senoh, Candela-Class High-Brightness Ingan/Algan Double-Heterostructure Blue-Light-Emitting Diodes. Applied Physics Letters, (1994). 64(13): p. 1687-1689.
- [126] Minami, T., M. Tanigawa, M. Yamanishi, and T. Kawamura, Observation of Ultraviolet-Luminescence from the ZnO Mis Diodes. Japanese Journal of Applied Physics, (1974). 13(9): p. 1475.
- [127] Faugier-Tovar, J., F. Lazar, C. Marichy, and C. Brylinski, Influence of the Lattice Mismatch on the Atomic Ordering of ZnO Grown by Atomic Layer Deposition onto Single Crystal Surfaces with Variable Mismatch (Inp, Gaas, Gan, Sic). Condensed Matter, (2017). 2(1): p. 3.
- [128] Kobayashi, A., S. Kawano, Y. Kawaguchi, J. Ohta, and H. Fujioka, Room Temperature Epitaxial Growth of M-Plane Gan on Lattice-Matched ZnO Substrates. Applied physics letters, (2007). 90(4): p. 041908.
- [129] Hong, S.-K., T. Hanada, H. Makino, Y. Chen, H.-J. Ko, T. Yao, A. Tanaka, H. Sasaki, and S. Sato, Band Alignment at a ZnO/GaN (0001) Heterointerface. Applied Physics Letters, (2001). 78(21): p. 3349-3351.
- [130] Vispute, R., et al., Heteroepitaxy of ZnO on GaN and Its Implications for Fabrication of Hybrid Optoelectronic Devices. Applied Physics Letters, (1998). 73(3): p. 348-350.
- [131] Willander, M., et al., Zinc Oxide Nanorod Based Photonic Devices: Recent Progress in Growth, Light Emitting Diodes and Lasers. Nanotechnology, (2009). 20(33): p. 332001.
- [132] Zheng, Z., Z.S. Lim, Y. Peng, L. You, L. Chen, and J. Wang, General Route to ZnO Nanorod Arrays on Conducting Substrates Via Galvanic-Cell-Based Approach. Scientific reports, (2013). 3: p. 2434.
- [133] Yang, Z.-P., Z.-H. Xie, C.-C. Lin, and Y.-J. Lee, Slanted n-ZnO Nanorod Arrays/p-GaN Light-Emitting Diodes with Strong Ultraviolet Emissions. Optical Materials Express, (2015). 5(2): p. 399-407.
- [134] Alivov, Y.I., J. Van Nostrand, D.C. Look, M. Chukichev, and B. Ataev, Observation of 430 nm Electroluminescence from ZnO/GaN Heterojunction Light-Emitting Diodes. Applied Physics Letters, (2003). 83(14): p. 2943.
- [135] Alvi, N., S.U. Ali, S. Hussain, O. Nur, and M. Willander, Fabrication and Comparative Optical Characterization of N-Zno Nanostructures (Nanowalls, Nanorods, Nanoflowers and Nanotubes)/p-GaN White-Light-Emitting Diodes. Scripta Materialia, (2011). 64(8): p. 697-700.
- [136] Park, S.-H., S.-H. Kim, and S.-W. Han, Growth of Homoepitaxial Zno Film on ZnO Nanorods and Light Emitting Diode Applications. Nanotechnology, (2007). 18(5): p. 055608.

- [137] Lupan, O., T. Pauporté, and B. Viana, Low-Voltage Uv-Electroluminescence from Zno-Nanowire Array/p-GaN Light-Emitting Diodes. Advanced Materials, (2010). 22(30): p. 3298-3302.
- [138] Guo, R., J. Nishimura, M. Matsumoto, M. Higashihata, D. Nakamura, and T. Okada, Electroluminescence from Zno Nanowire-Based p-GaN/n-ZnO Heterojunction Light-Emitting Diodes. Applied Physics B, (2009). 94(1): p. 33-38.
- [139] Kern, W., The Evolution of Silicon Wafer Cleaning Technology. Journal of the Electrochemical Society, (1990). 137(6): p. 1887-1892.
- [140] Garnier, J., R. Parize, E. Appert, O. Chaix-Pluchery, A. Kaminski-Cachopo, and V. Consonni, Physical Properties of Annealed ZnO Nanowire/Cusch Heterojunctions for Self-Powered UV Photodetectors. ACS applied materials & interfaces, (2015). 7(10): p. 5820-5829.
- [141] Hill, K., An Investigation of Palladium Oxidation in the Platinum/Palladium Thermocouple System. Metrologia, (2002). 39(1): p. 51.
- [142] Wrbanek, J.D. and K.L. Laster, Preparation and Analysis of Platinum Thin Films for High Temperature Sensor Applications. (2005).
- [143] Intertek Plastics Technology Laboratories. Available from: http://www.ptli.com/testlopedia/tests/DSC-d3417-more.asp.
- [144] Menczel, J.D. and R.B. Prime, Thermal Analysis of Polymers, Fundamentals and Applications. (2009): John Wiley & Sons.
- [145] Zachariasen, W.H., Theory of X-Ray Diffraction in Crystals. (2004): Courier Corporation.
- [146] Fultz, B. and J.M. Howe, Transmission Electron Microscopy and Diffractometry of Materials. (2012): Springer Science & Business Media.
- [147] Warren, B.E., X-Ray Diffraction. (1969): Courier Dover Publications.
- [148] Klug, H.P. and L.E. Alexander, X-Ray Diffraction Procedures: For Polycrystalline and Amorphous Materials. X-Ray Diffraction Procedures: For Polycrystalline and Amorphous Materials, 2nd Edition, by Harold P. Klug, Leroy E. Alexander, pp. 992. ISBN 0-471-49369-4. Wiley-VCH, May 1974., (1974). 1.
- [149] TEM. Nanotechnology. Access date 025/07/2016]; Available from: http://barrett-group.mcgill.ca/tutorials/nanotechnology/nano02.htm.
- [150] Butt, H.-J., Electrostatic Interaction in Atomic Force Microscopy. Biophysical journal, (1991). 60(4): p. 777.

- [151] Carpick, R.W. and M. Salmeron, Scratching the Surface: Fundamental Investigations of Tribology with Atomic Force Microscopy. Chemical Reviews, (1997). 97(4): p. 1163-1194.
- [152] Schroder, D.K., Semiconductor Material and Device Characterization. (2006): John Wiley & Sons.
- [153] Gfroerer, T.H., Photoluminescence in Analysis of Surfaces and Interfaces. Encyclopedia of analytical chemistry, (2000).
- [154] Sakurai, Y., K. Kakushima, K. Ohmori, K. Yamada, H. Iwai, K. Shiraishi, and S. Nomura, Photoluminescence Characterization in Silicon Nanowire Fabricated by Thermal Oxidation of Nano-Scale Si Fin Structure. Optics express, (2014). 22(2): p. 1997-2006.
- [155] KRISHNAN, K., A New Class of Spectra Due to Secondary Radiation Part I. Indian J. Phys, (1928). 2: p. 399-419.
- [156] Ultraviolet and Visible Spectroscopy. [cited 2016 21/7/2016]; Available from:

 https://upload.wikimedia.org/wikipedia/commons/9/95/Schematic of UV-visible spectrophotometer.png.
- [157] Tauc, J., R. Grigorovici, and A. Vancu, Optical Properties and Electronic Structure of Amorphous Germanium. physica status solidi (b), (1966). 15(2): p. 627-637.
- [158] Van Tong, P., N.D. Hoa, N. Van Duy, V. Van Quang, N.T. Lam, and N. Van Hieu, In-Situ Decoration of Pd Nanocrystals on Crystalline Mesoporous NiO Nanosheets for Effective Hydrogen Gas Sensors. International Journal of Hydrogen Energy, (2013). 38(27): p. 12090-12100.
- [159] Ladhe, R., K. Gurav, S. Pawar, J. Kim, and B. Sankapal, P-Pedot: Pss as a Heterojunction Partner with n-ZnO for Detection of Lpg at Room Temperature. Journal of Alloys and Compounds, (2012). 515: p. 80-85.
- [160] Zhang, L., J. Zhao, H. Lu, L. Gong, L. Li, J. Zheng, H. Li, and Z. Zhu, High Sensitive and Selective Formaldehyde Sensors Based on Nanoparticle-Assembled ZnO Micro-Octahedrons Synthesized by Homogeneous Precipitation Method. Sensors and Actuators B: Chemical, (2011). 160(1): p. 364-370.
- [161] Aswal, D.K. and S.K. Gupta, Science and Technology of Chemiresistor Gas Sensors. (2007): Nova Publishers.
- [162] Intertek. Plastics Technology Laboratories. [cited 2016; Available from: http://www.ptli.com/testlopedia/tests/DSC-d3417-more.asp.

- [163] Xie, X., S. Tjong, and R. Li, Study on in Situ Reinforcing and Toughening of a Semiflexible Thermotropic Copolyesteramide in Pbt/Pa66 Blends. Journal of applied polymer science, (2000). 77(9): p. 1975-1988.
- [164] Simoes, A., A. Gonzalez, M. Zaghete, J. Varela, and B. Stojanovic, Effects of Annealing on the Crystallization and Roughness of Plzt Thin Films. Thin solid films, (2001). 384(1): p. 132-137.
- [165] Akhavan, O., M. Mehrabian, K. Mirabbaszadeh, and R. Azimirad, Hydrothermal Synthesis of ZnO Nanorod Arrays for Photocatalytic Inactivation of Bacteria. Journal of Physics D: Applied Physics, (2009). 42(22): p. 225305.
- [166] Shin, C., et al., Effects of the Annealing Duration of the Zno Buffer Layer on Structural and Optical Properties of ZnO Rods Grown by a Hydrothermal Process. Applied Surface Science, (2009). 255(20): p. 8501-8505.
- [167] Yang, J., J. Lang, L. Yang, Y. Zhang, D. Wang, H. Fan, H. Liu, Y. Wang, and M. GaO, Low-Temperature Growth and Optical Properties of ZnO Nanorods. Journal of Alloys and Compounds, (2008). 450(1): p. 521-524.
- [168] Yang, M., G. Yin, Z. Huang, X. Liao, Y. Kang, and Y. Yao, Well-Aligned ZnO Rod Arrays Grown on Glass Substrate from Aqueous Solution. Applied surface science, (2008). 254(10): p. 2917-2921.
- [169] Banerjee, A., C. Ghosh, K. Chattopadhyay, H. Minoura, A.K. Sarkar, A. Akiba, A. Kamiya, and T. Endo, Low-Temperature Deposition of ZnO Thin Films on Pet and Glass Substrates by Dc-Sputtering Technique. Thin Solid Films, (2006). 496(1): p. 112-116.
- [170] Raoufi, D. and T. Raoufi, The Effect of Heat Treatment on the Physical Properties of Sol-Gel Derived ZnO Thin Films. Applied Surface Science, (2009). 255(11): p. 5812-5817.
- [171] Pankove, J.I., Optical Processes in Semiconductors. (2012): Courier Dover Publications.
- [172] Mulmi, D.D., A. Dhakal, and B.R. Shah, Effect of Annealing on Optical Properties of Zinc Oxide Thin Films Prepared by Homemade Spin Coater. Nepal Journal of Science and Technology, (2015). 15(2): p. 111-116.
- [173] Ji, L., S. Peng, Y.-K. Su, S.-J. Young, C. Wu, and W. Cheng, Ultraviolet Photodetectors Based on Selectively Grown ZnO Nanorod Arrays. Applied Physics Letters, (2009). 94(20): p. 203106.
- [174] Ghosh, T. and D. Basak, Highly Efficient Ultraviolet Photodetection in Nanocolumnar Rf Sputtered Zno Films: A Comparison between Sputtered, Sol-Gel and Aqueous Chemically Grown Nanostructures. Nanotechnology, (2010). 21(37): p. 375202.

- [175] Garcia-Martinez, O., R. Rojas, E. Vila, and J.M. De Vidales, Microstructural Characterization of Nanocrystals of ZnO and CuO Obtained from Basic Salts. Solid State Ionics, (1993). 63: p. 442-449.
- [176] Chen, G., Y. Hang, J. Yin, C. Zhao, L. Zhang, and P. Zhang, Optical Characteristics of ZnO Single Crystal Grown by the Hydrothermal Method. Materials Science: An Indian Journal, (2014). 10(4).
- [177] Qiu, J., B. Weng, L. Zhao, C. Chang, Z. Shi, X. Li, H.-K. Kim, and Y.-H. Hwang, Synthesis and Characterization of Flower-Like Bundles of ZnO Nanosheets by a Surfactant-Free Hydrothermal Process. Journal of Nanomaterials, (2014). 2014: p. 211.
- [178] Koutu, V., L. Shastri, and M. Malik, Effect of Naoh Concentration on Optical Properties of Zinc Oxide Nanoparticles. Materials Science-Poland, (2016). 34(4): p. 819-827.
- [179] Pung, S., C. Ong, K.M. Isha, and M. Othman, Synthesis and Characterization of Cu-Doped ZnO Nanorods. Sains Malaysiana, (2014). 43(2): p. 273-281.
- [180] Liu, J., C. Xu, G. Zhu, X. Li, Y. Cui, Y. Yang, and X. Sun, Hydrothermally Grown ZnO Nanorods on Self-Source Substrate and Their Field Emission. Journal of Physics D: Applied Physics, (2007). 40(7): p. 1906.
- [181] Jung, E.S., J.Y. LEE, H.S. Kim, and N.W. Jang, Structural and Optical Characteristics of ZnO Films with Oxygen Content. Journal of the Korean Physical Society, (2005). 47: p. S480-S484.
- [182] Huang, R., Z. Lin, Y. Guo, C. Song, X. Wang, H. Lin, L. Xu, J. Song, and H. Li, Bright Red, Orange-Yellow and White Switching Photoluminescence from Silicon Oxynitride Films with Fast Decay Dynamics. Optical Materials Express, (2014). 4(2): p. 205-212.
- [183] Su, J., S. Ye, X. Yi, F. Lu, X. Yang, and Q. Zhang, Influence of Oxygen Vacancy on Persistent Luminescence in Znga 2 O 4: Cr 3+ and Identification of Electron Carriers. Optical Materials Express, (2017). 7(3): p. 734-743.
- [184] Baruah, S., M.A. Mahmood, M.T.Z. Myint, T. Bora, and J. Dutta, Enhanced Visible Light Photocatalysis through Fast Crystallization of Zinc Oxide Nanorods. Beilstein journal of nanotechnology, (2010). 1(1): p. 14-20.
- [185] Lupan, O., V. Ursaki, G. Chai, L. Chow, G. Emelchenko, I. Tiginyanu, A. Gruzintsev, and A. Redkin, Selective Hydrogen GaS Nanosensor Using Individual ZnO Nanowire with Fast Response at Room Temperature. Sensors and Actuators B: Chemical, (2010). 144(1): p. 56-66.
- [186] Sze, S.M., Semiconductor Devices: Physics and Technology. (2002): John Wiley & Sons. p. 179.

- [187] Zhou, H., G.-J. Fang, N. Liu, and X.-Z. Zhao, Effects of Thermal Annealing on the Performance of Al/ZnO Nanorods/Pt Structure Ultraviolet Photodetector. Materials Science and Engineering: B, (2011). 176(9): p. 740-744.
- [188] Lu, L. and M. Wong, The Resistivity of Zinc Oxide under Different Annealing Configurations and Its Impact on the Leakage Characteristics of Zinc Oxide Thin-Film Transistors. IEEE Transactions on Electron Devices, (2014). 61(4): p. 1077-1084.
- [189] Verma, M. and V. Gupta, P1. 0.13 Highly Sensitive ZnO- SnO₂ Nanocomposite H₂ Gas Sensor. Proceedings IMCS 2012, (2012): p. 787-790.
- [190] Widanarto, W., C. Senft, O. Senftleben, W. Hansch, and I. Eisele, Characterization and Sensing Properties of Zno Film in Fg-Fet Sensor System for NO₂ Detection. International Journal of Basic & Applied Sciences IJBAS-IJENS, (2011). 11(1): p. 104-108.
- [191] Horrillo, M., P. Serrini, J. Santos, and L. Manes, Influence of the Deposition Conditions of SnO₂ Thin Films by Reactive Sputtering on the Sensitivity to Urban Pollutants. Sensors and Actuators B: Chemical, (1997). 45(3): p. 193-198.
- [192] Karthigeyan, A., R. Gupta, K. Scharnagl, M. Burgmair, M. Zimmer, S. Sharma, and I. Eisele, Low Temperature NO₂ Sensitivity of Nano-Particulate SnO₂ Film for Work Function Sensors. Sensors and Actuators B: Chemical, (2001). 78(1): p. 69-72.
- [193] Mukhopadhyay, S.C., G.S. Gupta, and Y.-M.R. Huang, Recent Advances in Sensing Technology. (2009): Springer.
- [194] Lin, Z.-H., Y. Xie, Y. Yang, S. Wang, G. Zhu, and Z.L. Wang, Enhanced Triboelectric Nanogenerators and Triboelectric Nanosensor Using Chemically Modified TiO₂ Nanomaterials. ACS nano, (2013). 7(5): p. 4554-4560.
- [195] Al-Salman, H.S. and M. Abdullah, Hydrogen Gas Sensing Based on ZnO Nanostructure Prepared by Rf-Sputtering on Quartz and Pet Substrates. Sensors and Actuators B: Chemical, (2013). 181: p. 259-266.
- [196] Hassan, K., A.I. Uddin, F. Ullah, Y.S. Kim, and G.-S. Chung, Platinum/Palladium Bimetallic Ultra-Thin Film Decorated on a One-Dimensional ZnO Nanorods Array for Use as Fast Response Flexible Hydrogen Sensor. Materials Letters, (2016). 176: p. 232-236.
- [197] Drmosh, Q., Z. Yamani, and M. Hossain, Hydrogen Gas Sensing Performance of Low Partial Oxygen-Mediated Nanostructured Zinc Oxide Thin Film. Sensors and Actuators B: Chemical, (2017).

- [198] Sett, D. and D. Basak, Highly Enhanced H₂ Gas Sensing Characteristics of Co: ZnO Nanorods and Its Mechanism. Sensors and Actuators B: Chemical, (2017). 243: p. 475-483.
- [199] Hassan, K. and G.-S. Chung, Catalytically Activated Quantum-Size Pt/Pd Bimetallic Core-Shell Nanoparticles Decorated on ZnO Nanorod Clusters for Accelerated Hydrogen Gas Detection. Sensors and Actuators B: Chemical, (2017). 239: p. 824-833.
- [200] Zhao, X., et al., Effects of Buffer Layer Annealing Temperature on the Structural and Optical Properties of Hydrothermal Grown ZnO. Applied Surface Science, (2009). 255(8): p. 4461-4465.
- [201] Mamat, M.H., Z. Khusaimi, M.M. Zahidi, and M.R. Mahmood, Performance of an Ultraviolet Photoconductive Sensor Using Well-Aligned Aluminium-Doped Zinc-Oxide Nanorod Arrays Annealed in an Air and Oxygen Environment. Japanese Journal of Applied Physics, (2011). 50(6).
- [202] Elfadill, N.G., M. Hashim, K.M. Chahrour, M. Qaeed, and M. Bououdina, The Influence of Cu₂O Crystal Structure on the Cu₂O/ZnO Heterojunction Photovoltaic Performance. Superlattices and Microstructures, (2015). 85: p. 908-917.
- [203] Sayago, I., et al., Hydrogen Sensors Based on Carbon Nanotubes Thin Films. Synthetic Metals, (2005). 148(1): p. 15-19.
- [204] Hassan, J., M. Mahdi, C. Chin, H. Abu-Hassan, and Z. Hassan, Room Temperature Hydrogen Gas Sensor Based on ZnO Nanorod Arrays Grown on a SiO₂/Si Substrate Via a Microwave-Assisted Chemical Solution Method. Journal of Alloys and Compounds, (2013). 546: p. 107-111.
- [205] Tronc, P., V. Stevanovic, I. Milosevic, and M. Damnjanovic, Symmetry Properties of ZnO Nanorods and Nanotubes. Physica Status Solidi B: Basic Research, (2006). 243(8): p. 1750-1756.
- [206] Youn, C., T. Jeong, M. Han, and J. Kim, Optical Properties of Zn-Terminated Zno Bulk. Journal of crystal growth, (2004). 261(4): p. 526-532.
- [207] Xing, Y., et al., Optical Properties of the ZnO Nanotubes Synthesized Via Vapor Phase Growth. Applied Physics Letters, (2003). 83(9): p. 1689-1691.
- [208] Polsongkram, D., P. Chamninok, S. Pukird, L. Chow, O. Lupan, G. Chai, H. Khallaf, S. Park, and A. Schulte, Effect of Synthesis Conditions on the Growth of ZnO Nanorods Via Hydrothermal Method. Physica B: Condensed Matter, (2008). 403(19): p. 3713-3717.
- [209] Li, J. and H. Li, Physical and Electrical Performance of Vapor-Solid Grown ZnO Straight Nanowires. Nanoscale research letters, (2009). 4(2): p. 165-168.

- [210] Venkatesh, P.S. and K. Jeganathan, Investigations on the Growth and Characterization of Vertically Aligned Zinc Oxide Nanowires by Radio Frequency Magnetronsputtering. Journal of Solid State Chemistry, (2013). 200: p. 84-89.
- [211] Khan, A., Raman Spectroscopic Study of the Zno Nanostructures. J. Pak. Mater. Soc, (2010). 4: p. 5-9.
- [212] Jha, S., J.-C. Qian, O. Kutsay, J. Kovac Jr, C.-Y. Luan, J.A. Zapien, W. Zhang, S.-T. Lee, and I. Bello, Violet-Blue Leds Based on p-GaN/n-ZnO Nanorods and Their Stability. Nanotechnology, (2011). 22(24): p. 245202.
- [213] Shih, H.-Y., S.-H. Cheng, J.-K. Lian, T.-Y. Lin, and Y.-F. Chen, Light-Emitting Devices with Tunable Color from ZnO Nanorods Grown on InGaN/GaN Multiple Quantum Wells. Optics express, (2012). 20(102): p. A270-A277.
- [214] Von Pezold, J. and P. Bristowe, Atomic Structure and Electronic Properties of the Gan/Zno (0001) Interface. Journal of materials science, (2005). 40(12): p. 3051-3057.
- [215] Umar, A., B. Karunagaran, E. Suh, and Y. Hahn, Structural and Optical Properties of Single-Crystalline ZnO Nanorods Grown on Silicon by Thermal Evaporation. Nanotechnology, (2006). 17(16): p. 4072.
- [216] Tong, F., et al., Growth of ZnO Nanorod Arrays on Flexible Substrates: Effect of Precursor Solution Concentration. ISRN Nanomaterials, (2012). 2012.
- [217] Shahedipour, F. and B. Wessels, Investigation of the Formation of the 2.8 Ev Luminescence Band in p-Type GaN: Mg. Applied Physics Letters, (2000). 76(21): p. 3011-3013.
- [218] Freitas Jr, J. and W. Moore, Optical Studies of Undoped and Doped Wide Bandgap Carbide and Nitride Semiconductors. Brazilian journal of physics, (1998). 28(1): p. 12-18.
- [219] Yu, Q.-X., B. Xu, Q.-H. Wu, Y. Liao, G.-Z. Wang, R.-C. Fang, H.-Y. Lee, and C.-T. Lee, Optical Properties of ZnO/GaN Heterostructure and Its near-Ultraviolet Light-Emitting Diode. Applied physics letters, (2003). 83(23): p. 4713-4715.
- [220] Monemar, B., et al., Properties of the Main Mg-Related Acceptors in GaN from Optical and Structural Studies. Journal of Applied Physics, (2014). 115(5): p. 053507.
- [221] Sze, S.M. and K.K. Ng, Physics of Semiconductor Devices. (2006): John Wiley & Sons.

- [222] Rogers, D., F.H. Teherani, A. Yasan, K. Minder, P. Kung, and M. Razeghi, Electroluminescence at 375 nm from a ZnO/GaN: Mg/C-Al~ 2o~ 3 Heterojunction Light Emitting Diode. Applied physics letters, (2006). 88(14): p. 141918.
- [223] AnChiu, C., W. Xian, and C.F. Moss, Flying in Silence: Echolocating Bats Cease Vocalizing to Avoid Sonar Jamming. Proceedings of the National Academy of Sciences of the United States of America, (2008). 105(35): p. 13116-13121.
- [224] Li, S., et al., Ultraviolet/Violet Dual-Color Electroluminescence Based on n-ZnO Single Crystal/p-GaN Direct-Contact Light-Emitting Diode. Journal of Luminescence, (2013). 140: p. 110-113.

APPENDICES

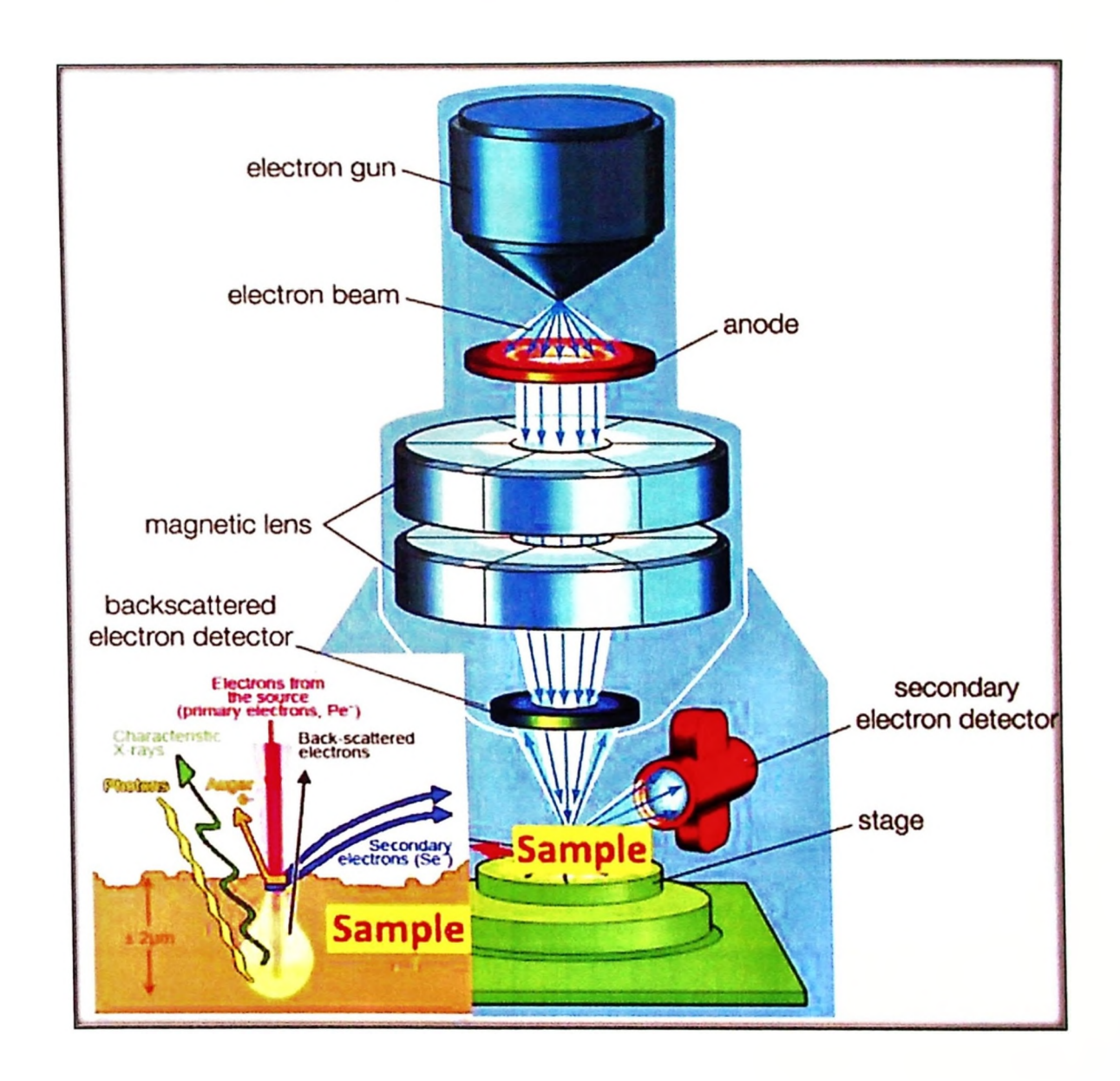
8.1 Appendix A

Tube furnace model: F21100.



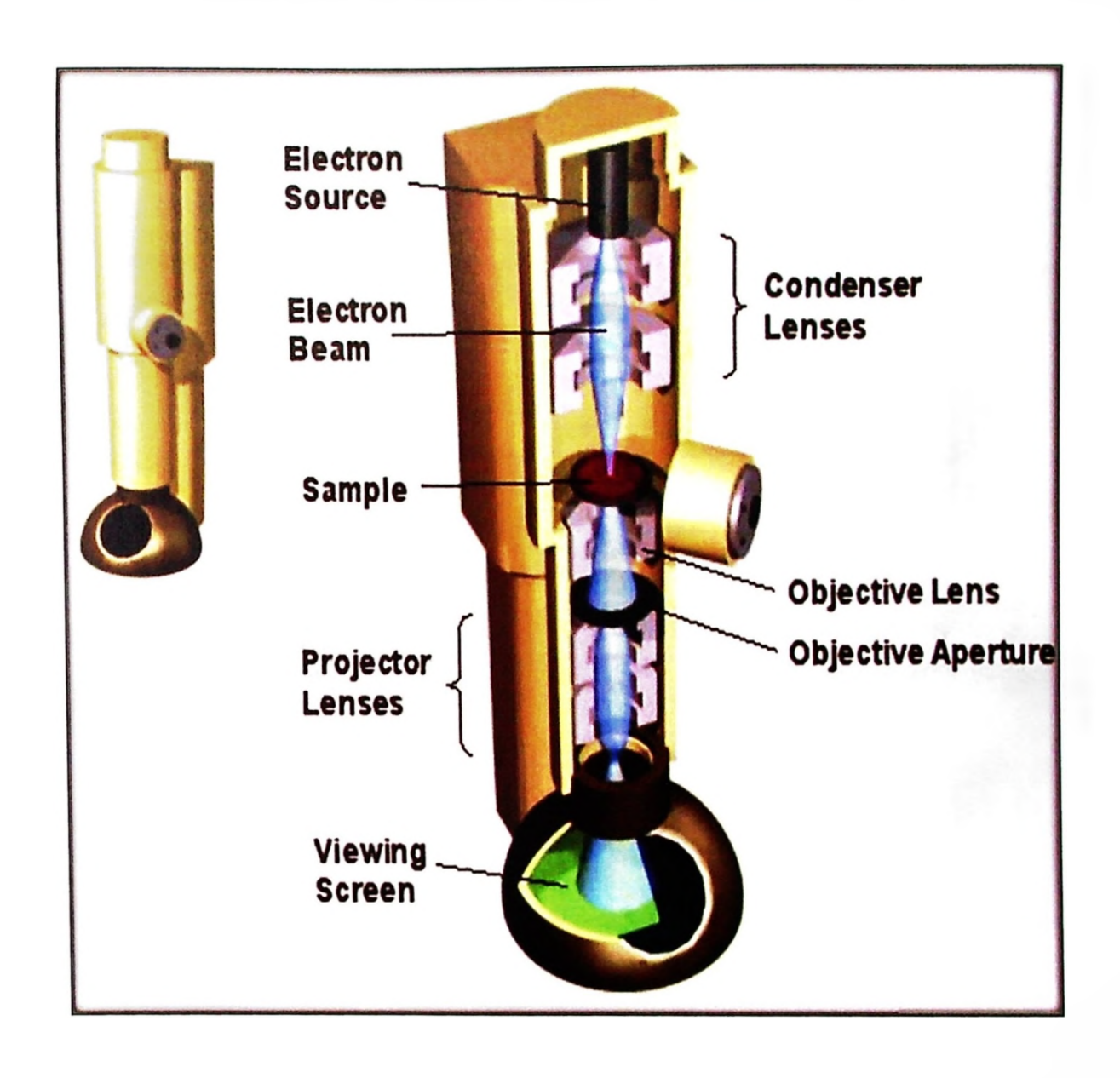
8.2 Appendix B

Schematic diagram of FESEM and various emissions from the sample when electron beams interact with the sample.



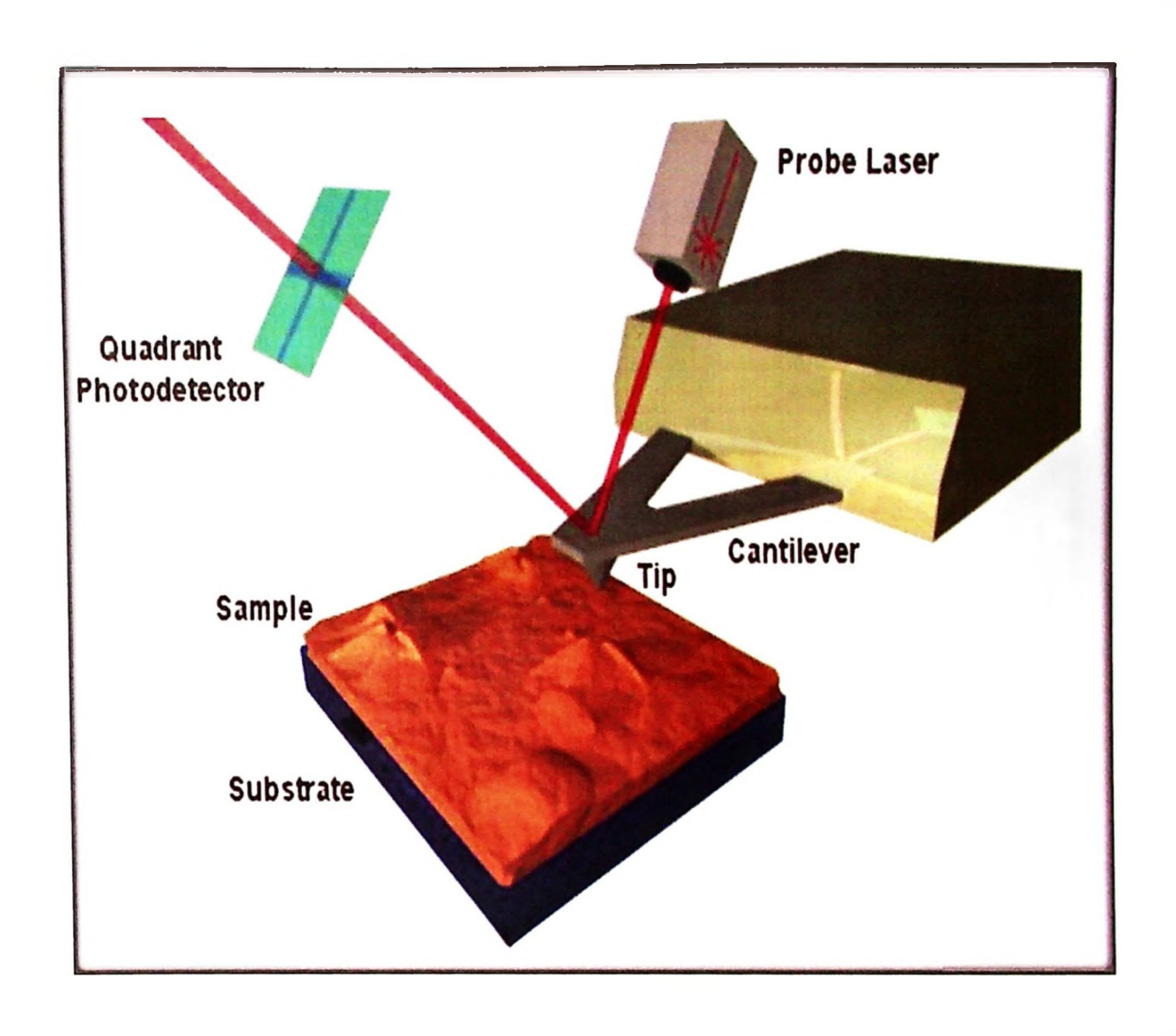
8.3 Appendix C

Real optical photo and schematic diagram for the cross section of TEM.



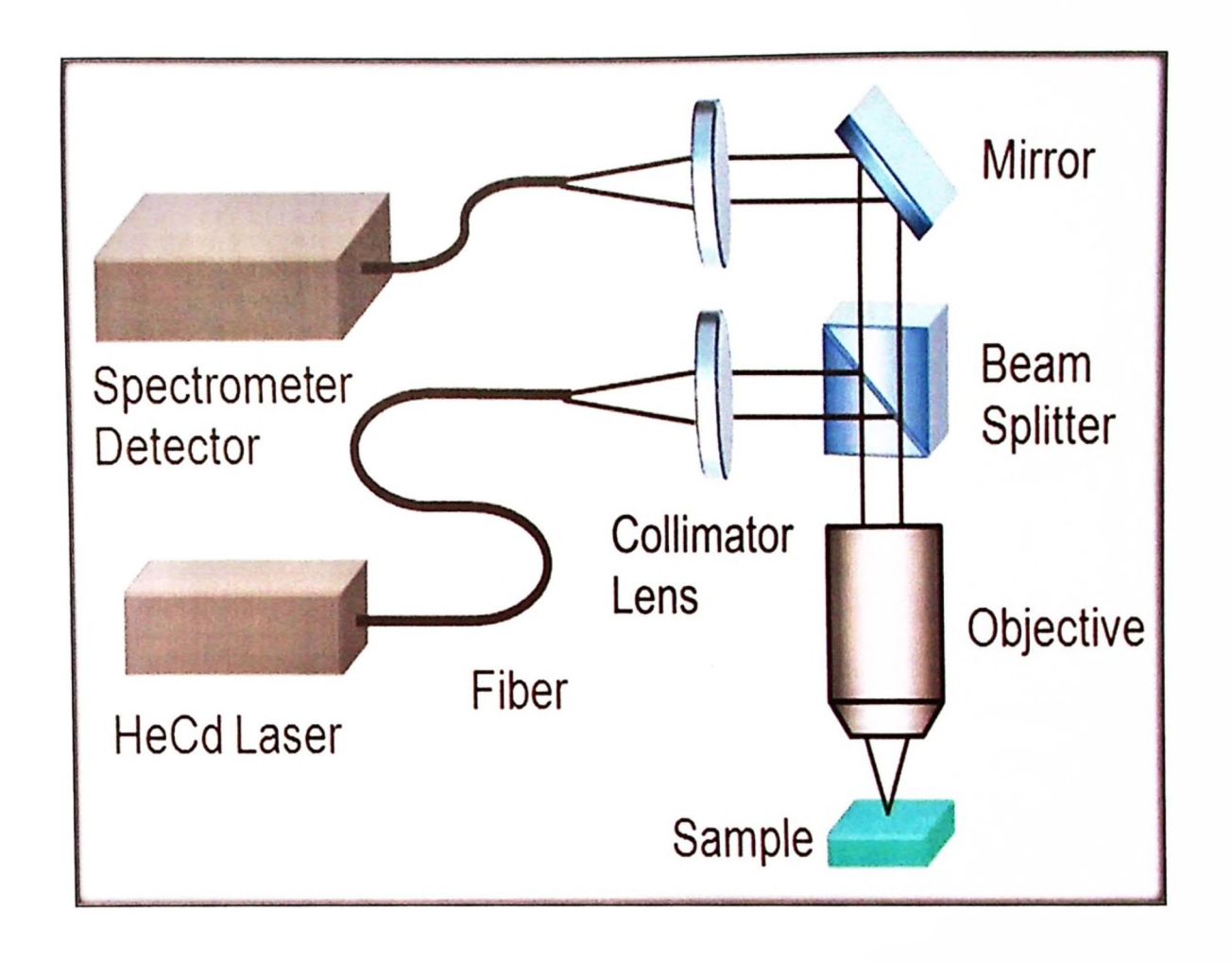
8.4 Appendix D

Schematic illustration of an atomic force microscope.



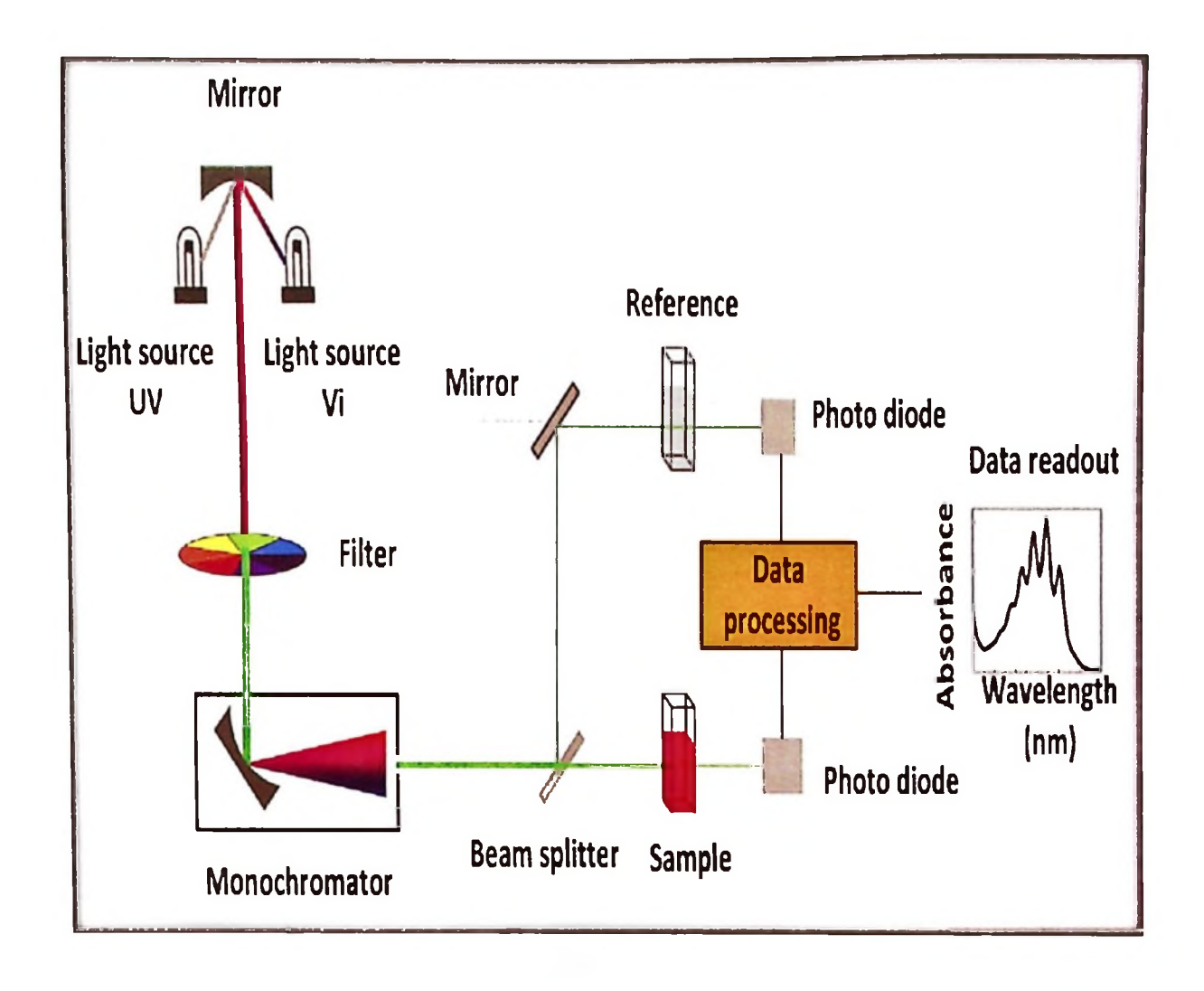
8.5 Appendix E

Schematic diagram of a PL system.



8.6 Appendix F

Schematic of a double beam UV-vis spectrophotometer.



LIST OF PUPLICATIONS

1- PATENT

1. Z Hassan, Sabah M. Mohammad, and Naser M. Ahmed: Direct heat substrate-modified chemical bath deposition system for growth of ultralong zinc oxide (ZnO) nanorods and process for fabrication of a nano-size junction LED. (2016). Application No: PI 2016702309, Filing Date: 22 Jun 2016.

2- INTERNATIONAL PUBLICATIONS

- 1. Sabah M. Mohammad, Z Hassan, Naser M. Ahmed, N.H. Al-Hardan, and M. Bououdina "Fabrication of low cost UV photo detector using ZnO nanorods grown onto nylon substrate." Journal of Materials Science: Materials in Electronics 26.3 (2015): 1322-1331.
- Sabah M. Mohammad, Z Hassan, Rawnaq A. Talib, Naser M. Ahmed, Mohammed A. Al-Azawi, Nabeel M. Abd-Alghafour, and C.W. Chin, N.H. Al-Hardan. "Fabrication of a highly flexible low-cost H₂ gas sensor using ZnO nanorods grown on an ultra-thin nylon substrate." Journal of Materials Science: Materials in Electronics: (2016) (Vol 27, issu 9).
- 3. Sabah M. Mohammad, Z Hassan, Naser M. Ahmed, Rawnaq A. Talib, Nabeel M. Abd-Alghafour, and A. F. Omar: "Hydrothermal growth and characterization of vertically well-aligned and dense ZnO nanorods on glass and silicon using a simple optimizer system". AIP Publishing. (IC-NET 2015) (Vol. 1733, No. 1, p. 020032).

3- CONFERENCES

- 1. Sabah M. Mohammad, Z Hassan, Naser M. Ahmed, Rawnaq A. Talib, Nabeel M. Abd-Alghafour, and A. F. Omar: "Hydrothermal growth and characterization of vertically well-aligned and dense ZnO nanorods on glass and silicon using a simple optimizer system". International Conference on Nano-Electronic Technology Devices and Materials 2015 (ic-net 2015) (vol. 1733, no. 1, p. 020032). AIP Publishing.
- 2. Sabah M. Mohammad, Z Hassan, and Naser M. Ahmed: "Ultraviolet photodetector of vertically aligned zno nanorods synthesized using hydrothermal method on glass substrate". The Regional Fundamental Science Congress 2014, (FSC2014). Code No. PHY-0014. UPM.

4- OTHER PUBLICATIONS

- 1. Mohammed A. Al-Azawi, Noriah Bidin, M. Bououdina, and Sabah M. Mohammad. "Preparation of gold and gold-silver alloy nanoparticles for enhancement of plasmonic dye-sensitized solar cells performance." Solar Energy 126" (2016): 93-104.
- 2. M. Z. Mohd Yusoff, A. Mahyuddin, Z Hassan, H. Abu Hassan, M. J. Abdullah, M.Rusop, S. M. Mohammad, and Naser M. Ahmed. "AlN/GaN/AlN heterostructures grown on Si substrate by plasma-assisted MBE for MSM UV photodetector applications". Materials Science in Semiconductor Processing 29 (2015): 231-237.
- 3. Naif H. Al-Hardan, Muhammad Azmi Abdul Hamid, Naser M. Ahmed, Azman Jalar, Roslinda Shamsudin, Norinsan Kamil Othman, Lim Kar Keng, Sabah M. Mohammed. "A study on the uv photoresponse of hydrothermally grown zinc oxide nanorods with different aspect ratios." IEEE Sensors Journal 15.12 (2015): 6811-6818.
- 4. Rawnaq A. Talib, M.J. Abdullah, Sabah M. Mohammad, Naser M. Ahmed, Nageh K. Allam "ZnO nanorods/polyaniline-based inorganic/organic heterojunctions for enhanced light sensing applications." ECS Journal of Solid State Science and Technology 5.3 (2016): P142-P147.
- 5. Rawnaq A. Talib, M.J. Abdullah, Sabah M. Mohammad, Naser M. Ahmed, Nageh K Allam". Efect of substrate on the photodetection characteristics of ZnO-PANI composites". ECS Journal of Solid State Science and Technology 5.6 (2016): P305-P308.
- 6. Rawnaq A. Talib, M.J. Abdullah, Husam S. Al-Salman, Sabah M. Mohammad, and Nageh K Allam "ZnO nanorods/polyaniline heterojunctions for low-power flexible light sensors." Materials Chemistry and Physics 181 (2016): 7-11.
- 7. Rawnaq A. Talib, M.J. Abdullah, Husam S. Al-Salman, Sabah M. Mohammad, N. M. Ahmed, and M. Bououdina. "Effect of growth time on structure, optical and photo-response characteristics of ZnO nanorods deposited onto various substrates." Journal of Ovonic Research Vol 12.3 (2016): 171-184.
- 8. N.M. Abd-Alghafour, Naser M. Ahmed, Z Hassan, Sabah M. Mohammad, and M. Bououdina, M.K.M. Ali "Characterization of V₂O₅ nanorods grown by spray pyrolysis technique." Journal of Materials Science: Materials in Electronics 27.5 (2016): 4613-4621.
- 9. Rawnaq A. Talib, M.J. Abdullah, Naser M Ahmed, Sabah M. Mohammad, and M. Bououdina. "UV sensing of twinned ZnO-PANI composite." Applied Physics A 122.5 (2016): 1-9.

- 10. N.M. Abd-Alghafour, Naser Ahmed, Z Hassan, Sabah M. Mohammad, M. Bououdina, and M.K. M. Ali. "Structural, morphological and optical properties of V₂O₅ nanorods grown using spray pyrolysis technique at different substrate temperature." Nanoscience and Nanotechnology Letters 8.2 (2016): 181-186.
- 11. Rawnaq A. Talib, M. J. Abdullah, and Sabah M. Mohammad. "Formation and analysis of ZnO-PAni hexagonal prisms composite prepared by chemical method." AIP Publishing, 2016. (IC-NET 2015). Vol. 1733. No. 1.
- 12. N. M. Abd-Alghafour, Naser M. Ahmed, Zai Hassan, Sabah M. Mohammad, and M. Bououdina "Growth and characterization of V₂O₅ nanorods deposited by spray pyrolysis at low temperatures." AIP Publishing, (IC-NET 2015). Vol. 1733. No. 1.
- 13. N.M. Abd-Alghafour, Naser M. Ahmed, Zai Hassan, and Sabah M. Mohammad."Influence of solution deposition rate on properties of V₂O₅ thin films deposited by spray pyrolysis technique." AIP Publishing, 2016. (ICOFM 2016). Vol. 1756. No. 1.

5- OTHER CONFERENCES

- N. M. Abd-Alghafour, Naser M. Ahmed, Zai Hassan, Sabah M. Mohammad, M. Bououdina. "Growth and characterization of V2O5 nanorods deposited by spray pyrolysis at low temperatures." International Conference on Nano-Electronic Technology Devices and Materials 2015 (ic-net 2015). Vol. 1733. No. 1. AIP Publishing, 2016.
- 2. Rawnaq A. Talib, M. J. Abdullah, and Sabah M. Mohammad. "Formation and analysis of ZnO-PAni hexagonal prisms composite prepared by chemical method." International Conference on Nano-Electronic Technology Devices and Materials 2015 (IC-NET 2015). Vol. 1733. No. 1. AIP Publishing, 2016.
- N. M. Abd-Alghafour, Naser M. Ahmed, Zai Hassan, and Sabah M. Mohammad. "Influence of solution deposition rate on properties of V₂O₅ thin films deposited by spray pyrolysis technique." The 2nd International Conference on Functional Materials and Metallurgy (ICoFM 2016). Vol. 1756. No. 1. AIP Publishing, 2016.